79

Near Surface Ocean Experimental Technology Workshop Proceedings

Richard C. Swenson, Chairman
Roderick S. Mesecar, Co-Chairman

February 1980

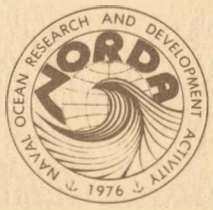

NAVAL OCEAN RESEARCH AND DEVELOPMENT ACTIVITY
NSTL Station, Mississippi 39529

FOREWORD

This collection of papers is the result of a workshop entitled "Near Surface Ocean Experimental Technology" held 6-8 November 1979 at the Naval Ocean Research and Development Activity (NORDA), NSTL Station, Mississippi.

The workshop was inaugurated by NORDA and sponsored by Chief of Naval Research to promote the exchange and mutual understanding between investigators and technologists from academic, industrial, and government laboratories committed to ocean research programs.

Participants in the workshop addressed the question of need versus measurement technique for programs investigating the physical phenomena in the upper 300 meters of the world's oceans. The contributed papers reflect the innovative equipment developments and investigative approaches currently in use.

Richard C. Swenson, Chairman
Roderick S. Mesecar, Co-Chairman

ACKNOWLEDGEMENTS

The Chairman and Co-Chairman of this workshop wish to express their appreciation to the participants for their written contributions and oral exchanges which adds the binder to this form of technology exchange.

At NORDA, special thanks to Jeannie McCoy for planning and coordination and to Carl W. Mueller for printing quality control and suggestions.

TABLE OF CONTENTS

* Presenter of Paper

* Presenter of Paper

Papers have been reproduced as received and reflect the original comments of the authors. A list of authors and addresses are appended. If further information is required, the authors should be contacted.

STATIC AND DYNAMIC ANALYSIS OF A DEEP-WATER SUBSURFACE MOORING FOR NEAR-SURFACE CURRENT MEASUREMENTS

Darrell A. Milburn
Naval Ocean Research and Development Activity
NSTL Station, MS 39529

and

Narender K. Chhabra
The Charles Stark Draper Laboratory, Inc.
Cambridge, MA 02139

Abstract

The performance of a single-point subsurface mooring for near-surface current measurements in the Gulf of Mexico is examined. Using state-of-the-art computer programs for static and dynamic analysis of single-point moorings, the response of a proposed design to forcing caused by ocean currents, waves, and deployment is predicted. These predictions are, in turn, compared with the performance criteria specified to evaluate the proposed design. It is found that the proposed design is reasonably rigid and, with high probability, will survive the environmental conditions assumed. Selected computer solutions are shown and discussed.

Introduction

The Naval Ocean Research and Development Activity is planning an oceanographic experiment to gather data on the high frequency, high wave number fluctuations occurring in the near-surface internal waves of the central Gulf of Mexico. As illustrated in Figure 1, the experiment will use three types of instrument platforms: A ship for taking environmental data; a NOAA data buoy for taking meteorological and surface wave data; and a single-point subsurface mooring for taking ocean current and mooring dynamics data. The single-point subsurface mooring, which was selected over other classes of moorings because of cost, reliability, and deployment considerations, is the primary instrument platform. It will contain 22 current meters — 17 located in the near-surface (upper 300 m of water) and the remainder spread over a significant portion of the water depth. It will be anchored near the data buoy in about 3300 m of water, and will take data for approximately seven weeks.

During the initial planning phase of the experiment, a preliminary design of the subsurface mooring was proposed. This design is shown schematically in Figure 2, and is intended to satisfy the need for a reasonably rigid measurement platform. As a next step in the design process, the performance of the proposed design was predicted by using several computer programs developed for static and dynamic mooring analyses. This is an important step since it allows the designer a comparison of the probable performance with that which is desired. Also, such analyses are useful in optimizing the design from the possibilities available.

This paper covers the problems analyzed during the initial planning phase of the experiment. Presentations include prediction of the mooring response to forcing caused by ocean currents, waves, and system deployment. Because the forcing considered can be classified as either time-independent or time-dependent, the paper is divided appropriately into two broad analytical categories. The first

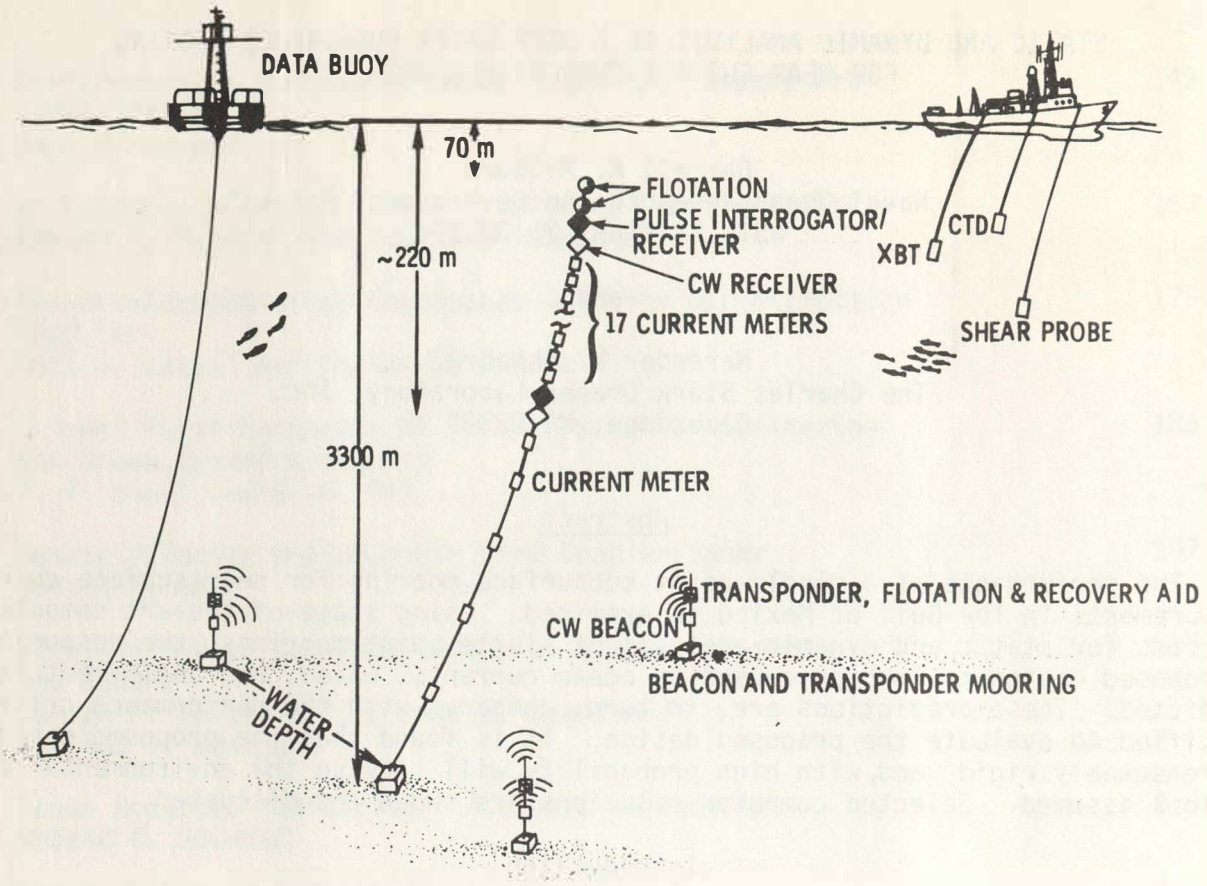

Figure 1. Schematic illustration of the experiment. As presently planned, the subsurface mooring shown in the center will be deployed in mid-December 1979. To evaluate and possibly correct the motion-contaminated current meter records, it will contain: acoustic receivers for motion measurement, and instruments for measuring such parameters as depth, temperature, tension, acceleration and inclination.

category considers the static analyses, and the second the dynamic analyses. The computer programs used to solve these analysis problems are briefly described at the beginning of each section. These computer programs are based on state-of-the-art mathematical models of cable moored systems[1] and, in addition to environmental forcing, require certain physical and hydrodynamic data for the mooring components as inputs. Reliable data for the components of the subject mooring were garnered from manufacturers data and from Reference 2.

Static Analyses

The computer programs used to solve the problems in this section are thoroughly described in References 3 and 4. They can model currents that vary in both magnitude and direction with depth. In solving the problems below, the following important features were considered: mooring line elasticity, normal and tangential hydrodynamic loading on mooring lines, forces due to gravity, in-line lengths of instruments and tackle, and drag forces on instruments.

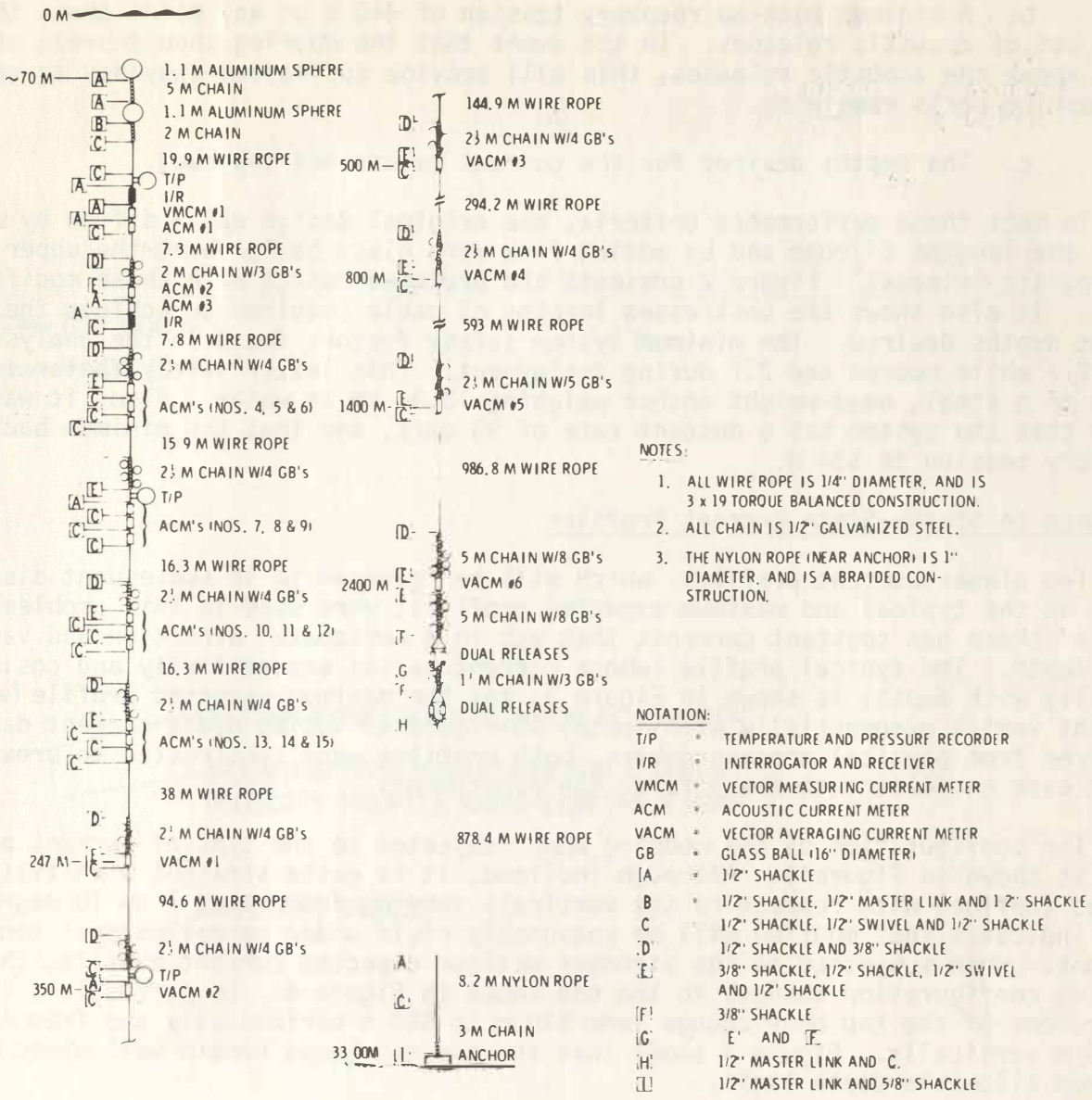

Figure 2. Preliminary design of the single-point subsurface mooring. The instruments denoted above by T/P and I/R are a tentative choice.

Design Check

The proposed design, as originally synthesized, was based on simple static, hand-calculations to size the mooring lines and tackle for adequate strength. These calculations did not include such important considerations as cable stretch, in-line lengths of instruments and tackle, back-up recovery tensions[5], and descent tensions resulting from system deployment. Hence, the problem here was to analyze the original design with the static computer programs mentioned previously, and to modify it, as necessary, to meet the following performance criteria in the absence of any currents:

a. A minimum system safety factor of 2.5 while moored and 2.0 during deployment.

b. A minimum back-up recovery tension of 440 N at any point above the upper set of acoustic releases. In the event that the mooring should break at any point above the acoustic releases, this will provide sufficient buoyancy to recover the mooring parts remaining.

c. The depths desired for the current meters and top buoy.

To meet these performance criteria, the original design was modified by shortening the lengths of rope and by adding five more glass balls above the upper set of acoustic releases. Figure 2 presents the proposed design with these modifications. It also shows the unstressed lengths of cable required to achieve the component depths desired. The minimum system safety factors found in the analysis were 2.7 while moored and 2.1 during deployment. This latter safety factor is based on a steel, dead-weight anchor weighing 13.34 kN in water. Also, it was found that the system has a descent rate of 90 cm/s, and that the minimum back-up recovery tension is 534 N.

Response to Steady-State Current Profiles

Two planar current profiles, which will be referred to in subsequent discussions as the typical and maximum expected profiles, were used in this problem. Each of these has constant currents that act in a horizontal direction and vary with depth. The typical profile (whose current varies exponentially and cosinusoidally with depth) is shown in Figure 3, and the maximum expected profile (whose current varies exponentially with depth) in Figure 4. Using ocean current data garnered from physical oceanographers, both profiles were constructed to provide worst case conditions at the site of the experiment.

The configuration of the mooring when subjected to the typical current profile is shown in Figure 3. Although inclined, it is quite straight with tilt angles (defined with respect to the vertical) varying from about 7 to 10 degrees. This indicates that mooring will be reasonably rigid under normal current conditions. When subjected to the stronger maximum expected current profile, the mooring configuration changes to the one shown in Figure 4. In particular, the excursions of the top buoy change from 510 m to 640 m horizontally and from 42 m to 65 m vertically. Figure 4 shows that the top two buoys remain well above their maximum allowable depth limit.

In each of the above mooring configurations, the tension distribution was found to be about the same as that of the no current mooring configuration. Hence, the system safety factor remains essentially unchanged for the current profiles. The largest horizontal component of tension at the anchor was found to be 2560 N, and occurs (as expected) when the mooring is subjected to the maximum expected current profile. Thus, to keep the mooring on station for the duration of the experiment, it is necessary to use an anchor that can resist this horizontal pull. It can be shown that a dead-weight anchor weighing 16 kN in water has sufficient holding power[5]. Another approach, however, is to use a dead-weight anchor weighing 13.34 kN in water in conjunction with a Danforth anchor weighing about 150 N. Because of its lighter weight, this latter approach is recommended.

To examine the effect of increased buoyancy and cable drag on mooring response, two cases with the typical current profile as forcing were considered. In the first case, the top buoy on the mooring was replaced by one having enough buoyancy to produce a system safety factor of 2, which is a lower limit. Relative to the response of the unmodified mooring, this change resulted in an 11% decrease in horizontal excursions and about a 25% decrease in system safety factor. On

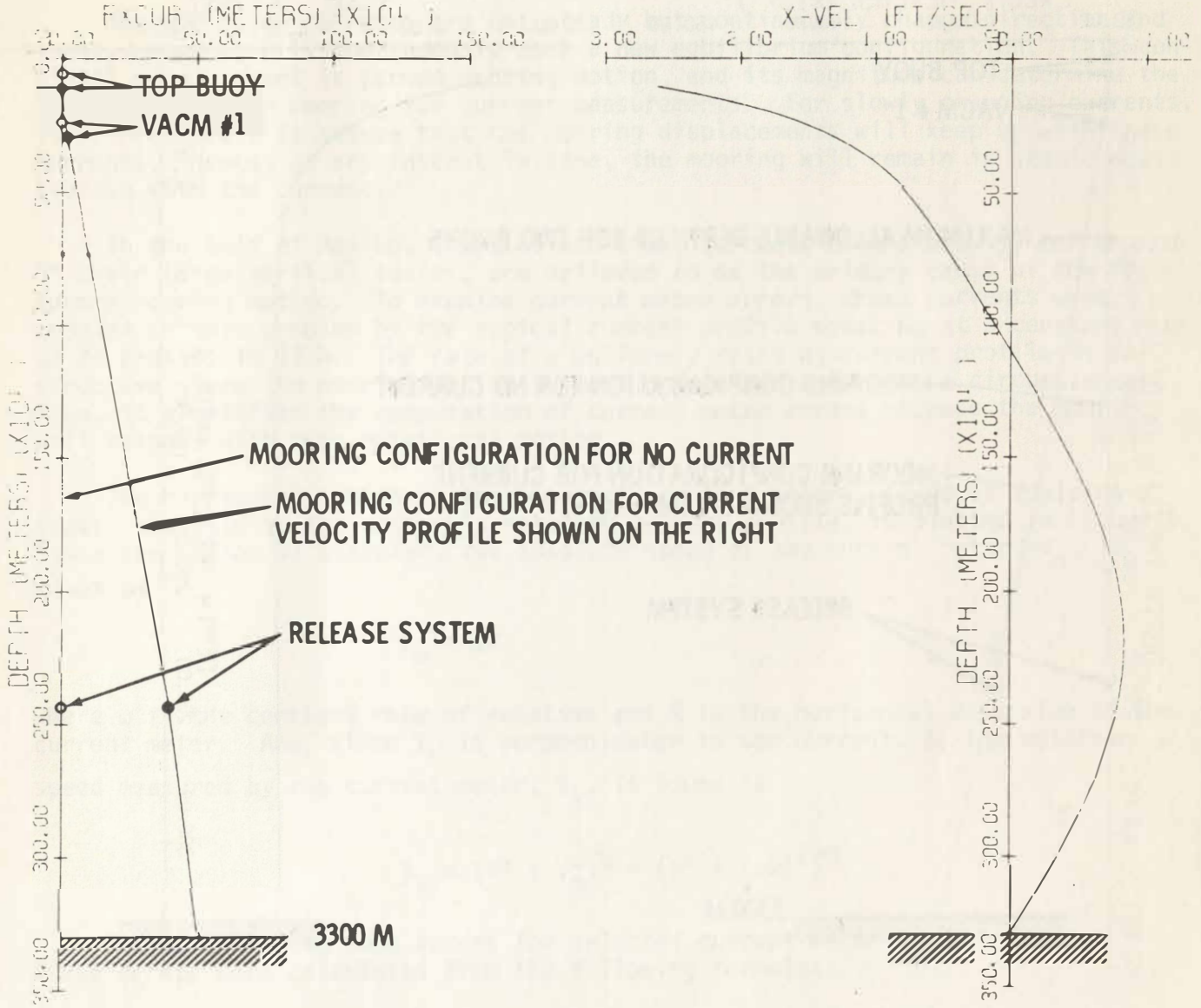

Figure 3. The mooring configuration (left) when subjected to the typical current profile (right). Note that the circles shown correspond to the no current configuration.

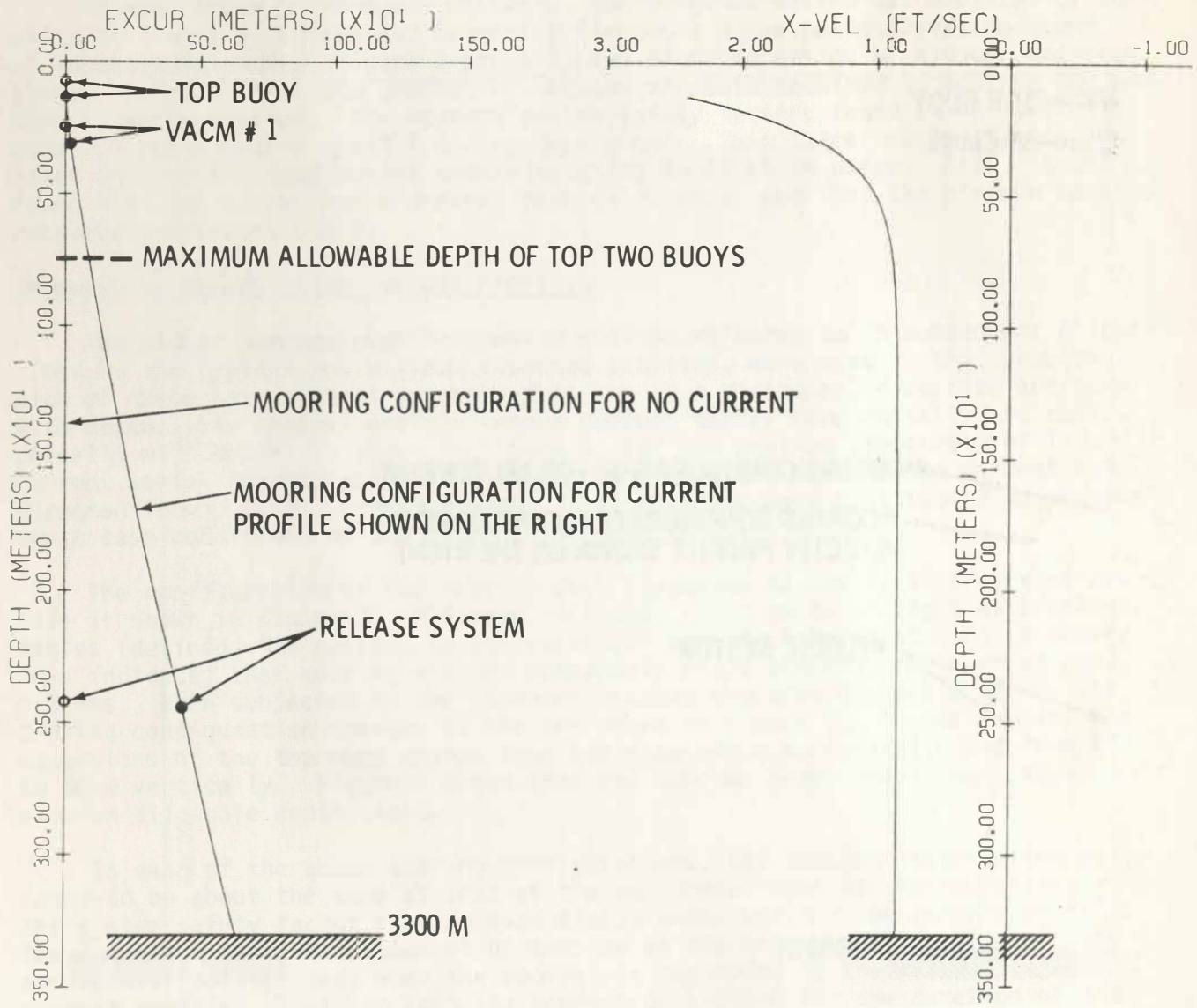

Figure 4. The mooring configuration (left) when subjected to the maximum expected current profile (right). Note that the circles shown correspond to the no current configuration.

weighing these results, it appears that the addition of buoyancy is not an attractive design consideration. For the second case, normal drag coefficients for the mooring ropes were increased from their nominal values of 1.4 to 1.8. This change, intended to account for some degree of cable strumming, resulted in a slight increase in horizontal excursions (about 3%) and essentially no change in the mooring tensions.

Response to a Uniformly Rotating Current Profile

Because ocean currents are not steady but continuously change direction and speed, a mooring will continuously seek a new equilibrium configuration. This continual readjustment is termed mooring motion, and its magnitude can determine the usefulness of the mooring for current measurements. For slowly changing currents, it is reasonable to assume that the mooring displacements will keep up with these currents. Hence, at any instant in time, the mooring will remain in static equilibrium with the current.

In the Gulf of Mexico, inertial and tidal currents change slowly; and, because of their large vertical scales, are believed to be the primary cause of low frequency mooring motion. To examine current meter errors, these currents were modeled in this problem by the typical current profile rotating at a constant rate of 2π radians in 12 h. The case of a uniformly rotating current profile is instructive since the mooring motion is most pronounced under these circumstances. Also, it simplifies the computation of current meter errors because the mooring will respond with pure rotational motion.

The horizontal motion of the mooring's current meters, found by applying a static analysis to the uniformly rotating current profile, is plotted in Figure 5. Since the motion is circular, the absolute speed of any current meter, V_m, is given by

$$V_m = \omega R$$

where ω is the constant rate of rotation and R is the horizontal excursion of the current meter. And, since V_m is perpendicular to the current, V, the relative speed measured by the current meter, V_R, is found as

$$V_R = (V^2 + V_m^2)^{\frac{1}{2}} = (V^2 + (\omega R)^2)^{\frac{1}{2}}$$

Table 1 presents some errors for selected current meters on the mooring. These errors were calculated from the following formulas:

$$E_m = (V_R - V)/V$$

and

$$E_p = \tan^{-1}(V_m/V)$$

where E_m is the speed error and E_p is the phase error. As can be seen, the speed of the uppermost meter through the water is 7.4 cm/s. Although the lower meters have less speed, some of them have significantly larger errors compared to the upper meters. This occurs, as shown in Table 1, when the meter speed approaches that of the current.

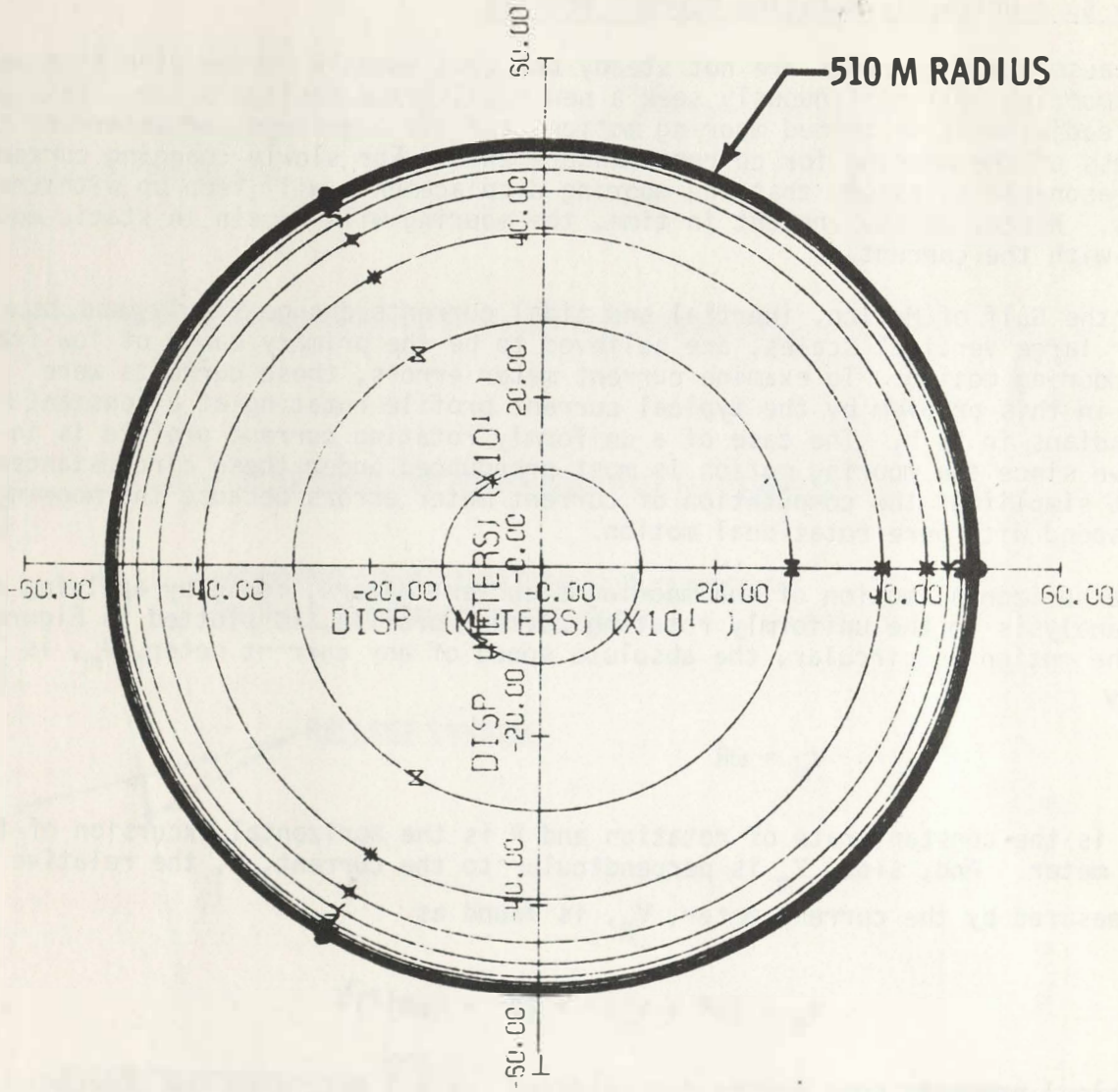

Figure 5. The circles shown represent the horizontal motion of the current meters when the mooring is subjected to the uniformly rotating current profile. The outer circles are for the uppermost current meters, and the origin of the coordinate system shown corresponds to the anchor.

TABLE 1

Mooring Response to Uniformly Rotating Current Profile

Component	Depth (m)	Horizontal excursion (m)	Tilt (degrees)	V (cm/s)	V_m (cm/s)	E_m (%)	E_p (degrees)
ACM #1	146	510	4	67.7	7.4	0.6	6.3
ACM #15	244	498	8	46.7	7.3	1.2	8.8
VACM #1	283	491	9	41.2	7.2	1.5	9.9
VACM #2	385	475	9	30.7	6.9	2.5	12.7
VACM #3	534	450	10	21.7	6.5	4.4	16.7
VACM #4	830	398	10	10.0	5.8	15.7	30.2
VACM #5	1421	292	10	-11.4	4.2	6.7	20.4
VACM #6	2405	118	10	-24.6	1.7	0.2	4.0

Dynamic Analyses

Two methods were used to solve the dynamic problems presented in this section. In one method, the mooring line was modeled as a continuous elastic material. In the other method, the mooring was represented by a lumped parameter model consisting (as shown in Figure 6) of seven masses joined by elastic springs that are capable of stretching only. The former method was used to solve the first problem given below, and the latter method the two remaining problems.

All three problems were solved in the time-domain by the computer programs described in References 6 and 7. In solving these problems, the following important features were considered: mooring line elasticity, nonlinear hydrodynamic drag forces, and inertia forces with added mass included.

Response to a Time-Varying Current Profile

In this problem, the mooring excitation is provided by ocean currents that change in magnitude and direction with depth and time. These currents, obtained from physical oceanographers who derived them from a Garrett-Munk spectrum, are believed to be the most expected currents in the area of the experiment.

Figure 7 presents the motion response of the top buoy. It can be seen that the motion is dominated by a semidiurnal oscillation, and has maximum horizontal excursions of 100 m and maximum vertical excursions of 2 m. This motion was observed throughout the mooring, but with excursions reducing from a maximum at

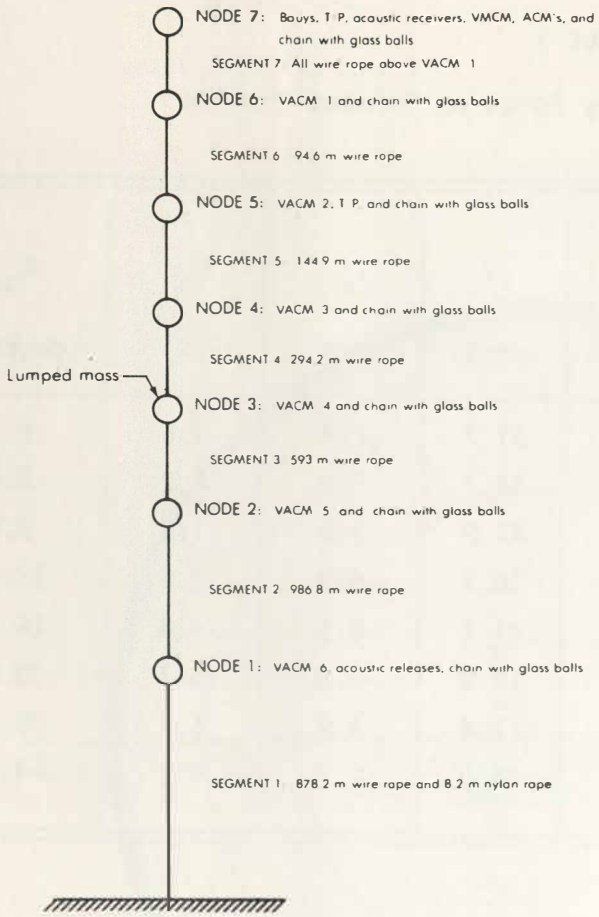

Figure 6. Lumped parameter model of the subsurface mooring shown in Figure 2.

the top buoy to zero at the anchor. In particular, excursions were reduced slightly down to the fifth VACM and by about 70% at the sixth VACM (see Figure 2). As shown on the left of Figure 7, the horizontal motion is not circular and, over the two successive cycles shown, has a zero mean displacement.

Response to Surface Gravity Waves

Three cases were considered to examine the effect of sea state on mooring response. The mathematical model used to simulate sea state is a simple harmonic wave whose direction of propagation is constant with time and whose amplitude decreases with depth in the classic fashion of surface gravity waves. To provide a worst case condition, no case included ocean currents which, if present, would mitigate the effect of waves on the mooring. Each case, described by sea state below, has the following physical characteristics:

	Case	Wave Period (Seconds)	Surface Wave Amplitude (Meters)	Percent Attenuation at 70 meter depth
I.	Sea State 4	7.5	1.0	0.6
II.	Sea State 6	10.0	2.0	6.0
III.	Sea State 7	15.0	5.6	29.0

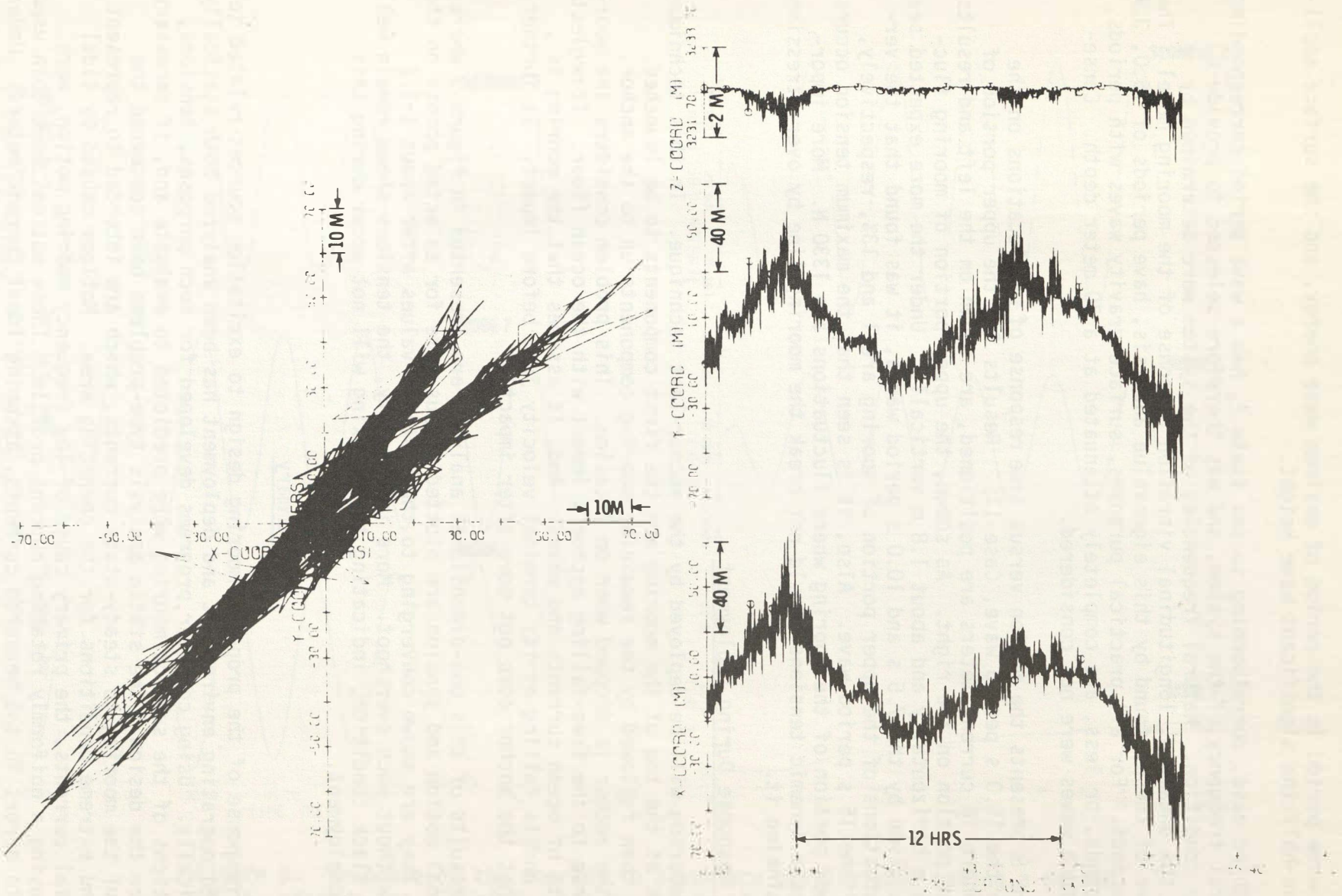

Figure 7. Motion response of the top buoy to ocean currents that change in magnitude and direction with depth and time: A time series of vertical (z-coordinate) and horizontal motion is shown on the right, and a top view of horizontal motions on the left.

where the wave period is the period of maximum wave energy, and the surface amplitude is one-half the significant wave height.

The third case, corresponding to sea state 7, has a wave period corresponding to a natural frequency of the system, and was therefore selected to provide a worst case condition. Natural frequencies of the system were determined by analyzing the undamped, longitudinal vibration response of the mooring model. The first three of these, found by this eigenvalue analysis, have periods of 15.0, 3.9, and 2.1 seconds. For all practical purposes, surface gravity waves with periods of 3.9 seconds, or less, are completely attenuated at a 70 meter depth. Consequently, such waves were not considered.

Figure 8 presents the motion versus time response of two locations on the mooring to the 15.0 s period wave, Case III. Results for the upper portion of mooring, where 16 current meters are positioned, are shown on the left and results for a lower portion on the right. As shown, the upper portion of mooring fluctuates 1.6 m horizontally and about 1.8 m vertically. Under the more expected sea conditions given by the 7.5 s and 10.0 s period waves, it was found that the vertical fluctuations of the upper portion of mooring are 1 and 13%, respectively, of that of the 15 s period wave. Also, it is seen that the maximum tension occurs in the lower portion of the mooring where fluctuations are 1330 N. More importantly, these dynamic tensions should not break the mooring line by over stressing it or by kinking it.

Transient Response During Deployment

The mooring will be deployed by the anchor-last technique. In this technique, the floats at the top of the mooring are the first components to be launched. These are then followed by the remaining mooring components up to the anchor. Finally, the anchor is dropped when on location. This problem considers the mooring response to the free-falling anchor's impact with the ocean floor. It neglects the effects of ocean currents and waves. And, it assumes that the mooring is vertical, and is falling at its terminal velocity just before impact. It further assumes that the anchor does not move after impact.

The results of this one-dimensional analysis are presented in Figure 9 where longitudinal motion and tension are plotted versus time for selected points on the mooring. They are shown converging to their static values after about 1-1/2 minutes, without much overshoot. More importantly, the tensions shown remain well above any slack condition, indicating that kinking will not occur during this phase of deployment.

Summary

The response of the proposed mooring design to excitation sources related to its planned operating environment and deployment has been analyzed both statically and dynamically. Using computer programs developed for such purposes, tensions, in and motions of the subject mooring were predicted to evaluate and, if necessary, to optimize the design. The static analysis type-problems have concerned the response of the mooring to steady-state currents, which are intended to represent typical and extreme conditions for the operating area. Motions caused by tidal and inertial currents, the primary cause of low frequency mooring motion, were computed using a uniformly rotating current profile. These motions were then used to estimate errors in the measured currents, assuming ideal current meters. Under these slowly changing currents, it was found that the errors in the uppermost current meters are considerably less than those found in most of the lower meters.

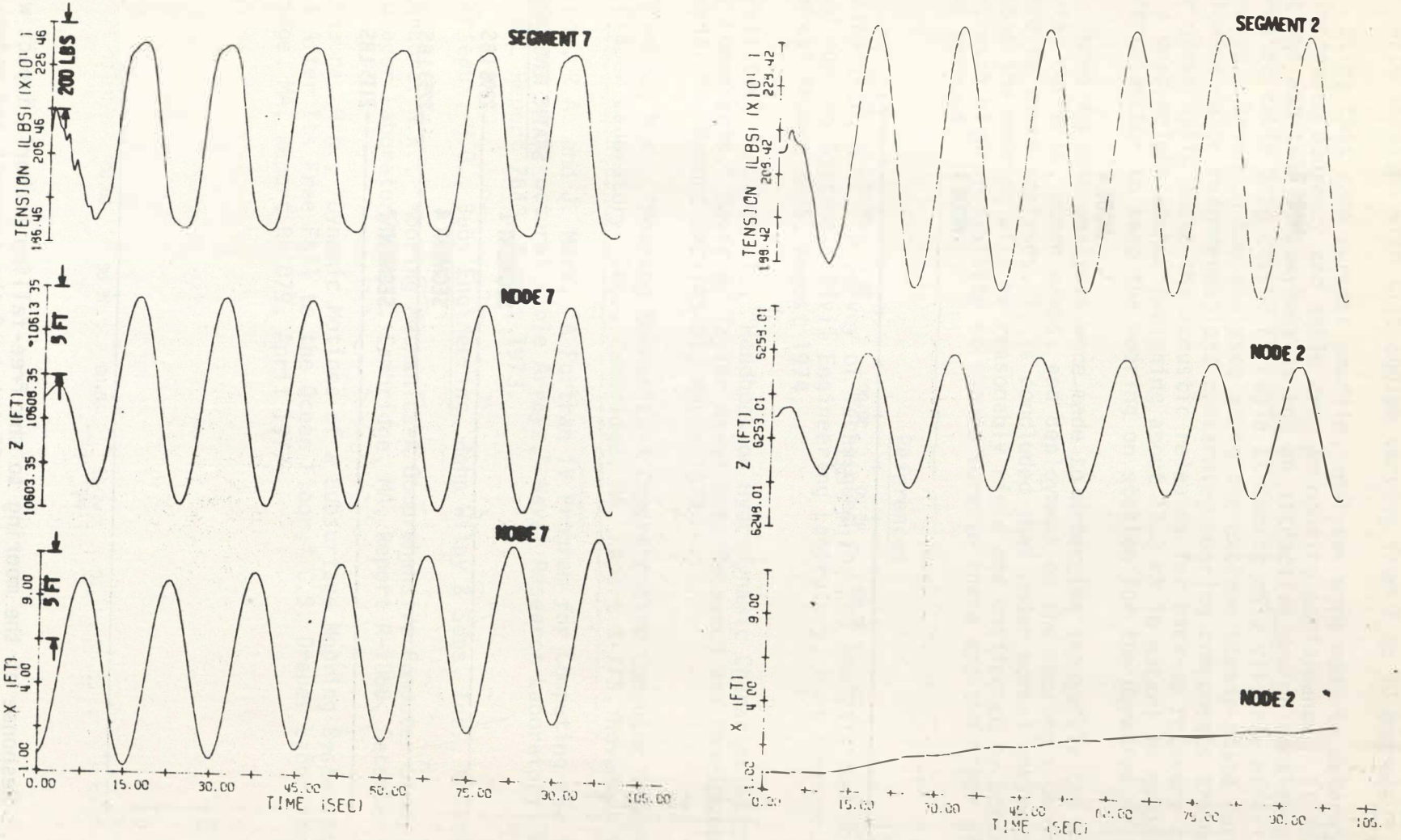

Figure 8. Response of the mooring to a surface gravity wave having a period of 15 seconds and a surface wave amplitude of 5.6 m. Refer to Figure 6 for the correspondence of mooring components to the segments and nodes shown. Note that z is the vertical coordinate measured relative to the ocean floor, and that the wave is propagating in the positive x-direction.

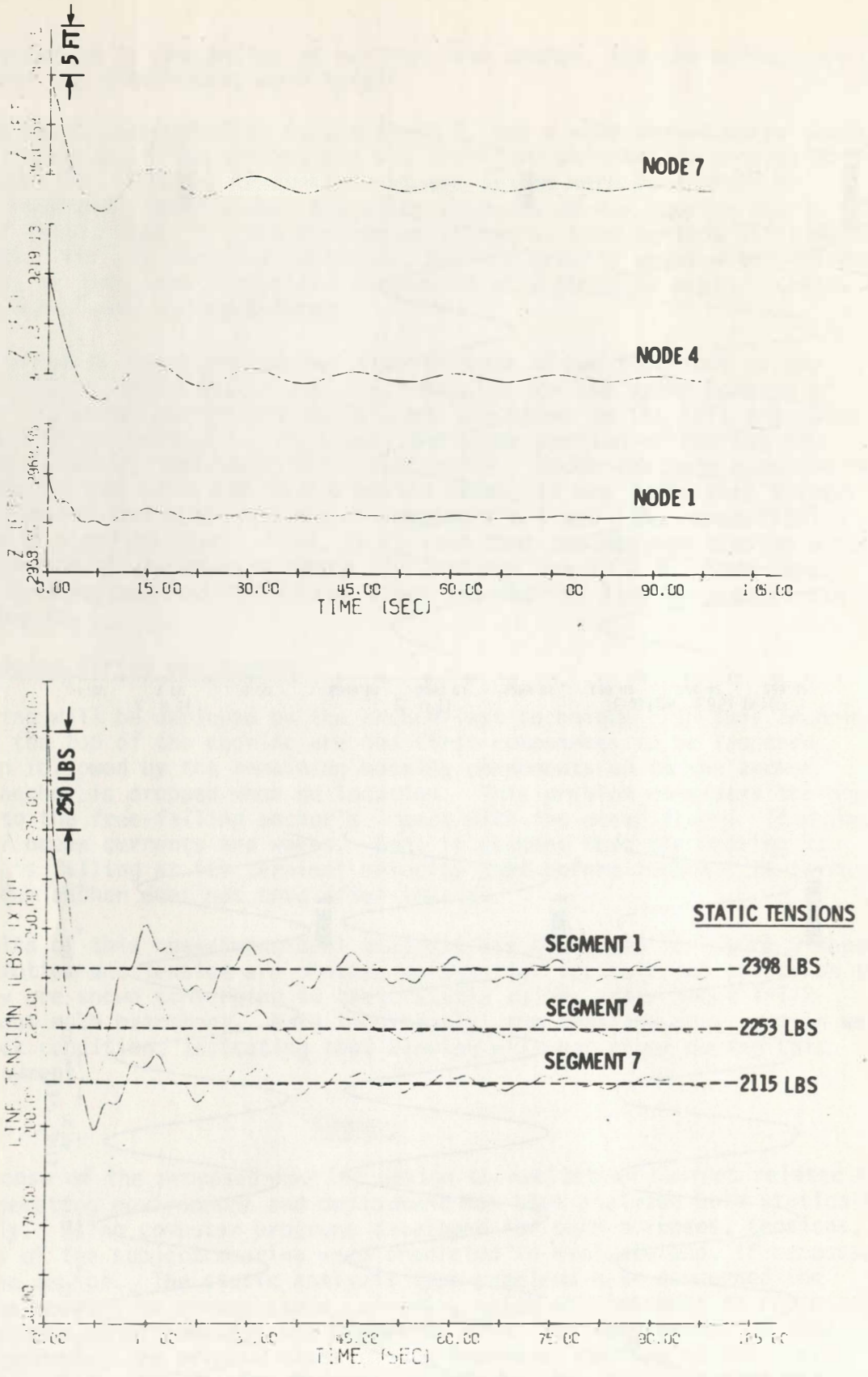

Figure 9. Response of the mooring to the free-falling anchor's impact with the ocean floor. See Figure 6 for the definition of the segments and nodes shown.

Also, at any instant in time, it was found that the mooring, although inclined, was quite straight with tilt angles varying from 7 to 10 degrees.

Using this same current profile, analyses were made to determine the effect of increased buoyancy and cable drag on mooring performance. It is concluded that the addition of buoyancy is not an attractive design consideration, and that increased cable drag caused by cable strumming only slightly effects mooring performance. Based on the analyses using the extreme steady-state currents, the following major recommendations concerning mooring components are made: Add five more glass balls above the acoustic releases for back-up recovery capability; and, use a dead-weight anchor (weighing about 13.3 kN in water) in conjunction with a Danforth anchor to keep the mooring on station for the duration of the experiment.

Three dynamic analyses were made to determine separately the effect of time-varying currents, ocean waves, and deployment on the mooring's performance. In regard to these analyses, it is concluded that under normal environmental conditions the mooring will be reasonably rigid and uneffected by ocean waves. Moreover, with high probability it should survive these and the other extreme conditions assumed.

References

1. Albertsen, N.D., "A Survey of Techniques for the Analysis and Design of Submerged mooring Systems," Civil Engineering Laboratory, Port Hueneme, CA, Technical Report R815, August 1974.

2. Pattison, J.H., et al., "Handbook on Hydrodynamic Characteristics of Moored Array Components," David W. Taylor Naval Ship Research and Development Center, Bethesda, MD, Report SPD-745-01, March 1977.

3. Chhabra, N.K., "Mooring Mechanics-A Comprehensive Computer Study," Volume I, C.S. Draper Laboratory, Inc., Cambridge, MA, Report R-775, November 1973.

4. Skop, R.A. and J. Mark, "A Fortran IV Program for Computing the Static Deflections of Structural Cable Arrays," Naval Research Laboratory, Washington, D.C., NRL Report 7640, August 1973.

5. Berteaux, H.O., Buoy Engineering, John Wiley & Sons, Inc., New York, 1976.

6. Chhabra, N.K., "Mooring Mechanics-A Comprehensive Computer Study," Volume II, C.S. Draper Laboratory, Inc., Cambridge, MA, Report R-1066, December 1976.

7. Chhabra, N.K., "Dynamic Motions of a Subsurface Mooring System at Anchor Impact After Its Free Fall to the Ocean Floor," C.S. Draper Laboratory, Inc., Cambridge, MA, Report R-1079, April 1977.

DRAPER LABORATORY INSTRUMENTATION FOR BUOY SYSTEM DYNAMICS

John Dahlen
The Charles Stark Draper Laboratory, Inc., Cambridge, Massachusetts

Abstract

Instruments developed at The Charles Stark Draper Laboratory for measurement of buoy system dynamics and their use in ocean testing are described. These instruments measure tension, acceleration, angular velocity, depth, and orientation. They are self-contained and packaged for use in buoys and on mooring lines deep within the ocean. Data interpretation and future developments are also discussed.

Introduction

Since 1972 the Draper Laboratory has been involved in the subject of "Mooring Dynamics", primarily under ONR sponsorship. Our long-range objective may be stated as follows:

> Improve the accuracy and reliability of oceanographic measurements obtained from moored and drifting buoy systems by advancing the technology of buoy system dynamics and by developing engineering methods founded upon an understanding of buoy system dynamics.

Before discussing our approach to obtaining the stated long range technology objective, we should attempt to justify the relevance of mooring dynamics models to the critical problem of near-surface current measurement. The relevance of these models to design for survival is obvious.

The dynamics of the near-surface layer is of central importance to models of the energy transfer between the atmosphere and the ocean. Because of the recent expanded emphasis upon experimental programs designed to provide these models, the long-standing need to develop current sensing instrumentation for the near-surface layer has become an urgent need. The difficulty of avoiding serious, and often prohibitive, errors induced by the surface wave field is universally recognized. These difficulties exist with all instruments, including moored current meters and drogues or current meters suspended from drifting buoys. Even the most advanced current meters under development will, in some applications, exhibit nonlinearities which result in serious errors. Most applications will require the use of current meters which can compute north and east components of the ocean current with respect to a nonrotating frame of reference, preferably the ocean floor. These components can then be low-pass filtered within the instrument to conserve the data storage medium, while providing a frequency band sufficiently wide for the upper layer dynamics of interest. If the nonrotating frame of reference is moving, as is the case with current meters on moorings or under drifting buoys, the velocity of the reference frame in the frequency band of interest can usually be measured, estimated, or neglected.

The problem which has eluded present technology is the computation of north and east components of the ocean current relative to the current meter. There is a straightforward engineering concept for accomplishing this: combine a two- or three-axis linear relative flow component sensor, a three-axis attitude reference package, a resolving computer to formulate the north and east components, and low-pass filters to remove the unwanted high frequency content from these stabilized flow components. Unfortunately, because of fluid wake turbulence, and sometimes other problems, the straightforward concept cannot be implemented because the linearity of even the best sensors breaks down when the flow approaches them from certain sectors of their field-of-view. When the sensor is fixed to the line, the relative flow must sometimes enter these sectors either due to wave-induced water particle motion or velocity or inclination of the line to which the meter is attached.

To alleviate the field-of-view problem and to simplify the resolving computer, the current meter/buoy system may be designed such that, in the specific application, the current meter will see the relative flow in its preferred field-of-view sector (except perhaps in well-defined environmental extremes). For example, we have evidence that suggests some fixed current meters, having short response times and earth-axes component averaging, when suspended beneath a properly tuned spar buoy will exhibit acceptable errors for many experiments so long as the sea state remains below a prescribed value depending upon the depth of the instrument. Similarly, we may be able to show that some current meters will provide acceptable errors when suspended directly benearth surface-following buoys. The Profiling Current Meter being developed at CSDL, because it is axially uncoupled from the mooring line, is expected to exhibit accuracy superior to any fixed meter.

Given these circumstances, we feel the most responsible engineering approach to system design must involve early evaluation of candidate configurations in the specific application by means of quantitative dynamic response models, and later, demonstration by experiment of actual system performance. To pursue this approach we must, of course, have buoy and sensor subsystem response models whose errors can be described quantitatively. We have models now. It is important to undertake the task of defining and minimizing the errors inherent in these models.

Our approach to obtaining the stated objective involves the following four tasks:

1. Develop computerized math models of buoy system dynamics utilizing full-scale ocean test data for model accuracy evaluation and improvement.

2. Develop instruments to record ocean test data required for model development.

3. Devise techniques for correcting oceanographic data to minimize dynamic errors.

4. From proven math models derive design tools which predict buoy system stresses, motions, and dynamic sensing errors.

It is the intention of this paper to describe the engineering instruments we have developed for the above-stated purpose.

Existing Instruments and Past Experience

This section is intended to give a brief summary of the instrument configurations we have built and the history of their use in ocean testing.

Temperature/Pressure Recorder (T/PR)

The T/PR was originally designed for long-duration measurement of temperature time series in the Mid-Ocean Dynamics Experiment (MODE-1973). A pressure measurement was added to monitor instrument depth which can change significantly on a mooring line.

The instrument, as shown in Figure 1, is housed in an 11.5 in. (29 cm) dia. aluminum alloy sphere. Housing wall thickness is 0.75 in. (1.9 cm), permitting the instrument to be used at any ocean depth. The sphere is swivel-clamped to a 16 in. (41 cm) steel bar which is inserted in the mooring line. Weight in water is 18 lb (8.1 kg) and in air 49.5 lb (22.4 kg). Contained in the sphere are:

1. A thermistor package in intimate thermal contact with the housing wall (FENWAL).

2. A diaphragm/strain gauge pressure transducer which penetrates the housing wall (BLH).

3. An electronic data acquisition system which conditions, converts, and formats the sensor signals.

4. A digital incremental magnetic tape cassette recorder (capacity over 2 million bits) (MEMODYNE).

5. Battery pack of encapsulated alkaline primary cells.

The instrument has much built-in flexibility. The data acquisition system provides the functions necessary for handling up to four separate sensors, not limited to temperature and pressure (conductivity and temperature gradients have been added). Data conversion and recording rates are flexible, as is recorded word length. Digital averages (accumulators) are provided for each channel, and electronic analog filtering may be used for up to two sensors. As configured for POLYMODE, the instruments record 16 binary bit temperature, pressure, time, and system integrity data words every 32 minutes for 16 months. Temperature and pressure are sensed, converted to 10 bit words, and stored in accumulators every 30 seconds. It is the sum of 64 such samples which is recorded on magnetic tape. In a current NORDA application the sample and record periods are 3.75 s and 2 m, respectively. The thermistor is mechanically packaged to exhibit an equivalent first order lag time-constant of 200 s. The time-constant of the pressure sensor is less than 1 s.

Our best current estimate of system accuracy is as follows. The crystal oscillator clock drifts less than 1 s-d^{-1}. This drift is sufficiently stable to permit its determination to better than 1/4 s-d^{-1} by time checks before and after any experiment.

The thermistor temperature sensor has inherent characteristics which, in the present application, permit absolute measurements accurate to 0.01°C and a resolution of about 0.001°C. All sensors are calibrated to permit full advantage to be taken of the inherent accuracy. Instruments destined for use at 2000 meters or deeper are scaled for 1°C range; hence, the least bit in each conversion represents about 0.001°C and full advantage of inherent sensor resolution is obtained. However, instruments destined for use in the main thermocline are scaled for a 13°C range which requires that the least bit in each conversion represent about 0.013°C.

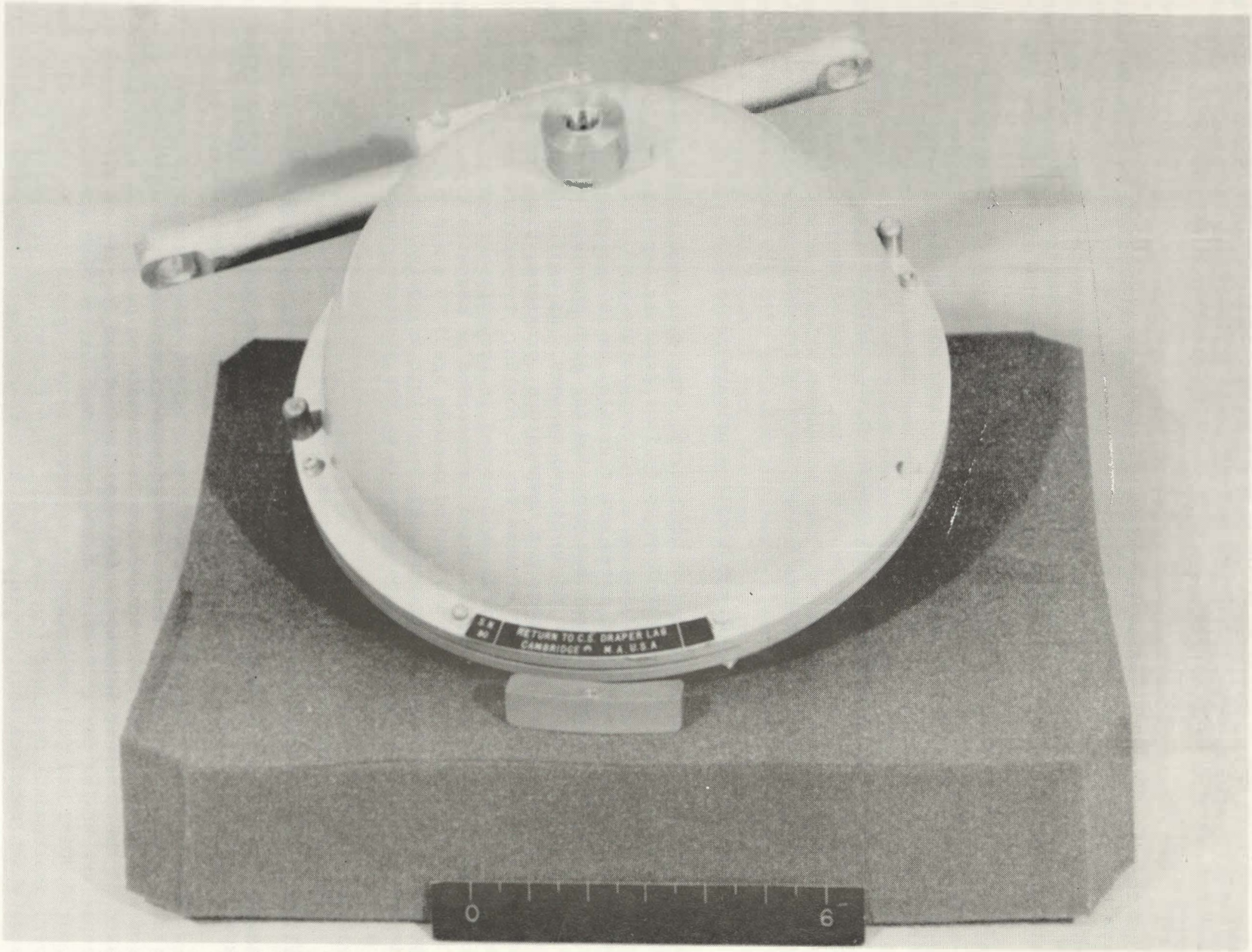

Figure 1. Temperature/pressure recorder.

Resolution is sometimes improved by the fact that 64 conversions are averaged in each recorded data word.

The pressure measurement error is more difficult to define. In most cases, calibrations before and after sea trials are consistent with BLH's claim that the sensor absolute error is about ±0.03% of rated full scale output. However, data from three units placed on bottom moorings for 6 d exhibited a drift, ending after 2-3 d, of +0.03% to +0.10% of rated full scale output. Further tests of long-term drift under sustained high pressure have been conducted. Tests indicate that pressure changes over short periods, of the order of hours or less, can be measured with much greater accuracy, usually limited only by electronic digitizing errors. Most units have been scaled so that the least significant bit (in any single 10 bit conversion) represents 0.03% of the sensor full-scale output. The digitizing error is primarily a round-off error, so that the rms conversion error is about 0.01% of sensor full-scale output. Resolution is often improved by the fact that 64 successive conversions are summed in each recorded pressure word. Since sensors are selected to have a full-scale output slightly larger than the maximum pressure the instrument will see, the magnitude of error, both long- and short-term, is proportional to the depth at which the instrument is expected to operate. For example, an instrument destined for 2000 meters depth would have an absolute error of the order of 1 meter and a short-term pressure change measurement error of less than 0.2 meter. In near-surface applications, of course, we can resolve to a few centimeters. Corrections to pressure for in situ temperature changes are typically 1 bit/5°C. In normal use, this correction is negligible.

We built 89 T/PRs between 1972 and 1976. They have been used in numerous programs throughout the world for a variety of purposes, most frequently for monitoring temperature fields and the depth excursions of moorings. A considerable number have been configured as bottom-mounted shallow water tide gauges capable of resolving 1 centimeter fluctuations in sea level. In this latter application, a rapid sampling capability is added to sample and average wave frequency pressure oscillations which would otherwise alias the data.

High Frequency Temperature/Pressure Recorder (HFTP)

HFTPs utilize a modified T/PR data acquisition system to provide burst sampling with selectable sample rate, burst duration, and burst repetition period. In its fastest mode a HFTP records 10-bit temperature samples every 2 s and 10-bit pressure samples every 0.5 s. Continuous sampling at this rate will fill the tape cassette in 12 h. Longer duration monitoring must, therefore, be performed in bursts. HFTPs may be synchronized with each other and with the other high-frequency recording systems described below. Accurate clocks in these instruments maintain synchronous operation within 0.25 s for 10 d. The power consumed by these clocks limits the operating life to 40 d (using mercury batteries).

Figure 1 shows one of the four HFTPs built for the 1976 ONR/NDBO Mooring Dynamics Experiment (MDE). Their location on the MDE Tethered Spar Buoy System is illustrated in Figure 2. The unit under the subsurface buoy measured vertical displacement. The two units under the spar buoy measured buoy heave and, using the pressure difference, local wave height. The HFTPs were also used on the NDBO Discus Buoy System and the CEL Near-Surface Buoy System. Essentially 100 percent data return was achieved.

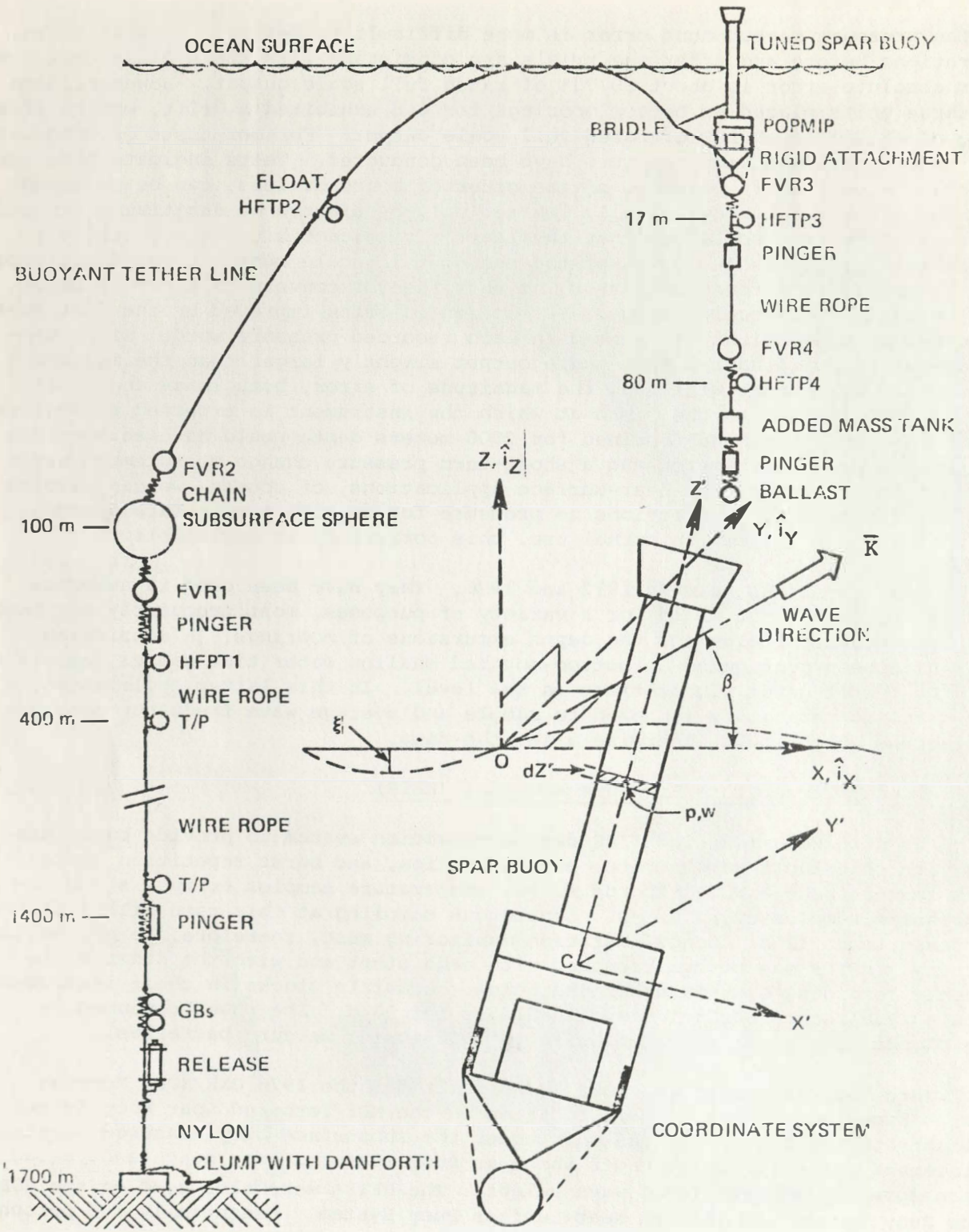

Figure 2. Tuned spar buoy system.

Force Vector Recorder (FVR)

The FVR shown in Figure 3 is a self-contained instrument which digitally records the outputs of six sensors on a magnetic tape casette. It is an outgrowth of the T/PR. A short cylindrical section was inserted between the T/PR hemispheres to provide the volume required for the added sensors. A wire-wrap board was added to the T/PR data acquisition system to provide a high frequency burst sampling capability, with selectable sample rate, burst duration, and burst repetition period. In its fastest mode the FVR records 10-bit samples of all sensors simultaneously every 0.5 s. Continuous sampling at this rate will fill the tape cassette in 3 h. Long duration monitoring must be accomplished by recording the same volume of data in bursts separated by relatively long idle periods. The clock is identical to that used in the HFTP, thus FVRs and HFTPs maintain synchronism within 0.25 s for 10 d. Again, as with the HFTPs, the operating life is limited to 40 d unless a low-power, less-accurate clock is substituted.

The sensors which have been used in the FVR include:

1. Linear Accelerometers (SYSTRON-DONNER). These are single-axis, force balance, seismic mass units. Typically we install two or three units with orthogonal input axes and full-scale ranges of ±1 g or ±2 g. With careful calibration to account for misalignments an overall error of 0.3 percent of full scale is achievable.

2. Magnetometers (INFINETICS). These are small, single-axis, flux gate units used to define FVR azimuth. Ideally, one should use three of these sensors to define the geomagnetic field density vector. Because of the competition for data channels we have used the magnetometers in pairs mounted with their input axes perpendicular to the longitudinal (usually vertical) axis of the FVR. Field calibration near the deployment site has, therefore, been necessary because of magnetic field density magnitude and dip angle variations.

3. Tensiometer (BLH). This strain gauge load cell is mounted in the cylindrical center section along the longitudinal axis. Thus, the FVR is mounted in-line and carries the full tension load. The 3000 lb (13,300 N) FSO units we have used have been scaled for recording over a 1000 lb (4,450 N) range. Resolution has thus been governed by the LSB size, 1 lb (4.45 N). Absolute error is approximately 2 lb (8.90 N).

4. Pressure Transducer (BLH). This strain gauge unit has been described above under the T/PR section.

Typically the FVR weighs 85 lb (380 N) in air and 45 lb (200 N) in water. A 19 inch (48 cm) diameter syntactic foam floatation sphere may be wrapped around the FVR to render it neutrally buoyant, in which case the weight in air becomes 130 lb (580 N).

During the 1976 MDE four FVRs were used with nearly 100 percent success on each of the buoy systems tested: the Tethered Spar, the NDBO Discus, and the CEL Near-Surface. Each FVR contained one tensiometer, three accelerometers, and two magnetometers. By smoothing and manipulating the accelerometer and magnetometer data one can obtain the low-frequency history of FVR orientation. The higher, wave frequency data are directly useful in procedures to test mooring dynamic models. The four FVRs were used again, with 100 percent data return, in the 1978 NSF/NDBO/ONR Drifter Dynamics Experiment (DDE). Figure 4 shows FVRs 1 and 4 on the SIO/TAMU parachute drogue configuration. FVR 4 was equipped with the same sensor

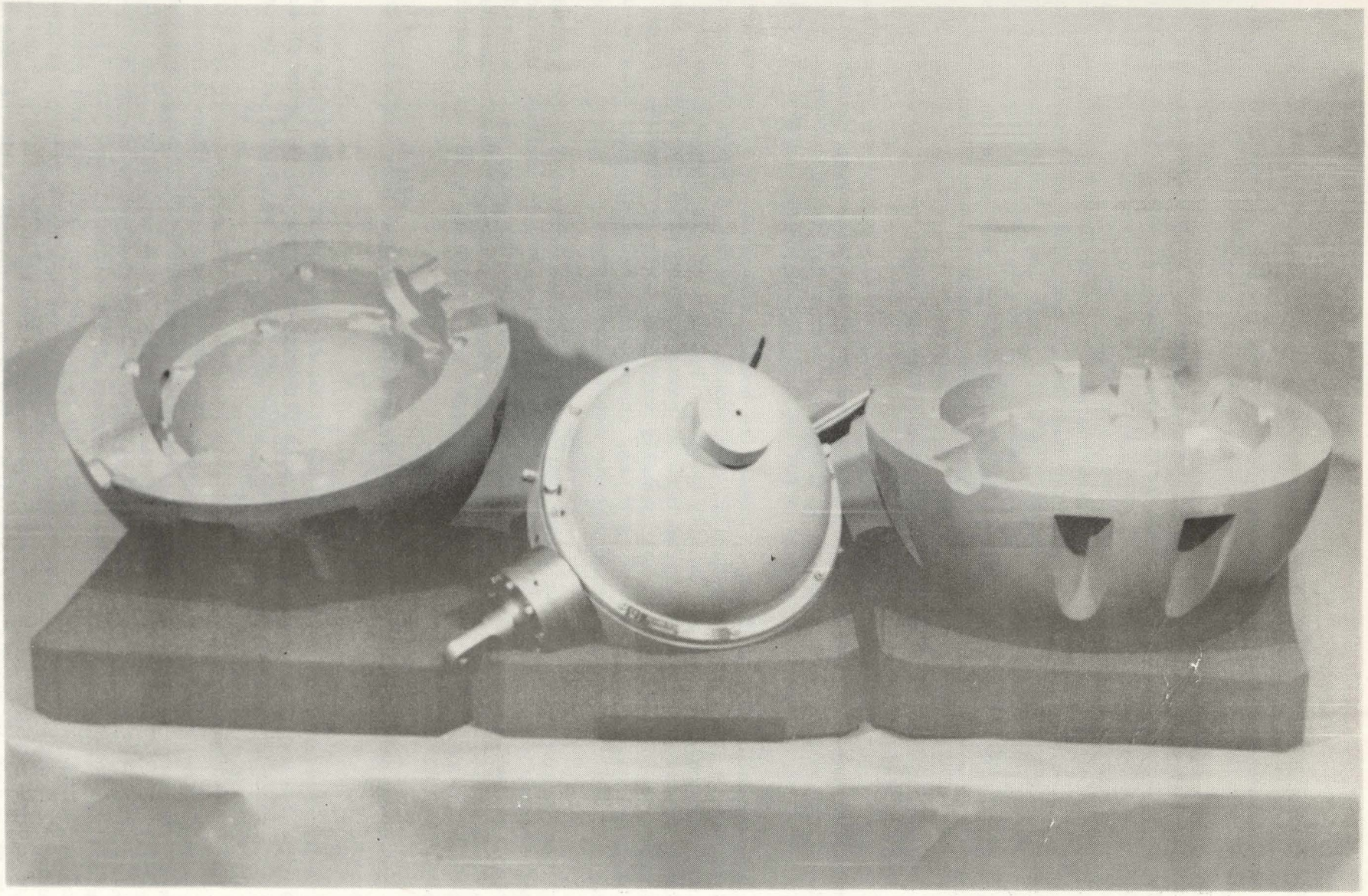

Figure 3. Force vector recorder.

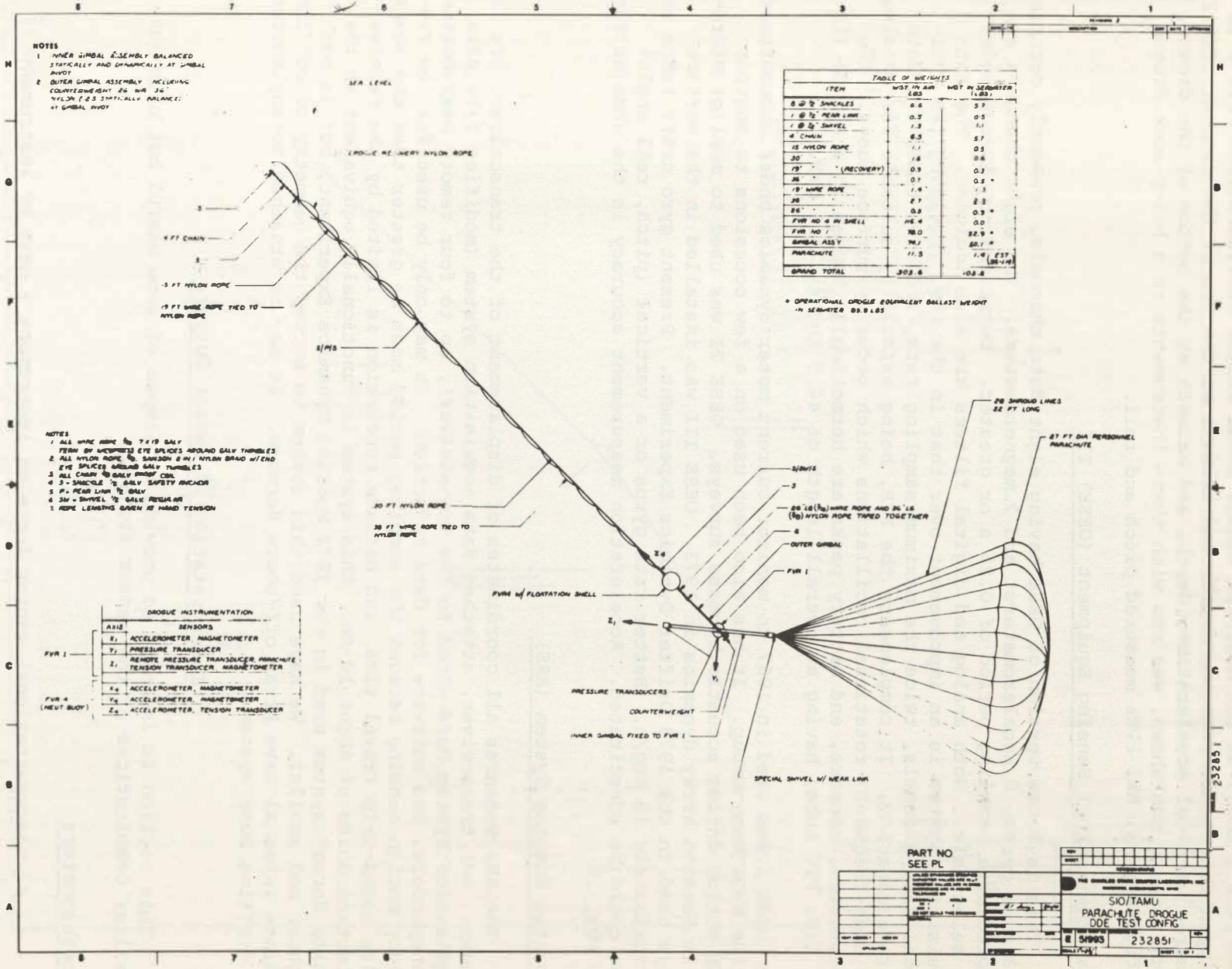
NOTES
1 INNER GIMBAL ASSEMBLY BALANCED STATICALLY AND DYNAMICALLY AT GIMBAL PIVOT
2 OUTER GIMBAL ASSEMBLY INCLUDING COUNTERWEIGHT 26 OR 36' NYLON IS STATICALLY BALANCED AT GIMBAL PIVOT
SEA LEVEL
TABLE OF WEIGHTS
ITEM
WGT IN AIR (LBS)
WGT IN SEAWATER (LBS)
8 @ ½ SHACKLES 6.6 3.7
1 @ ½ PEAR LINK 0.3 0.5
1 @ ½ SWIVEL 1.3 1.1
4 CHAIN 6.5 3.7
15 NYLON ROPE 1.1 0.5
30 1.6 0.6
19 (RECOVERY) 0.9 0.3
36 0.7 0.5 *
19 WIRE ROPE 1.9 1.3
30 2.7 2.3
26 0.8 0.3 *
FVR NO 4 IN SHELL 116.4 0.0
FVR NO 1 78.0 32.9 *
GIMBAL ASSY 78.1 50.1 *
PARACHUTE 11.5 1.9 (EST 30-1/2)
GRAND TOTAL 303.6 103.8
* OPERATIONAL DROGUE EQUIVALENT BALLAST WEIGHT IN SEAWATER 89.9 LBS
LENGTH AS NEEDED NYLON ROPE
3
4 FT CHAIN
4
.5 FT NYLON ROPE
19 FT WIRE ROPE TIED TO NYLON ROPE
5/8WS
30 FT NYLON ROPE
30 FT WIRE ROPE TIED TO NYLON ROPE
Z4
FVR4 w/ FLOATATION SHELL
Z1
Y1
PRESSURE TRANSDUCERS
COUNTERWEIGHT
INNER GIMBAL FIXED TO FVR 1
SPECIAL SWIVEL w/ WEAK LINK
5/8WS
3
26 LB (5/8) WIRE ROPE AND 36 LG (5/8) NYLON ROPE TAPED TOGETHER
4
OUTER GIMBAL
FVR 1
20 SHROUD LINES 22 FT LONG
87 FT DIA PERSONNEL PARACHUTE
NOTES
1 ALL WIRE ROPE 5/16 7 x 19 GALV TERM BY MACKREEL'S EYE SPLICES AROUND GALV THIMBLES
2 ALL NYLON ROPE 5/8 SAMSON 8 IN 1 NYLON BRAID w/ END EYE SPLICED AROUND GALV THIMBLES
3 ALL CHAIN 5/16 GALV PROOF COIL
4 3 - SHACKLE 1/2 GALV SAFETY ANCHOR
5 1 - PEAR LINK 1/2 GALV
6 3/8 - SWIVEL 1/2 GALV REGULAR
7 ROPE LENGTHS GIVEN IS HAND TENSION
DROGUE INSTRUMENTATION
AXIS
SENSORS
FVR 1
X1 ACCELEROMETER, MAGNETOMETER
Y1 PRESSURE TRANSDUCER
Z1 REMOTE PRESSURE TRANSDUCER, PARACHUTE TENSION TRANSDUCER, MAGNETOMETER
FVR 4 (NEUT BUOY)
X4 ACCELEROMETER, MAGNETOMETER
Y4 ACCELEROMETER, MAGNETOMETER
Z4 ACCELEROMETER, TENSION TRANSDUCER
PART NO SEE PL
SIO/TAMU
PARACHUTE DROGUE
DDE TEST CONFIG
E 54903
232851
232851

Figure 4.

suite it had for the MDE. FVR1 had two pressure sensors, separated by one meter, to measure pitch of the inner gimbal and parachute axis; a tensiometer to measure parachute drag; and two magnetometers to measure parachute azimuth. Figure 5 shows FVRs 2 and 3 on the NDBO/PRL window shade drogue configuration. FVR 3 is equipped to measure tension, depth, and azimuth at the top of the drogue. FVR 2 measured vertical acceleration, depth, and azimuth at the bottom of the drogue. Another test, not shown, was run with these instruments on a holey sock drogue configuration. All FVRs measured pitch and roll.

Ocean Environment Sensing Equipment (OESE) III

This is a new version of OESE having eight data channels, presently occupied by 3 rate gyros, 3 accelerometers, and 2 magnetometers. The eight channels are sampled at a sampling period of 0.25 s or greater. Burst and continuous modes are selectable. Both analog and digital filters are also included. The data acquisition system is an improvement over that in the FVR, providing two additional data channels, twice the maximum sampling rate, and five times the data storage capacity. It complements the FVR, being especially suitable for sensing the high-frequency rotational oscillations which occur on surface buoys. The electronics, sensors, and battery packs are hermetically housed in a 6 inch (15 cm) I.D. PVC tube, having an overall length of 44.5 inches (113 cm).

OESE I was used in 1967 to monitor current meter dynamics under subcontract to the WHOI Buoy Group. It has also been used on a few occasions to monitor ship motion during acoustic biomass surveys. OESE II was used to monitor Microscale Sensing Array dynamics in 1973. OESE III was installed in the surface buoys used in the 1978 Drifter Dynamics Experiment. Present gyro drift rates are approximately 15 deg/h. Better rate gyros or a vertical (pitch, roll angle) gyro could be substituted. Acceleration measurement accuracy is the same as for the FVR.

Acoustic Ranging System (ARS)

The ARS measures all coordinates of displacement of the transceiver. It includes: AMF transceiver, attached data acquisition system (modified T/PR data acquisition system hard-wired to the transceiver), up to four remote near-bottom transponders, and software for data reduction. It may only be used for low frequency motion sensing because the sampling period must be greater than the sound pulse round-trip travel time, and because resolution is limited by the receiver detection noise of about 10 cm. This system is functionally equivalent to the "White Horse" system used in our 1972 Mooring Dynamics Experiment, but is much lighter and smaller. We have used this system to survey the geometry of our Intermediate Internal Wave Array off-shore Bermuda. It may be attached to any moored or drifting buoy system.

Interpretation of Sensor Outputs

This section is intended to provide a glimpse of some useful but often unfamiliar combinations of the sensor signals.

Accelerometers

$\vec{f} \equiv$ nongravitational vector force on instrument ÷ mass of instrument

$\vec{g} \equiv$ local gravity vector

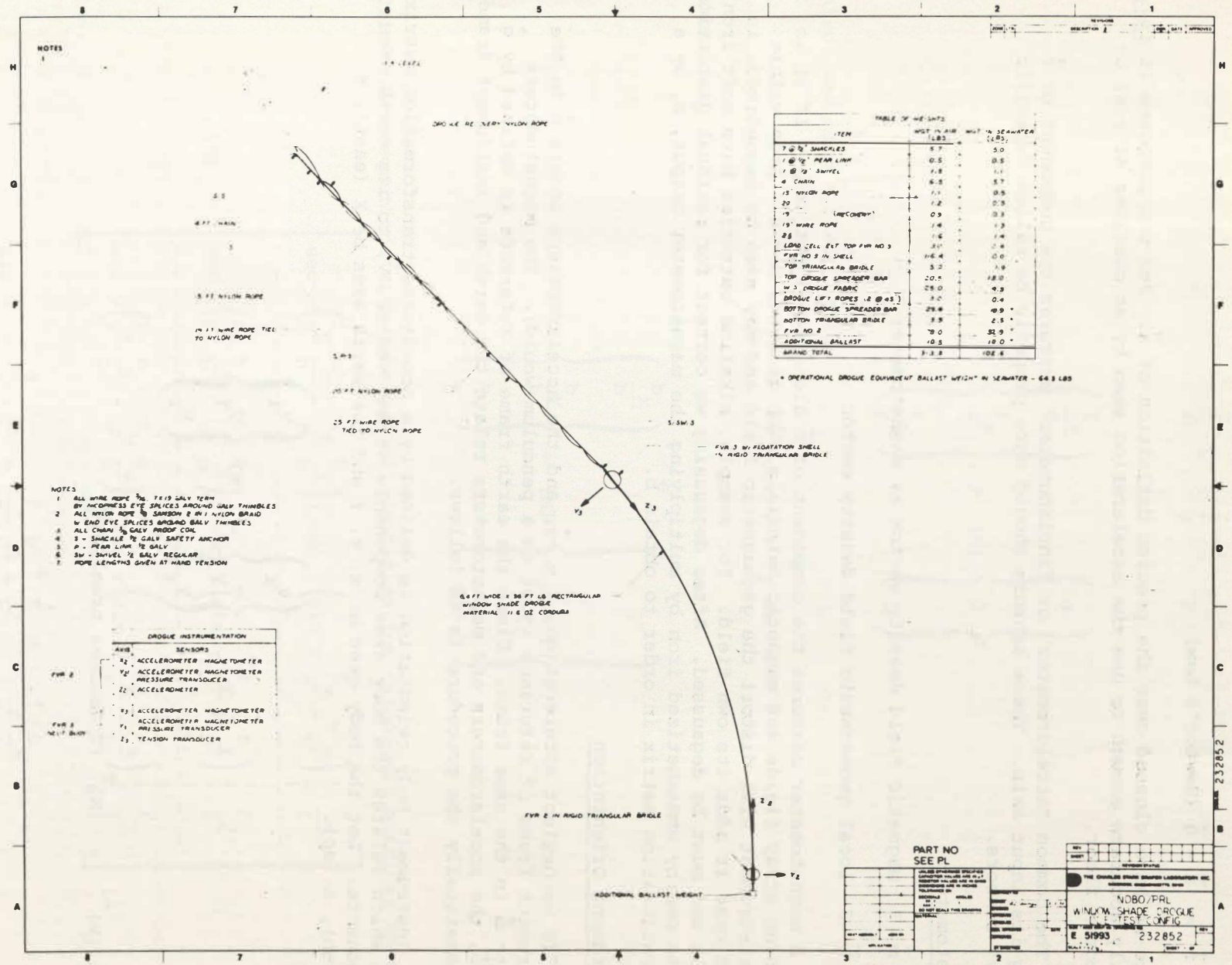
NOTES
1
TABLE OF WEIGHTS
ITEM
WGT IN AIR (LBS)
WGT IN SEAWATER (LBS)
7 @ 5/8" SHACKLES 5.7 5.0
1 @ 1/2" PEAR LINK 0.5 0.5
1 @ 1/2" SWIVEL 1.8 1.1
6 CHAIN 6.5 5.7
15' NYLON ROPE 1.1 0.5
20 1.2 0.5
19 (RECOVERY) 0.9 0.3
19' WIRE ROPE 1.4 1.3
25 1.6 1.4
LOAD CELL EXT TOP FVR NO 3 3.1 2.6
FVR NO 3 IN SHELL 14.4 0.0
TOP TRIANGULAR BRIDLE 5.2 1.9
TOP DROGUE SPREADER BAR 20.4 12.0
NO 3 DROGUE FABRIC 25.0 9.3
DROGUE LIFT ROPES 12 @ 45' 3.2 0.4
BOTTOM DROGUE SPREADER BAR 29.4 19.9 *
BOTTOM TRIANGULAR BRIDLE 3.9 2.5 *
FVR NO 2 78.0 52.9 *
ADDITIONAL BALLAST 10.5 10.0 *
GRAND TOTAL 212.2 106.6
* OPERATIONAL DROGUE EQUIVALENT BALLAST WEIGH IN SEAWATER - 64.3 LBS
DROGUE RECOVERY NYLON ROPE
6.5 FT CHAIN
5 FT NYLON ROPE
19 FT WIRE ROPE TIED TO NYLON ROPE
5 SW 3
15 FT NYLON ROPE
25 FT WIRE ROPE TIED TO NYLON ROPE
FVR 3 W/ FLOATATION SHELL IN RIGID TRIANGULAR BRIDLE
Y3
Z3
9.6 FT WIDE x 36 FT LG RECTANGULAR WINDOW SHADE DROGUE MATERIAL 11.6 OZ CORDURA
FVR 2 IN RIGID TRIANGULAR BRIDLE
Z2
Y2
ADDITIONAL BALLAST WEIGHT
NOTES
1 ALL WIRE ROPE 3/16 7X19 GALV TERM BY MECHANICAL EYE SPLICES AROUND GALV THIMBLES
2 ALL NYLON ROPE 3/8 SAMSON 8 IN 1 NYLON BRAID W END EYE SPLICES AROUND GALV THIMBLES
3 ALL CHAIN 3/8 GALV PROOF COIL
4 3 - SHACKLE 1/2 GALV SAFETY ANCHOR
5 P - PEAR LINK 1/2 GALV
6 SW - SWIVEL 1/2 GALV REGULAR
7 ROPE LENGTHS GIVEN AT HARD TENSION
DROGUE INSTRUMENTATION
AXIS
SENSORS
FVR 2
a_{x_2} ACCELEROMETER MAGNETOMETER
a_{y_2} ACCELEROMETER MAGNETOMETER PRESSURE TRANSDUCER
a_{z_2} ACCELEROMETER
FVR 3 NEXT BUOY
a_{x_3} ACCELEROMETER MAGNETOMETER
a_{y_3} ACCELEROMETER MAGNETOMETER PRESSURE TRANSDUCER
T_3 TENSION TRANSDUCER
PART NO SEE PL
NDBO/FRL WINDOW SHADE DROGUE TEST CONFIG
E 51993
232852
232852

Figure 5.

$\vec{a}$ ≡ instrument linear acceleration vector

Then

$$\vec{f} = \vec{a} - \vec{g} \text{ (Newton's Law)}$$

Notice we have glossed over the precise definition of $\vec{a}$. For our purposes it is usually accurate enough to use the acceleration seen by an observer at rest on the ocean floor.

The common "accelerometer" or "inclinometer" measures the component of $\vec{f}$ along its input axis. These sensors should more properly be called "specific force" sensors.

Magnetometers

$\vec{m}$ ≡ magnetic field density vector at magnetometer

$\vec{b}$ ≡ local geomagnetic field density vector

A magnetometer measures the component of $\vec{m}$ along its input axis. If it is far from stray fields and magnetic materials such as iron, $\vec{m} = \vec{b}$. Iron within the instrument will distort the geomagnetic field and may even be magnetized, in which case it adds its own field. For example, alkaline batteries have soft iron shells and must be degaussed. After degaussing we correct for residual distortions due to nearby unmagnetized iron by multiplying the magnetometer output, $\vec{m}$, by a 3×3 calibration matrix in order to obtain $\vec{b}$.

Instrument Orientation

If we neglect acceleration, $\vec{f} = -\vec{g}$, and the accelerometers locate $\vec{g}$ in the instrument frame of reference (just as a pendulum would). The magnetometers locate $\vec{b}$ in the same frame. Since the earth frame of reference is defined by $\vec{g}$ and $\vec{b}$, the accelerometers and magnetometers relate the earth and instrument frames. Mathematically the procedure is as follows.

Instrument body orientation is defined by a coordinate transformation matrix, [M], which relates the body axes components of any vector, $\vec{V}$, to its earth axes components. Let the body axes be x, y, z and the earth axes be X (east), Y (north), Z (up).

$$\begin{Bmatrix} V_x \\ V_y \\ V_z \end{Bmatrix} = [M] \begin{Bmatrix} V_X \\ V_Y \\ V_Z \end{Bmatrix}$$

note $[M]^{-1} = [M]^T$ (T denotes transpose)

Let f, g, b denote the magnitudes of $\vec{f}$, $\vec{g}$, $\vec{b}$, respectively. Still assuming zero acceleration

$$\frac{\vec{f}}{f} = -\frac{\vec{g}}{g} = \vec{1}_Z$$

thus

$$\begin{Bmatrix} \frac{f_x}{f} \\ \frac{f_y}{f} \\ \frac{f_z}{f} \end{Bmatrix} = [M] \begin{Bmatrix} 0 \\ 0 \\ 1 \end{Bmatrix}$$

Also, defining $\gamma \equiv$ dip angle:

$$\frac{\vec{b}}{b} = -\vec{1}_Y \cos\gamma + \vec{1}_Z \sin\gamma$$

thus

$$\begin{Bmatrix} \frac{b_x}{b} \\ \frac{b_y}{b} \\ \frac{b_z}{b} \end{Bmatrix} = [M] \begin{Bmatrix} 0 \\ -\cos\gamma \\ \sin\gamma \end{Bmatrix}$$

Using these equations with some useful identities for orthogonal matrices we find

$$[M] = \left[\begin{array}{c|c|c} \sec\gamma\left(\frac{f_y}{f}\frac{b_z}{b} - \frac{f_z}{f}\frac{b_y}{b}\right) & \sec\gamma\left(\sin\gamma\,\frac{f_x}{f} - \frac{b_x}{b}\right) & \frac{f_x}{f} \\ \hline \sec\gamma\left(\frac{f_z}{f}\frac{b_x}{b} - \frac{f_x}{f}\frac{b_z}{b}\right) & \sec\gamma\left(\sin\gamma\,\frac{f_y}{f} - \frac{b_y}{b}\right) & \frac{f_y}{f} \\ \hline \sec\gamma\left(\frac{f_x}{f}\frac{b_y}{b} - \frac{f_y}{f}\frac{b_x}{b}\right) & \sec\gamma\left(\sin\gamma\,\frac{f_z}{f} - \frac{b_z}{b}\right) & \frac{f_z}{f} \end{array}\right]$$

$$\sin\gamma = \frac{\vec{f}}{f} \cdot \frac{\vec{b}}{b} = \frac{f_x}{f}\frac{b_x}{b} + \frac{f_y}{f}\frac{b_y}{b} + \frac{f_z}{f}\frac{b_z}{b}$$

The elements of [M] are the direction cosines. They may also be related to Euler Angles or any other convenient set of orientation angles. We can, of course, use [M] to find the earth axes components of the tension vector or the specific force vector. See where the FVR got its name?

The assumption of zero acceleration leads to a tilt error identical to the acceleration error suffered by a pendulum having our transient response characteristics. Also note that a compass is pendulous to keep its magnet rotation axis vertical. Thus, when we assume zero acceleration, our azimuth determination error is the same as the acceleration error in a conventional compass having our transient response characteristics. Neglecting response delays, this error is

$$(\varepsilon)AZ \cong -\frac{\frac{A_E}{g}\tan\gamma}{1+\frac{A_N}{g}\tan\gamma}$$

where

$A_E \equiv$ acceleration to east

$A_N \equiv$ acceleration to north

It is assumed the accelerations are small compared to g.

The azimuth and tilt angle errors due to finite acceleration may be estimated by means of computer simulations of the mooring/instrument system excited by the surface wave field. Sometimes we find it necessary to smooth the sensor outputs before computing orientation, in which case, we loose the higher frequency information. In such cases, we must use gyros to get the wave frequency attitude oscillations.

Wave Height

Two synchronous pressure recorders, one a fixed distance directly above the other, may be used to determine local wave height.

If the sea level fluctuation above the transducers is given by

$$\sum_i A_i \sin(\omega_i t + \phi_i)$$

then the two transducers at depths h_1 and h_2 below mean sea level sense a pressure difference given by

$$\frac{p_2 - p_1}{\rho g} - (h_2 - h_1) = \sum_i A_i \left(e^{-\frac{\omega_i^2 h_2}{g}} - e^{-\frac{\omega_i^2 h_1}{g}} \right) \sin(\omega_i t + \phi_i)$$

The left hand side is known from the data record. Its Fourier transform yields

$$A_i \left(e^{-\frac{\omega_i^2 h_2}{g}} - e^{-\frac{\omega_i^2 h_1}{g}} \right) , \omega_i , \phi_i$$

from which we get A_i.

Future Developments

Having a variety of reliable sensors and a powerful data acquisition system in hand, instruments may readily be packaged to satisfy unique test requirements. The hardware and software techniques have almost become routine. Significant improvements may now be developed upon a solid foundation.

Greater operational life and more power-consuming sensors may be accommodated by the use of lithium batteries, which are slowly becoming practical. Dramatically more information may be stored in the ever-limiting memory devices once we begin to manipulate sensor information through microprocessors. Greater reliability may be possible when solid-state memory replaces the electromechanical tape recorder. Periodic telemetry dump of solid-state memory is feasible and may be economically justified in some applications.

References

1. Gifford, J. "Cruise Report, R/V CHAIN 107, 22 Oct. - 10 Nov. 1972," WHOI Report WHOI - 73-4, Jan. 1973.

2. Chhabra, N.K., Mooring Mechanics - A Comprehensive Computer Study, Volume I, C.S. Draper Laboratory, Inc., Report R-775, Nov. 1973.

3. Chhabra, N.K., J.M. Dahlen, M.R. Froidevaux, Mooring Dynamics Experiment: Determination of a Verified Dynamic Model of the WHOI Intermediate Mooring, C.S. Draper Laboratory, Inc., Report R-823, June 1974.

4. Wunsch, C., and J. Dahlen, A Moored Temperature and Pressure Recorder, Deep Sea Research, Vol. 21, 1974.

5. Chhabra, N.K., Verification of a Computerized Model for Subsurface Mooring Dynamics Using Full-Scale Ocean Test Data, Proceedings, MTS Tenth Annual Conf., Sept. 1974.

6. Dahlen, J.M., MIT/Draper Lab Temperature and Pressure Recorder. In: Instrument Description and Intercomparison Report of the MODE-I Intercomparison Group, Dec. 1974. (Unpublished manuscript available from the MODE Executive Office, 54-1417, MIT, Cambridge, MA 02139).

7. Chhabra, N.K., Mooring Mechanics - A Comprehensive Computer Study, Volume II, Three Dimensional Dynamic Analysis of Moored and Drifting Buoy Systems, C.S. Draper Laboratory, Inc., Report R-1066, Dec. 1976.

8. Chhabra, N.K., Correction of Vector-Averaging Current Meter Records from the MODE-1 Central Mooring for the Effects of Low-Frequency Mooring Line Motion, Deep-Sea Research, 24, 279-287, March 1977.

9. Chhabra, N.K., Dynamic Motions of a Subsurface Mooring System at Anchor Impact After Its Free Fall to the Ocean Floor, C.S. Draper Laboratory, Inc., Report R-1079, April 1977.

10. Vachon, W.A. and J.R. Scholten, Final Report on the C.S. Draper Laboratory Role in the Mooring Dynamics Experiment, C.S. Draper Laboratory, Inc., Report R-1093, April 1977.

11. Dahlen, J.M., et. al., Draper Laboratory Profiling Current and CTD Meter (Prototype Design Description), C.S. Draper Laboratory, Inc., Report R-1095, July 1977.

12. Walden, R.G., D.H. DeBok, D. Meggitt, J.B. Gregory, and W.A. Vachon, "The Mooring Dynamics Experiment - A Major Study of the Dynamics of Buoys in the Deep Ocean", Paper No. 2883, Proc. Offshore Tech. Conf., 1977.

13. Chhabra, N.K., Optimization and Evaluation of the Applied Physics Laboratory Current Profiler Design Configuration, C.S. Draper Laboratory, Inc., Report R-1152, March 1978.

14. Chhabra, N.K., Dynamics of a Tethered Spar Buoy System - Validation Using Full-Scale Ocean Test Data, Proceedings, ASCE Conference: Civil Engineering in the Oceans, San Francisco, CA, Sept. 10-12, 1979, pp. 208-223.

SOME NEW APPROXIMATION TECHNIQUES FOR MOORING SYSTEM DESIGN

R. A. Skop and F. Rosenthal

U.S. Naval Research Laboratory
Washington, DC 20375

Abstract

As the measurements desired by oceanographers and acousticians have become increasingly refined, the need to accurately design to experimental requirements the mooring systems used as instrumentation platforms has increased correspondingly. In this paper, some new approximation techniques that promise to result in more accurate mooring system designs than are presently possible are developed. These techniques deal with two topics in mooring dynamics The first topic concerns the effects of flow-induced strumming vibrations on the static configuration of mooring systems that have one or more horizontal legs. The second topic concerns the dynamic response to time varying ocean currents of taut, single point moors.

Introduction

Over the past score years, oceanographers and acousticians have sought increasingly more refined measurements of the ocean environment. These investigations have placed increasingly stringent requirements on the allowable response to the environmental forces of the mooring systems used as instrumentation platforms. Examples include Pacific Sea Spider[1] and the Atlantic Test Bed[2] for acoustics experiments, the IWEX moor[3] for internal wave measurements, the SEACON II moor[4] for engineering validation studies, and the High Density Current Meter moor[5] for detailed current measurements.

In response to these stringent requirements on mooring performance, ocean engineers have undertaken studies that have led to better definitions of the environmental forcing functions and improved techniques for the design and analysis of mooring systems. Examples in these categories include work on flow-induced vibrations and their consequences[6], investigations of methods to suppress flow-induced vibrations[7], the DESADE computer program[8] for static and quasi-static mooring analyses, and a number of computer programs for various aspects of dynamic analysis[9].

In this paper, some new approximation techniques that promise to result in more accurate mooring system designs than are presently possible are developed. These techniques deal with two topics in mooring dynamics. The first topic concerns the effects of flow-induced strumming vibrations on the static configuration of mooring systems that contain one or more horizontal legs. The second topic concerns the dynamic response to time varying ocean currents of taut, single point moors.

An Approximation for Strum Amplified Cable Drag Coefficients

It is well known experimentally that a bluff cylindrical object in a uniform flow experiences flow-induced strumming vibrations that result in an amplified drag coefficient for the object[6]. This phenomena is illustrated in Figure 1 where the ratio of the measured drag coefficient C_D on a strumming rigid circular cylinder to the drag coefficient C_{DO} on the stationary cylinder is plotted as a function of the wake response parameter w_r. This parameter is defined by

$$w_r = (1 + 2Y/d)\ \omega/\omega_S \tag{1}$$

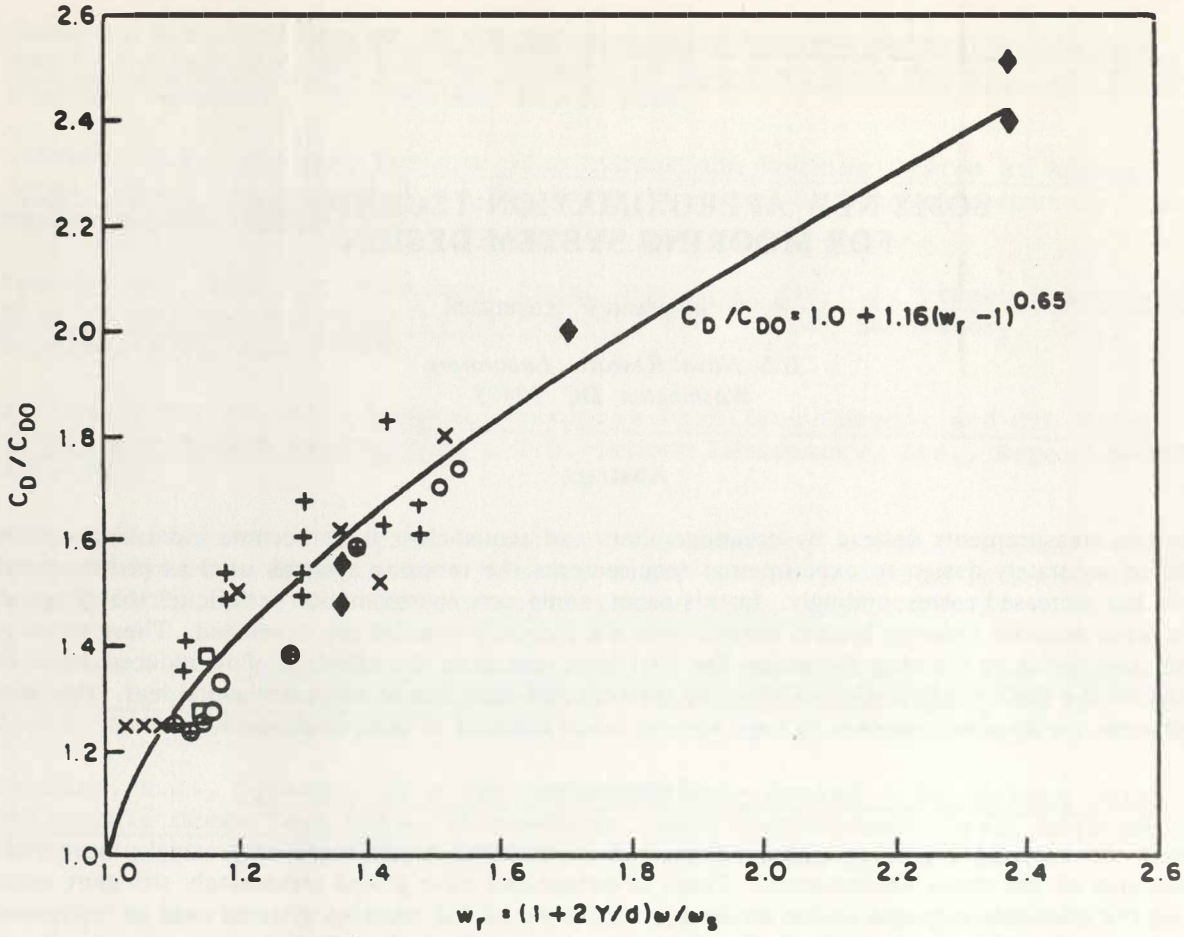

Figure 1. The ratio of the drag coefficient C_D of a strumming rigid circular cylinder to the drag coefficient C_{DO} of the stationary cylinder as a function of the wake response parameter w_r. The solid line is a least squares fit to the data points that are denoted by various symbols.

where $2Y$ is the peak-to-peak cylinder vibration amplitude, d is the cylinder diameter, ω is the cylinder vibration frequency, and ω_S is the naturally occurring shedding frequency from the cylinder.

In a mooring system that requires effectively horizontal legs as part of the experimental program, it is necessary to account for the amplified drag coefficient on these legs in order to produce an accurate mooring design. This is because the horizontal legs, both in actuality and design, are likely to experience essentially uniform currents along their lengths and hence are subject to strumming oscillations.

A formula for approximating the value of the strum amplified drag coefficient C_{DA} for an effectively horizontal cable in a uniform flow has previously been derived by Skop[10]. This approximation is given by

$$\frac{C_{DA}}{C_{DO}} = 1 + \frac{1.69\ R_N^{1.09}}{(\sqrt{R_N} + 4.61)^{2.18}} \tag{2}$$

Here, R_N is the Reynolds number for the flow based on the component of current normal to the cable axis. That is

$$R_N = V_N\, d/\nu \tag{3}$$

where V_N is the normal component of current and ν is the kinematic viscosity of the fluid.

The above formula is intended for use in mooring system design studies and, in this regard, is conservative in that it yields an upper bound for the strum amplified drag coefficient. The value of C_{DA}/C_{DO} versus R_N is shown graphically in Figure 2. It should be apparent from this figure that the accurate design of a mooring system that contains one or more horizontal legs requires taking into account the strum amplified drag coefficients for these legs. Equation (2) can be easily incorporated in the DESADE computer program[8], and the necessary modifications to the program are detailed in Appendix A.

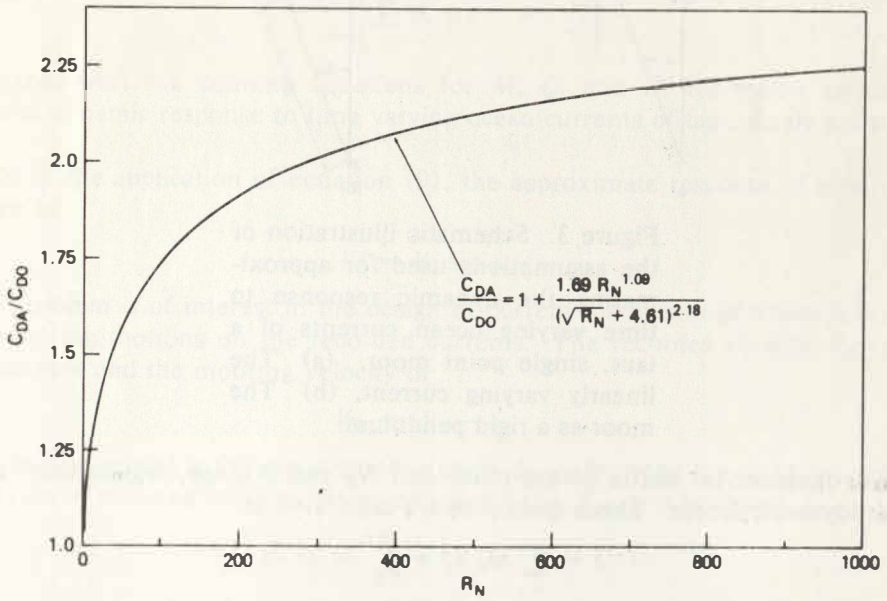

Figure 2. The approximation for the amplified drag coefficient C_{DA} of a cable undergoing flow-induced strumming oscillations plotted against the Reynold number R_N based on the component of current normal to the cable axis. C_{DO} is the drag coefficient of the stationary cable.

An Approximation for the Dynamic Response of Taut, Single Point Moors

One of the more difficult problems in mooring system design is that of designing a system to have particular dynamic response characteristics to time varying ocean currents. Although the requisite computer programs[9] exist, the problem still is difficult because it is nonlinear, the number of free design parameters is large, and the precise definition of the time varying currents is intractable.

In this section, a method for approximating the dynamic response to time varying ocean currents of taut, single point moors is developed. The approximation is quite crude but should prove useful for homing in on a preliminary system design. Detailed dynamic analyses can then be used to refine this design.

The underlying assumptions behind this approximation are that a taut, single point moor can be treated, in the crudest sense, as a rigid pendulum undergoing a small angular deflection θ and that the magnitude of the time varying current increases linearly with height above bottom z as shown in Figure 3. The assumption of small angular deflection is equivalent to specifying that the arc length along the moor $s \sim z$. Thus, the current V along the moor is given by

$$V(s,t) \sim V(z,t) = (z/L)\ V_L(t) \sim (s/L)\ V_L(t) \tag{4}$$

where L is the total length of the moor and $V_L(t)$ is the current at $z = L$.

Under the above conditions, the equation of motion of the moor is obtained as

$$I\ddot{\theta} = N_B + N_H \tag{5}$$

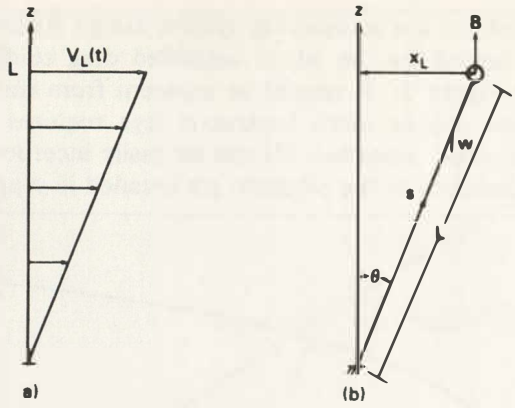

Figure 3. Schematic illustration of the assumptions used for approximating the dynamic response to time varying ocean currents of a taut, single point moor. (a) The linearly varying current. (b) The moor as a rigid pendulum.

where I is the mass moment of inertia of the moor and N_B and N_H are, respectively, the torques due to buoyancy and hydrodynamic forces. These quantities are calculated as

$$I = \sum_n M_n s_n^2 + \int_0^L m s^2 \, ds \tag{6a}$$

$$N_B = -\theta \left[\sum_n B_n s_n - \int_0^L w s \, ds \right] \tag{6b}$$

$$N_H = \sum_n \tfrac{1}{2} \rho C_{Dn} A_n [V(s_n,t) - s_n \dot{\theta}] \mid V(s_n,t) - s_n \dot{\theta} \mid s_n + \int_0^L \tfrac{1}{2} \rho C_D d [V(s,t) - s \dot{\theta}] \mid V(s,t) - s\dot{\theta} \mid s \, ds \tag{6c}$$

Here, M_n, B_n, C_{Dn}, and A_n are, respectively, the virtual mass, buoyancy, drag coefficient, and frontal area of the nth discrete object on the taut moor. The location of this object on the moor is denoted by s_n. Similarly, m, w, C_D and d denote, respectively, the virtual mass per length, weight per length, drag coefficient, and diameter of the mooring cable. The density of the water is represented by ρ. In calculating the torque due to hydrodynamic forces, the contribution caused by the fluid acceleration V_L has been neglected in comparison to that caused by the fluid drag. This is valid for situations (realized in most mooring dynamics problems) in which a fluid particle travel several cable diameters before reversing its direction of travel.

On substituting equation (4) into equation (6c), recasting the s_n as

$$s_n = \alpha_n L \tag{7}$$

where the α_n are length proportionality constants, and putting

$$x_L = L\theta \tag{8}$$

where x_L is the horizontal deflection at the top of the moor, equation (5) is transformed into an equation for x_L given by

$$M \ddot{x}_L + Q (\dot{x}_L - V_L) \mid \dot{x}_L - V_L \mid + K x_L = 0 \tag{9}$$

Here,

$$M = \sum_n M_n \alpha_n^2 + mL/3 \tag{10a}$$

$$Q = \tfrac{1}{2}\rho\left[\sum_n C_{Dn} A_n \alpha_n^3 + C_D d L/4\right] \tag{10b}$$

and

$$K = \frac{1}{L}\left[\sum_n B_n \alpha_n - w L/2\right] \tag{10c}$$

Equations (9), together with the defining equations for M, Q, and K, represents an approximation for roughly calculating the dynamic response to time varying ocean currents of taut, single point moors.

As an example of the application of equation (9), the approximate response of a taut moor to a time varying current given by

$$V_L = V_o \sin \omega t \tag{11}$$

is considered. This problem is of interest in the design of current meter strings where it is desired to ascertain the effects of mooring motions on the recorded currents. The recorded current V_{RL} is the difference between the actual current and the mooring velocity or

$$V_{RL} = V_L - \dot{x}_L \tag{12}$$

and the quantity to be determined is the worst possible error E_{MAX} between the recorded and actual currents over a steady-state cycle of mooring motion. From equation (12), E_{MAX} is found as

$$E_{MAX} = |V_{RL} - V_L|_{MAX} = |\dot{x}_L|_{MAX} \tag{13}$$

Before proceeding to the solution of the above problem, it is useful to introduce the dimensionless displacement y_L and time τ defined by

$$y_L = (\omega_n/V_o)\, x_L \tag{14a}$$

$$\tau = \omega_n t \tag{14b}$$

where the natural frequency of the moor ω_n is

$$\omega_n = \sqrt{K/M} \tag{14c}$$

On substituting equations (11) and (14) into equation (9), the governing equation for y_L becomes

$$y_L'' + q\left[y_L' - \sin\frac{\omega}{\omega_n}\tau\right]\left|y_L' - \sin\frac{\omega}{\omega_n}\tau\right| + y_L = 0 \tag{15a}$$

where (′) denotes differentiation with respect to τ and

$$q = \frac{QV_o}{M\omega_n} = \frac{Q\,V_o}{\sqrt{KM}} \tag{15b}$$

Similarly, from equation (13), E_{MAX} becomes

$$\frac{E_{MAX}}{V_o} = \frac{|V_{RL} - V_L|_{MAX}}{V_o} = |y_L'|_{MAX} \tag{16}$$

In Figure 4, (E_{MAX}/V_o) is plotted against the frequency ratio (ω/ω_n) for various values of the parameter q. The results were obtained by a numerical integration of equation (15a).

Summary

Two new approximation techniques for treating certain topics in mooring system dynamics have been developed. The first topic concerns an approximation for the amplified drag coefficient resulting from flow-induced strumming oscillations. The second topic concerns an approximation for the dynamic response to time varying ocean currents of taut, single point moors. Both techniques should prove useful in mooring system design problems and lead to more accurate system designs than are presently possible.

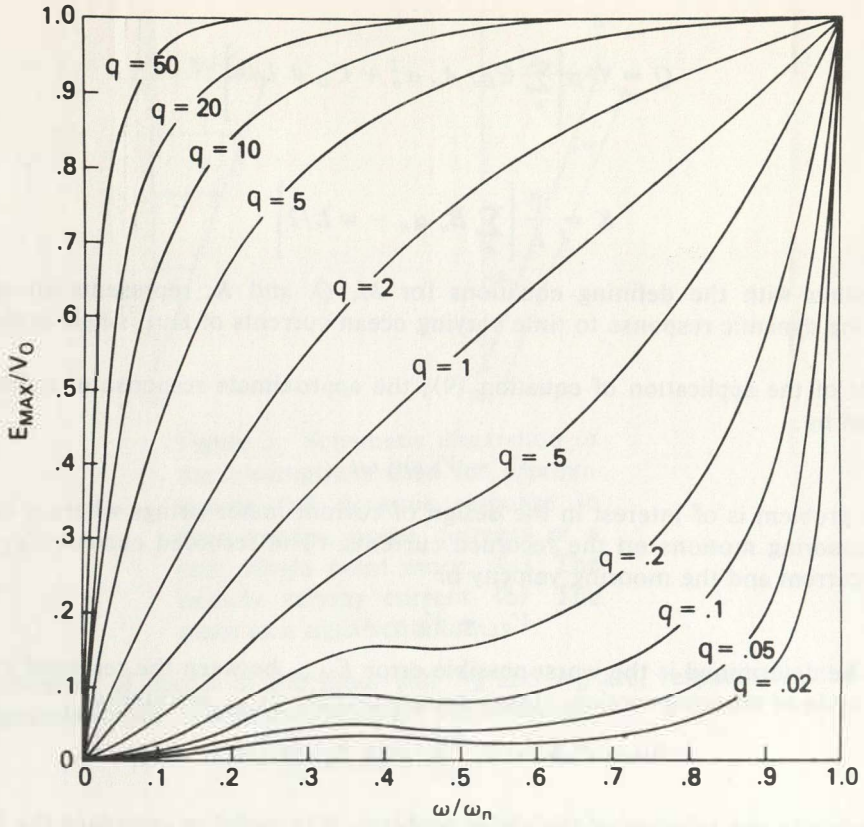

Figure 4. The worst possible error $E_{MAX} = | V_{RL} - V_L |_{MAX}$ between the current V_{RL} recorded by a current meter on a taut moor and the actual current $V_L(t) = V_o \sin \omega t$. E_{MAX}/V_o is plotted against the frequency ratio ω/ω_n for various values of the parameter q (equation (15b)).

References

1. G.H. Savage and J.B. Hersey, "Project Seaspider: The Design, Assembly, Construction and Sea Trials of a Tri-Moored Buoyant Structure to Provide a Near Motionless Instrument Base for Oceanographic Research," Marine Technology Society Journal, Vol. 3, No. 2, pp. 95-112, March 1969.

2. J.D. Wilcox, "A Description of the LRAPP Atlantic Test Bed Array for Motion Prediction Studies (U)," NUSC Technical Memorandum SA23-C275-73, December 1973, CONFIDENTIAL.

3. R.G. Walden and H.O. Berteaux, "Design and Performance of a Deep-Sea Tri-Moor," Proceedings of Tenth Annual Marine Technology Society Conference, pp. 81-86, 1974.

4. T.R. Kretschmer, G.A. Edgerton, and N.D. Albertsen, "Seafloor Construction Experiment, Seacon II: An Instrumented Tri-Moor for Evaluating Undersea Cable Structure Technology," Civil Engineering Laboratory Technical Report R-848, December 1976.

5. D.A. Milburn, "Design and Analysis of a High Density Current Meter Mooring," NORDA Workshop on Near Surface Ocean Experimental Technology, November 1979.

6. O.M. Griffin, et al., "Vortex-Excited Vibrations of Marine Cables," Journal of the Waterways, Port, Coastal and Ocean Division, ASCE, to be published.

7. W. Kline, et al., "A Survey of Recent Investigations into the Nature of Cable Strumming, Its Mechanisms and Suppression," MAR Report No. 210, July 1978.

8. R.A. Skop and J. Mark, "A Fortran IV Program for Computing the Static Deflections of Structural Cable Arrays," NRL Report 7640, August 1973.

9. D.B. Dillon, "An Inventory of Current Mathematical Models of Scientific Data-Gathering Moors," Hydrospace-Challenger Report 4450-0001, February 1973.

10. R.A. Skop, "An Analysis, Including Strumming Effects, of the Predicted Versus Measured Motions of the Atlantic Test Bed (U)," NRL Memo Report 3718. February 1978, CONFIDENTIAL.

Appendix A — Incorporation of the Strum Amplified Drag Coefficient Formula in DESADE

For mooring system design purposes, equation (2) for the strum amplified drag coefficient can be incorporated into DESADE through a program modification in the CFØRCE subroutine. The required modification consists of replacing cards CF0065 and CF0066 by the following set of cards:

```
      CD =CDCAB(N)
      IF   (N.EQ.n1) GØ TØ 6
      IF   (N.EQ.n2) GØ TØ 6
                .
                .
                .
      IF   (N.EQ.nI) GØ TØ 6
```

($n_1 \ldots n_I$ are the cable numbers of those cables expected to undergo strumming oscillations.)

```
      GØ TØ 7
    6 REN = VNMAG *(DCAB(N)/12.) / (19.4E-6)
```

(Based on original DESADE units of VNMAG in ft/sec and DCAB(N) in inches.)

```
      SUB = (1.69) *(REN **1.09) / ((SQRT(REN) + 4.61) **2.18)
      CD = CD *(1.+SUB)
    7 CFØRCE = WTCAB(I) + (RHØ /2.) *CD *(DCAB(N)/12.) *EXCAB(M,N) *
     1 VNMAG *VNØRM(I)
```

DEVELOPMENT AND PERFORMANCE OF A VECTOR MEASURING CURRENT METER (VMCM)

Robert A. Weller
Woods Hole Oceanographic Institution
Woods Hole, Massachusetts 02543

Abstract

To develop the capability of making accurate measurements of horizontal velocity in the upper ocean a vector measuring current meter (VMCM) has been developed. Orthogonal cosine response propeller sensors directly measure vector components. A flux gate compass senses the instrument heading, and the velocity components are vector averaged and recorded on cassette tape. The instrument has the capability of one year long deployment at depths of up to 5000 m. Laboratory tests have documented the performance of the VMCM, and both laboratory and field results show that the VMCM is capable of making accurate measurements of horizontal velocity in the upper ocean.

Introduction

One of the results of the Mid-Ocean Dynamics Experiment (MODE) that had an immediate and profound effect on those concerned with the technology of making near surface measurements was the very clear demonstration by Gould et al.[1] that the energy levels recorded by a surface moored current meter could be up to seven times higher than those recorded by a current meter near the same site but attached to a subsurface mooring. Though the inability of Savonius rotor current meters to accurately measure the mean horizontal velocity in the presence of high frequency vertical oscillation had been demonstrated earlier by Gaul[2], it was the MODE result that stimulated much of the present awareness of the difficulties associated with making velocity measurements in the upper ocean where the instruments would operate in the presence of high frequency motion associated with surface waves and/or mooring motion.

One result of that awareness was that some investigators restricted their efforts to the deep ocean. Few experiments were carried out in the upper ocean; and as interest in upper ocean dynamics increased, the need for upper ocean data became acute. In 1973, we planned participation in experimental programs that would include gathering upper ocean current meter data. Our scientific interest was in studying the response of the upper ocean to wind forcing, which placed the requirement on the current meters to be used that the mean and low frequency flows, whose magnitude might be small compared to the wave orbital velocities, should be accurately measured. However, existing current meters were not capable, when suspended from surface riding floats, of making accurate measurements of relatively small mean flows. Thus, in order to gain the capability of making accurate upper ocean velocity measurements, we undertook the development of a current meter.

The development of the propeller sensor, the current meter package, the results of performance testing, and a discussion of future development of the VMCM are discussed in the following sections.

Propeller Sensors

Three sensing techniques were investigated at the beginning of the development of the VMCM. Available electromagnetic sensors were unable to

make accurate measurements of relatively small mean flows in the presence of oscillatory motion.[3,4] Acoustic sensors showed great potential because of their ability to measure flow without disturbing the fluid, but the design of the supports for the sensors would require great care so as not to disturb the flow in the acoustic path. Mechanical sensors of two types were considered. Rotor/vane sensors measure speed, U, and direction, θ, from which the velocity components, (u,v), are later computed. The relation between (U,θ) and (u,v) is nonlinear; and, as a result, poor response of rotor or vane at high frequency leads to error in (u,v) at lower frequencies. Propeller sensors, in contrast, offered the advantage that they could be used as component sensors, sensors which measure u and v, the vector components, directly.

The extent to which a given propeller is a component sensor can be described by its angular response function, $F(\alpha)$, defined by the relation $\Omega = |\vec{U}|\ F(\alpha)$, where Ω is the revolution rate of a propeller in a flow (represented by the vector $\vec{U}$) of magnitude $|\vec{U}|$ where the angle between $\vec{U}$ and the propeller axle is α. $F(\alpha)$ is determined, typically, in a flume or two tank. Figure 1 shows $F(\alpha)$ for various propellers.

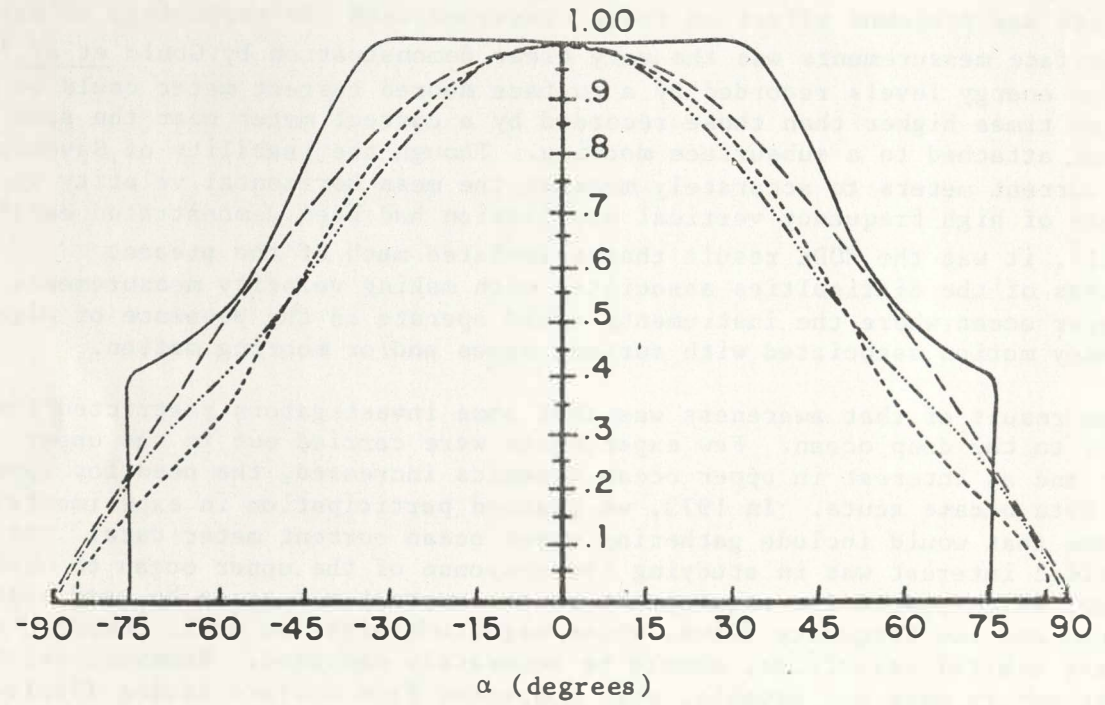

Figure 1. $F(\alpha)$ vs. α. The solid line is the response of a ducted or shrouded propeller. The dashed line below that is a cosine curve. The dotted dashed line is the response of a Gill[5] propeller. The line of short dashes marks the response of Cannon and Pritchard's[6] propeller.

Two or more propellers with known $F(\alpha)$ can be used to sense (u,v); Cannon and Pritchard[6] discuss the technique. Some computation is involved and the instrument must either do the computation internally at a rapid rate or store instrument heading and propeller revolution rates at frequent intervals; the high frequency of computation or sampling is necessary to avoid introducing

error associated with inferring the average flow direction over intervals approaching the period of flow fluctuations. Ideally $F(\alpha)$ would be $\cos(\alpha)$, for in that case the component of velocity parallel to the axle is measured directly and two such sensors mounted at right angles with their axles in the horizontal plane would measure horizontal velocity directly with no sensitivity to the vertical component and no need for computation. Vector averaging would require only summing the measured components.

Propellers turn in response to torque exerted on them by the fluid. The lift and drag forces can be parameterized as $1/2\rho\ C_L|\vec{U}|U$ and $1/2\rho\ C_D|\vec{U}|U$ respectively, and models of propeller response can be used to make predictions of propeller performance.[7] Walrod[8] attempted to use a theoretical model to guide development of a propeller with cosine response. The models fail, however, to accurately predict angular response or dynamic performance because effects such as flow separation and flow interference are not included.

The development of a cosine response propeller was achieved by empirical methods. Model propellers were built (200 of them). Blade pitch, blade size, blade shape, number of blades, and number of propellers per axle were varied; one variable was altered while all others were held fixed. Each model was wind tunnel tested to determine its angular response function. Eventually it was determined how to alter propeller design in order to manipulate the angular response function and to design sensors with $F(\alpha) \simeq \cos(\alpha)$. This process is described in more detail by Weller[9].

That sensor was then taken to a tow tank to verify its steady flow performance characteristics. The angular response, Figure 2, in the horizontal plane was close to cosine; the r.m.s. deviation of the response from a cosine of the same maximum amplitude was approximately 1.5% of full scale. Two such sensors were combined, mounted at right angles and attached to a mock-up of a pressure case so that an instrument configuration could be found where the proximity of the two propellers to each other and to the pressure case would not degrade the cosine response. A spacing of 35 cm between propeller axles and 39 cm between pressure case and closest axle was found not to degrade horizontal cosine response and gave a vertical response function that was also close to cosine as shown in Figure 3. Tests were made to document the linearity of the response to flow at zero degree angle of attack, Figure 4, and to step changes in flow, Figure 5.

The sensor, in summary, had characteristics that suggested that it could be used in the upper ocean: low threshold (1.5-2.0 cm s^{-1}), linearity, and responsiveness ($L \simeq 9$ cm). Development of the current meter package itself began next.

VMCM Design

The sensor, hopefully, would meet the scientific requirement of being able to accurately measure small mean flows in the presence of high frequency oscillatory flow. Other design requirements were necessary to make a durable and useful instrument:

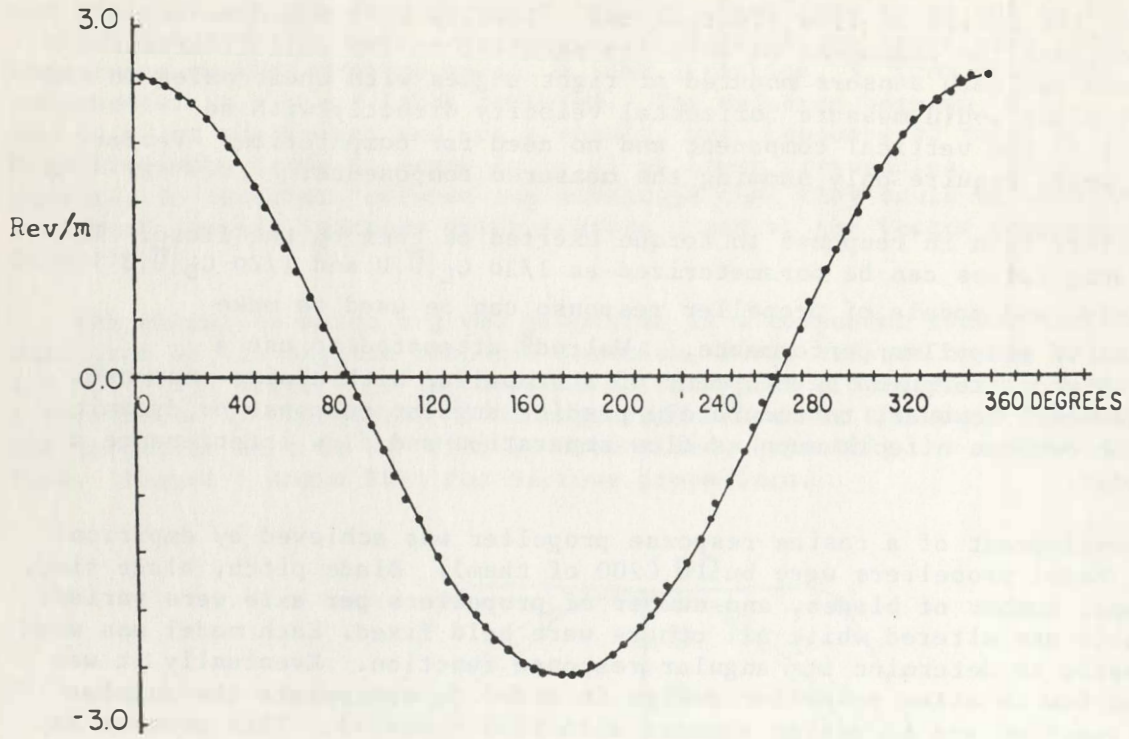

Figure 2. Propeller response in revolutions per meter of horizontal flow vs. angle of attack. Data (black dots) taken every five degrees. Cosine curve is drawn so that it has the amplitude of the response at zero degree angle of attack.

Mechanical Requirements

1) Usable to depths of up to 5000 m
2) Able to withstand 45000 Newton (10000 lb) of tension
3) Corrosion resistant
4) Fouling resistant
5) Relatively light and easy to handle without sacrificing durability

Electronic Requirements

1) Internally vector averaging
2) Able to record up to six channels of digital data
3) Able to sample at various selectable rates
4) Deployable for up to one year

The design met these goals and is pictured in Figures 6a and 6b.

The external structure of 1.27 cm diameter rod is the load cage which takes the mooring load and protects the sensor during deployment and recovery. (Tow tests showed that the load cage did not alter the cosine response of the sensors.) The load cage is fabricated from 6Al-4V titanium

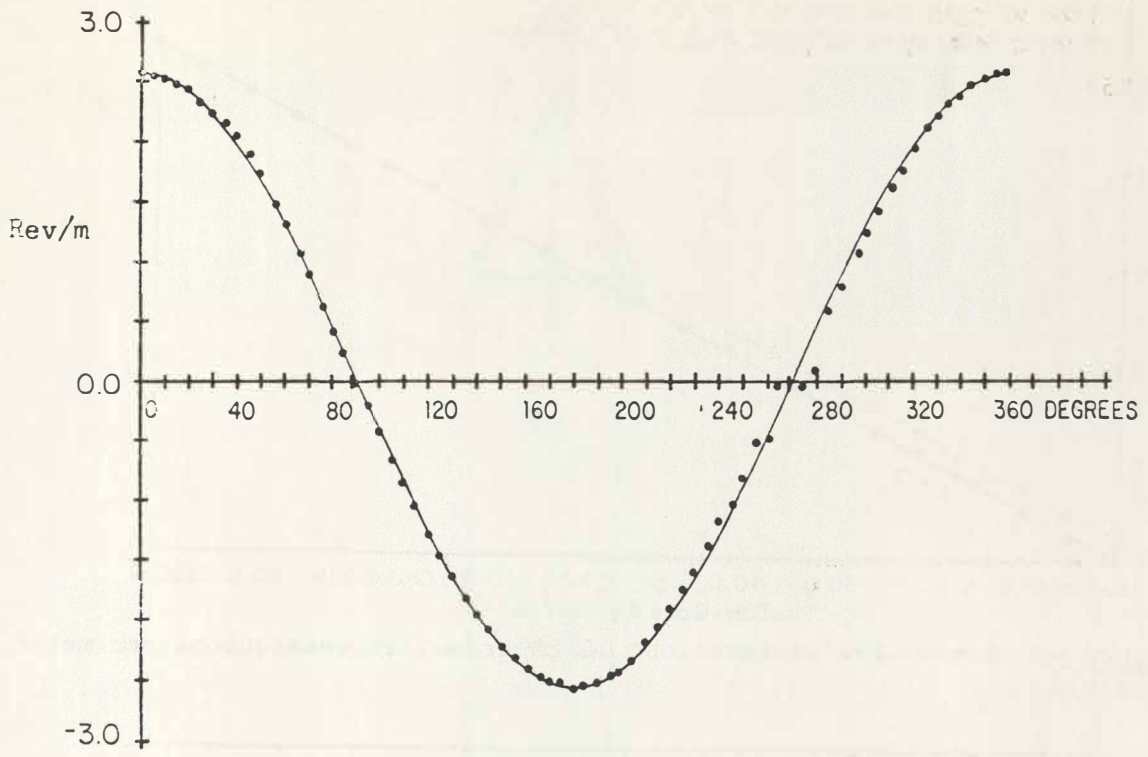

Figure 3. Propeller response in revolutions per meter to flow in a plane perpendicular to the horizontal.

alloy rod. Titanium was chosen in favor of stainless steel because of its lower weight, higher yield strength, and superior resistance to corrosion and fatigue in sea water and because manufacturing costs (in southern California) of titanium and stainless steel were comparable. The cage, under 45000 Newton load, extends only .3 cm. The instrument package, made from 6061-T6 aluminum alloy, is held inside the cage by plastic (Noryl) bushings so that the load cage and instrument housing are electrically isolated and so that no tension is transferred to the instrument package.

The pressure housing and the probe-like appendage holding the propeller sensors are 6061-T6 aluminum. The parts are machined, welded, heat-treated, hard anodized, and epoxy coated on the exterior. With 1.7 cm thick walls the pressure case has a safe working depth of 5000 m. Zinc anodes on the pressure case and base plate of the sensor improve corrosion resistance.

The combination of the titanium alloy load cage and aluminum instrument housing made a relatively light but rugged instrument possible. The mass of the complete VMCM is 34.5 kg, and it displaces 15.5 kg of water. Several major deployments (MILE and JASIN) have proven the basic mechanical design of the load cage and instrument package.

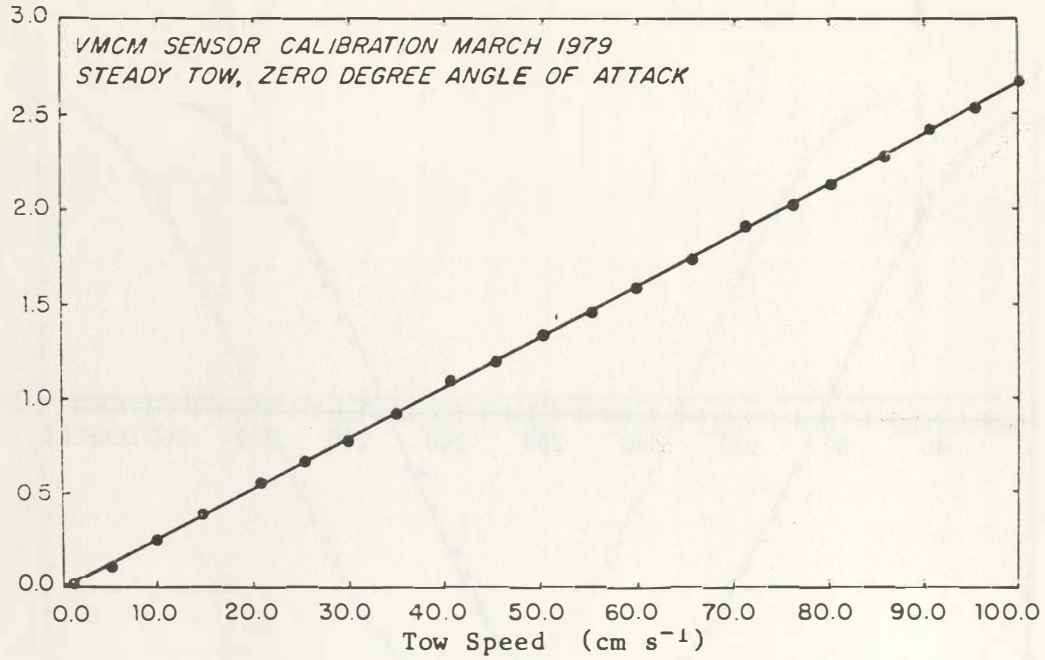

Figure 4. Steady tow calibration: 2.67 propeller revolutions per meter of fluid.

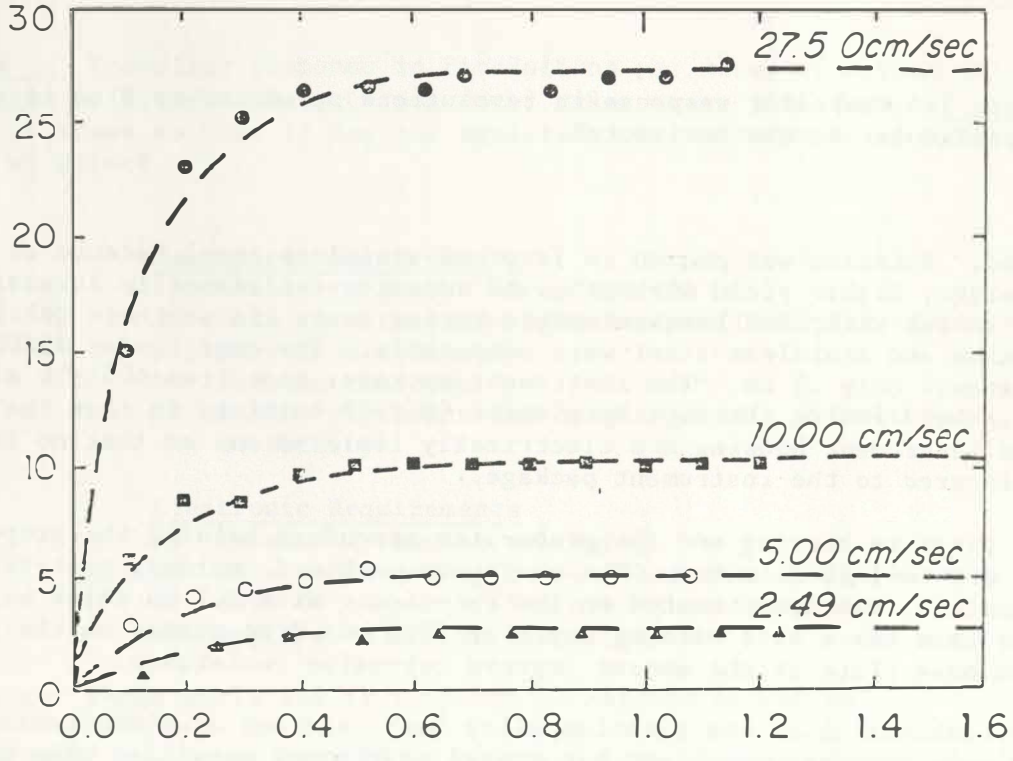

Figure 5. Response to a step change in velocity. Response fits the form $U(1-e^{-X/L})$, where U is the new speed; X, the displacement since the step change occurred; and L is the "distance constant" peculiar to that propeller and is approximately 9 cm in this case.

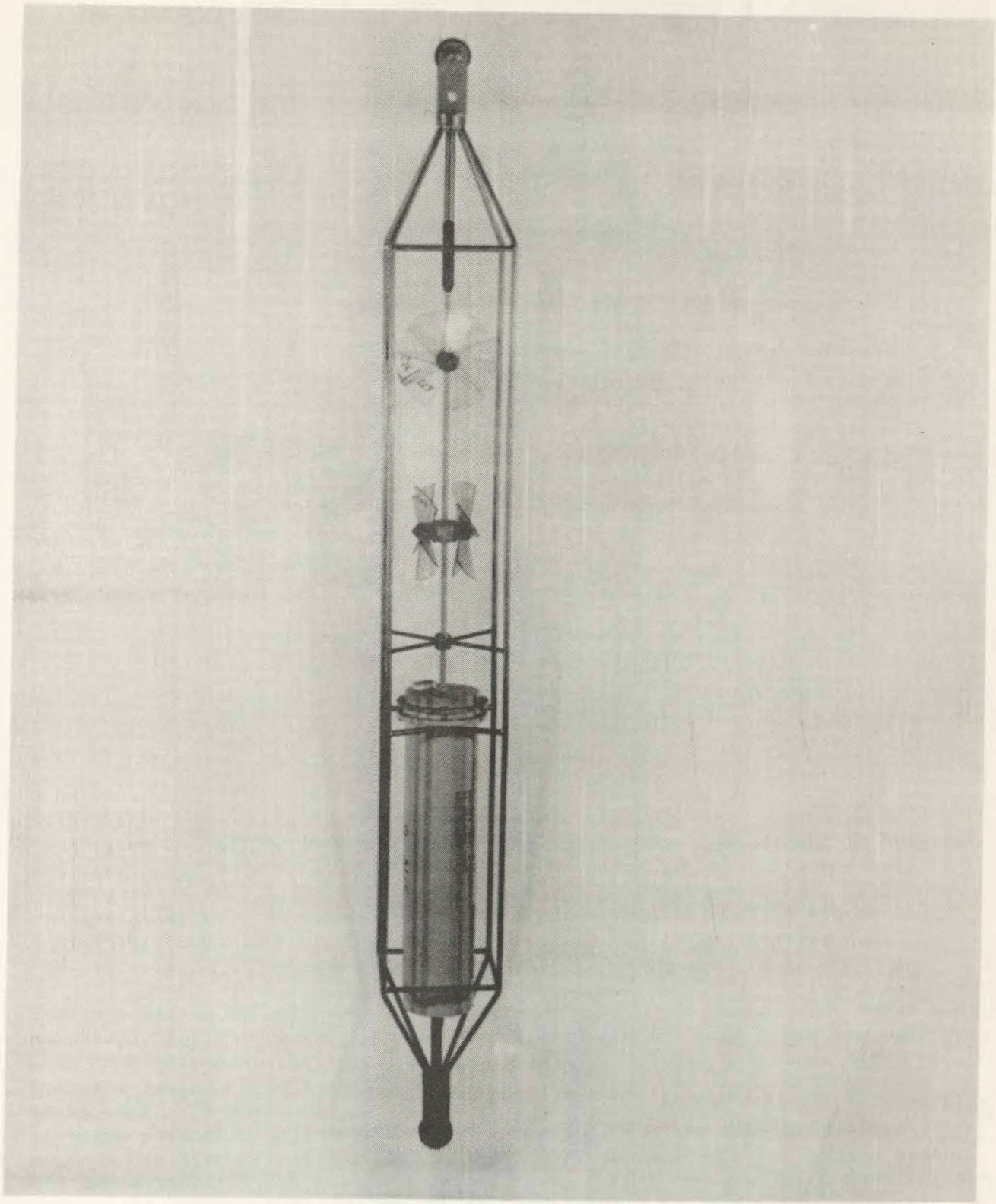

Figure 6a. The VMCM. 2.56 m in length, shown as deployed in the ocean.

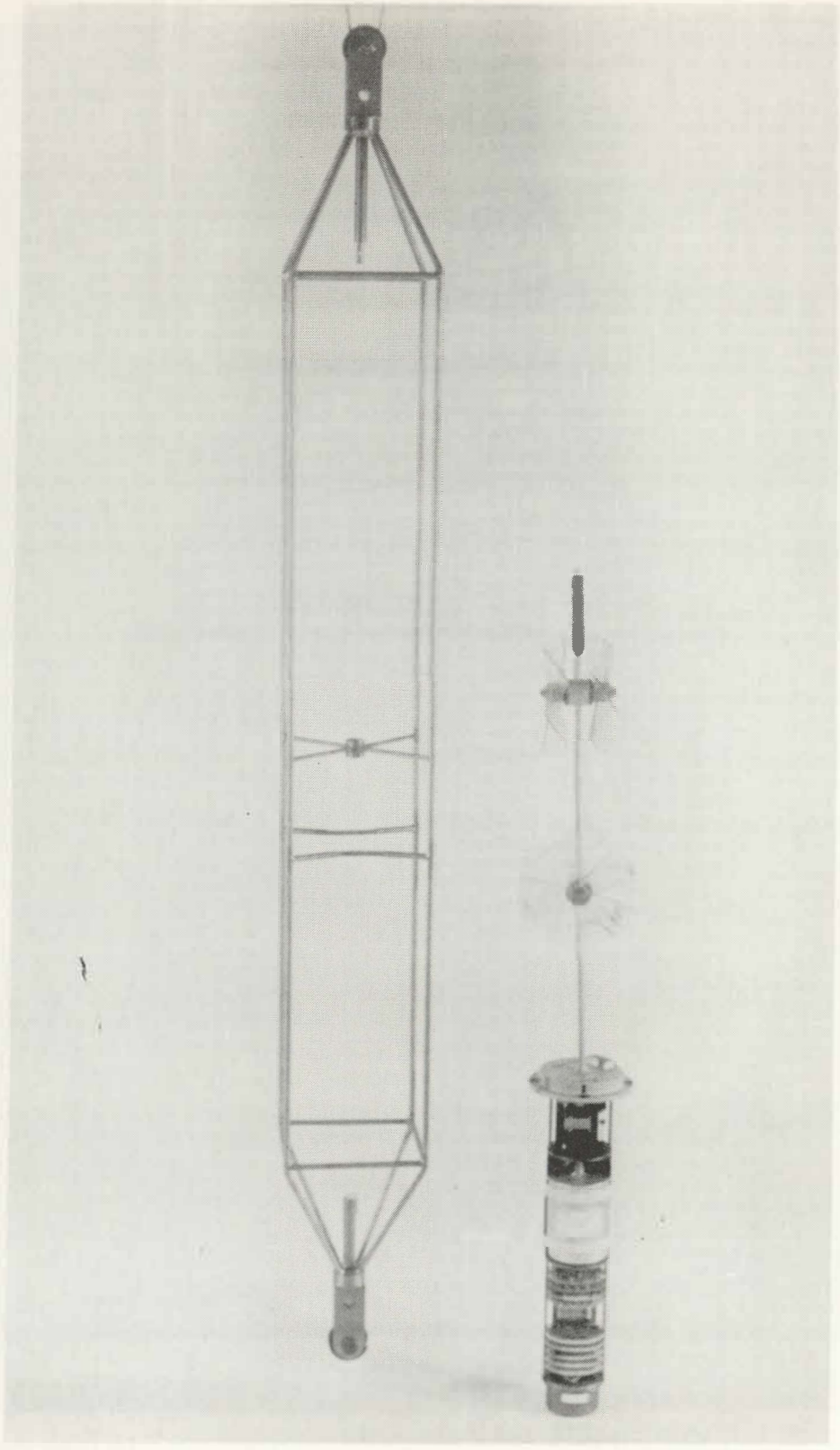

Figure 6b. The VMCM load cage (left) and the electronics chassis (right). The electronic chassis contains (from the bottom) a flux gate compass, circuit cards with room for additional cards, battery pack, and cassette recorder.

The design of the sensor, as shown in Figure 7, evolved over several years.

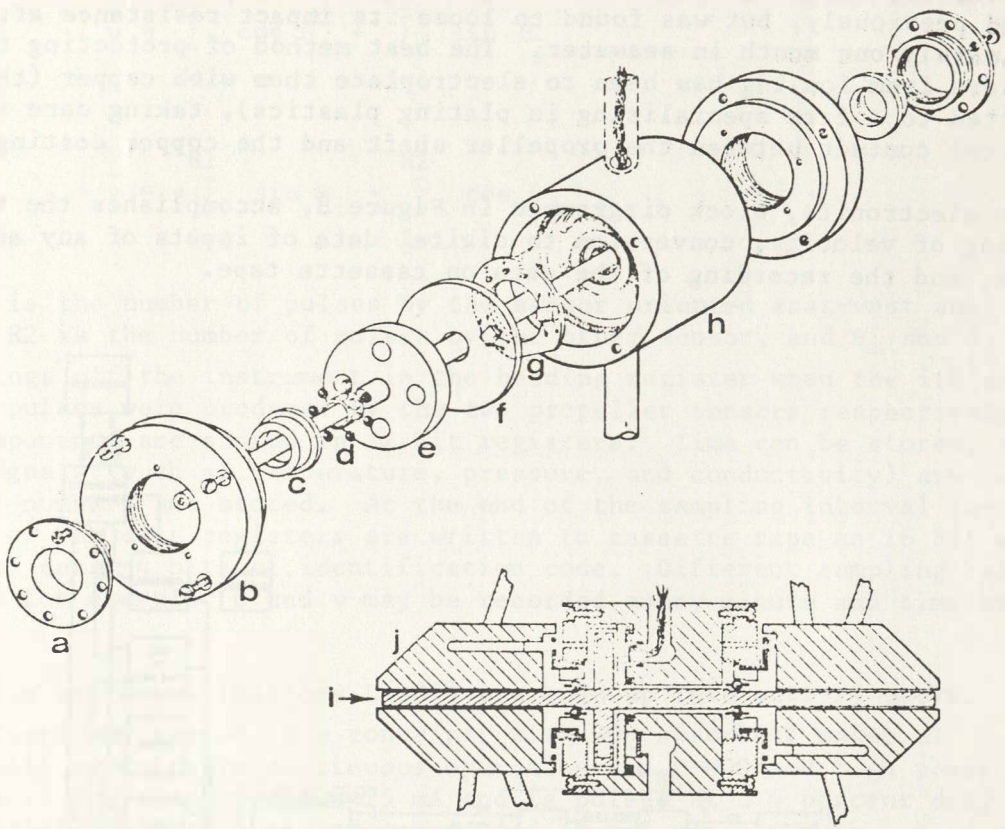

Figure 7. Sensor design. The various parts are: a) adjustable bearing retainer, b) end cap, c) outer race of bearing, d) balls and ball separator, e) disc with four magnets, f) aluminum disc that seals out the seawater, g) magnetodiodes on annular printed circuit board, h) sensor hub, i) propeller axle, and j) partial view of propeller.

Bearings had to be corrosion resistant and have low friction. The balls were purchased, but the other components were machined in-house. Success was had with combinations of 316 stainless steel shafts and 316 stainless steel or Stellite balls. Such bearings were corrosion free and free running after three months in seawater. Attached to the propeller shaft is a disc with high strength permanent magnets embedded (in epoxy) near the perimeter. The magnets are symmetrically placed in the disc, while in the hub of the sensor are two asymmetrically located magnetodiodes. When the propeller revolves the passage of the magnets over the diodes generates a voltage pulse from each diode; the frequency of the pulses is proportional to the propeller revolution rate, while the phase of the pulses indicates the direction of rotation. A thin (.23 cm) anodized aluminum disc seats on O-rings over the magnetodiodes, sealing the interior of the sensor off from the free flooding space the

bearings occupy; the thickness of this disc can be increased to match the depth capability of a thicker wall pressure case.

The propellers themselves are machined from Noryl plastic. Noryl was chosen for its impact strength and long term durability in seawater. LEXAN was used previously, but was found to loose its impact resistance after approximately one month in seawater. The best method of protecting the propellers from fouling has been to electroplate them with copper (this is contracted to a firm specializing in plating plastics), taking care to have no electrical contact between the propeller shaft and the copper coating.

The electronics, block diagrammed in Figure 8, accomplishes the vector averaging of velocity, conversion to digital data of inputs of any analog sensors, and the recording of the data on cassette tape.

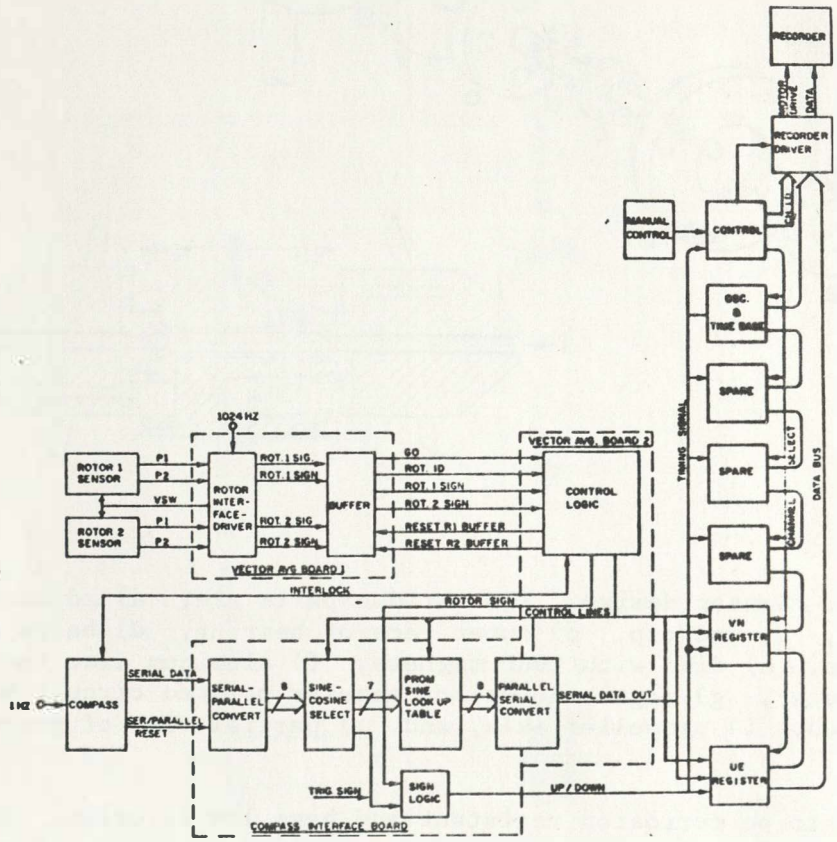

Figure 8. Block diagram of the VMCM electronics.

At a 1Hz rate the heading, θ, of the instruments is determined with a flux gate compass and stored in a register. Sufficient rotation by either of the two propellers so that a magnetodiode pulse is sensed ($\sim$9 cm of fluid

displacement along the axle generates one pulse) causes the cosine and sine of the heading to be added to registers storing u and v components. At the end of the sampling interval the registers contain

$$\bar{u} = \sum_{i=1}^{R1} \cos \theta_i + \sum_{j=1}^{R2} \sin \theta_j$$

$$\bar{v} = -\sum_{i=1}^{R1} \sin \theta_i + \sum_{j=1}^{R2} \cos \theta_j$$

Where R1 is the number of pulses by the sensor oriented east-west when $\theta = 0$ degrees, R2 is the number of pulses by the other sensor, and θ_i and θ_j are the headings off the instrument in the heading register when the ith and jth pairs of pulses were produced by the two propeller sensors respectively. These components are stored in 12 bit registers. Time can be stored, and analog signals (such as temperature, pressure, and conductivity) are converted to 12 bit numbers and stored. At the end of the sampling interval the contents of the data registers are written to cassette tape as 16 bit words, 12 bits of data, 4 bits of identification code. Different sampling rates are possible; for example, u and v may be recorded every minute and time every hour.

Lithium batteries (Mallory $LiSO_2$) are made up into battery packs. The pack is fused and sealed in a container with SO_2 absorbent material inside. All circuits in continuous operation are C-MOS and high power devices are pulsed. The compass draws 25 mA and is pulsed at a 4 percent duty cycle; the magnetodiodes draw 6 mA and are pulsed at a 5 percent duty cycle; and the tape recorder draws 80 mA and has a duty cycle of approximately one percent. To some extent, the power consumption is proportional to the fluid velocity since the vector averaging circuitry is powered on only if a magnetodiode pulse is sensed. At present, cassette length is the limiting factor in sampling rate/deployment length considerations.

Thus, an attempt has been made to meet all the design requirements. Initial problems with the durability of LEXAN propellers have been eliminated by using NOYRL. The long term fouling resistance has not been adequately tested; both MILE and JASIN deployments were in cold water, characterized by low incidence of fouling. The cassette decks (Memodyne) have been unreliable in that, even after great care and effort, they fail 10-20 percent of the time.

Performance Testing

The steady flow characteristics and the design of the VMCM made it suitable for use in the upper ocean. but the critical requirement was that it be able to accurately measure relatively small, low frequency horizontal velocities in the presence of large amplitude, high frequency oscilatory motion associated with surface waves and/or mooring motion. To evaluate whether or not that design goal had been met a series of laboratory tests were conducted in simulation of the unsteady conditions expected in the ocean. The VMCM was tested. Then, as basis for comparison, a Neil Brown acoustic current meter (ACM) was tested and test data recovered from the literature for other current meters.

The laboratory tests were conducted by mounting on the two cart a fixture which could swing the instrument back and forth through a shallow arc. Both T, the period, and A, the amplitude of the arc, could be varied and the oscillation could be either parallel to or perpendicular to the mean flow. The flows experienced by the current meter under test were thus $V + u' \cos \omega t$ and $V + v' \cos \omega t$, where U was the mean two speed, u' ($= A\pi/T$) and v' ($= A\pi/T$) were the peak oscillatory velocities in the along-tank and cross-tank directions respectively, and ω ($= 2\pi/T$) was the frequency of oscillation.

The results of the VMCM tests can be summarized as follows: 1) no rectification when U = 0.0 and 2) Accurate measurements of mean speeds when $0.0 \text{ cm s}^{-1} \leq U \leq 60.0 \text{ cm s}^{-1}$, $5 \text{ cm} \leq A \leq 177 \text{ cm}$, and $1.5 \text{ s} \leq T \leq 17 \text{ s}$ except in two unique situations. In the first situation, U was approximately equal to u' and oscillation was parallel to two direction; the sensor would, as a result, encounter its own wake which had a lower velocity than the undisturbed fluid. In the second situation the propeller axle was parallel to the direction of tow but the oscillation was perpendicular to the tow direction; when v' was very large and U small, the threshold of the propeller increased, presumably due to either increased bearing friction resulting from the side load imposed by the drag on the propeller or by the propeller seeking a preferred orientation with respect to v'. In both cases the error was such that the measured mean, U, was less than U, with the result that the error, $U_E = U - V$, was negative.

Similar tests were performed on a Neil Brown ACM and data from these tests were combined with data found in the literature in Figure 9. The plot is of error (i.e., the difference, U_E, between U and the measured mean against the ratio U/u' (or U/v' as the case may be). Error occurs when U/u' drops below about 2 or 3. For the electromagnetic, Savonius rotor, Aanderaa, and VACM current meters, the error grows quickly as U/u' decreases. These instruments over-respond; they measure a mean flow much larger than the true mean flow. The ACM also errs when $U/u' \leq 3$, but the error is under-response; the ACM measures a mean smaller than the true mean. The VMCM shows error, as discussed above, near $U/u' \approx 1$ in one set of tests (open squares) and at smaller values of U/u' (solid squares) in the test where the threshold was increased. Note that the bulk of the VMCM tests, in other than those two geometries, in which no error was seen are not plotted.

Summarized in Figure 10 are the results of tests when U = 0. The VMCM does not rectify. However, the other current meters do rectify, and in some cases measure quite large means flows.

The laboratory tests indicated that the worst case VMCM errors were smaller than the errors to be expected from other current meters. Judging oceanic performance from these laboratory tests is difficult. In the case of the VMCM and ACM, however, where error is caused by wake effects or by other unfavorable geometry of flow with respect to the sensor, it was expected that oceanic performance would show less error. This was expected because in the ocean, especially near the surface, the flow is more three dimensional than the shallow arc used in the tests; and, as a result, the instrument would not frequently encounter its own wake nor remain in a unique flow geometry.

VMCMs were deployed in the MILE and JASIN experiments. The analysis of the current meter intercomparison data has been tedious; the details are

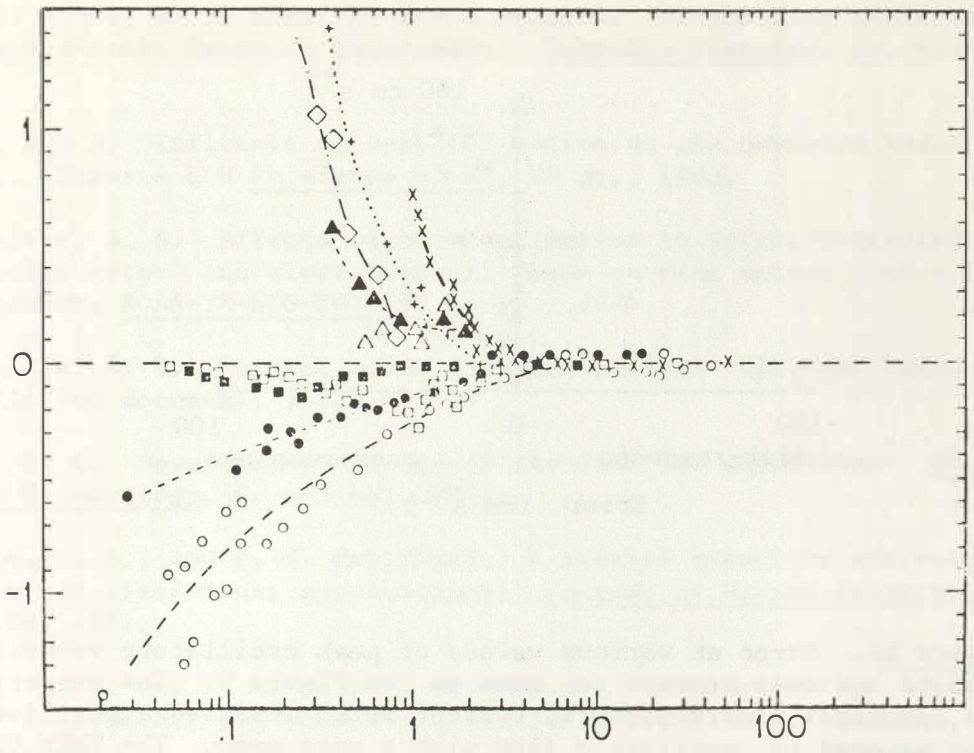

Figure 9. Error vs. signal to noise. An error of 1 is 100 percent over-response; similarly an error of -1 is 100 percent under-response. "X" is for a Savonius rotor[10], "+" for an Aanderaa[4], "◇" for a spherical electromagnetic sensor[3], "▲" and "△" for VACMs experiencing vertical oscillation when inclined 14.6 degrees and when not inclined[3], "○" and "●" are test data from the ACM experiencing horizontal and vertical oscillation[11], and "□" and "■" are for the VMCM[11] experiencing oscillation parallel to tow and propeller axle and oscillation perpendicular to tow and axle.

reported by Briscoe et al.[12] and by Halpern et al.[13]. Very generally, however, the VMCM was found to provide accurate measurements of horizontal velocity out to 1-2 cph when suspended beneath a surface riding float at depths of up to 85 m; VACMs and ACMs operated with error in certain depth ranges when deployed from surface riding floats. Thus, both laboratory tests and field deployments document that, more so than any other available current meter, the VMCM is capable of making accurate velocity measurements in the upper ocean.

Future Developments

Improvements in performance of the VMCM may be possible by using smaller, helical propellers. The hope there would be that they would disturb the flow less than the present flat bladed propellers. Their wake would then be less noticable. Development of such a propeller might require one to two years of work and is not likely to be carried out. If smaller propellers were to be

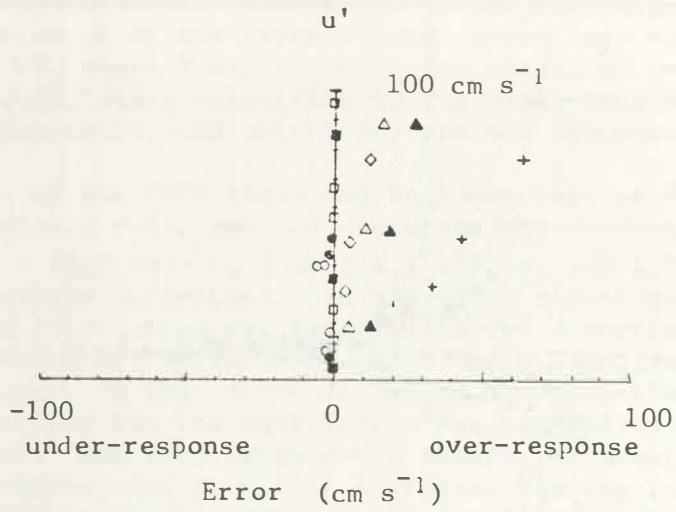

Figure 10. Error at various values of peak oscillatory velocity, u'. Symbols and data sources the same as for Figure 9. The Aanderaa, VACM, and spherical electromagnetic current meter measured a positive mean flow when exposed to oscillatory flow with a zero mean. The VMCM did not err, and the ACM measured small negative means. (The sign is significant only for the vector averaging instruments.)

designed, however, the next logical step would be to scale the entire instrument down. The introduction of large scale integrated circuits (LSI) and bubble memory would decrease the size of the electronics package. An instrument 1/2 to 2/3 the size, weight, and cost of the present version would be possible.

Current development, however, is directed toward the addition of temperature and pressure sensors. Also in progress is the development of a wind recorder based on the VMCM. With the capability of recording more channels (sea surface temperature, air temperature, solar radiation, and relative humidity) a surface meteorology package could be developed to provide the surface boundary conditions for future upper ocean experiments.

Acknowledgements

The VMCM was developed with the support of the Office of Naval Research under contract N00014-75-C-0152 with the Scripps Institution of Oceanography. The development was initiated by Professor Russ E. Davis; the author worked on developing the VMCM while at Scripps as Davis' graduate student. Steve Wald was responsible for the design of the VMCM electronics. United States Patent 4152934 covers the Vector Measuring Current Meter and is assigned to the United States Navy.

References

1. Gould, W. M., W. J. Schmitz, and C. Wunsch. Preliminary field results for a mid-ocean dynamics experiment. Deep-Sea Research, 31, 911-931, 1974.

2. Gaul, Roy D. Influence of vertical motion on the Savonius rotor current meter. Texas A & M Reference 63-4T, 29 pp., 1963.

3. Kalvaitis, A. N. Effects of vertical motion in vector averaging (Savonius rotor) and electromagnetic type current meters. NOAA Technical Memorandum, NOAA-TM-NOS-NOIC-3, 17 pp., 1974.

4. Kalvaitis, A. N. Current meter dynamic testing. POLYMODE News, No. 28, unpublished document, 1977.

5. Gill, G. C. Development and use of the Gill UVW anemometer. Boundary Layer Meteorology, 8, 475-495, 1975.

6. Cannon, G. A., and D. W. Pritchard. A biaxial propeller current-meter system for fixed-mount applications. Journal of Marine Research, 29, 181-190, 1971.

7. Davis, R. E. and R. A. Weller. Propeller current sensors. In NATO text, Instruments and methods in air-sea interactions, Ustaoset, Norway, (in press).

8. Walrod, R. A. Propeller current sensor response to off-axis flow. Masters thesis, Massachusetts Institute of Technology, 90 pp., 1970.

9. Weller, R. A. Observations of horizontal velocity in the upper ocean with a new vector averaging current meter. Ph.D. thesis, University of California, San Diego, 169 pp., 1978.

10. Karweit, M. Response of a Savonius rotor to unsteady flow. Journal of Marine Research, 32, 359-364, 1974.

11. Weller, R. A., and R. E. Davis. A vector measuring current meter. submitted to Deep-Sea Research, 1979.

12. Briscoe, M., J. McCullough and R. Weller. JASIN current meter and mooring intercomparison. JASIN News, No. 12, published by IOS, Wormley, U.K., April 1979

13. Halpern, D., R. A. Weller, M. G. Briscoe, R. E. Davis, and J. McCullough, JASIN and MILE current meter intercomparisons, in preparation.

A HIGH PRECISION ACOUSTIC CURRENT SENSOR

Neil L. Brown & Kenneth D. Lawson
Neil Brown Instrument Systems, Inc.
Cataumet, Massachusetts

ABSTRACT

This paper describes an acoustic differential travel time method of sensing fluid flow (e.g. ocean currents). For each axis of the sensor array a pair of acoustic transducers is simultaneously and repetitively connected to the same output of a crystal oscillator (typically 0.5 to 3mHz) to produce pairs of continuous wave bursts travelling in opposite directions. Before the acoustic signals arrive, each transducer is simultaneously connected to receiving circuits which then compare the phase of the arriving signals. The phase difference is directly proportional to the fluid flow velocity component parallel to a line joining the two transducers. Although this concept is not new, the method of processing the discontinuous received signals is novel and yields results which are essentially identical to truly continuous wave operation. The impossible problem of distinguishing simultaneously transmitted and received signals of the same frequency is avoided while superior zero stability and noise performance are achieved.

INTRODUCTION

In 1974, when the authors commenced work on acoustic current meters, it was generally recognized that the commercially available current meters of the propellor or Savonius rotor type were not at all suited to specialized measurement requirements such as those involving near surface ocean phenomena. These problems have been extensively discussed elsewhere[1].

Electro-magnetic current meters have the disadvantage that their output is proportional to their internally generated magnetic field wich decreases rapidly with distance from the field coil. Thus, they are sensitive only to fluid flow in the immediate vicinity of the coil, which due to its bulk, significantly affects the flow being measured. The open Helmholtz coil electro-magnetic current meter described by Olsen[2] does offer some relief from this problem. The low sensitivity and susceptability to external electrical fields of practical E.M. current sensors are due to the extremely low induced voltages (typically 0.1 to 0.5uV/cm/sec.) which results from the limited power available to excite the field coil. The problems are even more serious in fresh water. The acoustic backscatter type[3] has attractive characteristics in theory,but has not been generally successful due to the scarcity and poor distribution of suitable scatterers in most parts of the ocean. Thus, it was felt that current sensors in which current is sensed by measuring the differential travel time of two acoustic signals travelling in opposite directions in the fluid offered better possibilities. The reasons were (1) response is inherently linear and fast (2) sensitivity is uniform over the acoustic path (3) the transducers are small (4) signal to noise ratio is usually excellent (5) ideal cosine response is inherent and in practice can be achieved by the use of suitable geometrical design (6) calibration can be inferred from frequency, sound velocity and transducer spacing and is independently of other physical properties of the fluid medium.

Numerous acoustic current meters using this basic concept have been described in the literature. The concept has been implemented in a number of different ways some of which are (1) short pulses with 2 transmitters and 2 receivers for each axis[4] (2) short pulses with 2 transducers each acting as both a transmitter and receiver[5] (3) dual "sing-around" sound velocimeters with straight line sound paths in opposite directions[6] (the difference in the "sing-around" frequency being a

linear function of current.) (4) continuous wave using two widely different high frequency carriers (e.g. 1.1 and 1.6mHz) but modulated with an identical signal of lower frequency (e.g. 20kHz) where the phase difference of the modulating signal on the received carriers is a linear function of current velocity[7]. (5) continuous wave bursts using a single frequency (e.g. 2mHz) on a single pair of transducers, the burst interval being approximately equal to the acoustic travel time between the two transducers[7]. The received bursts resynchronize "slave" oscillators which maintain phase information between bursts. The continuous output of the "slave" oscillators is heterodyned with a local oscillator resulting in outputs of 8kHz. Phase difference between the 8kHz signals is a linear function of current[8].

The first three methods require the measurement of travel time difference (ΔT) of the order of 1 nanosecond to resolve currents less than 1 cm/sec. For example it can be shown that

$$\Delta T = \frac{2vd}{c^2}$$ (v= velocity; d= transducer spacing; c= velocity of sound)

For d=10cm, c=1500m/s, the time difference is 9×10^{-10}sec/cm/sec. Time resolution of this order requires extremely high speed circuitry and auto calibration features such as those described by Gytre[5]. The combination of extreme detector bandwidth implicit in this fast time response and the relatively low pulse rate (must be less than $\frac{c}{d}$) result in aliasing "errors" which significantly increase the electronic noise at all frequencies including frequencies close to zero. The first and third methods using separate transducers for receiving and transmitting suffer the additional disadvantage of requiring extremely stable relative position between the receiver and transmitter of each pair. For example, a change in relative position of 10^{-6}m for an acoustic path length of 4 cm causes a change in arrival time equivalent to a current change of 2cm/s. The fourth method while free of the problems associated with threshold detection of pulses, etc. does require the measurement of phase difference to the same time resolution as types 1, 2 and 3 above. The fifth method (e.g. continuous wave burst) has the advantage that the phase angle measured at the relatively low beat frequency is the same phase angle difference that occurs at the acoustic carrier frequency, thus tremendously reducing the time resolution required to achieve a given fluid velocity resolution. However at these frequencies it is difficult to achieve phase lock in the slave re-synchronization circuitry to the required precision (typically the sensitivity to phase uncertainty is 2cm/sec/degree). Also it is difficult to adequately isolate the high level output of the slave oscillators from the acoustic receiving circuits.

The authors were funded in 1975 to develop a moored 2 axis vector averaging current meter by the Office of Naval Research and a high speed 3 axis acoustic current meter for small scale turbulence measurements by the Johns Hopkins University Applied Physics Lab. The initial result of these activities was the development of a continuous wave technique (described in a previous paper[8]) where each transducer transmits one frequency and simultaneously receives a slightly different frequency transmitted acoustically form the other transducer resulting in the same difference frequency at each transducer. Subsequent signal processing (described in previous paper) results in two signals having twice the frequency of the beat frequency and whose phase difference was directly proportional to fluid velocity. Notwithstanding the excellent performance of the several prototypes built using this technique there were several undesirable characteristics, viz, (1) the circuit was relatively complex (2) spurious electrical signals coupled by

means other than the desired water borne acoustic path, had to be less than 1 part in 10^5 of the transmitted electrical signal to avoid unacceptable zero uncertainties. Since the transmitting and receiving circuits utilize the same power supply and were in close proximity, extreme care had to be taken to avoid spurious signals, particularly where the transducers need to be mounted remotely from the main housing.

To avoid these difficulties the authors decided to use the continuous wave burst (CWB) technique described by R. A. Lester[7] in 1961, but using a substantially different signal processing technique resulting in excellent zero stability and signal to noise ratios. Since the CWB technique does not involve simultaneous transmission and reception, the problems mentioned above simply do not occur. The technique has been applied to a number of instruments: (1) 2 axis vector averaging, internally recording current meter for moored applications (2) 3 axis horizontal profilers (3) 2 and 3 axis vertical profilers.

The profilers were equipped with various combinations of conductivity, temperature and pressure sensors, accelerometers and magnetometer compasses. In all cases theory and experimental results (discussed later) showed that the zero stability was independent of sound velocity changes, normal stress induced changes in transducer spacing and modest amounts of marine fouling.

For applications requiring a 360° horizontal response (moored current meters) or omni-directional response, the only serious limit to accuracy is the flow distortion caused by the presence of the transducer mounts, support structure and electronics housing, etc. and is a problem which is common to essentially all techniques of small scale self-contained current meters. Even though none of the geometrical arrangements designed by the authors pretends to have solved the flow distortion problems for omni-directional measurements it is felt that there are design approaches which would result in acceptable solutions. For example, one instrument recently designed and constructed by the authors showed no significant loss in performance with the transducer assembly mounted at the end of a 3 meter cable. This suggests that a multi-acoustic path sensor array with the use of a micro-processor to select the acoustic path least contaminated by structure induced flow distortion could lead to a satisfactory omni-directional design.

THE CONTINUOUS WAVE BURST TECHNIQUE

For the purposes of describing the basic technique, its implementation in the Neil Brown Instrument Systems Model ACM-2 Acoustic Current Meter will be described. This instrument uses the sensor geometry illustrated in Figures 1A and 1B. Figure 1a illustrates the sensor geometry for one of the two axes of the ACM-2. The two transducers are aimed directly at an acoustic mirror in such a way that the reflected acoustic signal from each transducer is aimed directly at the other. The transducers are discs approximately 3/8" diam x 0.04" thick made from a commercially available piezo-electric material known as PZT-5. Fig. 1b is a photo showing the complete 2 axis geometry. Figure 2 illustrates the timing of transmitted and received acoustic signals and the resulting outputs of the unfiltered and filtered outputs of the square law detectors (see Fig. 3). The operation is as follows: Every 610μs a 91.5μs long burst at 1.605000 mHz is simultaneously applied to each of a pair of transducers resulting in acoustic signals simultaneously starting out in opposite directions. In Fig. 1a the signal from the transducer #1 arrive at #2 sooner than the other because it is travelling in the same direction as the indicated current. Consequently the phase of the signal received at transducer #2 will be advanced relative to that received at transducer #1. The total phase shift between each transmitted and received burst is

dependent on the following variables:

(1) Total acoustic path length (d)
(2) Velocity of sound in water (c)
(3) Flow velocity of water (v)
(4) The electro-acoustic parameters of the transducers
(5) Frequency of acoustic signals (ω_c)

However, it will be shown that the method developed by NBIS results in the following simple relationship between phase shift (θ) between the received signals and current velocity (v) is given by

$$\theta = \frac{2vd\omega_c}{c^2}$$

PROPERTIES OF CONTINUOUS WAVE BURST SIGNALS

The CWB signal is transmitted from each transducer for a period long enough to result in a continuous wave train of length equal to about 60% of the total path from one transducer to the other. The remaining time allows the mechanical oscillation in each transducer to decay to a negligible level before the acoustic signal from the other transducer arrives (see Fig. 2). The "receive gate" is then opened resulting in an input to each of the square law detectors (see Fig.3). A CWB signal is essentially a continuous wave carrier (Eco) modulated by a signal M consisting of repetivite rectangular pulses.

The Fourier series for a repetitive rectangular pulse M is as follows:

$$M = K_1 + \frac{2}{\pi} \sum_{n=1}^{n=\infty} \left[\frac{1}{n} \sin(nK_1\pi) \cos(n\omega_2 t) \right]$$

K_1 = ON/OFF ratio of S_1 and S_2 (see Fig. 3)

n= an integer from 1 to infinity
$\omega_2 = 2\pi$ x pulse repetition frequency

The carrier signal E_{co} is given by $E_{co} = E_o \sin(\omega_1 t)$
Therefore the CWB transmitted signal E_T is given by

$$E_t = M.E_{co}$$

$$= K_1 E_o \sin(\omega_1 t) + \frac{2}{\pi} E_o \left[\sin(\omega_1 t) \sum_{n=1}^{n=\infty} \left(\frac{1}{n} \sin(nK_1\pi) \cos(n\omega_2 t) \right) \right]$$

For all values of n it can be shown that since ω_1 is approximately 10,000,000 and ω_2 is 10,000 the term is parenthesis contains frequency components that are side bands to ω_1 which are either of totally insignificant amplitude or result in outputs from the square law detectors (see Fig. 3) that are completely outside the band-pass frequencies (100 to 400 rad/sec) of the band-pass filters. Therefore for purposes of assessing phase angles between the outputs of the band-pass filters E_5 and E_6 we can assume that the transmitted signal E_T is given by

$$E_T = K_1 E_o \sin(\omega_1 t)$$

Since the receive gates (#1 & #2 in Fig. 3) are enabled after the received signals from the preamplifiers (#1 & #2 in Fig. 3) have achieved steady state, the inputs to the square law detectors can for the same reasons be expressed as follows:

$$E_{RC1} = K_2 \sin(\omega_1 t + \theta_1) \quad \text{--- (1a)}$$

E_{RC1} = carrier frequency component of E_{R1}

θ_1 = total phase shift between E_{RC1} and E_{co}

Now $\theta_1 = \phi_{T2} + \omega_1 T_1 + \phi_{R1}$

Where ϕ_{T2} = phase angle between electrical and acoustic signals at transducer #2 during transmit mode

T_1 = acoustic travel time from transducer #2 to #1

ϕ_{R1} = phase angle between acoustic and electrical signals at transducer #1 during receive mode.

Similarly $\theta_2 = \phi_{T1} + \omega_1 T_2 + \phi_{R2}$

Phase angle θ between the carrier frequency components of E_{R1} and E_{R2} (i.e. E_{RC1} & E_{RC2}) is given by

$$\theta = \theta_2 - \theta_1$$
$$= (\phi_{T1} - \phi_{R1}) + \omega_1 (T_2 - T_1) + (\phi_{R2} - \phi_{T2})$$

Let $\phi = (\phi_{T1} - \phi_{R1}) + (\phi_{R2} - \phi_{T2})$ ----------(1)

Therefore $\theta = \omega_1 (T_2 - T_1) + \phi$

$= \omega_1 \Delta T + \phi$ ----------(2)

Now $T_1 = T_{AM} + T_{MB}$ (see Fig. 1a)

$$T_{AM} = \frac{d}{2(c + v\sin\theta)\sin\theta}$$

$$T_{MB} = \frac{d}{2(c + v\sin\theta)\sin\theta}$$

Therefore $T_1 = \frac{d}{(c + v\sin\theta)\sin\theta}$

Similarly $T_2 = \frac{d}{(c - v\sin\theta)\sin\theta}$

Therefore $\Delta T = \frac{2vd}{(c^2 - v^2\sin^2\theta)}$

since $c >>> v$

Then $\Delta T = \frac{2vd}{c^2}$ ----------(3)

It is of interest to note that the travel time difference (ΔT) depends on the direct distance (d) between the transducers and is independent of the total acoustic path length.

Substituting in equation (2)

we get $\theta = \frac{2\omega_1 vd}{c^2} + \phi$ ----------(4)

(from equation (1)) $\phi=(\phi_{T1}-\phi_{R1})+(\phi_{R2}-\phi_{T2})$ ----------(5)

$= \phi_1-\phi_2$

Where ϕ_1 and ϕ_2 are the differences in phase angles between the transmit mode and receive mode of each transducer. Ideally ϕ_1 and ϕ_2 should each be zero or if not zero, should be equal. If ϕ is zero equation (4) shows that θ is zero when current flow is zero i.e. that ϕ is a zero offset term. Obviously the exact value of ϕ and its stability with time, temperature and pressure, etc. is a most critical determanent of zero stability in the current meter. The following is a discussion of the factors influencing ϕ_{T1}, ϕ_{R1}, ϕ_{T2} which in turn determine ϕ_1, ϕ_2 and ϕ.

Behavior of Piezo-Electric Transducer

Piezoelectric materials produce an electric charge Q (with resulting electric field) when strained. Conversely a mechanical force is produced within the material when it is subjected to an electric field. Consequently a piezoelectric disc transducer in an acoustic pressure field (i.e. acting as a receiver) will have forces produced at its surface that will result in a surface velocity μ given by

$\mu=\frac{p}{Z_m}$ where p = pressure and Z_m = complex mechanical impedance

Therefore the displacement (y) of the surface is given

$$y=\int \mu dt = \frac{1}{Z_m}\int p dt$$

The strain $S = \frac{y}{W}$ (W = thickness)

The resulting charge Q is given by

$$Q= SK_1 = \frac{yK_1}{W} = \frac{K_1}{WZ_m}\int p dt \ldots . (K_1 = \text{constant})$$

The short circuit current I_s is given by

$$I_s = \frac{dQ}{dT} = \frac{K_1 p}{WZ_m} \text{ ----------(6)}$$

When an piezoelectric transducer is used as a generator the force (f) acting at the surface of the transducer is given by

$f= K_2V$ (K_2 = constant)

where V= applied voltage

The resulting velocity μ of the surface is given by

$$\mu= \frac{f}{Zm} = \frac{K_2V}{Zm}$$

$p= \rho c\mu$ (ρ = density of fluid medium----------(7)

$$= \frac{\rho c K_2 V}{Zm} \text{ ----------(8)}$$

The above discussion assumes that the acoustic signals in each case are plane waves normal to the surface of the transducer. In actual operation the

acoustic wave propagation is normal to the surface and since the transducers are approximately 10 wave lengths in diameter the transmitted signals are essentially plane wave. However any small curvature is essentially the same at each transducer and consequently results in negligible net effects.

In equations (6) and (8) the only time variant parameters are I, p and V and the only frequency dependent parameter is the complex mechanical impedance (Zm) which is the same for both transmitting and receiving modes.

Now $Zm = Zo\ e^{j\varepsilon}$

Where Zo = mechanical impedance at resonance

ε = phase angle between force acting on transducer and the velocity

From (6) $I_s = \dfrac{K_1 p\ e^{-j\varepsilon}}{WZ_o}$

From equation (8) $p = \dfrac{\rho c K_2 V\ e^{-j\varepsilon}}{Zo}$ ----------(10)

In other words the phase angle between the short circuit current I_s and the acoustic pressure signal when acting as a receiver (ε) is the same as the phase angle between generated pressure and the applied voltage when acting as a generator.

Referring to equations (4) and (5) we can say that if in the transmitting mode the transducers are driven from exactly the same voltage and if in the receiving mode they are each shunted by a very low value resistor Rs (i.e. Rs <<< transducer electrical impedance) then $\phi_{T1} = \phi_{R1}$ and $\phi_{T2} = \phi_{R2}$ and $\phi_1 = \phi_2 = 0$

and $\theta = \dfrac{2\omega_1 vd}{c^2}$ ----------(11)

In other words if the conditions for the transmit and receive mode postulated above are satisfied there is no offset and θ is exactly zero when v is zero. However in practice some compromise must be made in the value of R_s. The circuit shown in fig. 4 is the equivalent circuit of the piezoelectric transducers at frequencies close to their fundamental resonance (i.e. the actual operating frequency). Therefore if we consider transducer #1 only (see fig. 3) we must examine the effect of R_3 and R_5 on the output current phase relative to the short circuit current in the receive mode. In the transmit mode we must consider the effect of R_3 and R_5 on the phase of the voltage directly across the transducer to the phase of E_{co} (see fig. 3). To simplify this discussion we shall assume that the impedance matching transformers have unity turns ratio. This assumption leads to the simplified circuits shown in figs. 4a and 4b. L_o is the inductance of matching transformer, C_o is the "static" capacitance of transducer. Co, R, L and C are equivalent electrical circuit of the piezoelectric transducer. The values or R, L and C are determined by the mechanical resonance coupled with the piezoelectric properties. R represents the combined effects of internal mechanical losses and the radiated or absorbed acoustic energy.

In the transmit mode the phase shift between E_T and E_{co} is given by

$$\gamma = \text{Tan}^{-1}\left[\frac{(R^2+Z^2)(Y)Rg + ZRg}{(R^2+Z^2)+Rg}\right] \quad \text{----------(12)}$$

Where $Z=(\omega L - \frac{1}{\omega C})$

$$Y = (\frac{1}{\omega L_o} - \omega C_o)$$

Rg = generator impedance (see fig 4a)

In the receive modes the phase angle between the output current I_1 and the generator voltage E_i is given by

$$\beta = \text{Tan}^{-1}\left[\frac{RR_sY-Z}{R+R_s+R_sZY}\right] \quad \text{----------(13)}$$

Where R_s = Source impedance (see fig 4b)

When $R_s = 0$

Then $I_1 = I_{sc}$ (I_{sc} = short circuit current)

Then $\beta = \beta_o$ (β_o = phase angle between I_{sc} & E_i)

Therefore

$$\text{Tan } \beta_o = \frac{-Z}{R} \quad \text{----------(15)}$$

The difference in phase shift β' is given by

$$\beta' = \beta - \beta_o$$

$$\text{Tan } \beta' = \text{Tan}(\beta - \beta_o)$$

Substituting we get β' given by

$$\beta' = \text{Tan}^{-1}\left[\frac{(R^2+Z^2)(Y)R_s+ZR_s}{(R^2+Z^2)+RR_s}\right] \quad \text{----------(16)}$$

Obviously from equations (12) and (16) if Rg = R_s then $\beta' = \gamma$
The phase angles γ and β' are of course the same as the angles Φ_{T1} and Φ_{R1} in equation (5) and $\gamma - \beta' = \phi_1$. Therefore if the generator impedance (Rg) in the transmit mode is the same as the load impedance (R_S) in the receive mode, then the angles ϕ_1 and ϕ_2 are zero and the offset angle ϕ (see eq. (5)) is also zero. This is true of course irrespective of any of the other parameters in figures 4a and 4b. For example if C_o changes due to temperature or pressure or any other reason the "offset" angle ϕ is always zero.

Heterodyned Received Signals

In the receive mode the signals E_{R1} & E_{R2} (ref. fig. 3) consists of the acoustically received signals and the local oscillator signal E_{lo}. Since the impedances across the matching transformers (T_{X1} & T_{X2}) are large (typically 2400

ohms) and are designed to be essentially resistive at the operating frequency (1.605000 MHz) it can be assumed for simplicity that the local oscillator signal components of E_{R1} and E_{R2} are exactly in phase with E_{lo} and are equal to E_{lo} Therefore E_{R1} is given by

$$E_{R1} = E_{lo} + E_{RC1}$$

Where E_{RC1} = acoustically received signal at transformer #1

$$= K_2 \sin(\omega_1 t+\theta_1)$$

From previous discussion θ_1 is given by

$$\theta_1 = \phi_{T2}+\omega T_1+\phi_{R1}$$

Similarly $E_{R2} = E_{lo}+E_{RC2}$

where E_{RC2} = acoustically received signal at transducer #2

$$= K_3 \sin(\omega_1 t+\theta_2) \qquad (K_3 = \text{constant})$$

where $\theta_2 = \phi_{T1}+\omega T_2+\phi_{R2}$

Now $E_{lo} = K_4 \sin(\omega_2 t) \qquad (K_4 = \text{constant})$

Therefore $E_3 = K_5 (E_{R1})^2 \qquad (K_5 = \text{constant})$

$$= K_5 \left[K_4^2 \sin^2(\omega_2 t) + K_2^2 \sin^2(\omega_1 t+\theta_1) + 2K_2 K_4 \sin(\omega_2 t)\sin(\omega_1 t+\theta_1) \right]$$

The first two terms contain only components of zero frequency and frequencies of $2\omega_1$ and $2\omega_2$ and will be totally removed by the band pass filter #1. Therefore the remaining component of E_3 is given by

$$E_3 = K\sin(\omega_2 t)\sin(\omega_1 t+\theta_1)$$

$$= \frac{K}{2}\left[\cos((\omega_2-\omega_1)t-\theta_1) - \cos((\omega_2+\omega_1)t + \theta_1) \right]$$

The band-pass filter is designed to be centered on a frequency of ω where $\omega = \omega_2-\omega_1$. Therefore the first term of E_3 will be passed by the band-pass filter and the second term will be eliminated.

$$\text{Therefore } E_5 = \frac{K}{2}\cos(\omega t-\theta_1) \qquad \text{---------- (17)}$$

Equation 17 assumes that at a frequency of ω the phase shift through the band-pass filter is zero. Using the same reasoning E_6 is given by

$$E_6 = \frac{K}{2}\cos(\omega t-\theta_2)$$

Therefore the phase shift θ between E_5 and E_6 as measured by the phase-meter is given by

$$\theta = \theta_2-\theta_1$$

$$= \omega_1 \Delta T + \phi \qquad \text{----------from equation (2)}$$

$$= \frac{2\omega_1 vd}{c^2} \qquad \text{----------from equation (11)}$$

The signals E_5 and E_6 at the inputs of the phasemeter are at 34 Hz (i.e. the difference between the carrier and local oscillator frequencies) but contain the same phase shifts due to current velocity (v) as the acoustic signals (1.6mHz) Since they are approximately 47000 longer in period than the carrier, the time discrimination (ΔT) in the phasemeter is given by

$$\Delta T = \frac{\theta}{\omega} = \frac{2\omega_1 vd}{\omega c^2}$$

For d = 10 cms, $\omega_1 = 10^7$ rad/sec, ω= 200 rad/sec.

$$\frac{\Delta T}{\Delta v} = \frac{2\omega_1 d}{\omega c^2} = 44.4\mu S/cm/sec.$$

This requirement is very easily met with the use of readily available micropower integrated circuits (both linear and logic).

In the foregoing discussion no mention was made of the phase shift or time delay in the preamplifiers or square law detectors. Since E_{R1} (ref, Fig. 3) consists of both the local oscillator signal and the acoustically received signal it is obvious that since they are almost identical in frequency (i.e. 1.605000 and 1.605034 MHz) there will be essentially no differential phase shift between the two frequencies even though each may be substantially phase shifted.

Band-Pass Filters

The band-pass filters used in the ACM have several vital requirements.

(1) They must have identical and very stable phase shift at the beat frequency i.e. 34 Hz).
(2) They must provide extremely high attenuation of the 1600 Hz pulse modulation frequency of carrier signal.

The above requirements cannot be readily met using conventional LP passive or active filters. If the filters are to have very high attenuation at 1600 Hz (say 50db) then there will be substantial phase shift at the beat frequency (34 Hz). Conventional tuned amplifiers (i.e. BP filters) have a large rate of change of phase around the center frequency thus requiring extreme component stability and accuracy of tuning. The circuit shown in fig. 5 consists of two band-pass amplifiers (commonly referred to as "second order infinite gain multiple feed-back filters"). These amplifiers are connected in cascade with an overall feed-back network consisting of resistors R3 and R4. This complete circuit has the very valuable property of predictable low phase shift and low rate of change of phase .022rad/red/sec.) at center frequency combined with the desired attenuation at 1600 Hz.

The Phasemeter:

The phasemeter circuit contains limiting amplifiers which convert the 34 Hz input sine waves E_5 and E_6 (ref. Fig. 3) to square waves. These square waves are processed by a simple logic circuit to produce a 68Hz pulse signal whose positive or negative polarity indicates leading or lagging phase and whose "duty cycle" is proportional to absolute phase angle difference between E_5 and E_6. This pulse signal is filtered to result in a D. C. voltage the magnitude of which is propor-

tional to the component of fluid velocity parallel to the acoustic path and whose polarity indicates whether the component is in the same or opposite direction to the reference direction.

PERFORMANCE

The table below gives a brief summary on test data on several different types of recently designed and manufactured instruments for profiling applications. In each case the acoustic frequency was 2.75 mHz and the transducers (discs of PZT-5A piezo-electric material--diameter 0.188 inches) were mounted in 0.25 inch diameter stainless steel rods (basically transverse direction to axis of rod) and encapsulated with polyurethane. The rods were oriented into the intended profiling direction. Consequently a typical profiling speeds (50 to 200 cm/sec.) the maximum instantaneous angle between the incident flow vector and the orientation of the transducer mounting rods was small enough to avoid significant flow distortion in the acoustic path from the wakes of the transducer mounts, etc. Consequently the cosine response was generally within 1% of the theoretical response.

TABLE

No.	Application	No. of Axes	Acoustic Path (cm)	Full Scale Velocity (cm/s)	Band-Width (Hz)	Zero Stability (cm/s)	RMS Noise cm/s/Hz	Linearity Percent of Reading
1	Vert. Profiling	2	20	100	1	.1	.3	1%
2	Near Surface	2	10	200	15	.2	.025	1%
3	Submarine	3	20	100	15	*1,(.1)	.03	1%
4	Submarine	3	4	500	50	*3,(.5)	.005	1%

*The zero stability figures originally obtained for these two devices were subsequently found to be caused by mechanical energy imparted magnetostrictively during transmission in a ferrite cored inductor and released in random phase by the reverse process during the receive mode. Modification of this component eliminated this source of zero drift resulting the improved figures shown in parenthesis. Of the above devices the noise figures for 1, 2 and 3 are almost certainly contaminated by the test procedure. For example, residual motion in towing tanks such as the David Taylor Model Basin can be as high as 1 to 3 cm/sec. Therefore, it is felt that the actual instrument noise is substantially lower than shown for the first three. Instrument number 4 was evaluated under carefully controlled conditions in a small laboratory tank and therefore the noise data is considered valid.

CONCLUSION

The excellent zero stability and noise of this technique is due to a number of factors. Firstly, the acoustically received signals are large (typically 10 millivolts) even when the transmitted energy is only about 100 microwatts. Secondly, all the critical signal processing is done in stable narrow band circuits at low frequencies (34→300Hz). Since the square law detectors and preamplifiers simultaneously carry the acoustically received signal and the local oscillator signal, the very small frequency difference will result in essentially zero relative phase shift even though the absolute values may be appreciable and subject to drift. Thirdly, the use of a "psuedo" continuous wave technique with each transducer driving or being driven by a very low impedance ensures excellent reciproc-

ity between the transmit and received mode.

For many applications the most serious problem with this and other techniques is the flow distortion caused by the wake and potential flow effects from the sensor mounts, support structure, and instrument housing, etc. As mentioned earlier the acoustic transducers are very small and can be operated remotely (say up to 5 meters) from the electronics housing. Therefore, by using a microprocessor to select only those transducer pairs having signals not contaminated by flow distortion it is probable that a satisfactory design having good omni-directional responses for near surface measurements would be evolved.

ACKNOWLEDGEMENTS

The authors wish to express their gratitude to the U. S. Navy (Office of Naval Research), NOAA (National Data Buoy Office) and the Johns Hopkins University Applied Physics Laboratory for the financial support provided for much of this work. Also we wish to express our thanks to Dr. David Johnson and Dr. David Wenstrand (both of Johns Hopkins University/Applied Physics Lab.), Mr. Gerald F. Appell (NOAA/National Ocean Survey), Mr. William E. Woodward (NOAA/Office of Ocean Engineering) and Mr. James R. McCullough of the Woods Hole Oceanographic Institution for their valued work in the performance of various tow tank and field tests on these instruments.

REFERENCES

(1) McCullough, R. R., *In Search of Moored Current Sensors,* MARINE TECH. SOC., 10th Annual Conf., September, 1974.

(2) Olson, J. R., *Two-component Electromagnetic flowmeter,* MARINE TECH. SOC. JOUR., Vol 6 (1972).

(3) Koczy, F. F., M. Kronengold and J. M. Lowenstein, *A Doppler Current Meter,* INST. SOC. OF AMER., MAR. SCI. INSTRUMENTATION, Vol 2 (1962).

(4) Rester, G. F., and G. P. Erickson, *An Acoustic Oceanographic Current Meter,* INST. SOC. OF AMER., 26th Annual Conf., October, 1971.

(5) Gytre, T., *Ultrasonic Current Meter,* Christian Michelson Inst. Report 377208, Bergen, Norway, January, 1975.

(6) Suellentrop, F. J., A. E. Brown and E. Rule, *An Acoustic Ocean-Current Meter,* INST. SOC. OF AMER., MARINE SCIENCE INSTRUMENTATION, Vol 1 (September, 1961).

(7) Lester, R. A., *High-Accuracy, Self Calibrating Acoustic Flow Meters,* INST. SOC. OF AMER., MARINE SCI. INSTRUMENTATION, Vol 1 (September, 1961).

(8) Lawson, K. D., N. L. Brown, D. H. Johnson and R. A. Mattey, *A Three-Axis Acoustic Current Meter for Small Scale Turbulence,* INST. SOC. OF AMER., ASI, 1976, pp 501-508.

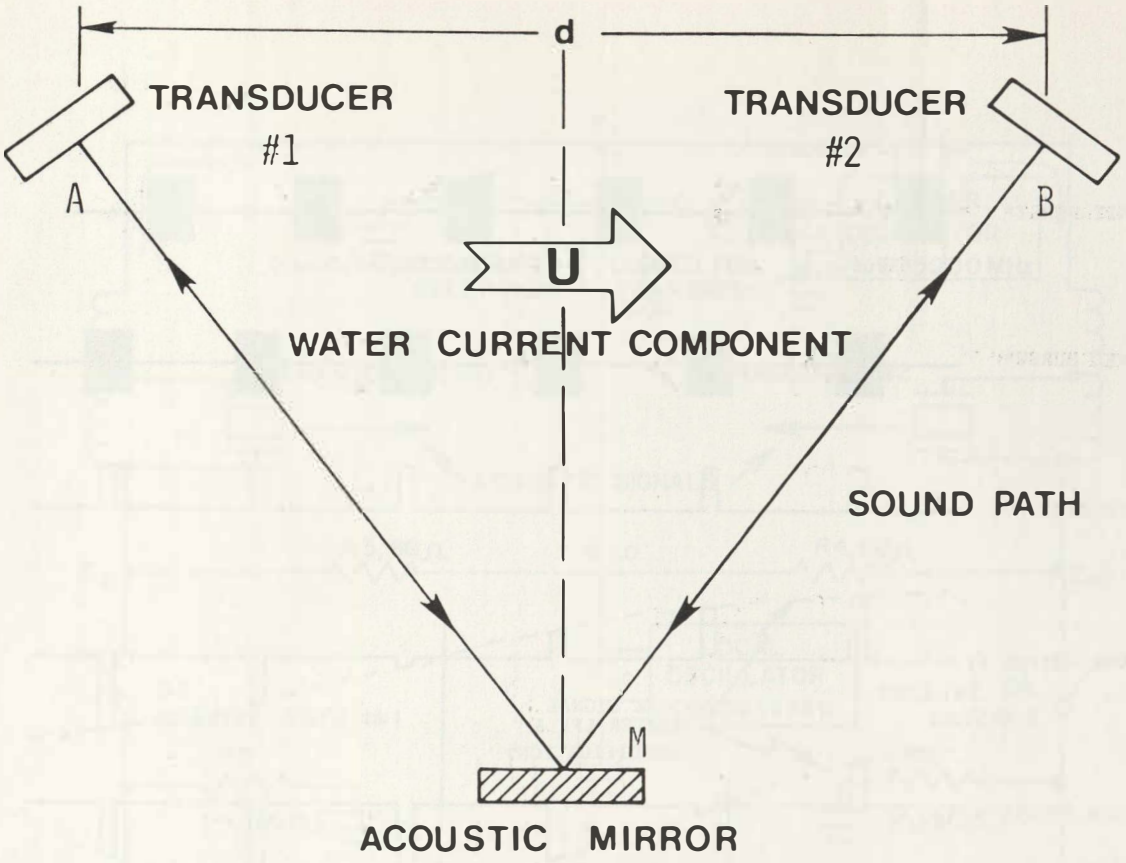

FIG 1A

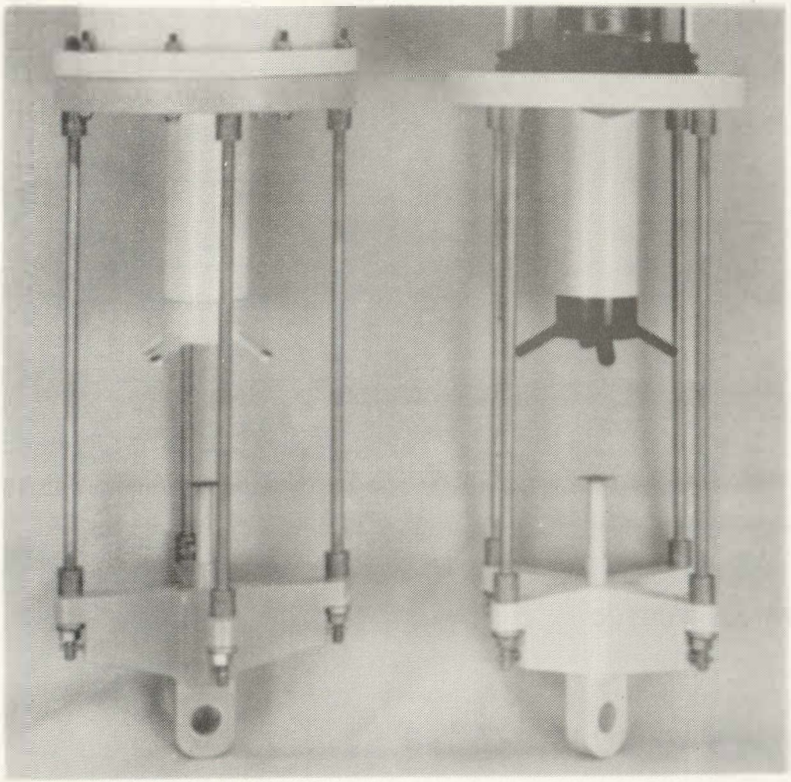

FIG 1B

2 AXIS SENSOR
GEOMETRY

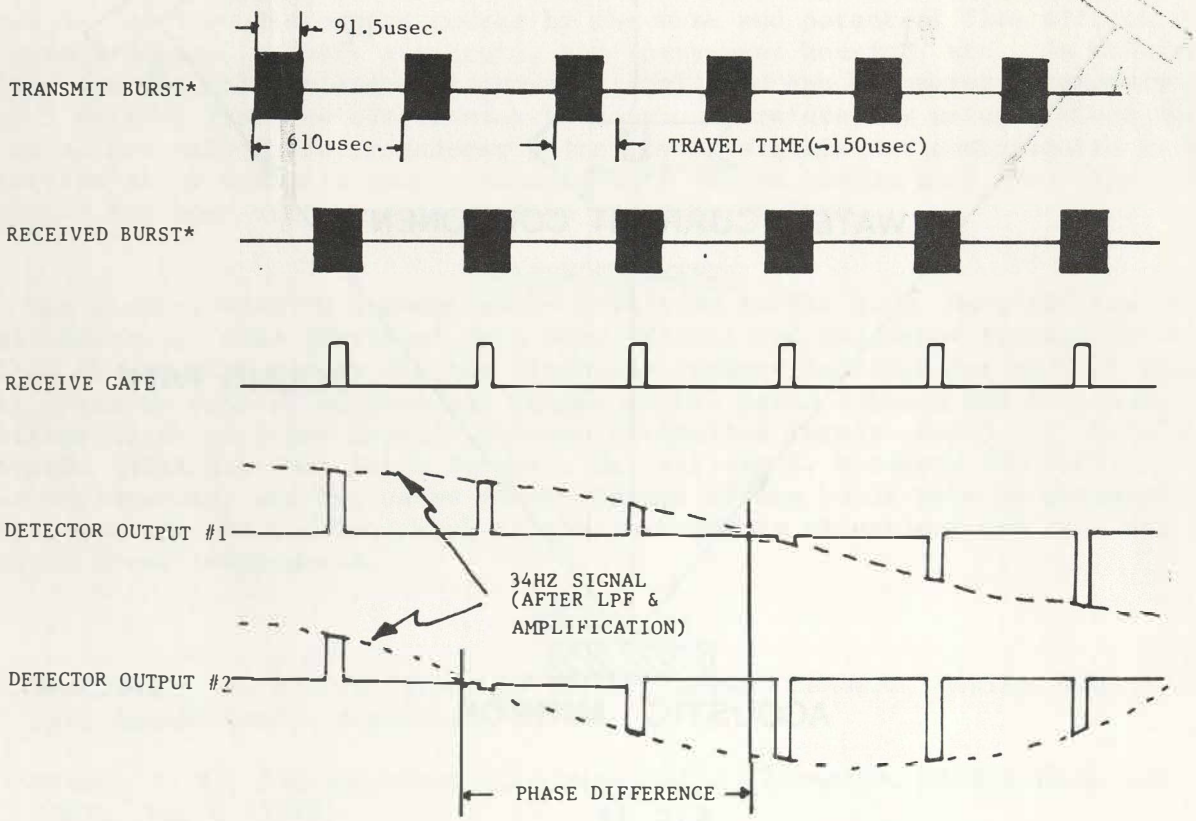
91.5usec.
TRANSMIT BURST*
610usec.
TRAVEL TIME(≒150usec)
RECEIVED BURST*
RECEIVE GATE
DETECTOR OUTPUT #1
34HZ SIGNAL
(AFTER LPF &
AMPLIFICATION)
DETECTOR OUTPUT #2
PHASE DIFFERENCE

FIG. 2

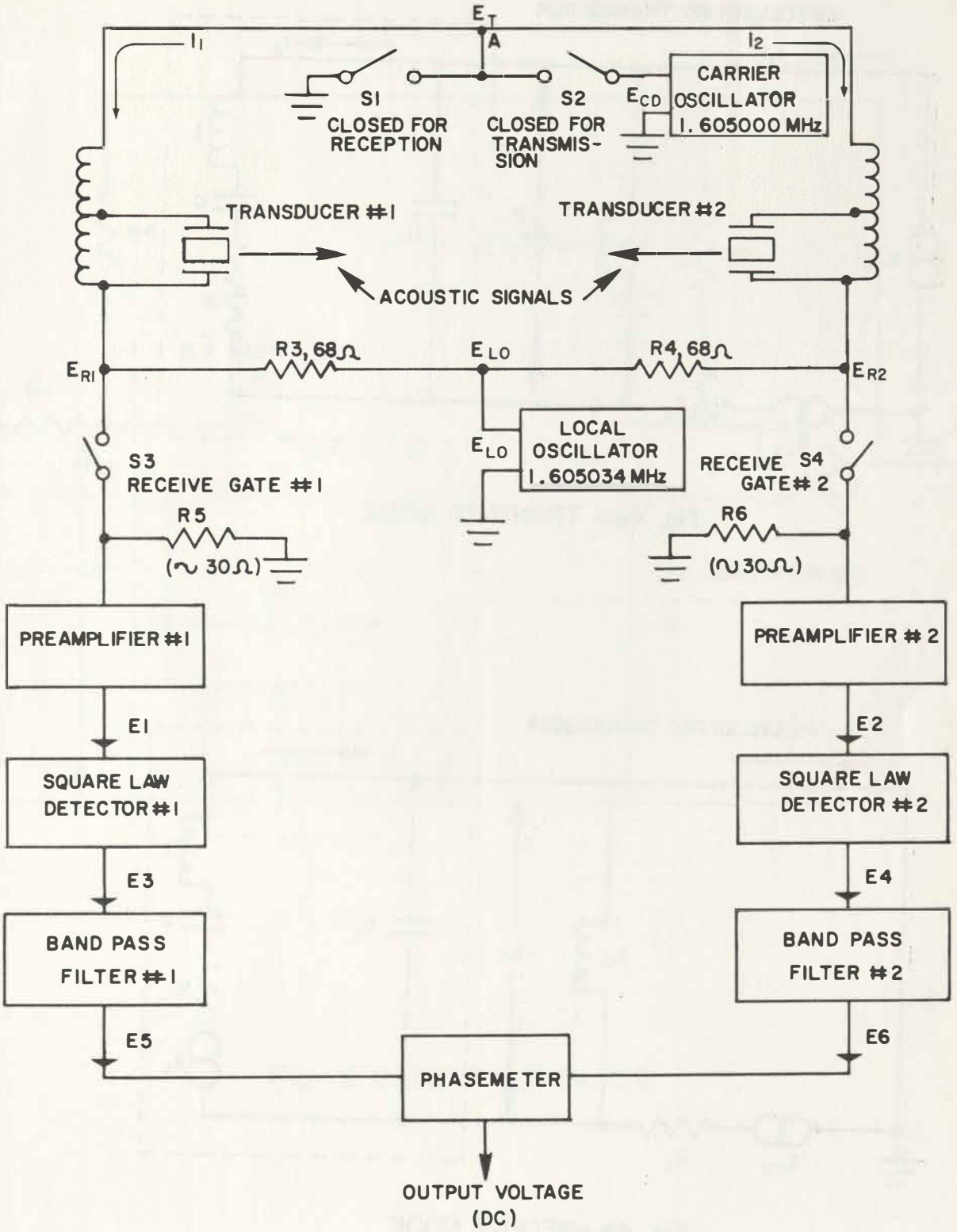

Fig. 3 – VELOCITY SENSOR CIRCUIT

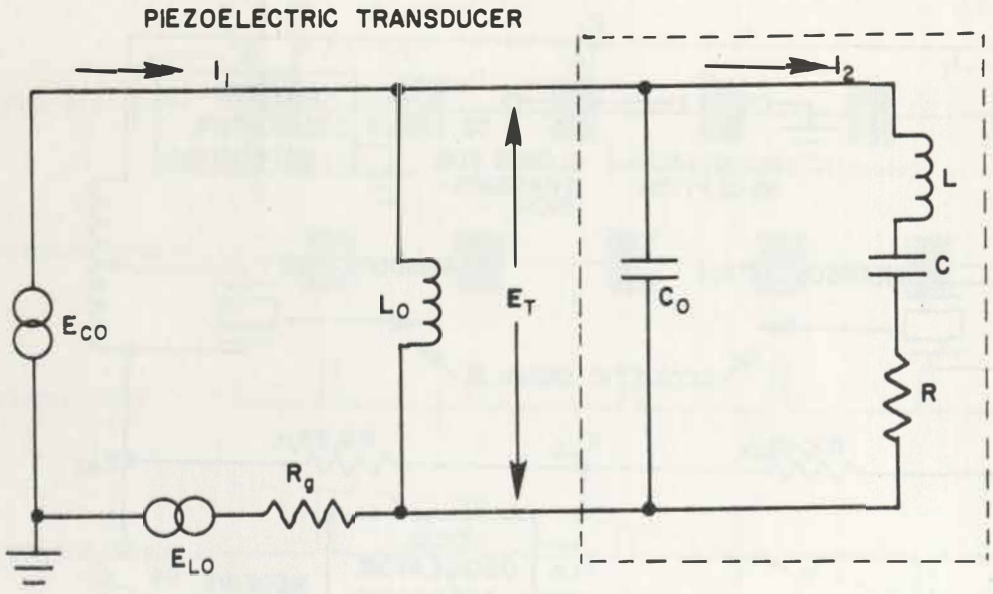

Fig. 4a– TRANSMIT MODE

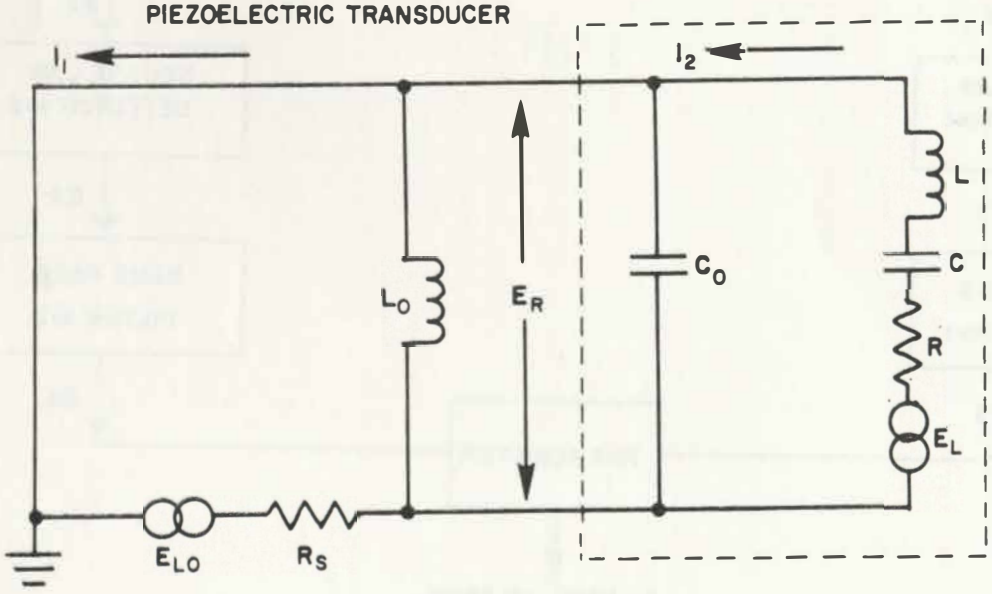

Fig. 4b - RECEIVE MODE

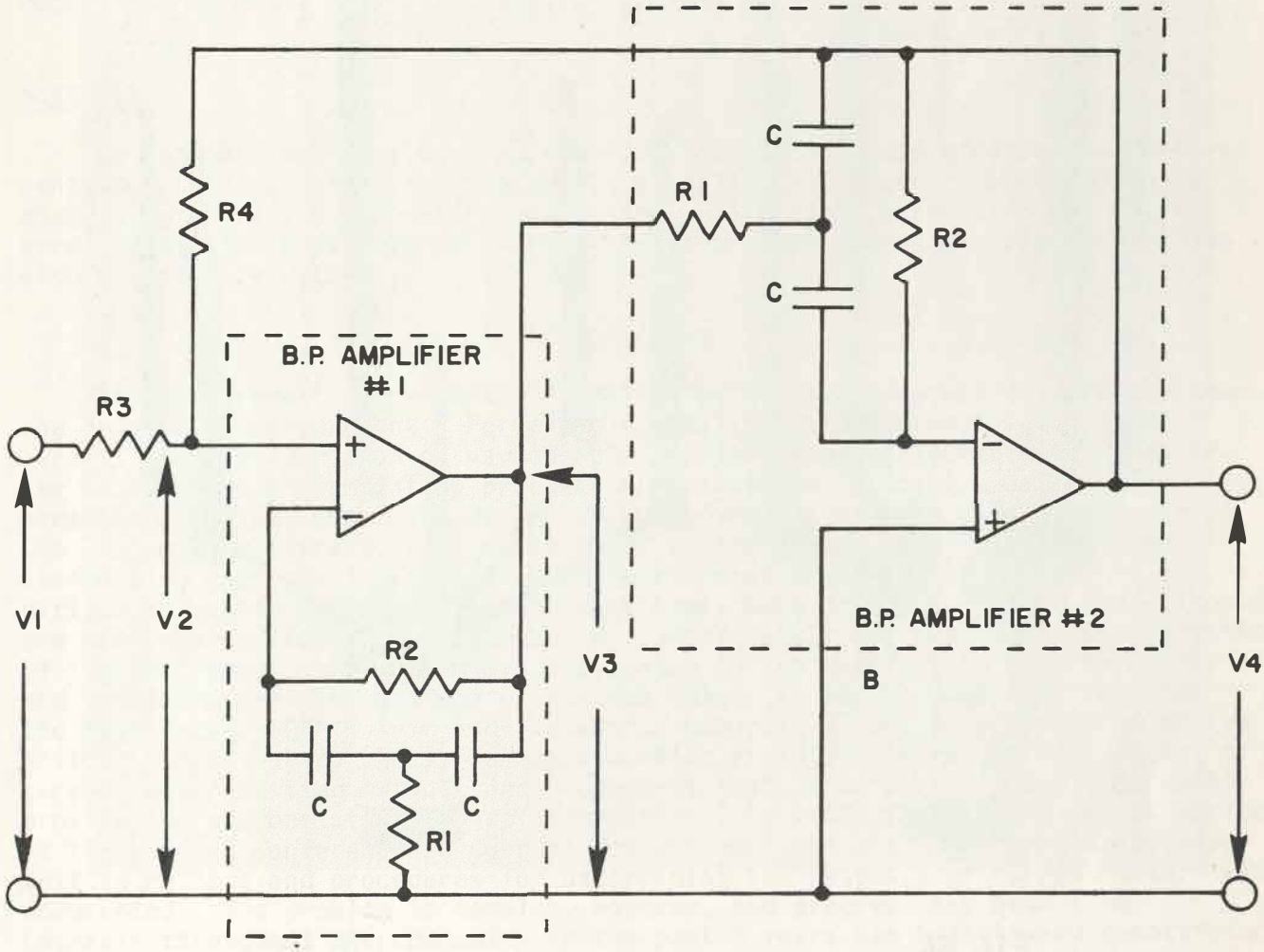

Fig-5 BAND PASS FILTER

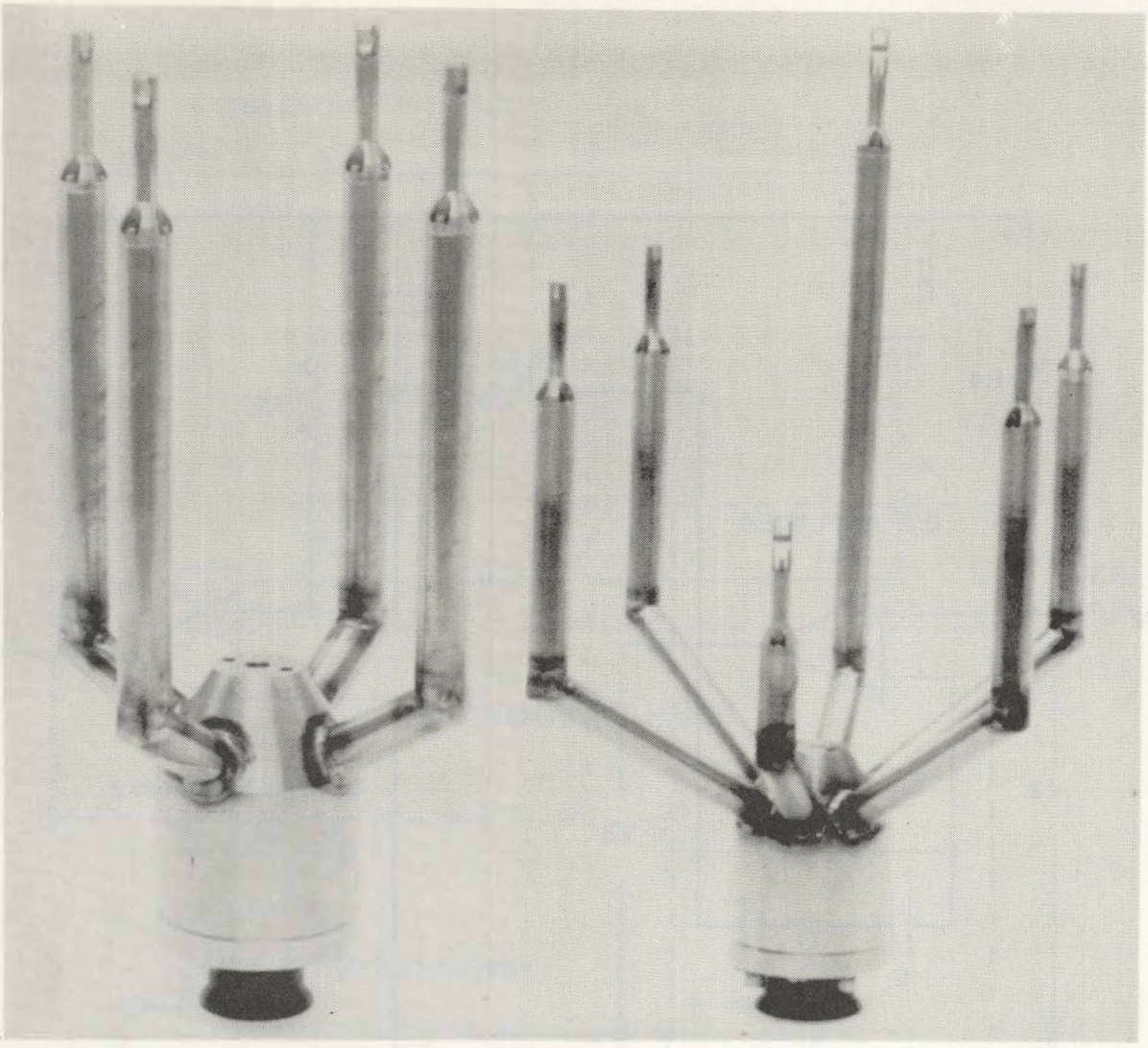

FIG 6A FIG 6B

TYPICAL 2 AXIS AND 3 AXIS SENSOR GEOMETRIES

PREDICTING THE RESPONSE OF CURRENT METERS IN SHALLOW WATER

Gerald F. Appell
NOAA/National Ocean Survey
Rockville, MD 20852

William E. Woodward
NOAA/Office of Ocean Engr.
Rockville, MD 20852

James McCullough
Woods Hole Oceanographic Institution
Woods Hole, MA 02543

Abstract

An approach was developed to quantify the response and predict the measurement uncertainties of current meters in a shallow water environment. A three-phase program of (1) laboratory evaluation, (2) a field experiment and (3) an error prediction model was developed. These program phases are discussed along with preliminary results.

Introduction

The measurement of currents in shallow water is approached differently than the deep water measurement. For example, shallow water current measurement permits the consideration of various platform/mooring configurations. However, the measurement contamination problems are magnified in shallow waters. Fouling, abrasion, vertical shear and water particle dynamics effects also contribute to the list of considerations in measurement system design. The main problem confronting the user is what will be the response of his current meter in a particular system configuration, or what type, make or model current meter should one use in a particular configuration? Unfortunately the response characteristics of the instruments are not always documented in the manufacturers' literature and published experiences from within the community may be questionable. For the last decade NOAA's Test and Evaluation Laboratory (T&EL), a component of the National Ocean Survey (NOS), has been working steadily toward the development of current meter testing methods and procedures that, when properly applied, would provide the appropriate response information. In 1978, the problem was summarized at the Working Conference on Current Measurement[1] and the need for standardized testing methods and procedures for determining the response of current meters was documented. The problem is complex, however, and progress has been slow. Emphasis throughout the community in the past 5 years has been toward quantifying the response of current meters in a dynamic environment.

At T&EL the most significant advancement in testing capability has been the development in 1977 of an apparatus (the Vertical Planar Motion Mechanism, VPMM)[2] to simulate environmental dynamics in the laboratory. This device, which provides a capability for dynamically testing current measurement instrumentation over a wide range of simulated single period and amplitude planar wave motions, has been a valuable tool in the testing research process. An opportunity to apply this tool came in 1978.

The NOS Strategic Petroleum Reserve (NOS/SPR) Support Project, sponsored by the Department of Energy, requested the support of T&EL to develop uncertainty statements for a variety of environmental measurements. The measurements include currents, conductivity, temperature, dissolved oxygen, wave height spectrum, water level and meteorological parameters. The NOS/SPR project objective was to characterize the physical oceanography of two candidate salt brine disposal sites located in shallow water off the coast of Louisiana. The project provided an

opportunity for T&EL to apply test methods and procedures towards quantification of insitu measurement errors. A program to develop techniques for this project was initiated by T&EL and supported in part by NOAA's Office of Ocean Engineering (OOE). This paper reports on that portion of the SPR program related to current measurements taken by Grundy model 9021 current meters.[3]

A three-phased effort, concerned mainly with dynamics contamination and the quantification of its contribution to the measurement uncertainty of mean currents, was developed. The three phases were: (1) a laboratory evaluation of the current meters' performance under simulated steady and dynamic flow conditions; (2) design and implementation of a field experiment to determine site-specific environmental conditions; and (3) correlation of the lab and field data and development of a current measurement error prediction model.

Laboratory Evaluation

The objective of the laboratory evaluation was to determine the response characteristics of the Grundy meters under controlled hydrodynamic conditions. Steady flow conditions were simulated by towing the current meters through still water at the David Taylor Naval Ship Research and Development Center (DTNSRDC) tow basin, Carderock, Md. These tests provided data to derive the measurement uncertainty of the current meters in a steady flow environment. These tests were performed on the combined current meter and platform to ensure an understanding of the response of the total system. Laboratory dynamic flow simulation was accomplished through use of the VPMM at the DTNSRDC facility. Tests were performed under simulated horizontal and orbital oscillations at various attack angles to the simulated steady flow vector. The data analysis technique[4] examines the dynamic response characteristics as a function of the flow signal-to-noise (S/N) ratio. The flow signal is the simulated steady tow component of velocity, and the "noise" is the dynamic velocity superimposed by the VPMM. This technique appears useful for characterizing the effects of dynamic measurement contamination encountered during the actual survey. Because the representativeness of laboratory test conditions is always of concern, an important objective was to verify the laboratory predicted response for the dynamics present at the measurement sites.

Field Experiment

A field experiment, the Gulf At-Sea Performance (GASP) Experiment[5], was designed to determine the environmental flow S/N characteristics and provide data necessary to correlate with lab test results. The experiment was conducted at a survey site in the West Cameron area of the Louisiana shelf, 11 km south of Holly Beach. The GASP Experiment began on April 5, 1979 and continued for a 33-day period.

The strategy for the experimental design shown in figures 1 and 2 were to: (1) obtain a measure of the horizontal homogeneity of currents within the array; (2) determine the flow S/N ratio of the horizontal currents; and (3) determine the vertical shear of the horizontal current. The experimental data collected allowed us to determine the above and to provide a basis for correlation with laboratory test data. The Neil Brown Instrument Systems acoustic current meters (NBIS-ACM I) at the extreme ends of the array were employed to determine the horizontal homogeneity of currents within the array; these operated in the continuous vector averaging mode and recorded data at 5-minute intervals. Applied Microsystems Incorporated (AMI) pressure-type wave gauges were deployed with an

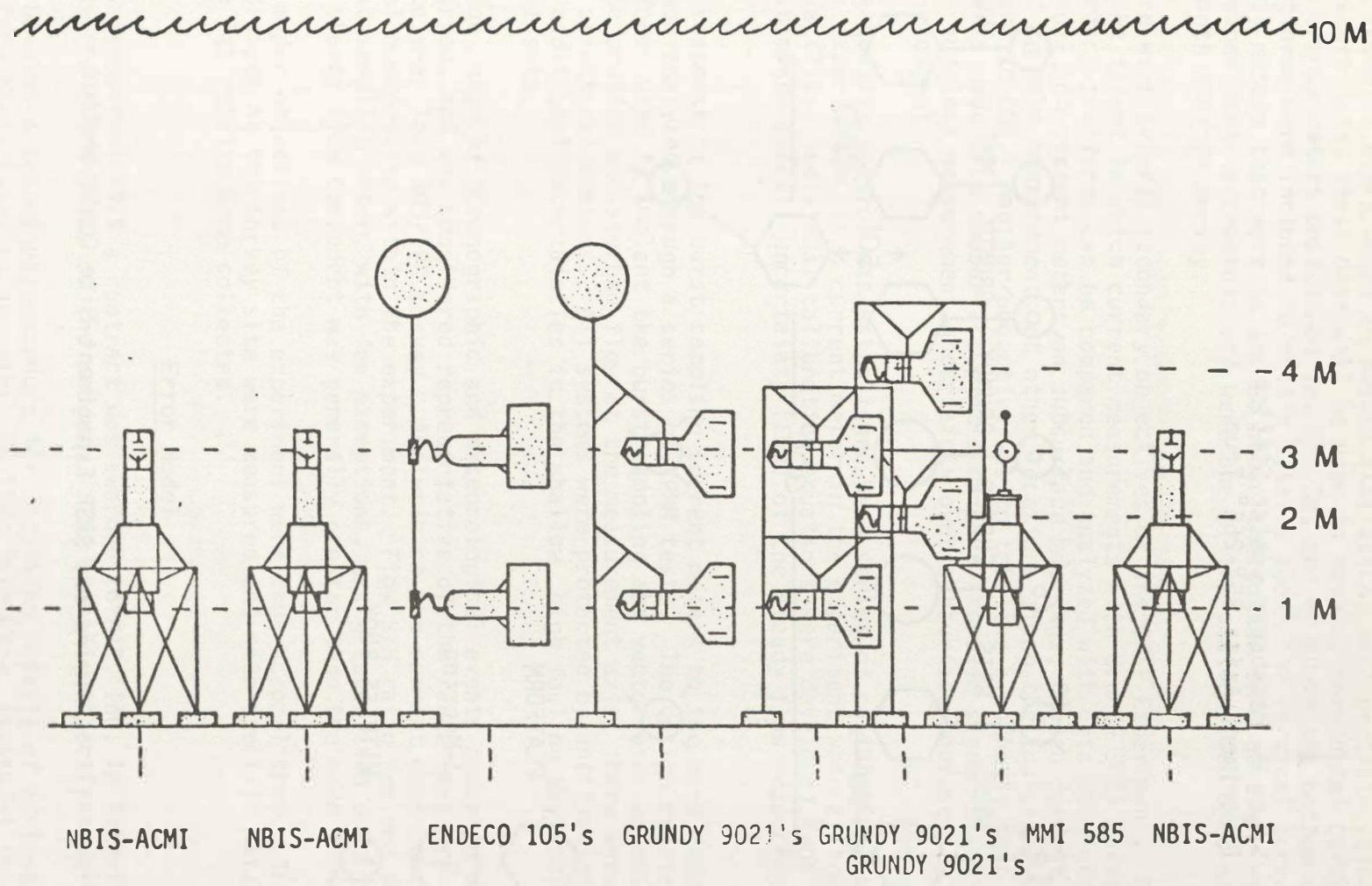

Figure 1. CASP Experiment Current Meter Configuration

Site: W. Hackberry Center Station
Experiment Axis: 85°-265° True

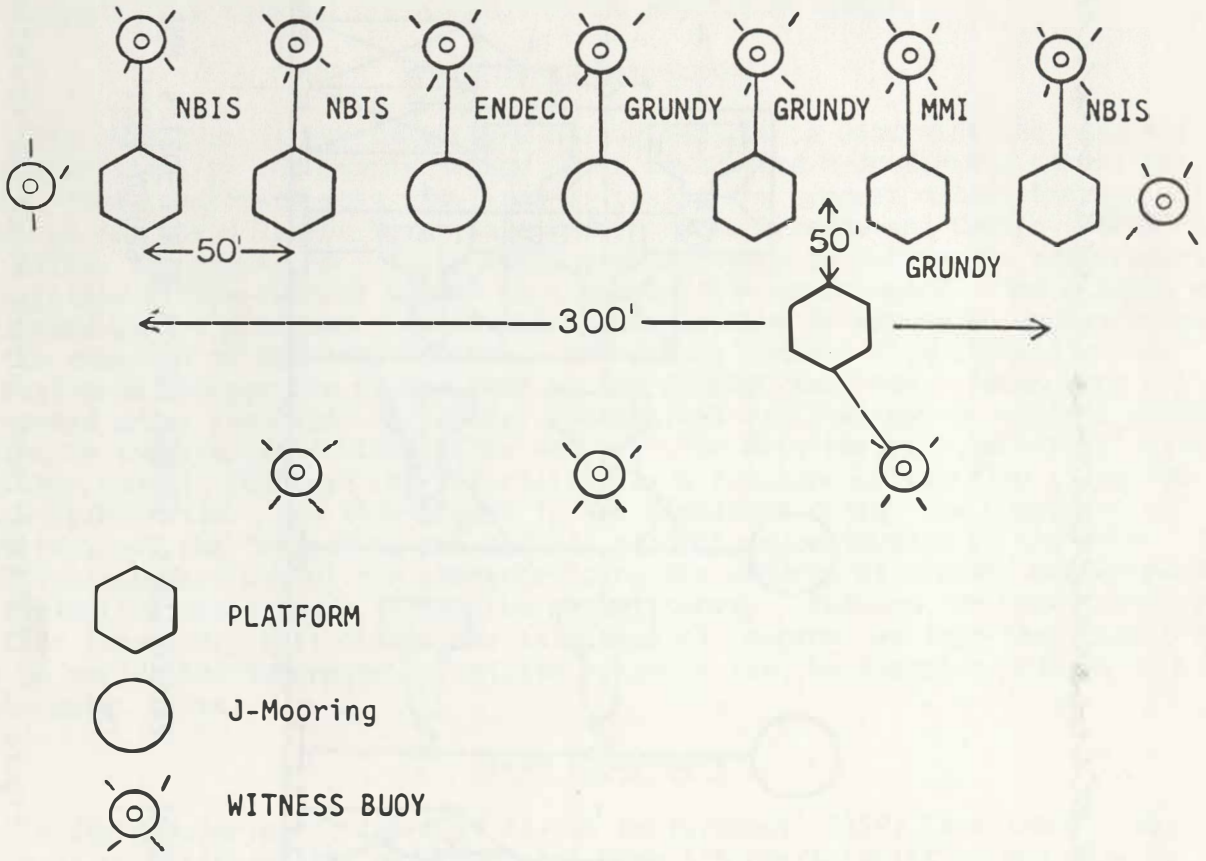

Figure 2. CASP Experiment Site Configuration

NBIS acoustic meter and a Marsh McBirney Incorporated (MMI) Model 535 electromagnetic current meter, each in a burst-sampling mode (1 second samples for 60 seconds, repeated every hour) to obtain statistical wave particle velocity and wave pressure data; these data will be used to develop horizontal current S/N ratios. Grundy meters positioned 1m, 2m, 3m, and 4m above the bottom on subsurface platforms were included to obtain details about the vertical current shear. The Grundy meters that were 1m and 3m above the bottom on a platform were the primary experiment instruments and were one of the stations deployed as part of the 12-month NOS/SPR survey.

There were several secondary objectives of the GASP Experiment. One was to examine the extent to which current measurements with Grundy 9021 current meters on subsurface platforms can be compared and analyzed with data obtained with Endeco Model 105 current meters on subsurface moorings; Endeco current meters were used to make measurements at other locations along the Louisiana coast by contractors to DOE. Another objective was to test the hypothesis that current measurements made from subsurface platforms have improved signal-to-noise characteristics and less measurement uncertainty over subsurface moorings in a shallow water environment.

Data quality control was established by a series of calibrations before and after the experiment. Each current meter in the experiment was calibrated at the DTNSRDC facility, individual calibration equations were developed from the data, and an estimated overall uncertainty (EOU) of the steady flow measurements was derived.

The response of the burst sampling current meters to the wave induced motions was analyzed through a series of VPMM tests. The design requirements for the platforms used to implant the burst sampling and vector average meters were defined to provide undisturbed flow at the measurement axis; there were no flow-blocking structural members. All systems were protected by antifouling paint to minimize additional uncertainties in the shallow, high fouling environment at the experiment site.

A wide range of oceanographic and meteorological events occurred during the 33 day period, and was considered representative of the range that prevailed during the year long NOS/SPR survey. Analysis of the current meter data confirmed horizontal homogeneity within the experiment. Flow S/N ratio derived from the NBIS burst sampling meter, with few exceptions, was greater than one; indicating that the steady flow component was generally greater than the wave induced flow.

The major objectives of the experiment were thus accomplished. The dynamic flow conditions at the survey site were measured and site specific data to correlate with lab results were collected.

Error Model

In September of 1979 a contract was awarded to MAR, Inc. in Rockville, Md. to address the third phase of the program. The specific objectives were:

(1) Develop a technique/procedure for combining results of various laboratory tests (static, dynamics, fouling, blockage, attitude) to estimate the overall uncertainty in speed and direction measurements made by the Grundy current meter during the NOS/SPR project.

(2) Examine field data measured during the GASP experiment and compare to the results of Task 1.

(3) Develop a current measurement error prediction model.

This work is now in progress and will be completed in January 1980.

Discussion

Environmental measurements, particularly in the coastal areas, are coming under increased scrutiny as the likelihood of the measurements becoming the object of legal proceedings grow. As a result, a rigorous analysis and determination of the uncertainties in the measurements is a vital and necessary element in environmental study programs. Technical data has not been presented here because it is still in a preliminary stage. However, based on the efforts to date, it is clear that steady flow accuracies and calibration equations are of value only if error bounds can be established by quality control tests and procedures. Also, the level of dynamic motions encountered in the environment and the individual instrument and system characteristics in the environment must be established.

Although the three-phased effort described here relates to a specific instrument and a specific project, we expect that the approach and the techniques developed will have direct application to future current measurement programs. Within NOAA the results of this program will be used as guidance for the development of future NOS data quality assurance programs. The adoption of these or similar methods and techniques by the ocean community could be a significant beginning to assure the collection of environmental data of known quality. The process is expensive, however, and requires advance planning to assure adequate funding. Yet, there are no alternatives. Unqualified data implies lack of verification and validity by its author and hence, questionable technical and economic value.

References

1. Woodward, W., Mooers, C.N.K., and Jensen, K. (Eds.), Proceedings of a Working Conference on Current Measurement. Tech. Report DEL-SG-3-78, College of Marine Studies, Univ. of Delaware, Newark, DE 19711, 372 pp., June 1978.

2. Kalvaitis, A.N., "The Vertical Planar Motion Mechanism; a Dynamic Test Apparatus for Evaluating Current Meters and Other Marine Instrumentation." Dept. of Commerce-Environmental Protection Agency Energy/Environment R&D Program Report, EPA-600/7-78-145, 37 pp., July 1978.

3. Appell, G.F., "A Summary of the Grundy Model 9021 Recording Current Meter Performance in a Shallow Water Environment." Presented at the Fifth STD/ Ocean Systems Conference and Workshop, San Diego, CA, March 13-15, 1979.

4. Woodward, W., Mooers, C.N.K., and Jensen, K. (Eds.), Proceedings of a Working Conference on Current Measurement. McCullough, J.R. "Near Surface Ocean Current Sensors: Problems and Performance." College of Marine Studies, Univ. of Delaware, Newark, DE 19711, 9-33 pp., June 1978.

5. Appell, G.F., Frey, H.R., Crump, D.R., Woodward, W., "An At-Sea Current Meter Performance Experiment in the Gulf of Mexico." presented at MTS Fifteenth Annual Conference, New Orleans, LA, 156-159 pp., October 10-12, 1979.

Technology Illustrations for a Towed Distributed Instrumentation Profiling System

by

Staff*
Technical Planning and Development Group
School of Oceanography
Oregon State University
Corvallis, Oregon 97331

Abstract

Towed instrumentation has been developed for use in the marine research community to obtain profile measurements of some physical oceanographic parameters down to 100 m and over a lateral range. The Technical Planning and Development Group at Oregon State University has been progressively expanding and improving the capability and reliability of a faired instrumented cable system called DIPS (Distributed Instrumentation Profiling System) that can be conveniently deployed and maintained by a four-man research team on a 30 m research vessel.

DIPS, schematically illustrated in Figure 1, is instrumented to measure 30 vertical temperature stations, 4 pressure (depth) stations, and 6 conductivity stations during a tow. The sensor stations can be repositioned along the cable at sea. During past month-long cruises** in 1977 and 1979, DIPS functioned reliably.

The purpose of this paper is to augment previous publications about DIPS and to provide additional illustrations on newly integrated technology.

Introduction

Early in 1976, the Johns Hopkins Applied Physics Laboratory tested a thermistor chain that had been developed in collaboration with Fathom Oceanology, Ltd. and Sippican Corporation.[1,2] Their tests had confirmed a smaller and more manageable cable system was practical. After we reviewed their cable system, it was apparent that incorporated into the cable assembly was a components modularity that made it feasible for a small group to attain the same instrumented cable capability. The key feature that makes it possible to duplicate this capability is a cable fairing developed by Fathom Oceanology, Ltd. The fairing module functions as a retainer and protective sheath for the individual sensor signal wires to the surface. It also serves as a mounting for the sensors and a distributed coupling to the load-bearing tow cable.

---

* Contributors: Dr. R. Mesecar, Head
Mr. F. Evans
Dr. J. Wagner

** Mixed Layer Experiment (MILE)
Joint Air-Sea Interaction (JASIN)

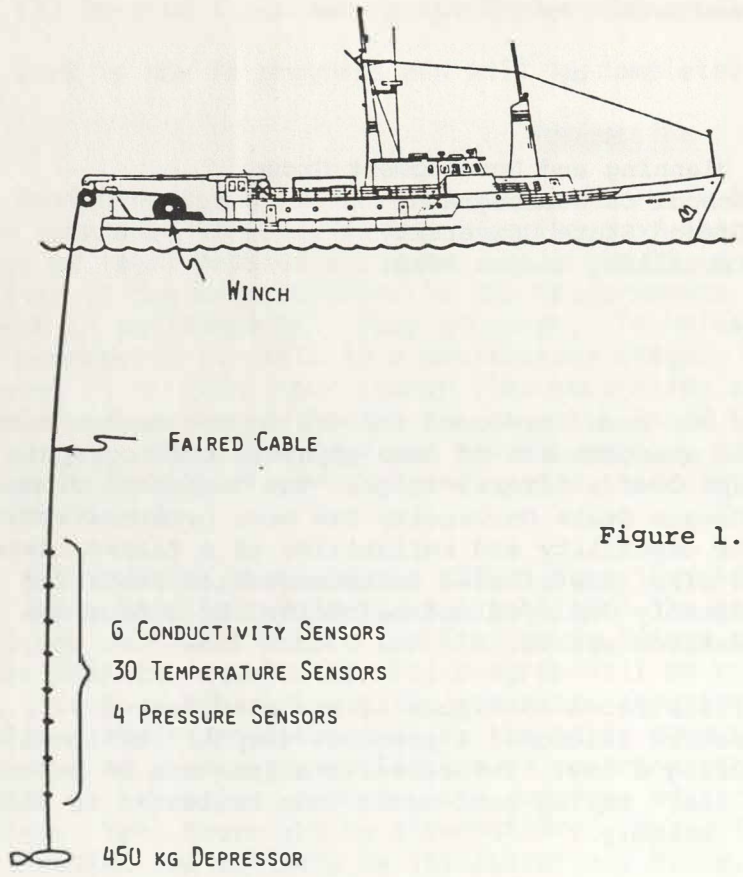

Figure 1. Schematic view of the deployed Distributed Instrumentation Profiling System

Because of the nature of operating personnel, budgets, and the goals of the research program, it was not possible to replicate the APL cable system. On the practical side, the OSU research group owned and wanted to use a PDP-11/10 computer for shipboard data acquisition and data management. Experience with underwater cable connections and sensor calibration and replacement also provided direction on how the sensor output signals would be conditioned before being sent to the surface. For instance, one system goal was to isolate the sensor electronic characteristics and calibrations from the electrical features of the tow cable.

The last major element in the cable system was the winch. Again our plan, for cost reasons, was to improvise a simple winch system to provide minimum cable handling and storage features.

The Cable System

The Fathom Oceanology, Ltd. fairing is the essential building block around which DIPS is assembled. The model 770T fairing is supplied in three parts: a flexible polyurethane nosepiece that is free to swivel about the support cable and two rigid ABS plastic tailsections that can be screw-mounted to each other and socketed to the nosepieces. This modularity made

it possible to use a "divide and conquer" approach to the problems inherent in merging electro-mechanical design features when developing an instrumented cable system. Some obvious system design advantages provided by the fairing modules are:

- All subsystems (fairings, cable wire bundles, tension members, etc.) can be specified independently of each other, purchased, and assembled at our facility under our quality control.
- The fairing modularity permits a mechanical separation of the tension cable and signal wires.
- There is ready access to the signal wire bundles by simply unscrewing the fairing parts.
- Sensors can be integrated into the fairings.
- Sensors can be readily moved to new locations.
- The fairings provide reduced cable drag.

Several sections of the fairing are shown assembled in Figure 2 on a steel load-bearing cable. Each fairing is approximately 10 cm high, 2 cm thick and 15 cm long. Also shown are three bundles of 19-pair signal wires. It is through these color coded signal wires that power to, and signals from, the sensors are transmitted. The bundles are clamped once in each fairing to incorporate a relief loop to allow the fairing tails to part when passing over the winch drum on the sheave. The bottom terminals of the three cable bundles are potted in one block of polyurethane. All subsequent breakouts along the cable are made with a special wire splice technique.

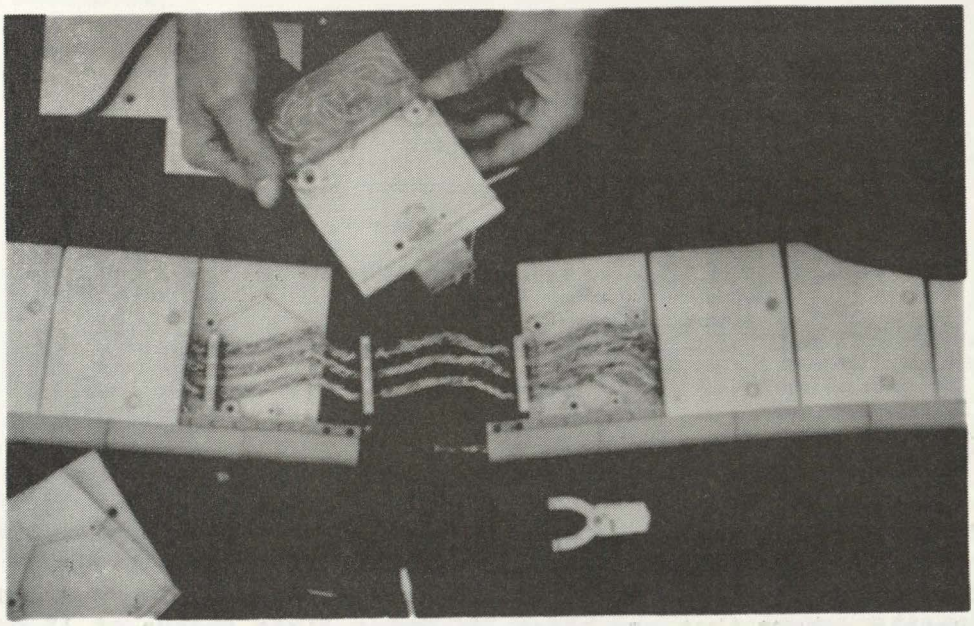

Figure 2. Shown are the components of the Fathom Oceanology fairing in states of assembly for DIPS. Included in this figure is a temperature sensor module that is being inserted in a previously assembled faired cable section.

The signal wires have a Tefzel® coating which offers a very abrasion-resistant surface, but one that is difficult to find a bonding agent for. In addition, the fairing compartment, where connections to the signal wires can be made, is space limited. These two conditions, plus the need for making expedient connections between sensors and the signal wires at sea, required the development of a unique splice technique.

Figure 3 shows the miniature splice developed for this project.[3] The splice incorporates a meltable tubing of two diameters and two very small O-rings within a single clear shrink tube. The O-ring is a standard part (Minnesota Rubber 8001) and the shrink tubing and clear melt tubing are AMP Special Industry Products. The splice relies on the O-ring for seal to the Tefzel® while utilizing the melt material for void fill and self-forming O-ring position seats. These splices have been very reliable in field trials. From a population of over 200 splices originally installed, two possible splice failures were suspected. Approximately 40 additional splices were made at sea over a 4-week period and one of these splices gave evidence of failure. These splices have also been exposed to 1000 psi of pressure in the laboratory for sustained periods and they have maintained isolation resistance above 100 megohms.

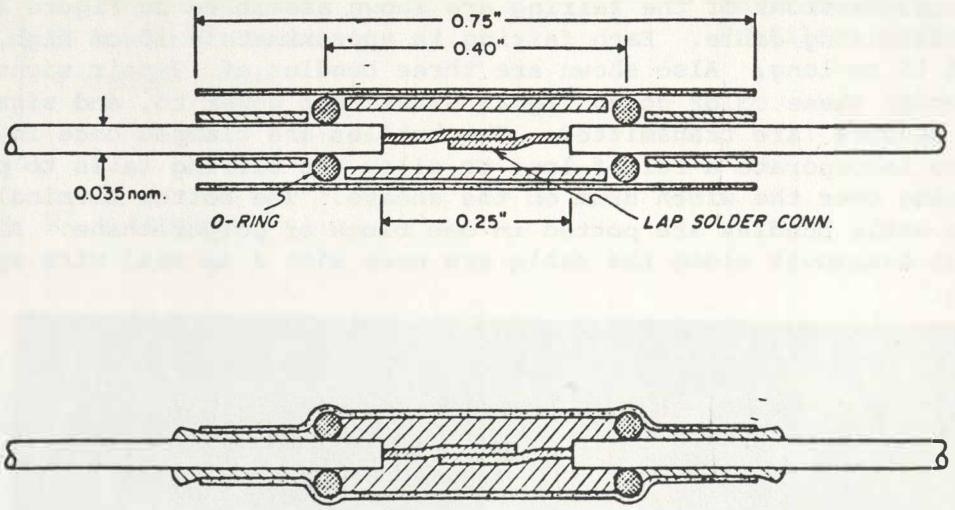

Figure 3. This illustration shows the before and after phase of a thermo shrink splice developed for the small diameter signal-wire connections in DIPS.

Winch System

A 1.3 m diameter winch drum was needed to handle and store the 100 m of faired cable used for DIPS. Because winches reflect the character of their application and budgets, they are generally custom designed. The one used with DIPS is no exception. The photographs in Figure 4 show a winch assembly scheme that can hoist 700 kg at fixed speeds of 15 or 30 cm/sec. Once the deadweight cable depressor and faired cable deployment

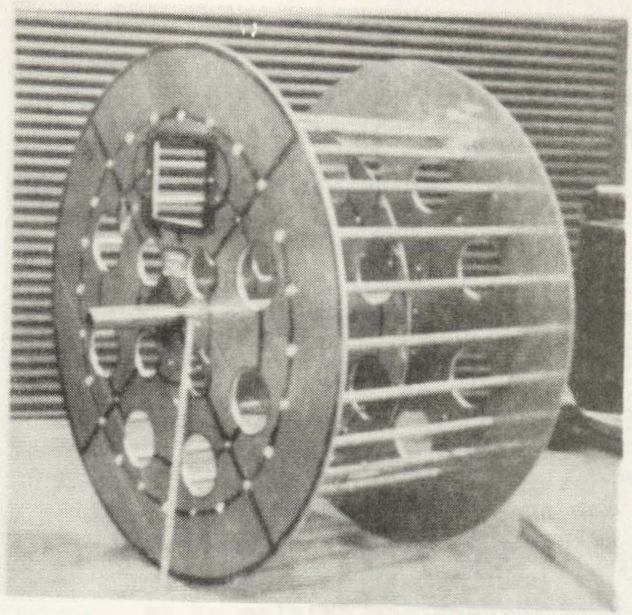

Figure 4a. The cable drum support discs were cut round with a metal band saw. Next, the discs were gang drilled for all the hole patterns. Twenty-four holes in the discs serve as sockets for the spacer rods that form the drum support structure. A metal inert gas (MIG) welder is used to weld the rods to the discs. A 70-mm thick skin is clamped over the support rods and welded as seen in Figure 4b.

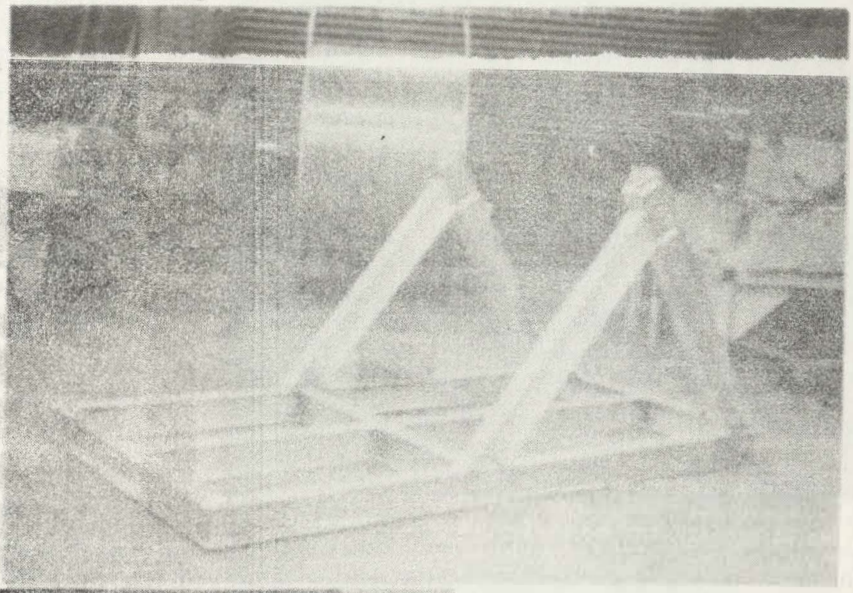

Figure 4b. The winch base is made from 12.5 cm structural "I" beam stock that has been cut on the band saw and welded into a box frame. The drum rotates on a 7.6 cm OD by 1.27-cm-thick wall steel shaft which is supported by pillow blocks that bolt to the base frame. The shaft is keyed to the drum, but it is not the drive attachment for the power train. The power train drives a sprocket attached to one of the discs.

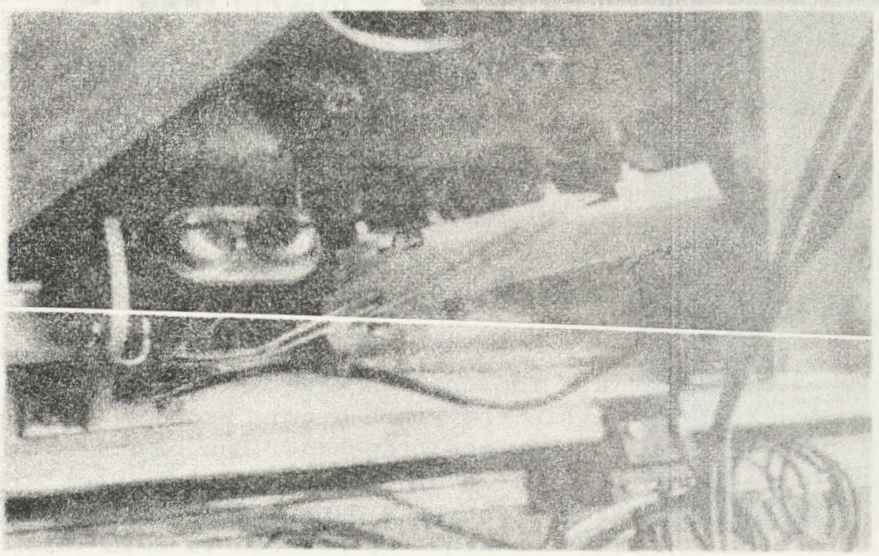

Figure 4c. Hydraulic automobile disc brakes, operating at the outer periphery on one of the drum discs, provide the drum breaking function. Two disc brake assemblies and a master cylinder are securely attached to the base frame. The brake control, which includes an electric cutout to the motor, can be manually operated from either side of the winch.

has been inititated, only one winch operator is necessary. A 10 m cord on the motor control wand allows the operator freedom to completely circle the winch. The payout rate of the cable is done under control of the motor drive train.

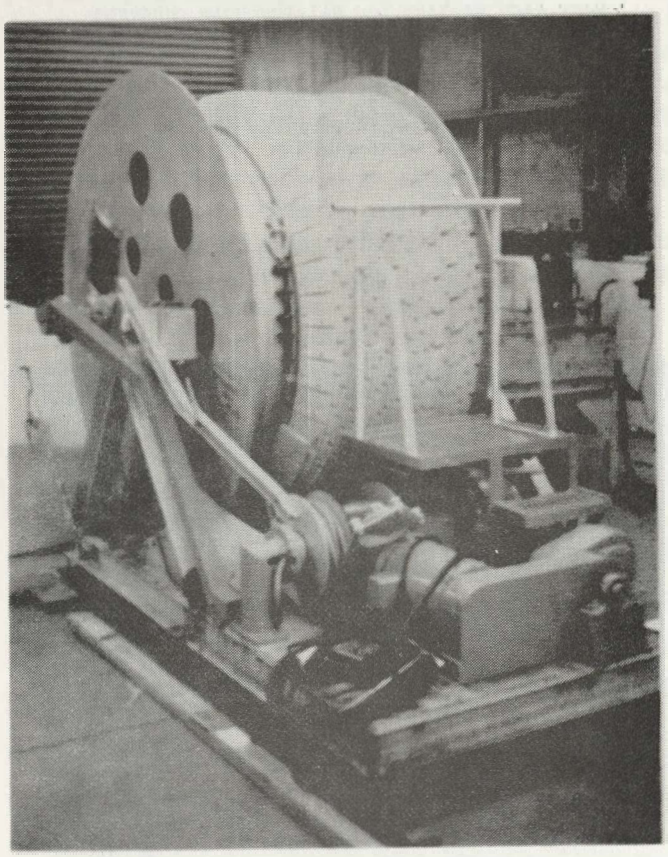

Figure 4d. The completed winch is shown with 100 m of faired cable on the drum. The operator's pedestal is mounted over the power train. From this position the operator can inspect the fairing as it is being spooled. This fairing does not require a fair lead system. The lay of the cable is determined by a preformed plastic groove cemented to the drum surface. With the exception of the power train the majority of the winch is made of aluminum.

A manually operated disc brake system, shown in Figure 4c, can be used to control cable payout when the motor control is off or the drum is to be locked up. This brake can be reached from either side of the winch. In the event that the drum drive chain parted, a mechanical deadfall would lock up the drum.

Bonded to the winch drum surface is a plastic extrusion contoured to mate with the radius of the fairing nosepieces. This extrusion circles around the drum, similar to a LEBUS groove, and functions to protect the shape of the nosepiece and guide the lay of the fairings. By proper separation of the extrusion wraps around the drum it is possible to pay cable in and out without a separate fair-lead mechanism.

The upper ends of the signal wire bundles are fed through a water blocked feed-through into a function box located within the winch drum. From barrier strips in the junction box, signal wires are branched. One branch is a connector mounted into the side of the drum. This connector port can be used to connect a cable to the surface electronic data systems; however, it has to be disconnected each time the winch is powered to move the faired cable.

A capability was added later that makes it possible to keep the signal wires electrically coupled to the surface data system while the winch is being powered. The mechanism that accomplishes this function is called a "sidewinder" and is similar to a design for an equivalent function manufactured by Fathom Oceanology. The second branch from the junction box is connected to the sidewinder (shown in Figure 5) with a jacketed 50-pair cable.

The sidewinder consists of two coaxial drums, a slipclutch/racket drive assembly, and a transfer sheave. One drum is attached to, and rotates with, the winch drum. The second drum does not rotate and is attached to the winch frame with a torque arm. In Figure 4d, the sidewinder is in a shipping cradle position with the torque arm resting on the winch shaft. In use, the sidewinder mounts on the drum shaft and appears as shown in Figure 5. As the winch rotates, the 50-pair cable is transferred from the rotating drum to the stationary one by the slipclutch assembly and transfer sheave. This mechanism permits the winch to rotate and still keep solid signal wire connections from the sensors to the surface electronics.

The first deployment with the sidewinder was successful. The only degradation of system performance which might be attributed to its use is a slight increase in susceptibility to ship radio operations, which is probably due to the increased length of cabling involved on deck.

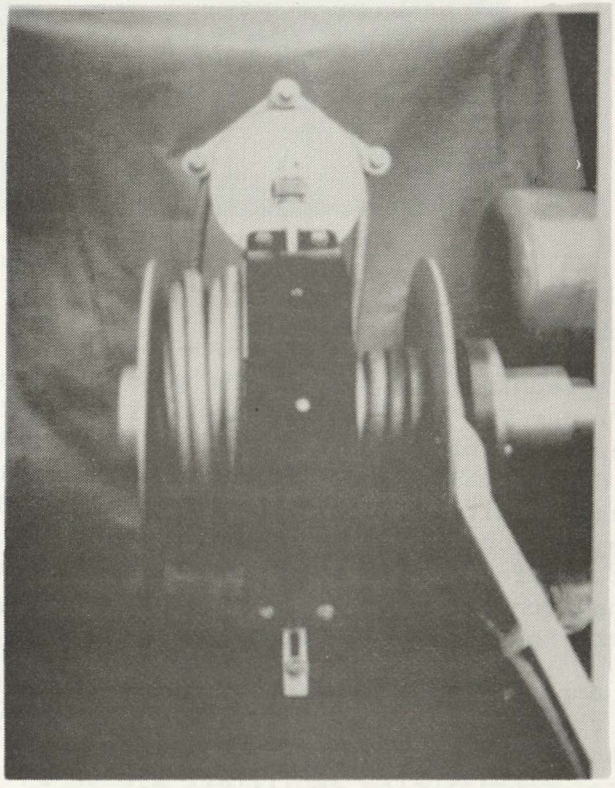

Figure 5. The sidewinder mechanism couples to the winch shaft and functionally serves as a set of electrical sliprings for the 80 pair of signal wires in the faired cable that passes through the rotating drum to the surface electronics.

Pictured in Figure 6 is the sheave used with the cable system. The design and assembly concepts used for the winch drum are also used in the sheave. A sheave diameter of 120 cm has been found to function satisfactorily with the fairing modules. The polyurethane nosepieces which couple one fairing to another are flexible. If the distance between the drum and sheave is over 2.5 m, the fairings deployed from the top of the drum spiral in orientation, as partially illustrated in Figure 6. This can pose a problem for the sensors mounted in the nosepieces of the fairings. To keep the approaching fairings oriented inplane with the sheave, a fairing-flipper mechanism (shown in Figure 6) was added to the sheave. Depending upon the direction of rotation, a drag-clutch will move the fairing-orientation wheel against the incoming cable and gently transform the fairings inplane with the sheave.

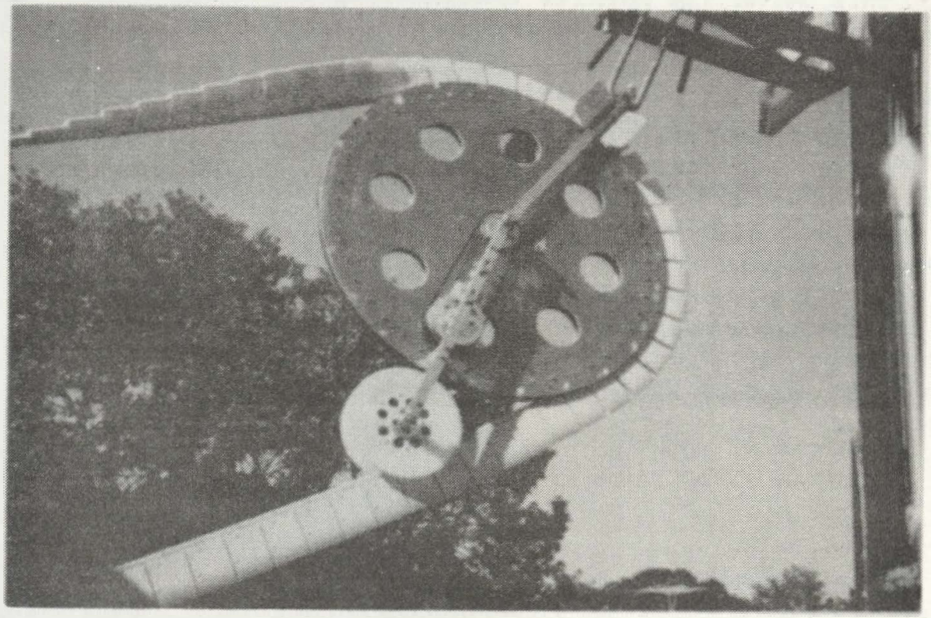

Figure 6. Shown is the sheave and fairing orientation wheel used. It is designed for use with the faired cable.

Instrumentation System

A simple block diagram of the electronic signal flow for DIPS is shown in Figure 7. Within the design criteria for DIPS is the need for sensor interchangeability and signal security which established the requirements for distributing some of the sensor signal conditioning electronics. Signal-conditioning amplifiers have been designed for temperature, pressure, and conductivity sensors. The circuit boards for the pressure and temperature sensors are essentially the same. The conductivity sensor signal conditioning is treated differently as will be noted later in the paper.

The amplifier/fairing/sensor assembly is integrated into the faired cable and connected to power and signal wires by the previously described method. The temperature and conductivity sensors with their associated signal-conditioning amplifiers are shown in Figures 8 and 9. The view ports cut in the fairing are for the reader's interest.

In all the conditioning amplifiers, low-offset amplifiers (Precision Monolothics OP-07) and precision resistors (Vishay networks) were used. This provided an amplifier with less than 0.1 percent tolerance in its zero and ± 1 percent tolerance in its gain parameters and reduced any limitations on dynamic range due to component tolerance bands. Amplifier output signals are ± 5 V dc.

With a low impedance drive to the signal wires, it is possible to sense the signal level with a high impedance surface instrumentation amplifier, with a common mode rejection ratio of greater than 100 dB, which rejects line pickup and eliminates the effects of signal wire resistance. A ground reference for the amplifers is obtained from the power source and a true differential signal sensing is possible without creating a source imbalance. With control of the worst-case error band, a high degree of signal data content (94%) is maintained.

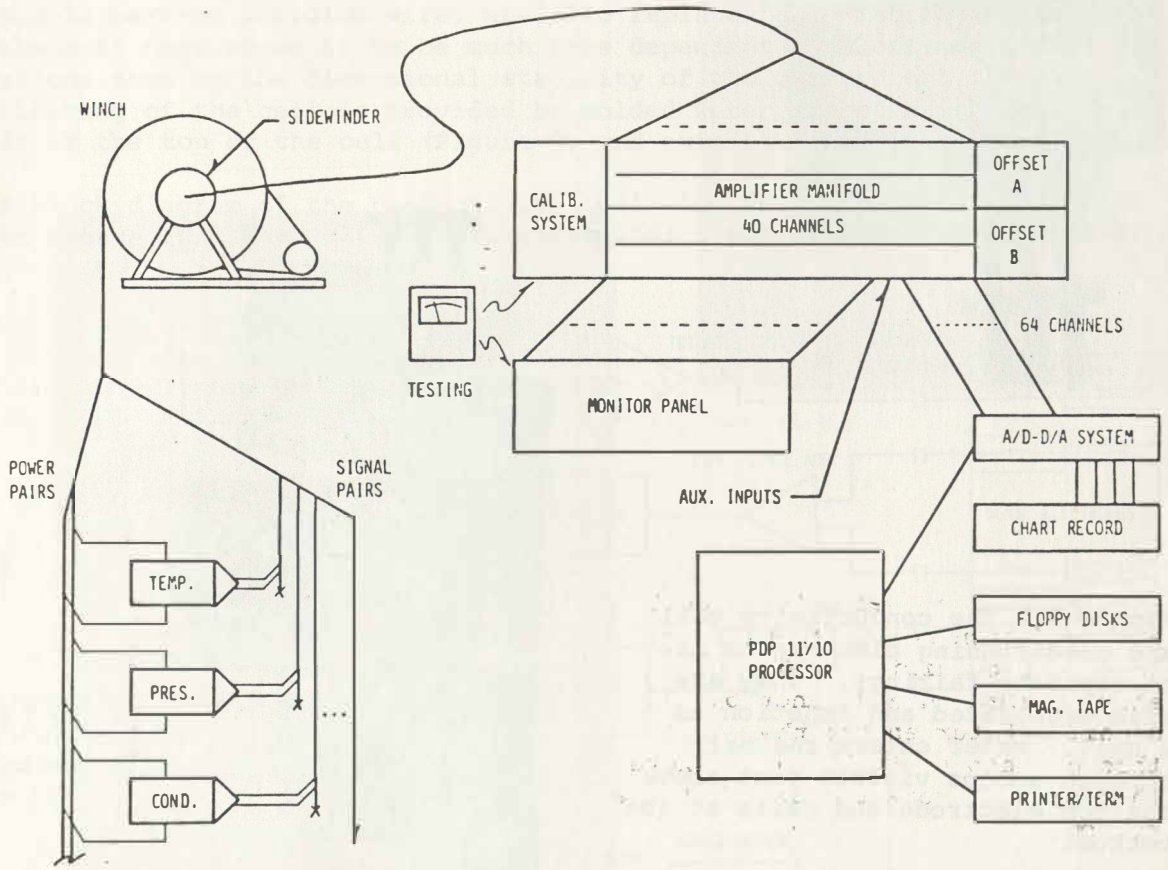

Figure 7. Electronics block diagram for DIPS.

From the temperature sensor through the output of the surface instrumentation amplifiers, resolutions better than .0005°C have been attained with a bandwidth of 5 Hz. To implement a .001°C resolution capability for a temperature span of 20°C, with a 12-bit analog-to-digital converter, it was necessary to provide quiescent offset voltage so that the digitizer

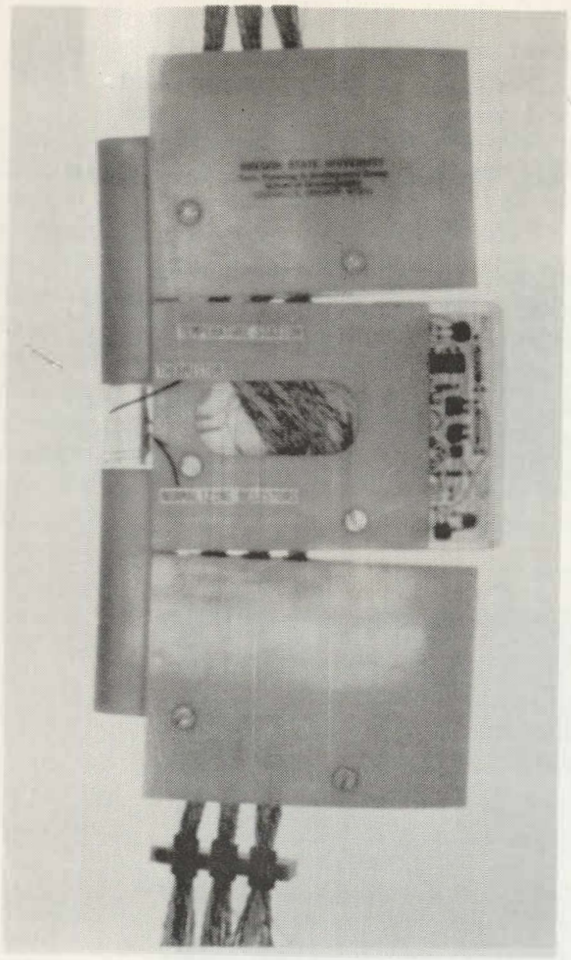

Figure 8. The thermistor for temperature sensing with its normalizing resistors is molded to fit within a segment of the fairing nosepiece. The thermistor/amplifier is calibrated as an assembly and then inserted into the faired cable as shown in Figure 2.

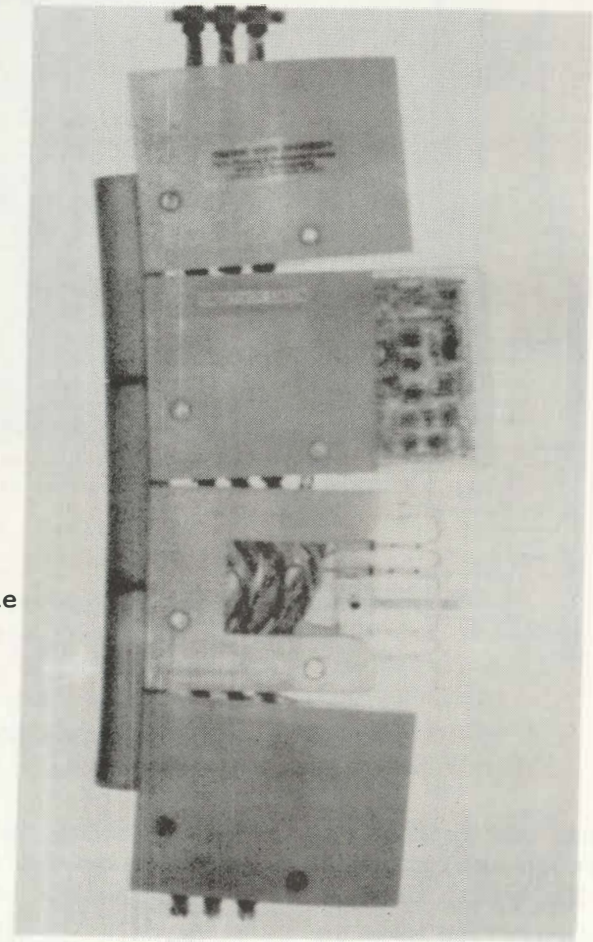

Figure 9. The conductivity cell and conditioning electronics are in separate fairings. They are also calibrated and function as a unit. Water enters the cell through scoops visible just above the top electrode and exits at the bottom.

could be devoted to the dynamic signal range. Each of the surface amplifiers are fitted with two offset voltage terminals that are under switch control on the amplifier manifold panel. These voltages have a reference accuracy of 5 p/m and a resetability of 100 p/m. This feature has been accomplished with a combination of switched one volt and vernier voltage offset references. The output from the offset reference voltages is independently digitized to 12-bits which provides a resolution of one part in 40,000 of the offset voltage used at the time of data acquisition. One offset voltage control is generally used with the conductivity sensors and the other with the temperature sensors.

Thermistors are used for temperature sensors and miniature semiconductor strain gauges for pressure sensors. For conductivity measurements, the four-terminal-electrode geometry was adapted. The cell, as shown mounted in the fairing in Figure 9, is made by a local glass blower of pyrexglass. Cells made in this manner have proven to be consistent for sensor interchangeability purposes. The electrodes, composed of 90 percent platinum and 10 percent irridium wire, are also replaceable. Laboratory tests on the cell have shown it to be much less dependent on electrode configurations than on the dimensional stability of the measurement chamber. Flushing of the cell is provided by molded water scoops which take water in at the top of the cell (Figure 9) and exit it from the bottom.

A block diagram of the conductivity cell electronics amplifier is shown in Figure 10. The cell is a four-terminal resistive device which is ac-

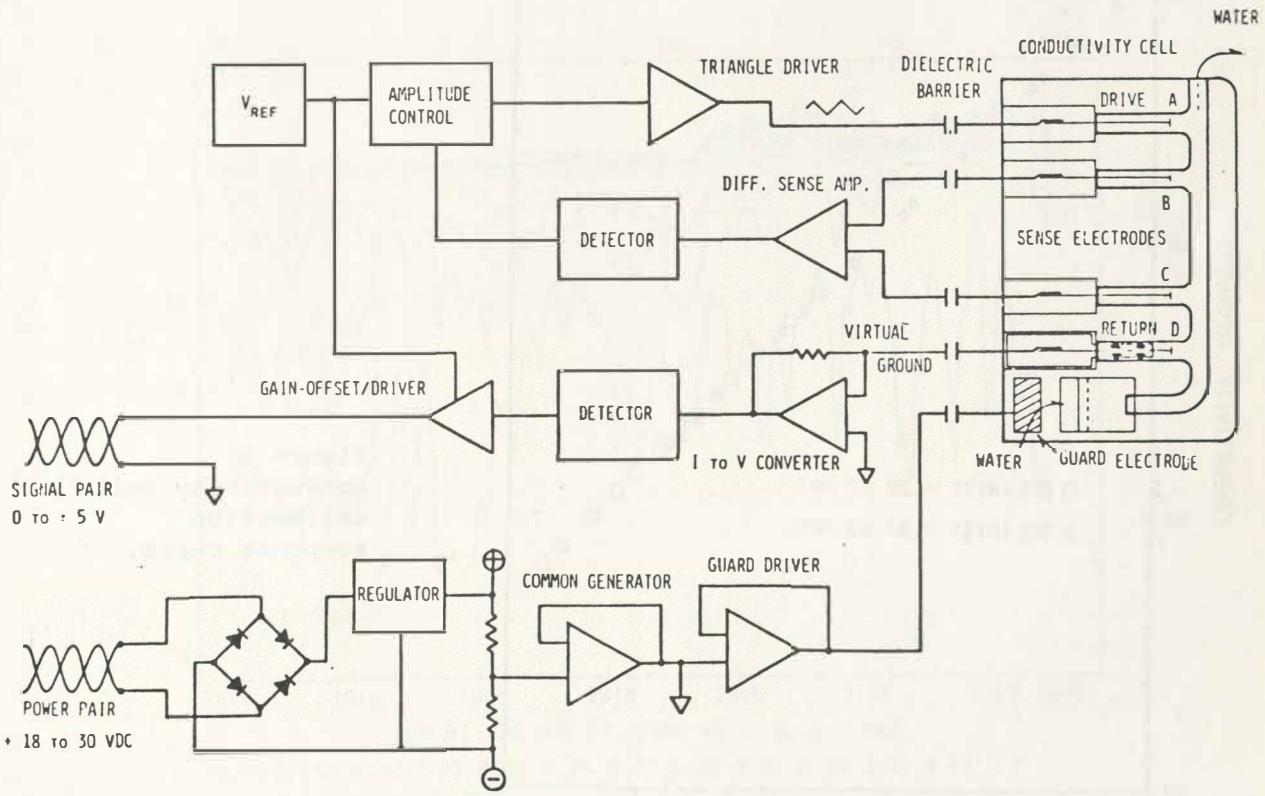

Figure 10. Block diagram for the conductivity cell and the in situ signal conditioning amplifier.

coupled to the conditioning amplifier. One of the outer two electrodes (A) is driven by a triangle waveform into the virtual ground created at the other of the outer electrodes (D). The triangle waveform was chosen to limit the slewing rate required of the amplifiers, thus allowing better accuracy at higher frequencies than any simple waveform, including the sine waveform. The two central electrodes (B and C), called the sense electrodes, measure the drop across the measurement volume between them, but at near zero current, thus eliminating electrode polarity problems often encountered at saline/metal boundaries. This also eliminates electrode geometry influences and the voltage drop due to nonzero impedance between the electrodes and the measurement volume. The sensed signal is used in a closed-loop control of the triangle waveform amplitude to sustain a constant voltage drop across the measurement volume. The cell output is derived by measuring the drive current into the return electrode (D). A current-to-voltage converter drives a detector for ac to dc conversion. The detected conductivity signal is then outputed to the surface through a gain and offset stage.

The fifth electrode is driven at ac common. The return electrode is connected to a virtual ground at the current-to-voltage converter. Any currents entering this terminal from the exterior environment contribute

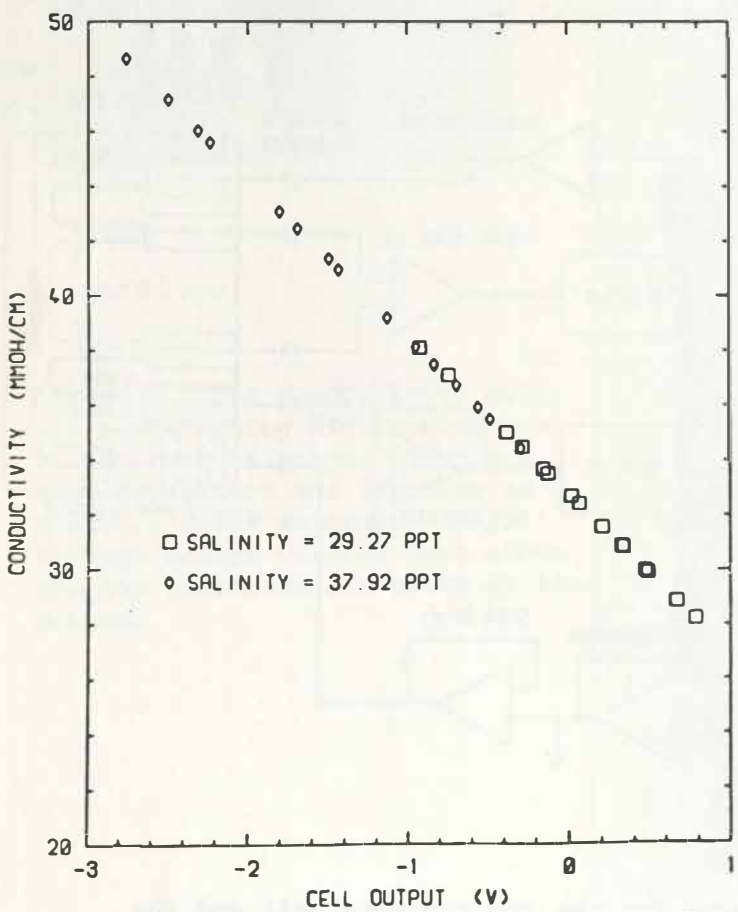

Figure 11. Conductivity cell calibration response curve.

to the output level. The guard electrode, being driven to ac common, "guards" the return electrode, which is also at ac common, by providing or sinking any current from other sources. Since equivalent voltages exist at the guard and return electrodes, no current should flow from the inlet (where the guard is) to the return electrode (next adjacent electrode). Some questions still exist about the procedures of laboratory calibrations and their transfer to the field environment. The field environmental influences appear to be constant and thus will contribute to the cell constant in the actual measurement. The guard electrode by removing near and far environmental influences assures that the calibration environment is a good model of the measurement environment.

A typical temperature structure towed profile from data acquired with the DIPS cable system is shown in Figure 12.[3,4] During the MILE program (1977), DIPS had only the temperature and pressure sensors. The conductivity sensor prototype was added to DIPS for the JASIN cruise in 1979. Data reports for that cruise are in preparation. The DIPS sensor configurations, as previously illustrated in Figures 8 and 9, will be used during the FRONTS cruise in early 1980.

Figure 11 shows the relationship between conductivity, as determined by laboratory salinity samples, and cell/electronics output. The system has exhibited good linearity and repeatability.

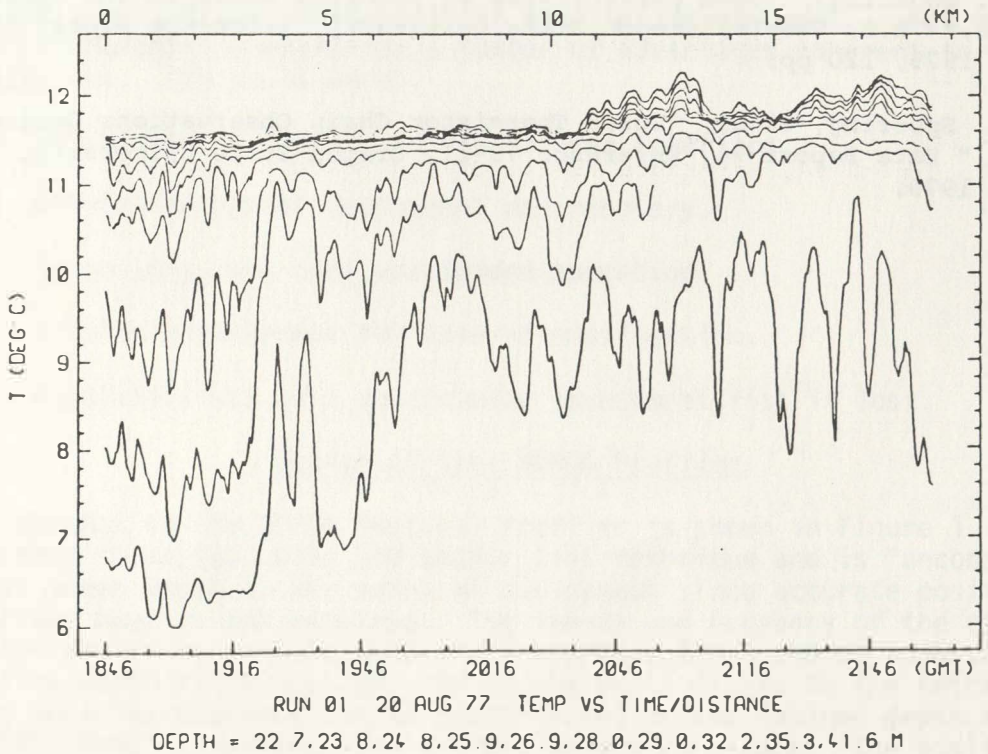

Figure 12. Some plotted upper ocean temperature structure measured with DIPS during the MILE program.

Conclusion

The capability to make towed temperature, depth, and conductivity measurements in the upper 100 m of the ocean has been realized through the progressive development of the DIPS faired cable system. A number of technological problems were anticipated in developing this unit; however, after the fact it appears that solutions to simple problems, like wire splicing, may have been the most signficant contribution to our success. As the operating team has matured with the system development, DIPS has proven to be reliable at sea.

References

[1] F. F. Mobley, et al, "A New Thermistor Chain for Underwater Temperature Measurement," *Ocean 76 Conference*, September 13-15, 1976, Washington D.C.

[2] Sippican Corporation, Marion Massachusetts (Restricted Report), "Feasibility Study for a Towed Thermistor Chain."

[3] J. Wagner, "A Miniature Submersible Wire Splice," *Exposure*, VI (2), pp. 6-8, May 1978.

[4] T. J. Spoering, "Towed Observations of Internal Waves in the Upper Ocean," M.S. Thesis, Oregon State University, Reference Report 79-10, July 1979, 120 pp.

[5] T. J. Spoering, et al, "Towed Thermistor Chain Observations During MILE," Data Report 74, Reference 79-11, Oregon State University, July 1979.

THE NORDA VERTICAL PROFILER

Clifford Randy Holland

Naval Ocean Research and Development Activity
Ocean Technology Division, Instrumentation Branch
NSTL Station, Mississippi 39529

Abstract

A variable buoyancy vehicle capable of profiling from the air/sea interface to depths of 1000 meters has been built and tested. The integral data acquisition package utilized in performance evaluation of the profiler can be easily interfaced to a variety of ocean parameter sensors. Because of its ability to penetrate the air/sea interface, this profiler can be used as a submersible telemetry link between subsurface and bottom mounted sensors and ship or land based data processing facilities.

Introduction

Profiling with a single sensor package can provide definite cost advantages over the use of distributed sensor arrays involving many stations, provided the environment being measured changes slowly compared to the profiling rate.

At the start of the NORDA Vertical Profiler development, a set of design goals were formulated to emphasize a number of advantages inherent to the profiling technique. The goals were:

(1) An ability to profile to the air/sea interface.

(2) An easy method of deployment and recovery.

(3) Reasonably long term unattended operation.

(4) Modular arrangement for ease of modification.

(5) Relatively low cost to minimize investment risk if lost.

Design of the NORDA Profiler

The concept of the NORDA Vertical Profiler is shown in Figure 1. The system is easy to deploy using the anchor last technique and is "unconscious" to the precise ocean depth at the point of deployment since accurate positioning of a near surface buoy is not required. The length and buoyancy of the tether which connects the profiling vehicle with the subsurface float can be adjusted to suit the profiling depth range desired. By adding small floats to the tether, the profiler's negative buoyancy can be counteracted at the desired depth and the vehicle will "hang" suspended like a small weight on a cork. The addition of an acoustic release mechanism(s) at the dead weight anchor permits easy recovery of the system.

The profiling vehicle consists of two spherical compartments arranged vertically in a fiberglass framework as shown in Figure 2. The upper pressure sphere contains the data collection instrumentation and profiling controls while the lower sphere houses the variable buoyancy system. This buoyancy system works

NORDA
VERTICAL PROFILER

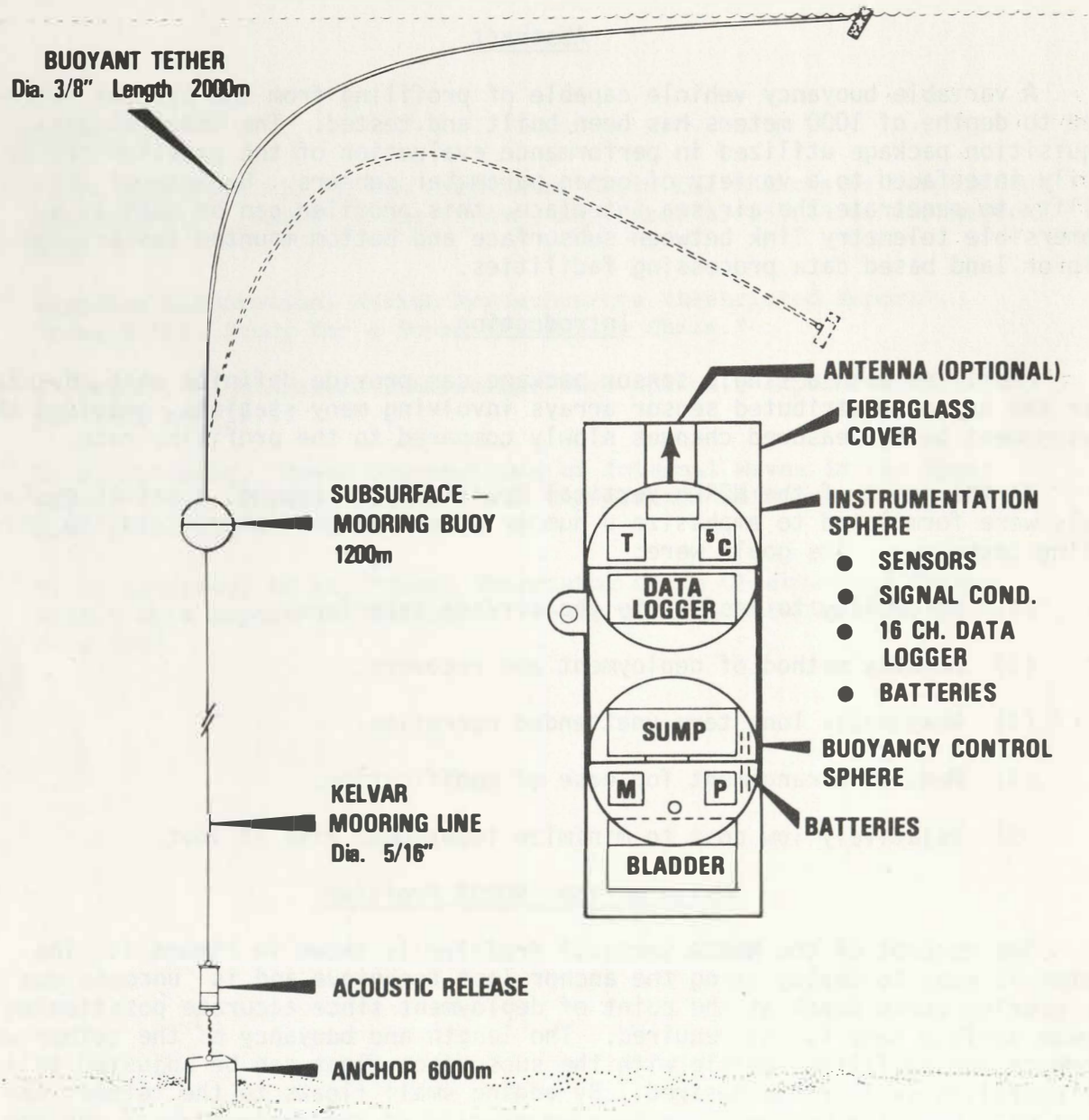

Figure 1

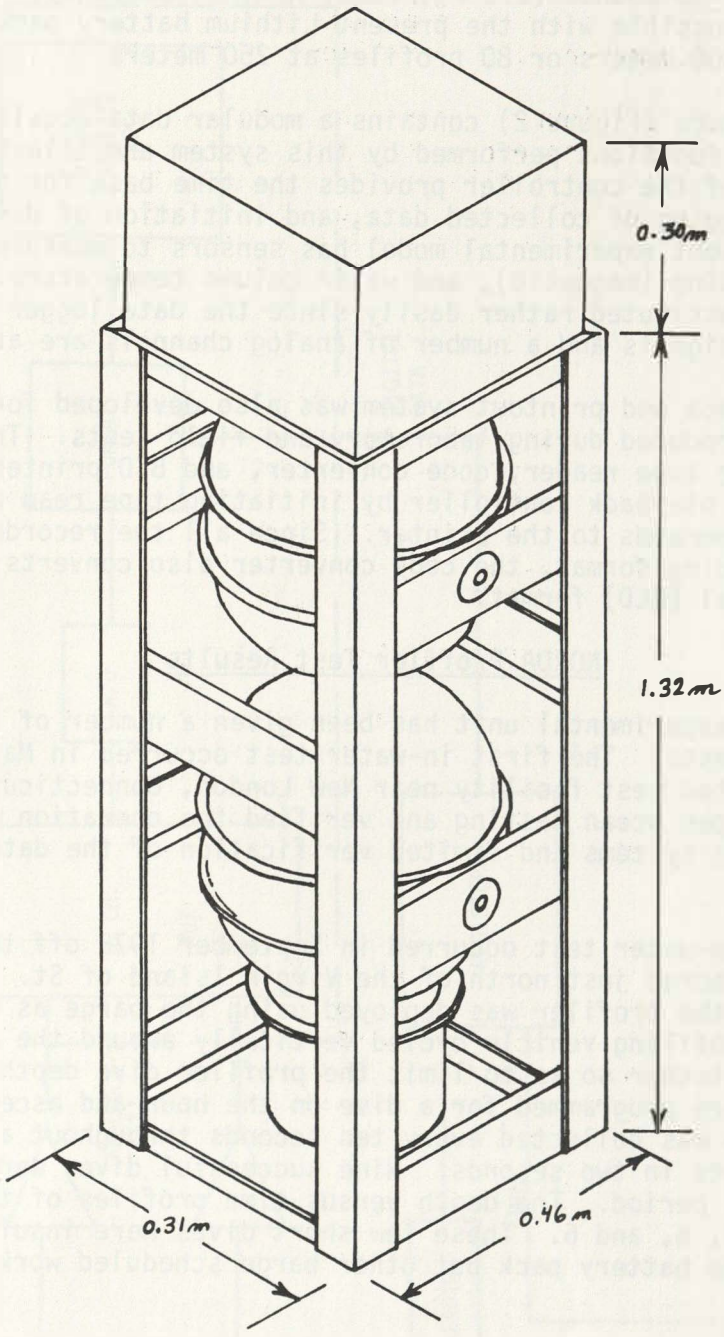

Figure 2

by pumping oil from an internal sump to an external bladder, thereby changing the displacement and, hence, buoyancy of the entire vehicle. Pumping is performed only at depth to conserve energy; the small sea pressure "head" is used to return the oil to the internal sump when the unit is at the air/sea interface. The buoyancy system of the experimental model is capable of a ten pound (4.4 kg) buoyancy change of $\pm$ 5 pounds (2.2 kg) about neutral buoyancy. About 20 profiles to 1000 meters is possible with the present Lithium battery pack which translates to 40 profiles at 500 meters or 80 profiles at 250 meters.

The upper sphere (Figure 2) contains a modular data acquisition and control system. The major functions performed by this system are illustrated in Figure 3. The clock portion of the controller provides the time base for data acquisition functions, time tagging of collected data, and initiation of dive and surface commands. The present experimental model has sensors to measure vehicle depth (pressure) and heading (magnetic), and water column temperature. Other sensors can be added or substituted rather easily since the data logger will accept analog or digital signals and a number of analog channels are at present unused.

A data playback and printout system was also developed for analysis of the engineering data produced during laboratory and field tests. This system consists of a cassette tape reader, code converter, and BCD printer. The code converter acts as the playback controller by initiating tape read commands to the reader and print commands to the printer. Since all the recorded digital data is not of the same coding format, the code converter also converts all data to a binary coded decimal (BCD) format.

NORDA Profiler Test Results

The present experimental unit has been given a number of laboratory tests and two in-water tests. The first in-water test occurred in May 1978 at Dodge Pond, a Navy operated test facility near New London, Connecticut. These tests were a prelude to open ocean testing and verified the operation of the buoyancy control and pumping systems and limited verification of the data acquisition system.

The second in-water test occurred in September 1978 off the Tracor Barge facility while anchored just north of the Virgin Island of St. Croix. During this test series, the profiler was deployed using the barge as the tether anchor point while the profiling vehicle cycled vertically around the barge. A float was placed on the tether so as to limit the profiler dive depth to 350 meters and cycle times were programmed for a dive on the hour and ascent on the half hour. Sensor data was collected every ten seconds throughout a dive at a rate of eight data points in two seconds. Nine successful dives were completed during the three day test period. The depth versus time profiles of these dives are shown in Figures 4, 5, and 6. These few short dives were insufficient to even begin depleting the battery pack but other barge scheduled work prevented extending the tests.

Adaptability of the NORDA Profiler Concept

The concept just described and the experimental hardware used to test it embodies a number of the design goals specified earlier.

First, the system is easy to deploy and recover; requiring no special ships or shipboard equipment.

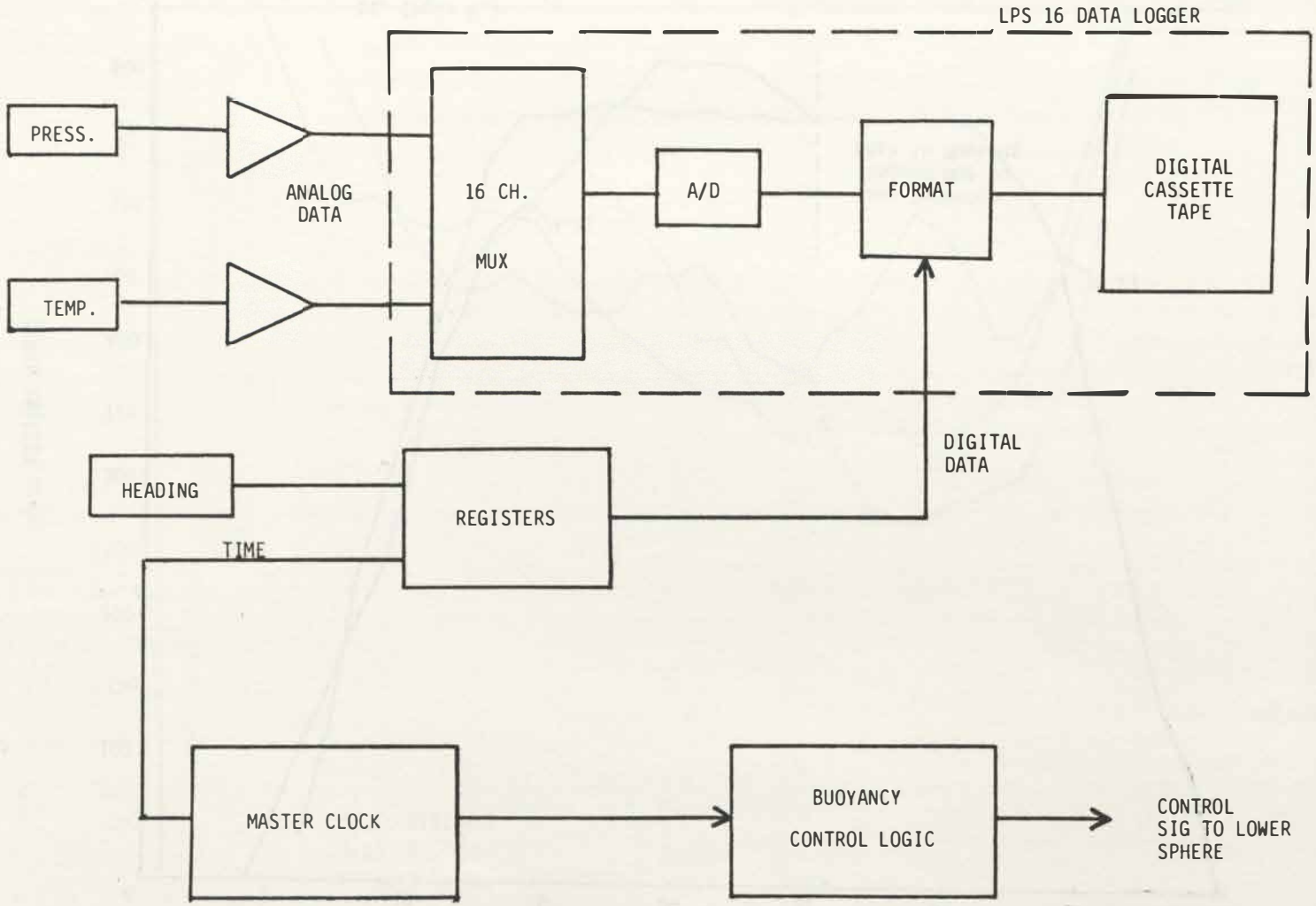
LPS 16 DATA LOGGER
PRESS.
TEMP.
ANALOG DATA
16 CH.
MUX
A/D
FORMAT
DIGITAL CASSETTE TAPE
DIGITAL DATA
HEADING
REGISTERS
TIME
MASTER CLOCK
BUOYANCY
CONTROL LOGIC
CONTROL SIG TO LOWER SPHERE

FIGURE 3

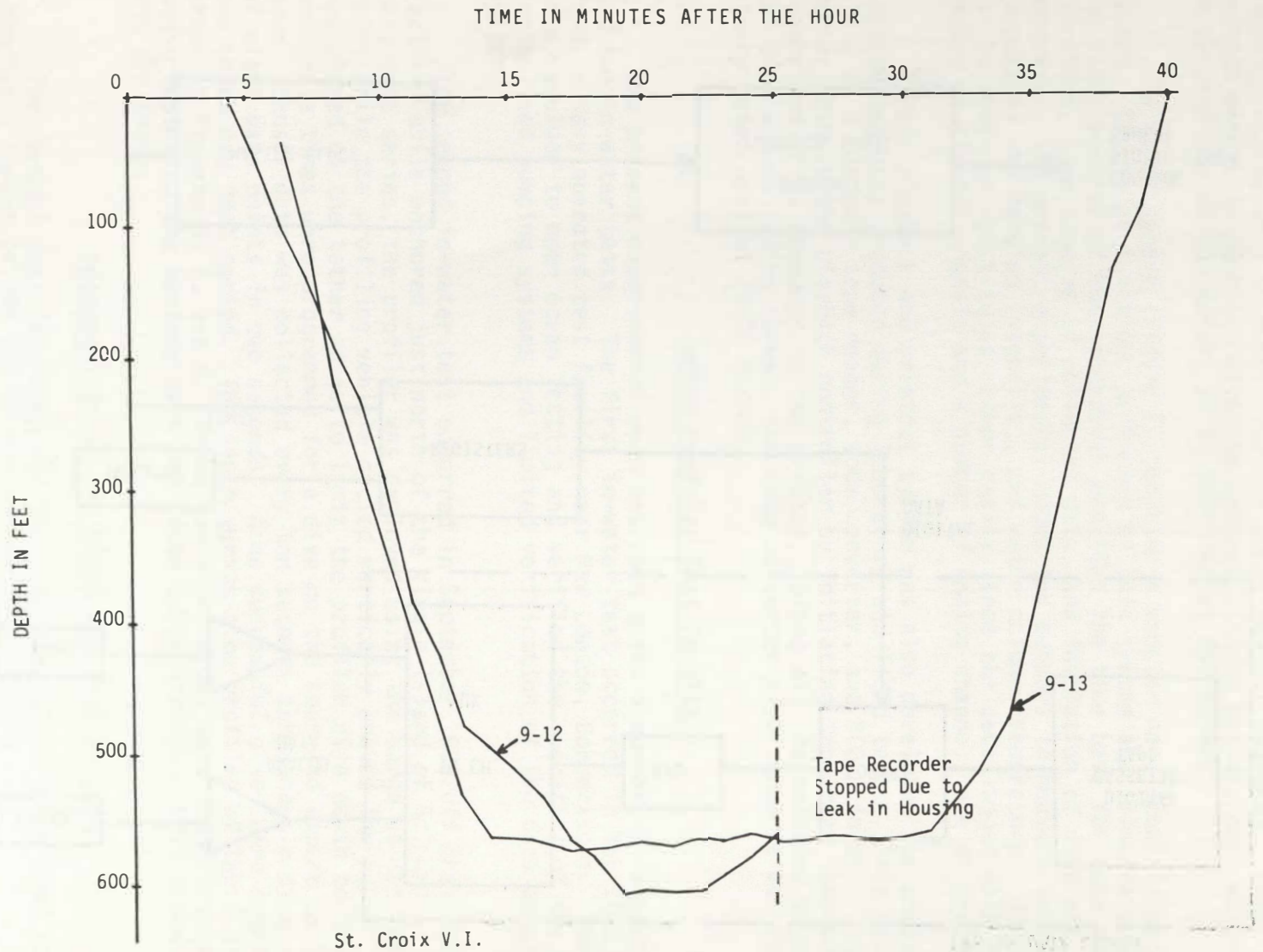

St. Croix V.I.
9-12-78
and 9-13-78

Figure 4

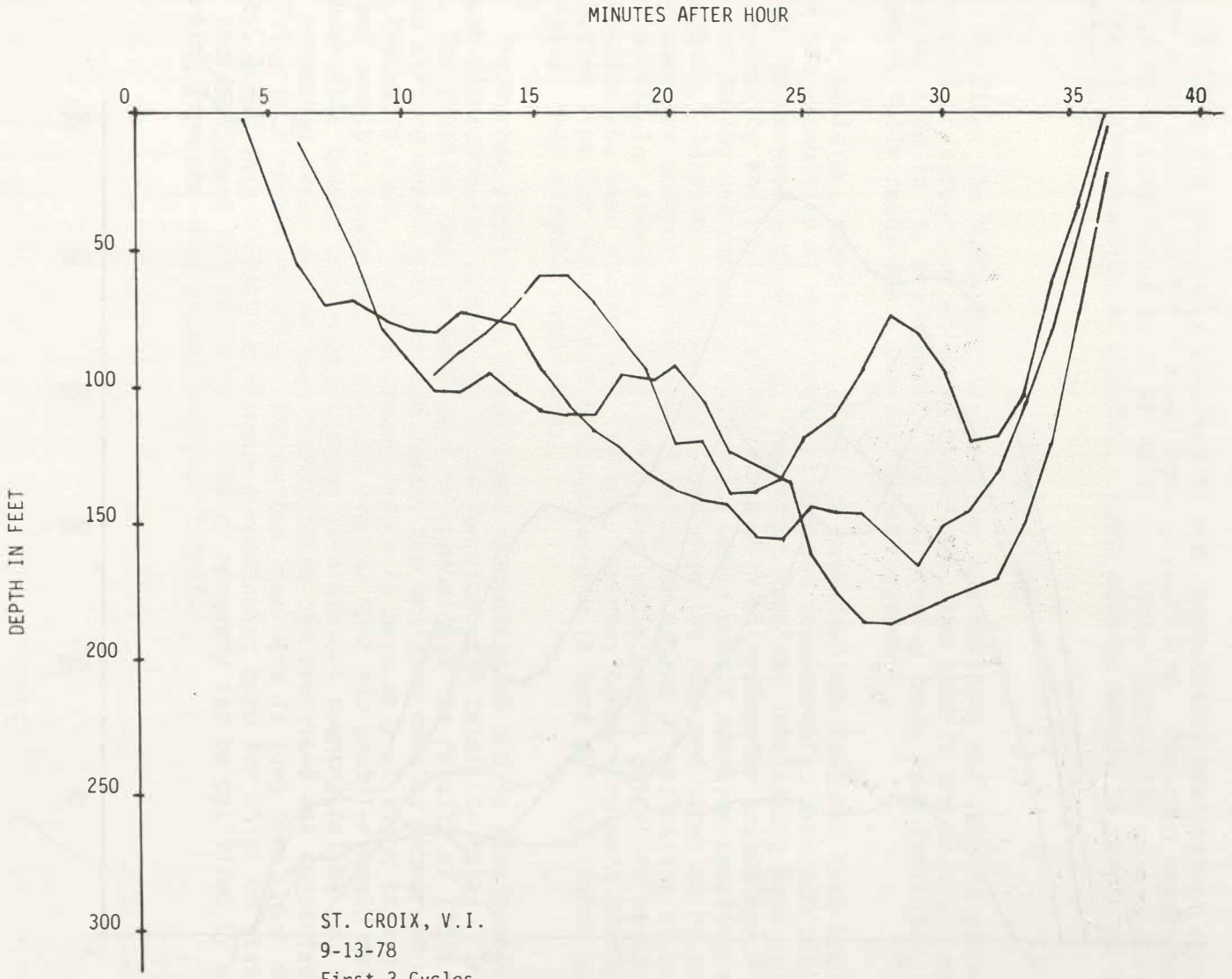
MINUTES AFTER HOUR
0
5
10
15
20
25
30
35
40
DEPTH IN FEET
50
100
150
200
250
300
ST. CROIX, V.I.
9-13-78
First 3 Cycles

Figure 5

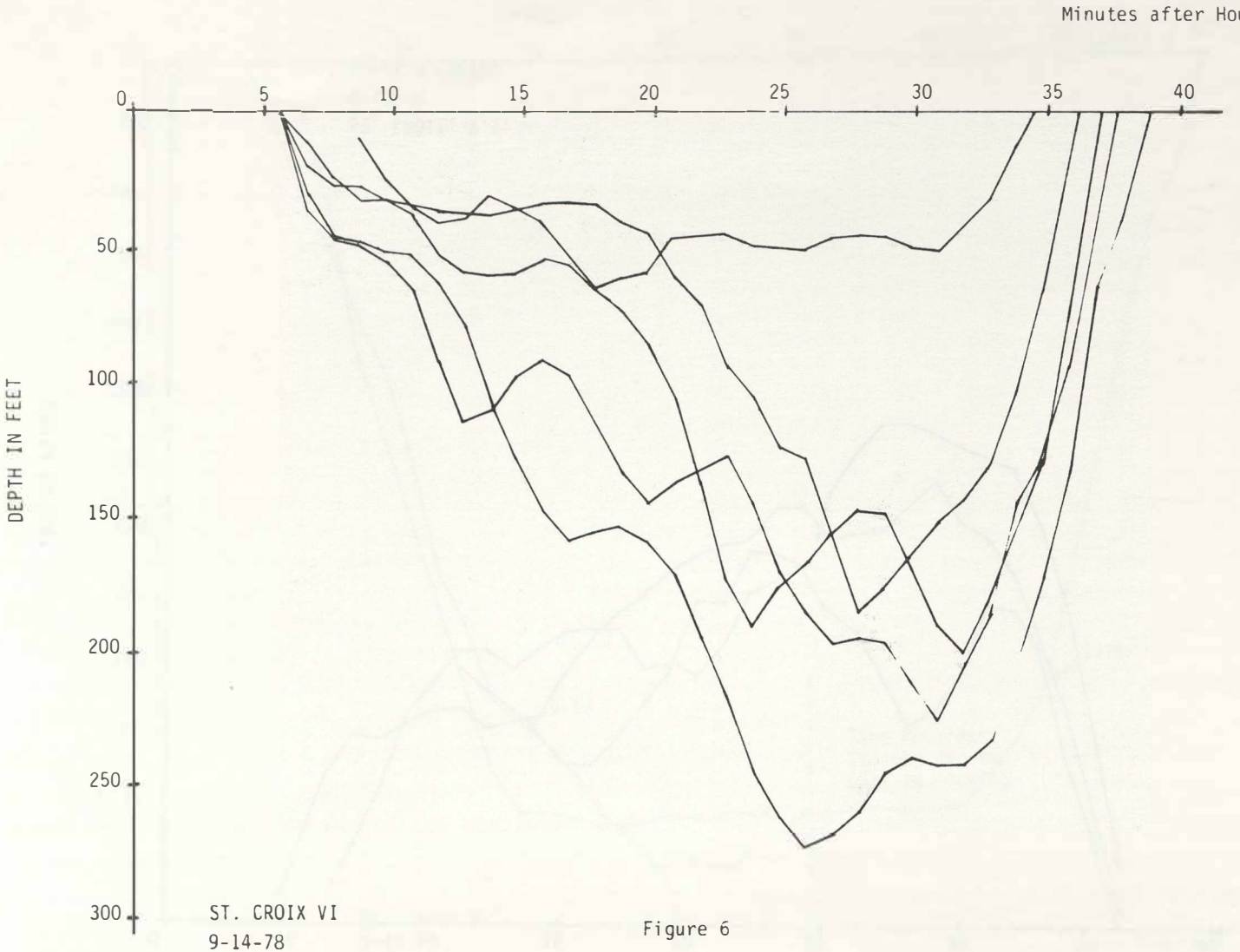
Minutes after Hour
0
5
10
15
20
25
30
35
40
DEPTH IN FEET
50
100
150
200
250
300
ST. CROIX VI
9-14-78
5 Cycles

Figure 6

Second, the sensor suit is modular and can be altered to optimize data collection for a particular experiment whether it be thermal or sound velocity profiling, measurement of water column optical properties for remote sensing ground truth, or listening for acoustic events.

Third, because this profiler pierces the air/sea interface, it can house a radio transmitter for communication of data to ships or shore based receivers using satellite relay such as GOES or ATS.

Efforts are presently underway to add conductivity measurement capability to the experimental unit for ocean density profiling. The data readout system is also being interfaced to an HP 9845S calculator system for data processing and graphic presentation of results. These efforts should be concluded by December 1979.

Future Plans

To date, the NORDA Vertical Profiler has not been utilized to gather scientific data in support of an ocean experiment, and that is the next and most important step in its evolvement. The engineering tests have indicated that the system is fully ready for a scientific application.

In addition, there are a couple of potential new features that would improve the capability of this profiler concept considerably, provided that they can be implemented economically. The first involves intelligent data collection and processing and could be accomplished with microcomputer technology. The decision making and computing capability would permit adaptive sampling and data compaction. Adaptive sampling would optimize the rate and duration of sampling under computer control to increase fidelity or extent of collection of data that is of particular interest. Data compaction would permit quiescent periods to be represented as, say, statistical values, thereby conserving data storage space. The bottom line for intelligent data collection is more data of higher quality at, hopefully, only slightly more cost.

The second addition is intelligent communication and is also possible through microcomputer technology in conjunction with satellite relay. In this mode, the profiler decides when best to communicate the results of its efforts. If sea surface conditions are too rough, the profiler remains submerged until a more favorable time. Perhaps communication is best only at night to avoid sighting and possible vandalism. It might even be that the profiler would only act as a submersible transmitter communicating with sensors mounted on the sea floor or in a suspended array and in turn transmitting the processed and compacted data via satellite to a receiving site. The bottom line here is long term, high survivability, ocean data collection without a continuing need for ships on station but only for deployment and recovery. Time of recovery can be optimized by status reporting from the intelligent profiler itself.

THE CYCLESONDE - A PRACTICAL PROFILER FOR UPPER OCEAN CURRENT AND CTD MEASUREMENTS

John C. Van Leer
University of Miami
Miami, Florida

Abstract

The Cyclesonde is an automatic autonomous vertical profiling device which rises and falls on a taut wire mooring making measurements on both the ascending and descending part of its profile cycle. About 30,000 velocity profiles have been recorded by Cyclesondes to date which is believed to be more than all other methods combined. Most of these recordings have been made during more than a dozen oceanographic experiments on continental shelves and in the upper 200-400 meters of the deep ocean. The remainder supplied crucial information during the installation of the largest offshore platform ever built (COGNAC) in the Gulf of Mexico at a depth of over 300 meters, Collipp et al. (1979). The discussion below will briefly cover the evolution of the Cyclesonde, the design philosophy, sampling errors and possible future direction.

The Cyclesonde Past and Present

These devices have gone through three distinct generations in the past seven years. This process started with free running mechanical systems with a four day maximum deployment time, a 10 bit Aanderaa recorder and an upper current speed limitation of ~ 1 knot, Van Leer, et al. 1974. Today deployments lasting months, Van Leer and Craig (1975), are possible with programmable frequency of profiling, electronically controlled valves, a 12 bit precision low power data acquisition system, CTD, current sensor, data/remote command capability, and an upper speed limitation yet to be reached in operation. These devices can be used on subsurface moorings on continental shelves, surface moorings either anchored or free drifting in deep water and may be cycled on a wire hung from a ship or drilling rig. Cyclesondes are particularly useful when real time data are required for decision making. Both local telemetry to shore or satellite telemetry have both been used with great success, Evans et al. 1975.

Design Philosophy

The design philosophy has been to stay away from exotic and expensive propulsion systems or those which depend on hazardous materials which may explode, burn violently or exude toxic chemicals or fumes. Expensive materials and high precision machine work have been avoided to keep costs within reason. Similarly elaborate power consuming on board control and computer systems have been avoided. This eliminates the need of expensive, untestable, expendable battery packs. Instead, the intelligence and control functions are kept ashore where they can be maintained and interacted with depending upon the state of the instrument and the data. Extensive experience with solar powered transceivers has shown them to be quite reliable and satisfactory for this purpose.

Cyclesonde systems are small and simple enough to be handled or maintained either from a rubber boat with divers; from very small research vessels with minimal winch capacity; or could be packaged on a self-deployable mooring system for use from ships or aircraft of opportunity. In short, these systems have been designed to be simple, safe and inexpensive enough to make their use practical in large numbers.

Sampling and Measurement Errors

Comparison of Cyclesonde velocity data taken on surface moorings and subsurface moorings with fixed level current meters mounted on subsurface moorings suggest that systematic disagreement of $\pm$ 1 or 2 cm/sec are usually found Van Leer and Leaman (1978). The standard deviation is sea state dependent since the primary noise source is surface gravity waves and may often be two or three times the systematic error in rough conditions. CTD errors are comparable to other 12 bit systems depending on which sensors and full scale ranges are used.

These errors, including time response are kept small by the modest vertical speed of the instrument relative to the water typically 10 $\pm$ 5 cm/sec and the decoupling action of the roller in eliminating wave forced heaving motions. Significant increases in accuracy of velocity in the wave orbital zone might be had with either acoustic or E-M probes. There errors are small compared to the sampling errors of omission found in typical current meter arrays, Van Leer (1979) thus this presumed improvement would have to be carefully traded off against cost.

Possible Future Directions

Because of the harsh nature of upper ocean environment and because single point measurements are often unrepresentative, due to sampling errors of omission (horizontally or vertically), larger numbers of inexpensive profile devices will usually give a more representative description of the upper ocean processes. For example, Price et al. (1977) found that horizontal advection of heat was as important as the local air sea exchange process in accounting for changes in mixed layer depth they were attempting to model.

Meteorologists have adopted the philosophy of large numbers of cheap expendable, (but returnable) probes simultaneously launched from many land based weather stations. Due to the rising costs of ship operation, weather ships are being phased out so it seems unlikely that oceanographers will ever enjoy the luxury of larger numbers of manned stations at sea. Thus, remote reporting low-cost semi-expendable instrumentation which can remain in an area for a few months without ship support seems attractive. If the instrument were lost, the data would still be in hand at about the same price per profile as present day expendable profiler data. Towards these ends, the major advances in Cyclesonde techniques revolve around shrinking the electronics and therefore the overall size, weight and cost of the housings and electronics involved.

References

COLLIPP, B.G., R.C. Hamilton, J.C. Van Leer and C.E. Abbott (1979): Currents and Current Meters for the COGNAC Platform Installation. MTS Fifteenth Annual Conference, October 1979, New Orleans, Louisiana.

EVANS, R. Jr., O.B. Brown, J.C. Van Leer, (1975): Computers at sea: Is satellite communication a viable alternative? In: Proceedings of a Working Conference on Oceanographic Data Systems, Woods Hole Oceanographic Institute, November 12-14, 1975, pp. 81-95.

PRICE, J., C.N.K. Mooers and J.C. Van Leer, (1978): Observations and simulation of storm-induced mixed-layer deepening. Journal of Physical Oceanography, 8, (4).

VAN LEER, J.C., W. Duing, R. Erath, E. Kennelly and A. Speidel, (1974): The Cyclesonde: An unattended vertical profiler for scalar and vector quantities in the upper ocean. Deep-Sea Research, 21, (5), 385-400.

VAN LEER, J.C., (1979): Profiling instruments. NATO Textbook, Instruments and Methods in Air-Sea Interaction. J.A. Stromml (Ed.), Ustaoset, Norway, April, 1978 (accepted for publication).

VAN LEER, J.C. and H.L. Craig, (1975): Eight-week Cyclesonde test off Bear Cut. TR75-2, University of Miami, Miami, Florida, 32 pp.

VAN LEER, J.C. and K. Leaman, (1978): Physical oceanographic research using the attended profiling current meter (APCM) and the Cyclesonde. Proceedings of a Working Conference on Current Measurement, NOAA/OEE, Newark, Delaware, January 1978.

DRAPER LABORATORY PROFILING CURRENT AND CTD METER (PCM)

John M. Dahlen
The Charles Stark Draper Laboratory, Inc., Cambridge, Massachusetts

Abstract

The design of the Draper Laboratory Profiling Current and CTD Meter (PCM) is described. This self-propelled instrument processes and records signals from its sensors in a programmed depth-time sequence. Its most noteworthy features are: an energy-efficient buoyancy control system for sustaining cyclic vertical motion throughout long-term immersion; accurate measurement of current, temperature, and conductivity in the surface wave field; and a microprocessor-centered programmable electronic system for sophisticated control of operational functions. The prototype system is configured to operate unattended on a mooring line while drawing its power solely from internal batteries. It is presently being evaluated in near-surface ocean pilot experiments.

Introduction

In July 1975, members of the Draper Laboratory involved in oceanography obtained Independent Research and Development discretionary funds for construction of a prototype system capable of precise long-term measurements of current and other parameters in the near-surface region of the open ocean. Existing current-monitoring systems, when placed within about 200 meters of the surface, exhibited gross dynamic errors induced by the surface wave field. As a result, science was severely constrained in its quest to understand this important region, where energy is transferred between the atmosphere and the ocean, and where a significant share of the horizontal transport of heat and momentum takes place.

During the first year, we examined approaches to configuration of the system and solution of the major technical problems. Guided by computer simulations of system response to the environment and hardware design studies, we decided to advance a powerful design concept: the Profiling Current Meter (PCM). The PCM is a self-propelled instrument which processes and records signals from its sensors at prescribed depths in the water mass. While the PCM concept is not new, the mechanization in mind promised dramatic improvements in measurement accuracy, operating life, mission flexibility, and cost effectiveness. During the next two years, we completed the design, fabrication, assembly, and lab testing of the prototype system, thus completing the IR&D phase of the project.

The second phase, involving design refinement, ocean testing, and field use in pilot scientific experiments, has been pursued under the sponsorship of the Office of Naval Research. During the summer of 1978, PCM (ALPHA and BETA) performed flawlessly in short-term demonstrations in the WHOI dockwell and in Martha's Vineyard Sound. It is scheduled for a four-month experiment off the shore of Bermuda starting in November 1979 (PCM GAMMA).

Prototype Design Description

The PCM is a self-propelled instrument which processes and records signals from its sensors at prescribed depths in the water mass. Its most noteworthy features are:

1. An energy-efficient buoyancy control system for sustaining cyclic vertical motion throughout long-term immersion.

2. Accurate measurement of current in the surface wave field.

3. A microprocessor-centered, programmable electronic system for sophisticated control of operational functions.

The PCM may be adapted to either moored or free-drifting modes of operation, and may be equipped with a variety of sensing and communication transducers for expanded measurement, telemetry, and battery charge capabilities. However, the prototype instrument described herein is designed to operate on a mooring line (drawing its power solely from internal batteries) and to record current, temperature, and conductivity in a programmable depth-time sequence. Its purpose is to explore its own capabilities and to provide a data base from which similar instruments may be confidently designed to perform specified missions. We are hopeful the prototype will demonstrate technology advances in the areas of near-surface current measurement accuracy and self-propelled profiler operating life. A thorough description of the PCM is given in Draper Laboratory Report R-1095, Draper Laboratory Profiling Current and CTD Meter, by John M. Dahlen, et. al., July 1977.

Mechanical Configuration

The essential form of the PCM is established by its 56-centimeter diameter titanium spherical housing and top-mounted 10-centimeter diameter electromagnetic current sensor (Marsh-McBirney) (see Figure 1). The housing and sensor are penetrated along the polar axis by a 1.43-centimeter diameter hole which serves as a conduit for the mooring line. Upper and lower roller assemblies minimize frictional resistance to axial motion along the line. Each roller assembly has three rollers staggered vertically and azimuthally (120 degrees apart), whose inscribed diameter is somewhat larger than the mooring line diameter. The spherical form was chosen for three principal reasons:

1. Operating Life. The total instrument must nominally be neutrally buoyant; thus, given any total mass, the displacement is fixed (94 kilograms and 0.091 cubic meters for the prototype). The spherical housing provides this displacement for minimum structural mass leaving the greatest space and mass allowance for batteries. Required net buoyancy and energy to overcome viscous drag and rolling friction while profiling were found to be comparable for the forms considered practical for typical mid-ocean near-surface applications, where highly variable relative current vectors are encountered by the instrument. In certain unique applications (such as a very strong current), a streamlined shape may be advantageous and could be provided by an add-on shell. Packaging is not so difficult as usually encountered because a significant amount of free space is needed if the instrument is to be neutrally buoyant.

2. Performance Analysis. The PCM is subjected to a wide range of flow magnitudes, directions, and frequencies. The hydrodynamic forces and instrument response can be analyzed and simulated on a computer more reliably for a spherical shape than

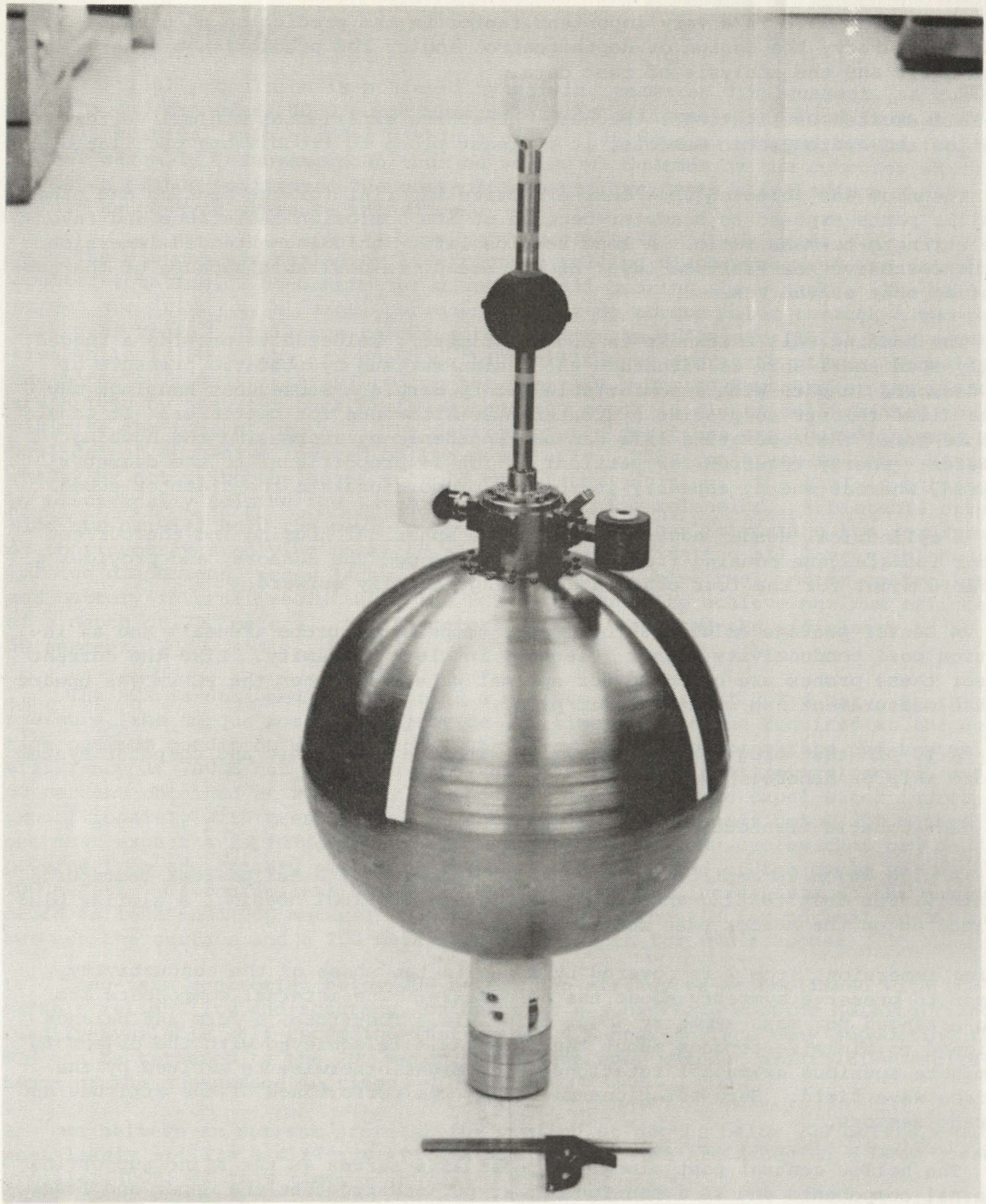

Figure 1. PCM (BETA) before installation of a toroidal swim bladder around lower roller assembly.

for any other. This is a very important factor in the prediction of current-sensing accuracy, the design of depth control logic, the prediction of energy requirements, and the analysis of test data.

3. Self-Excited Oscillations. Because the sphere experiences minimal vortex excitation and hydrodynamic moments, it is least prone to troublesome oscillations.

Titanium was selected as a cost-effective material for the housing and other metallic parts exposed to seawater because of its corrosion resistance and favorable strength-to-mass ratio. A long service life, including extended immersion in the corrosive near-surface layer of the ocean, is desirable because of the substantial cost of the PCM.

The housing wall thickness is 0.64 centimeter, selected to provide a rugged, easily spun shell able to withstand the design maximum hydrostatic pressure of 700 decibars (d bar) with a comfortable safety margin. Subsequent housings may be machined thinner to provide a greater mass allowance for batteries. It should also be noted that operating life can be lengthened by increasing the housing diameter: energy required for vertical motion is proportional to the diameter squared, whereas energy capacity is roughly proportional to the diameter cubed.

A cylindrical header housing between the spherical housing and the current sensor isolates the housing from water leaks through the sensors, and provides a suitable mount for the four objects extending radially outward:

1. A sensor package holding a thermistor temperature probe (Fenwal) and an induction coil conductivity sensor (Plessey) in close proximity. Like the current sensor these probes are oriented for optimal water flow when the PCM moves upward on the measurement leg of its cyclic path.

2. A 10-pin test plug for communication with the electronic and computer system aboard ship or ashore.

3. An acoustic transducer for underwater communication.

4. A plug which is replaced during header checkout by a helium-leak test/purge fitting. For leak testing and purging the main spherical housing, a similar plug is located on the header base bolt circle.

During immersion, item 2 is covered by a cap in the shape of the conductivity sensor to preserve symmetry about the polar axis. The internal components are also arranged for mass symmetry about this axis. Therefore, a form and balance designed to minimize torques about the polar axis is achieved with the object to eliminate spurious azimuthal rotations which might otherwise be excited by the surface wave field. Such rotations might tax the performance of the attitude and current sensors.

The hollow central post along the polar axis serves as the spine supporting internal components and as a tension member pulling together the upper and lower hemispheres. By threading the preload nut under the lower hemisphere, enough tension is developed to compress the equatorial O-rings. Stresses so developed during initial mating are relieved when the sphere compresses under hydrostatic pressure. An equatorial plate pilots the upper and lower hemispheres and supports the battery packs. Both hemispheres, the equatorial plate, and the battery packs may be removed for system testing, leaving the rest of the system intact and accessible.

Buoyancy Control System (BCS)

Vertical propulsion is achieved by varying seawater displacement. A dual-piston pump transfers 4080 cubic centimeters of silicone oil to and from an external, toroidal swim bladder within a protective housing wrapped around the lower roller assembly. Buoyancy can thus be varied 41 Newtons by the computer which commands piston position. The control laws utilize depth signals from a BLH strain gauge-type pressure transducer.

The pistons are sealed by low-friction rolling diaphragms, and are driven by counter-rotating, 2.54-centimeter diameter ball-bearing screw jacks. The ball screws are driven by a large, permanent magnet dc torque motor through a two-pass spur gear train. The large torque motor permits an efficient (36:1) gear reduction while it runs near its no-load, high-efficiency operating point. Normally, the motor only drives the piston on the upstroke. During downstroke, the pistons are driven by seawater back pressure, and the motor is electrically braked to minimize the rate of travel. The desired piston positions are locked in with a pawl-detent mechanism located on the motor axis. This conserves valuable battery energy by not using the motor to hold the piston position. The pawl is actuated by electrically pulsing the latching and unlatching solenoids. A bistable extension spring will hold the pawl in the desired positions, obviating the requirement of continuously supplying power to a solenoid. Considering all losses in the rolling diaphragms, screw jacks, gear train, motor, electronic motor controller, and battery internal resistance, the BCS is designed to achieve maximum efficiency at a depth of 200 meters. At 150 meters we have measured the efficiency to be 50 percent.

The BCS is designed to withstand a maximum pressure of 700 d bar. At this pressure, the torque motor must provide 3.5 times the torque required at the design optimum condition at 200 d bar. As a result, the pumping rate and system efficiency at 700 d bar are much less than the 18 cubic centimeters/second, and 50 percent obtained at 200 d bar. Since the output work to expel water increases proportionately with pressure, while the efficiency decreases below 200 meters one must expect a rapid decline in the number of profiling cycles that can be powered from the battery pack as one pushes the lower end of the cycle below 200 meters. Of course, the number of available cycles increases when the maximum depth is less than 200 meters. We chose to design the PCM for optimal operation between the surface and a 200 meter (or less) depth for two reasons:

1. Long-term monitoring below 200 meters can already be accomplished with comparable reliability and accuracy, by means of a subsurface mooring holding fixed, readily-available self-recording instruments. A near-surface buoy supporting the PCM can be tethered to the 200 meter subsurface buoy without prohibitive excitations of the subsurface mooring.

2. We believe an optimum profiler for cycling at depths below 200 meters would most likely utilize a different propulsion scheme. We are studying a Deep Ocean Profiler (DOP) at this time.

Attitude Reference Package (ARP)

The ARP provides signals to the computer for resolution of body axes current components from the EM probe into north and east components. A conventional compass was not used in order to avoid its nonlinear acceleration sensitivity and transient response. Instead, three small single-axis fluxgate magnetometers (Infinetics) are used for the primary azimuth signals. These are mounted with their orthogonal input axes parallel and perpendicular to the polar axis. Two miniature, lower-power, strain-gauge accelerometers (Entran) are mounted with their axes orthogonal and perpendicular to the polar axis. Essentially, these units provide the tilt signals needed to correct the magnetometers for the vertical component of the earth's magnetic field, and to correct the current sensed for the reduction due to tilt. The accelerometers are powered continuously during current sensing so that they may be continuously filtered to smooth out possible strumming-induced noise.

The computer forms unit vectors defining the geomagnetic field density and the local gravity in body axes. These vectors are combined to form the elements of the matrix which convert body-axes current components to north and east components. Our solid-state compass has the same dynamic acceleration error source as the conventional gimballed compass, however, in our case, the errors are more predictable. We have estimated the attitude and current resolution errors on a numerical simulation of the PCM/mooring excited by the surface wave field. These errors appear to be less than other current sensing errors.

Electronics and Computer System (ECS)

The ECS provides the following:

1. Conditioning, selection, and conversion of analog sensor signals.

2. Data formatting for recording.

3. Timing and sequencing for all operations.

4. Voltage regulation and switching of sensor power.

5. Motor control.

6. Computational capability for filtering.

7. Component resolution and buoyancy control.

8. Interfaces for communication with external equipment.

A CMOS microprocessor forms the core of the digital electronics. CMOS logic is used throughout to minimize energy consumption; and power switching is used for the sensors and analog electronics.

The prototype ECS occupies four 60-socket wire-wrap panels mounted in two cages. Packaged with these are the motor control electronics, tape-recorder electronics boards, and the electronics package furnished with the Marsh-McBirney current sensor. The electronics board servicing the Plessey conductivity sensor is mounted externally from these cages. Later packaging on PC boards will greatly reduce both cost and volume.

Processor:

Five large-scale-integrated circuits form the central processor: an Intersil IM6100 CMOS 12-bit microprocessor; three IM6101 parallel interface elements (PIEs) which gate data between the processor and other system elements; and an IM6402 universal asynchronous receiver/transmitter (UART) which provides serial communication with a teletypewriter and, eventually, an acoustic transducer.

Recorder:

The PCM uses a Sea-Data model 610 serial digital stepping recorder. This device records 800 4-bit characters per inch on standard 0.15-inch cassettes, giving a total capacity of 9.2×10^6 bits for 100-bit records with appropriate synchronizing gaps.

Memory:

The prototype memory contains 4096 12-bit words, all composed of random-access read-write memory (RAM). When programs become finalized, a portion of this is converted to read-only memory (ROM). The RAM card is provided with its own rechargeable nickel-cadmium battery so that data may be retained when the system is shut down or the board is removed. Jumpers on the board allow 1024-word segments to be designated as unwritable unless a special control signal is applied from the test panel, thus simulating ROM and preventing loss of contents in the event of software accidents.

Motor Controller:

The motor controller provides the functions of driving the motor in forward and reverse, dynamic braking, current limiting, and driving the detent solenoids. Diagnostic measurements are also provided to the A/D converter.

Analog Electronics:

Individual preconditioning and scaling amplfiers associated with each input produce outputs that vary from -10 to +10 volts over the chosen sensor range. Where possible, these amplifiers are powered by the same switched regulators as their respective sensors. A single channel is selected via a 24-input analog multiplexer and applied to a precision comparator along with the output of a 12-bit digital-to-analog converter. The comparator output connects to a processor sense input (DACHI) which may be tested by program. Analog-to-digital conversion is accomplished by a successive-approximation routine resident in program memory.

Power Supplies:

Regulators under control of an external on/off signal provide power to the microprocessor logic, the memory card, and the logic portion of the tape recorder. In turn, regulators under control of the processor provide power to the sensors and analog electronics. To conserve energy, power to the following sensors is strobed: magnetometers, thermistor, pressure transducer, conductivity sensor, and accelerometers (amplifiers only).

Lithium Battery Pack

For cost and schedule considerations the lithium battery packs for PCM GAMMA are being made at CSDL from commerically-available lithium primary cells. Higher energy densities can probably be achieved in the future with custom-designed packs. There are three basic lithium-chemistry primary cells on the market; lithium/sulphur dioxide, lithium/thionyl chloride, and lithium/carbon mono-fluoride. Because of their high energy density all cells are potentially dangerous if incorrectly used; and thus, safety of personnel and equipment is a primary consideration.

After a thorough investigation of each cell considering safety, cost, energy density and availability, and after many conversations with lithium cell manufacturers (Power Conversion, Mallory, GTE, Altus, Panasonic, Eagle Picher) and users (WHOI, AMF, SIO, NOSC, OSU, Sonotech), the Eagle Picher lithium mono-fluoride cell was chosen. The resulting PCM GAMMA battery pack is comprised of 71 LCFS-25 cells (25 AH each) divided as follows: +3 V, 1 cell; +7 V and -7 V, 12 cells each; +12 V, 6 cells; +18 V and -18 V, 9 cells each; and +60 V (motor), 22 cells. The total pack statistics are: volume = 590 $in.^3$, weight = 29 lb, energy density = 7.34 $WH/in.^3$ and cost = $3400.

The Eagle Picher system was chosen primarily because of its safety characteristics, even though it clearly was the most expensive. It is a low-pressure (internal pressure at elevated temperatures), hermetically sealed, vented (at 150 $lb/in.^2$) system with possible vented material somewhat less toxic and corrosive than other systems. The additional safety margin was considered to be particularly desirable for initial assemblies of so large a pack. The PCM spherical housing will vent through a relief valve if internal pressure exceeds external pressure by more than 15 $lb/in.^2$. Explosive rupture of the housing is thereby prevented.

An outgassing test was run with the result that no gas was released from the battery. Overheating tests were run for extreme current drain profiles to confirm the acceptability of the Eagle Picher cells. For additional safety the temperature of each cell in the motor pack will be monitored by the PCM computer. The computer also monitors all seven battery voltages to detect cell failure.

Biofouling Protection

The PCM will spend a significant amount of time operating at water depths conducive to biofouling. Fouling must be avoided because of weight and drag disturbances as well as mechanical interference with moving parts. External sensors also require protection. The various components requiring protection are made of titanium, stainless steel, plastic, glass, and rubber.

After considerable study and consultation with experts in this field, it was decided that more than one approach was required to protect various system components. Wherever possible, materials with inherent protective features are used. For example, the swim bladder is made of Goodrich NO-FOUL rubber. The Marsh-McBirney current probe is manufactured with NO-FOUL rubber protecting its spherical element. The possibility of employing metallic copper or copper nickel alloy is being evaluated for use inside the PCM central tube. Large surface areas might

ultimately be protected by a composite material fabrication (outer surfaces of protective material), but the present system must rely upon some type of paint. In general, painted surfaces will require surface preparation and priming before applying top coats of antifouling paint. Many test samples were prepared to evaluate coating systems for their ability to survive salt fog, salt water immersion, and mechanical peeling. These tests then formed the basis for selecting paint systems for further tests in Florida for antifouling properties. The antifouling paints presently on test include copper-base and tri-Butyl-tin paints as well as a Kennecott copper-epoxy formulation. Substrates of titanium, stainless steel, Delrin, Noryl, and G-10 have been used. In addition, the influence of trapped volumes simulating the swim bladder housing are being tested to evaluate paint protection schemes in these areas.

Coating adhesion and compatibility tests were started in January 1979 and continue to date. Salt water immersion and salt fog tests have successfully demonstrated that we can apply paint systems to the required materials. Biofouling test panels deployed in Florida (NOVA Univ.) have been there since early April 1979. Inspection of these tests will be made before finalizing the choice of paint systems for the PCM.

Method of Operation

The sampling, processing, recording and buoyancy control functions of the PCM are under program control, and may therefore be conducted in many ways. The specific method used in the upcoming PCM GAMMA mission seems appropriate to a variety of scientific purposes and is described herein. This description will hopefully enhance the reader's appreciation for the capabilities of the PCM and the credibility of our performance goals. Let us describe the method of operation by considering the various phases of a typical profiling cycle, starting at the bottom stop on the mooring line. The PCM has been resting at 150 meters depth awaiting the next measurement cycle, while enjoying the benefits of minimum mechanical agitation, minimum biological fouling, and minimum temperature, all of which conditions contribute to minimum mechanical and electronic failure rates.

Ascent mode is initiated by the PCM upon arrival of ascent start time, which occurs every 2 hours. Since we wish to record bottom conditions, the PCM first measures four one-minute averages of the current, temperature, and conductivity. Every second the current sensor, magnetometers, accelerometers, thermistor, and conductivity transducer signals are sampled, converted, and accumulated to obtain the desired temperature, conductivity, and north and east current component averages. The pistons must next be driven up to achieve an ascent speed of approximately 9 centimeters/second. However, the PCM is not smart enough at this time to predict the piston position required to achieve the desired ascent speed because of uncertainties in seawater density, friction, and drag coefficients, etc. However, equations relating the steady-state ascent speed as a function of current and net buoyancy indicate that the ascent speed will stabilize close to the target speed if the motor is shutdown when the PCM has risen 30 centimeters. The motor is driven accordingly, and after shutdown, the program monitors ascent speed. Whenever the indicated ascent speed is outside the established deadband (±3 cm/s), a Δ volume to accomplish $\dot{Z}$ = 9 cm/s is commanded from a simple control law

$$\Delta \text{ volume} = K\left[9\sqrt{9^2 + V^2} - \dot{Z}\sqrt{\dot{Z}^2 + V^2}\right]$$

where V = magnitude of current.

During ascent the program records parameter averages within 6-meter thick zones. Upon entering any zone, the program refers to memory for the pressure depth at the top of the zone, the ascent speed deadband limits, and the parameter sampling period. Entering Zone 1 after liftoff, the top of the zone is at 144 d bar, the deadband limits are 6 and 12 centimeters/second, and the sampling period is 1 second. Then commences the parameter averaging described previously and the ascent speed monitoring, which is accomplished by watching the pressure every 30 seconds.

The above procedure is continued until the pressure reaches 154 d bar, when the parameter averages are recorded and the second zone is started. Each succeeding zone is managed in the same manner until the top stop is encountered at 14 meters. The tape recorder has sufficient capacity to record more than 87,600 sets of zone parameters, or 20 zones/cycle at 1/2 cycle/hour for 1 year.

In addition to the above data, during the ascent phase, averages of 1-second samples of pressure and conductivity are recorded over 24 noncontiguous narrow temperature bands in order to reconstruct 24 isotherms and isopycnics.

Ascent velocity biases the relative flow to approach the current probe from the top hemisphere of its field of view. This bias is expected to enhance probe response by moving its turbulent wake downstream from its electrodes, and by positively keeping the probe out of the wake of the spherical housing. Axial motion of the mooring line excited by the near-surface buoy is uncoupled from the PCM. The wave field pressure gradients, which force oscillatory water particle motion, also force oscillatory PCM motion along the cable axis. As a result of the PCM's axial freedom, its current sensor sees only a small oscillatory flow component along the polar axis, thereby minimizing the need for accurate vertical cosine response.

Note that profiling while ascending provides space-time averages. It also conserves a great deal of energy. The PCM can be stopped to measure at fixed levels. However, the prototype is not equipped to extract energy from the sea pressure while retracting the pistons. Yet energy will have to be expended again in pushing out the pistons to resume the ascent. Thus, while the prototype PCM might store enough energy to profile continuously at a rate of 0.5 cycles/hour for 1 year, the same energy might be expended in profiling discontinuously (stopping 10 times on each ascent) at the same cycle rate for only 2 months.

The descent mode is commenced upon completion of the ascent mode. A dive is performed in a manner similar to that described for liftoff, resulting in the achievement of a descent speed calculated to arrive at the bottom well in advance of the next ascent start time. The descent mode is similar to the ascent mode, except that oceanographic parameter sensing is suspended during descent. Upon arrival at the bottom, a rest mode keeps watch, preventing inadvertent ascent due to changing conditions, while awaiting the next ascent start time.

PCM GAMMA will test the validity of sampling "on the fly" by stopping at mid-depth during the descent mode to record data at a fixed depth for comparison with ascent data. A hover mode will be commanded at 78 meters. A buoyancy control law designed to hold the PCM between 80 and 84 meters has been programmed into the ECS. During a prescribed time interval after depth stabilization the PCM will record 30 1-minute averages of current components, temperature, and conductivity. Upon completion of this mode the PCM will resume its descent to the bottom rest condition. An all-digital simulation is used to verify buoyancy control laws before they are programmed into the PCM computer. However, the complete software

package requires a sophisticated laboratory checkout. An analog simulator has been constructed to compute the dynamic relationship between piston position (input) and PCM vertical position or pressure (output), allowing for variations in parameters such as mooring-line angle, rolling friction coefficient, and ambient currents. It therefore simulates the real-world environment, providing the PCM with sensor stimuli properly related to PCM action. By running the PCM/Simulator system for many initial conditions and environment parameters we attempt to uncover any flukes in the software.

Performance Goals

Table 1 provides the operating range, digital resolution (least significant bit), and the smallest errors expected to be achieveable for each of the parameters processed by the prototype PCM.

Table 1. Performance goals.

Parameter	Units	Range	LSB	Absolute Error (Short Term)	In-Situ Drift/Year
Current	$cm\text{-}s^{-1}$	-400 to 400	0.20	>1.3, <3% of reading	2
Temperature	°C	-5 to 35	0.0040 @ -5° 0.033 @ 35°	0.01	0.005
Conductivity	mmho-cm^{-1}	28 to 60	0.0078	0.01	-----
Pressure	d bar	8 to 213	0.050	0.2	0.2
Specific Force	gravity acceleration	-5 to 5 (x, y axes)	0.0033	0.025	0.003
Magnetic Density	Earth's field at CSDL	-1.2 to 1.2	0.00059	0.01	0.0006
Piston Displ. Vol.	cm^3	0 to 4360	1.06	1	0
Recorded Time	s	0 to 6.87 $\times 10^8$	0.01	----	30

The operating life of the prototype has been estimated for two "typical" conditions assuming the use of 20.5 kilograms of lithium batteries.

1. Mid-Ocean, 35 centimeters/second maximum current, profiles from 0 to 200-meters depth: 3500 cycles, or 1 cycle every 2.4 hours for 350 days.

2. Continental Shelf, 100 centimeters/second maximum current, profiles from 0 to 200-meter depth: 1600 cycles, or 1 cycle every 1.5 hours for 100 days.

THE NAVOCEANO TOWED CTD

Ortwin H. von Zweck
Physical Oceanography Branch
U.S. Naval Oceanographic Office
NSTL Station, Mississippi 39522

ABSTRACT

A system capable of measuring conductivity, temperature and pressure while under tow near the surface of the ocean is being developed for the U.S. Naval Oceanographic Office. The tow body is based on a remotely controlled active depressor and contains the CTD electronics and pressure, conductivity and fast and slow response temperature sensors. Up to two additional sets of pressure, conductivity and temperature sensor platforms can be fastened to the tow wire within 10 m of the tow body to provide additional measurements. The system is expected to become operational late 1980.

INTRODUCTION

There exists considerable interest in the horizontal variability of the density field in the upper ocean on scales of 100 to 1000 m. In order to obtain observations at these scales, the Naval Oceanographic Office is presently acquiring a CTD system capable of sampling the upper ocean to a depth of 250 m while under tow from a ship at speeds of up to 10 knots. To minimize instrument development, and to insure the reliability of an operational system, the unit was designed to incorporate already existing components. The tow body and tow control electronics have recently been completed and tested in the David Taylor Naval Ship Research and Development Center (DTNSRDC) and tow tank. Initial sea trials of the tow body are to be completed by May 1980. The first field tests of the complete system are expected to take place during late summer 1980.

SYSTEM DESCRIPTION

The towed CTD system consists of a tow body with remote control electronics, cable and winch (Fig. 1). The sensor package consists of a CTD mounted in the body and two sets of remote sensors which can be clamped onto the tow wire. The tow wire serves as signal wire and links the CTD with the shipboard CTD data terminal and recording equipment.

The design of the NAVOCEANO tow body is based on a depressor (Fig. 2) developed by DTNSRDC for mine sweeping from helicopters. The configuration of the tow body is essentially that of an airplane with two cambered wings providing the downward force and the vertical and horizontal stabilizers maintaining flight stability and control. A gravitational pendulum-activated rudder built into the vertical stabilizer maintains lateral and roll stability. Limited adjustments in tow depth can be made with the elevator in the horizontal stabilizer which is controlled by an open or closed loop servomechanism based on a pressure transducer built into the tow body. The mean tow depth is controlled by the length of tow cable paid out. Previously conducted field tests of the mine sweeping tow body indicate that the system is capable of maintaining the tow body within 30 cm of a given pressure in the closed loop mode. Vertical cycling (without tow length adjustments) with amplitudes up to 8 m at periods longer than 5 seconds can be obtained in the closed loop mode of operation. The open loop mode can be used as manual override of the fine depth control and may be used for towing along isotherms.

The system is designed to tow at speeds of up to 10 knots. Tow wire tension at this speed is estimated at 4500 lbs. at a 4:1 wire scope at a 200 m tow depth. The tension coefficient (ratio of tension to dynamic pressure) ranges between .6 and 1.2. The tow/sea cable is a double armored 9 conductor cable, with the last 135 m of the cable being faired. Cable length presently limits the maximum operating depth to 250 m.

A Neil Brown Instrument Systems, Inc., CTD is housed within the nose cone of the tow body with the conductivity cell, PT and fast response thermistor sensors extending to the side of the body upstream of the tow cable and wings. The sensors are located in the undisturbed flow, outside the boundary layer formed around the body during tow and ahead of the flow disturbance generated by the wings and the tow cable.

Two additional sets of remote sensors, each consisting of a conductivity cell and fast and slow response temperature sensors, can be fastened to the tow wire above the tow body at distances up to 4 and 10 m. Cables trailing behind the tow cable connect the remote sensor platforms to the main tow body.

DATA HANDLING

The CTD data will be recorded digitally on a shipboard data logger directly from the NBIS CTD data terminal for later data processing on the main computer at NSTL (Fig. 3). A dedicated PDP 11/03 DECLAB microprocessor will be used for real time data monitoring. In addition the data stream will be sampled during data collection and basic first look data analyses will be conducted during tows.

The fast and slow temperatures will be recorded separately. The 10 variables will be sampled and recorded every 50 ms. The separation between samples on a horizontal flight at 10 knots is about 25 cm.

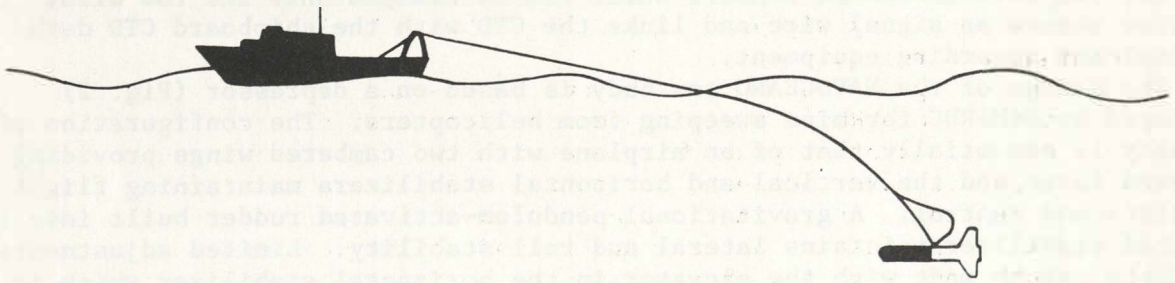

FIGURE 1. TOWED CTD SYSTEM

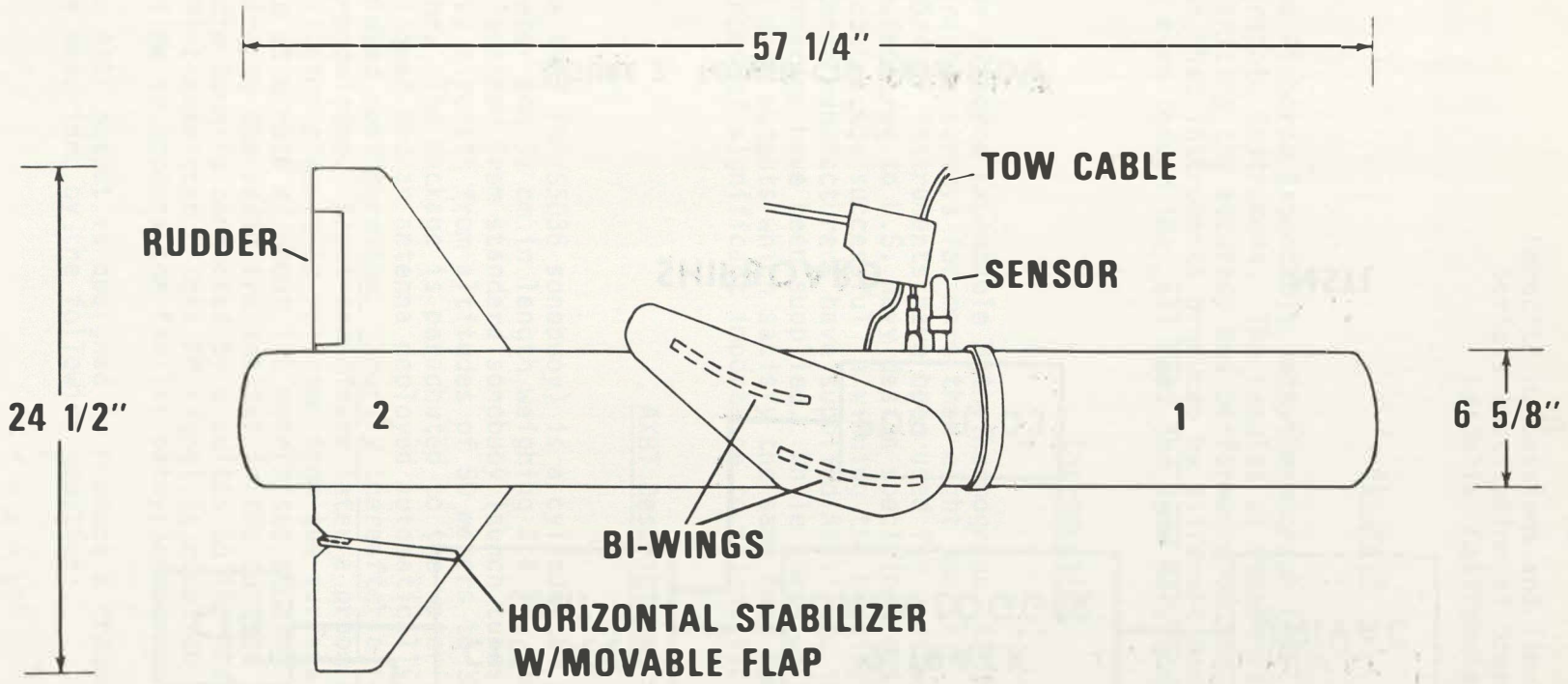

CRITICAL DIMENSIONS

Wing Span	51"
Air Weight	96 LBS
Water Weight	32.5 LBS

BODY SECTIONS

1 - Neil Brown CTD

2 - Flight Control Electronics

FIGURE 2. PHYSICAL CHARACTERISTICS OF THE NAVOCEANO CTD TOW BODY

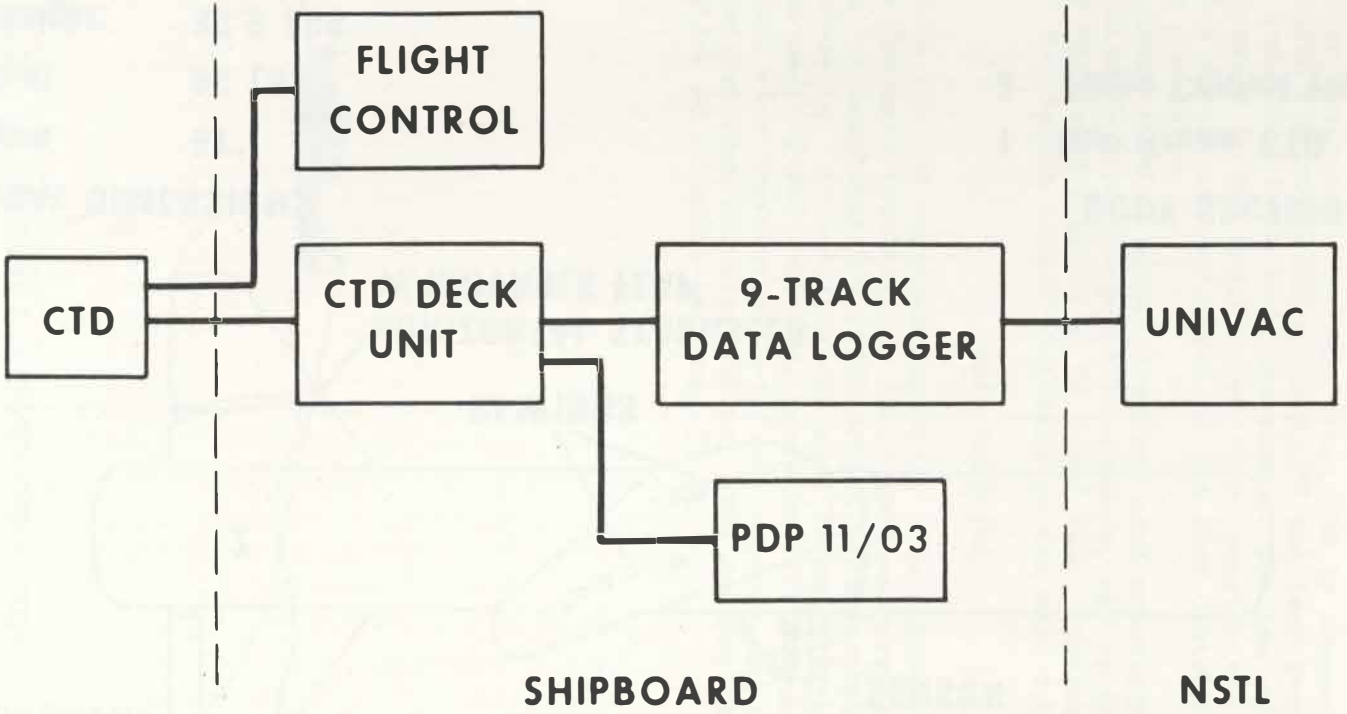

FIGURE 3. TOWED CTD DATA FLOW

THE AIRBORNE EXPENDABLE BATHYTHERMOGRAPH FOR OCEANOGRAPHIC MEASUREMENTS

Meredith H. Sessions and Tim P. Barnett
Scripps Institution of Oceanography
La Jolla, California

Abstract

The Airborne Expendable Bathythermograph (AXBT) system is described as an oceanographic instrument. The results of recent calibrations and field tests characterizing the accuracy and performance of the latest models are reported. It is shown that instruments produced by different manufacturers can produce varying results even though they all meet the same Navy specifications.

Introduction

The Airborne Expendable Bathythermograph (AXBT) system has been in use for oceanographic surveys for more than eight years[1,2]. During this period an increasing number of instruments have been used for various scientific programs. AXBT's are manufactured to U.S. Navy design specifications and procured in large batches from a contractor successful in winning the bidding contest. Over the past eight years three manufacturers have supplied AXBT's to the U.S. Navy from which scientific programs have been supplied. While these units are similar in design and produce data outputs which satisfy the same Navy specifications, they all exhibit differences of significant importance to scientific users.

AXBT Description

The AXBT (AN/SSQ36 sonobuoy) is a cylindrical package approximately 12.4 cm in diameter and 91 cm in length weighing 6.4 Kg, shown in Figure 1. This package can be launched from standard sonobuoy launch tubes found in several models of U.S. Navy aircraft from altitudes of 50 meters to 3050 meters and up to speeds of 450 Km/hr. The package is parachuted to the water's surface where the parachute is jettisoned and an antenna deployed automatically. Figure 2 shows the AXBT in the deployed configuration. Shortly thereafter a radio frequency carrier begins to be transmitted. About one minute later a probe containing a thermistor sensor and oscillator circuit is released from the surface floating package. This probe descends at a rate of about 1.5 meters/sec sending an audio signal via an insulated wire to the radio transmitter in the surface buoy. At the moment of release this audio tone is connected by a switch to the modulator of a frequency modulation (FM) transmitter. This FM signal is received by the aircraft and recorded versus time to produce the familar bathythermograph trace.

The AXBT output is designed to produce a frequency proportional to the temperature described by the following equation:

$$f = a + bT \qquad (1)$$

where f = audio frequency in Hertz (Hz)

T = temperature in degrees Celsius, and

a and b are constants.

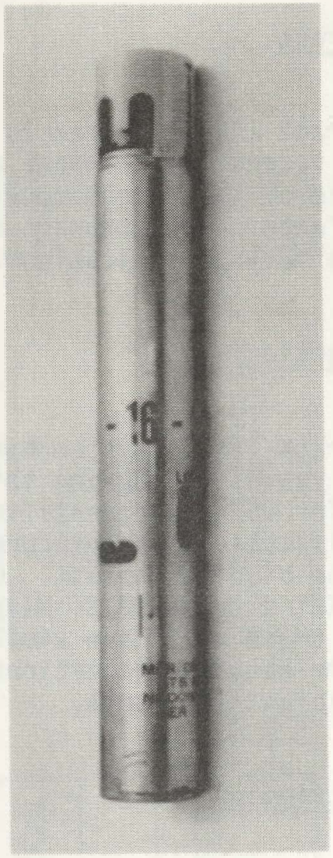

Figure 1 Hermes AXBT prior to launch

The standard Navy specifications call for a = 1440 Hz and b = 36, defining a straight line equation. The AXBT output must follow this function over the range of -2° to 35° C to within ±20 Hz, which is equivalent to ±0.56° C. More details for AXBT's can be found in handbooks on each type of instrument[3,4,5]. Errors of this order of magnitude have been reported by Brisco, Johannessen and Vincenzi[6] and led to the calibration work by the authors.

Calibrations

In 1974 a group of about 300 AXBT's manufactured by Motorola were calibrated for the NORPAX pole experiment[7]. The results of this showed that a linear relationship could be determined for the AXBT's that were somewhat different from the Navy standard to give accuracies of the order of ±0.17° C over a range of 7° to 17° C. Unfortunately, this required the calibration of each individual unit and the determination of a separate calibration coefficient for each unit.

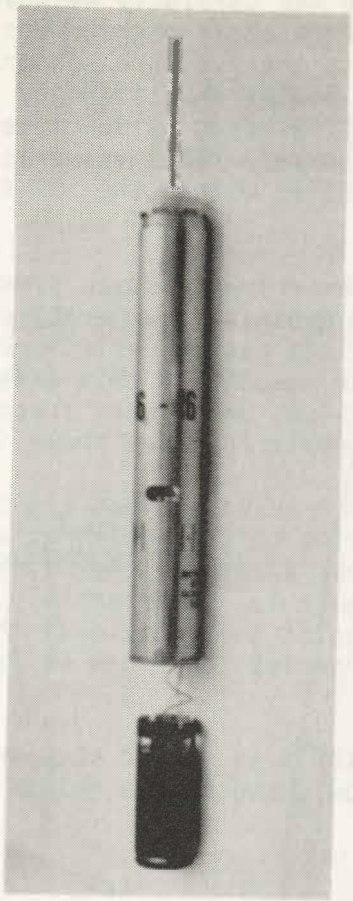

Figure 2 Hermes AXBT with temperature probe deployed

Beginning in 1974 a new design AXBT manufactured by Magnavox became available. This unit differed substantially from previous Motorola units in the area of thermistor, oscillator and probe design. Calibration of 57 units revealed that the entire population could be characterized by the following relationship:

$$T = a + bf + cf^2 \qquad (2)$$

where f = output frequency in Hertz (Hz)
T = temperature in degrees Celsius and
a = -45.11, b = +0.03381 and c = -1.676×10^{-6}

The maximum rms error over a range of 0° to 25° C was 0.16° C. Additionally, the temperature and voltage sensitivity of the oscillator circuit was greatly improved over the previous units resulting in a much better instrument for oceanographic purposes.

A question which remained unanswered regarding the accuracy of the overall system was the verification of probe descent rates. Some question regarding this quantity remained from differences noted in actual ocean tests.[8] To resolve this question thirteen Magnavox AXBT's were disassembled and fitted with small pressure sensors. Suitable electronics replaced the original temperature oscillator board

and units were reassembled. Each was carefully weighed so that it was within one gram of its original weight. The external package was unchanged save for a small (∿2mm) hole in the nose leading to the pressure sensor. These special AXBT's were deployed on 10 November 1976 off Southern California. Ten good records resulted yielding a mean descent rate of 1.59 m/sec to 300 meters depth. The standard deviation for these data was 0.043 m/sec. This value is 4.6% greater than the nominal value of 1.52 m/sec but still within the ±5% specification for descent rate.

During the above described experiment, seven previously calibrated AXBT's were deployed while simultaneous Salinity, Temperature and Depth (STD) profiles and Nansen Bottle casts taken. This was to verify previous laboratory tests and calibrations. Unfortunately, the results of this experiment show large deviations in AXBT temperature versus STD values which were supported at a number of points by Nansen Bottle reversing thermometer data as shown in Figure 3.

Research into this difference revealed that the manufacturer had changed thermistors, the newer types having thicker coatings which greatly modified the thermal time constant of the probe assembly. New time constant measurements yielded the results shown in Figure 4. Unfortunately, fairly large scatter in the data exists due to uneven coating of the individual thermistors. Since the probes contain pairs of thermistors in series there can be large differences in each thermistor in the pair.

The time response of the AXBT's to a unit step input (Figure 4), plus the physics of the problem (see below), suggests a relatively simple transfer function of the form:

$$h(t) = \sum_{n=1}^{N=3} A_n e^{-t/T_n} \qquad (3)$$

The parameters of this function were successively determined by the methods described by D'Azzo and Houpis [1966].[9] The appropriate numerical values were found to be:

n	A_n	T_n (sec)
1	0.851	3
2	0.038	43
3	0.111	184

The resulting empirically estimated transfer function is shown in Figure 4.

The representation of the transfer function as three exponentials was suggested physically from the causes of the thermal lag. Under the assumption that the thermistor coating and probe all touch at a common point, then one would expect the following situation:

1) The coupling between the plastic coating covering the thermistor and the thermistor itself has a time constant which corresponds to $T_1 \approx 3$ seconds.

2) The connection between the plastic coating and the water will affect the

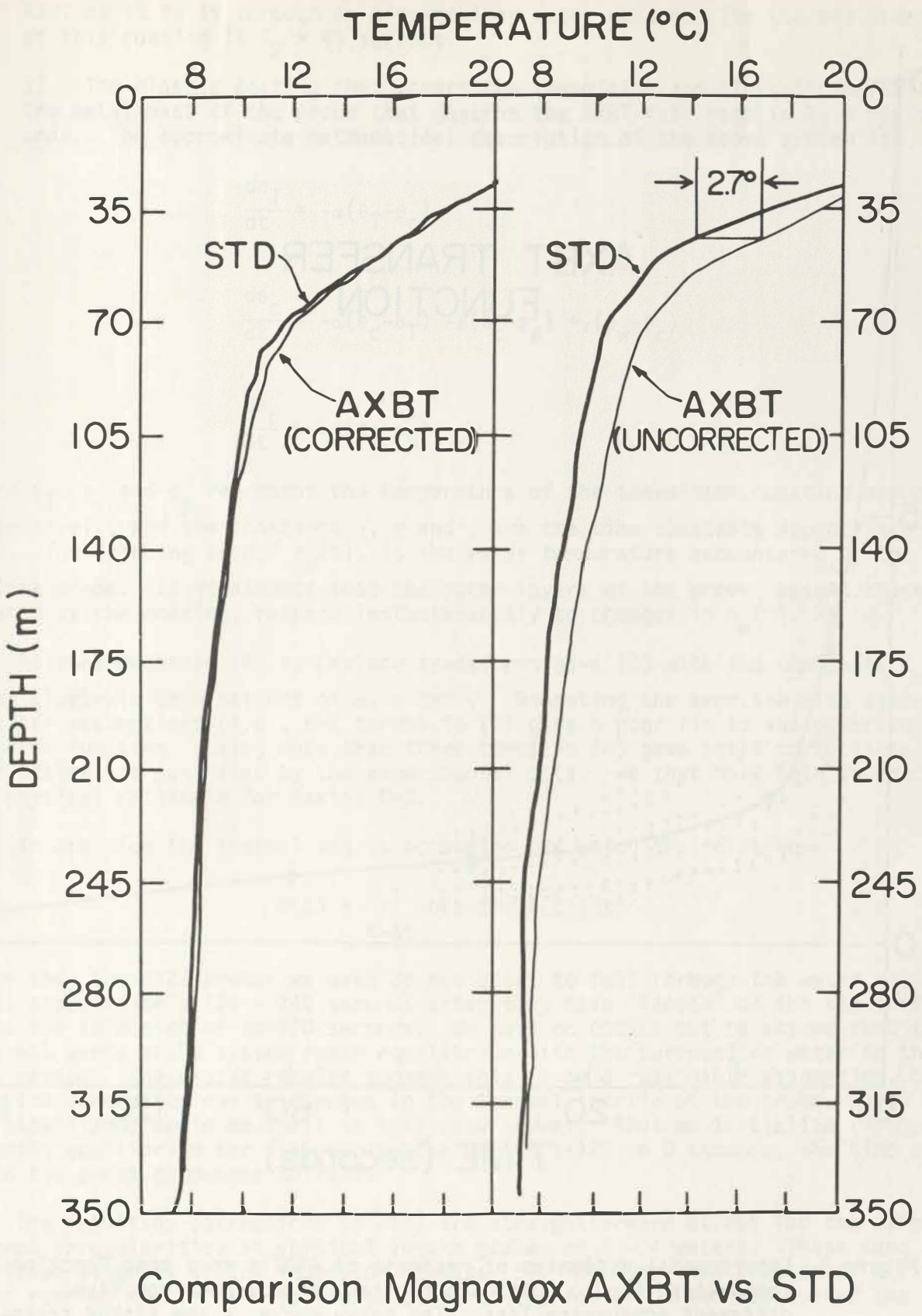

Figure 3 AXBT traces versus simultaneous STD casts

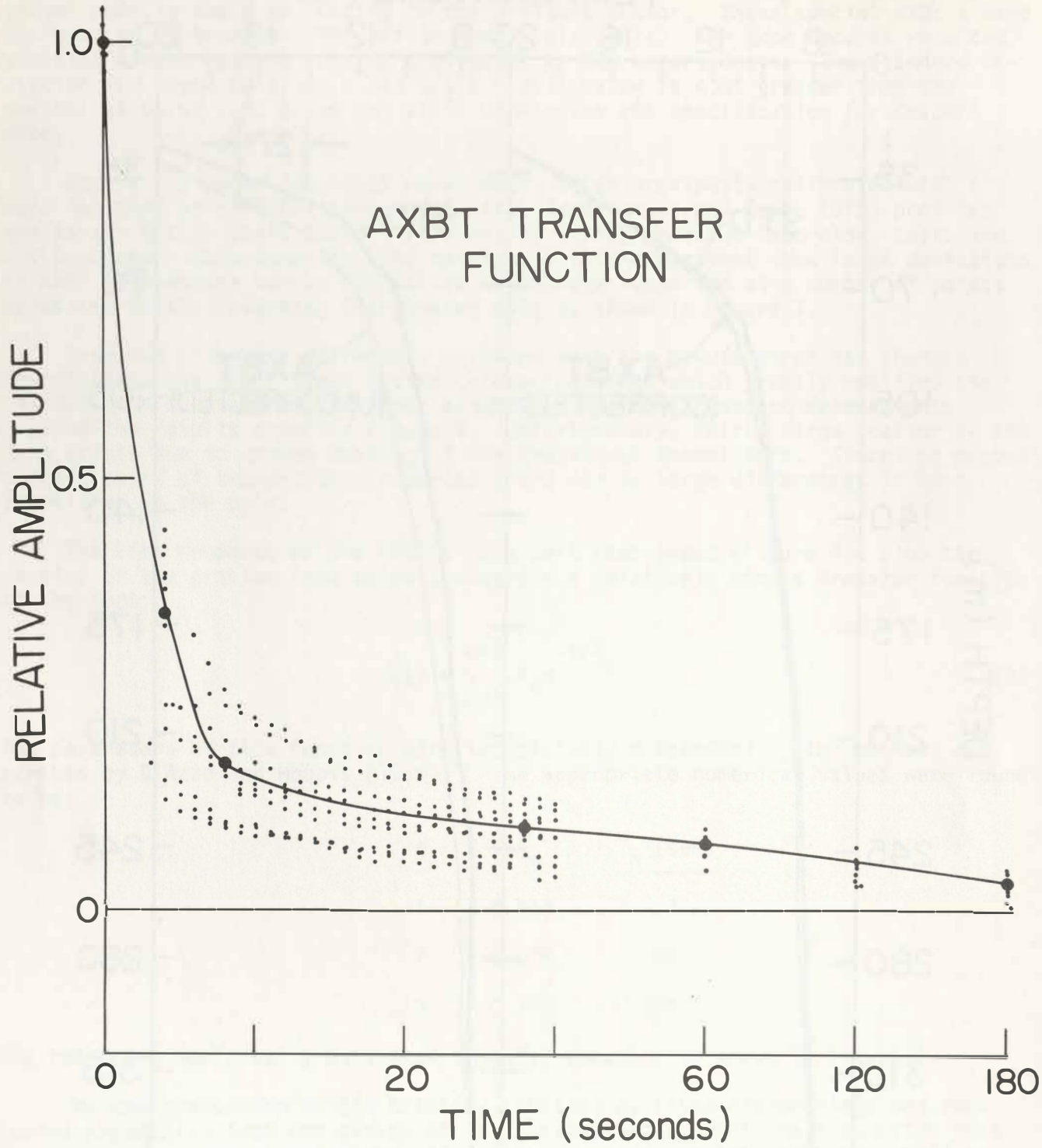

Figure 4 Experimental estimates of response of AXBT's to a step function temperature input. Data are for ten instruments from five different production lots. The heavy curve is the fitted transfer functions, equation (3).

AXBT as it falls through an ever-cooling water column. The thermal inertia of this coating is T_2 = 43 seconds.

3) The plastic coating that covers the thermistor and links it thermally to the metal mass of the probe that governs the AXBT fall rate is T_3 = 184 seconds. The approximate mathematical description of the above system is:

$$\frac{d\theta_T}{dt} = -\alpha(\theta_T-\theta_c)$$

$$\frac{d\theta_c}{dt} = -\alpha(\theta_c-\theta_T) -\beta(\theta_c-\theta_p) +\gamma(\theta_w-\theta_c) \qquad (4)$$

$$\frac{d\theta_p}{dt} = -\beta(\theta_c-\theta_p)$$

where θ_T, θ_c and θ_p represent the temperature of the thermistor, coating and probe, respectively, and the constants α, β and γ are the time constants appropriate to each. The "forcing term," $\theta_w(t)$, is the water temperature encountered by the falling probe. It is assumed that the outer layers of the probe, except those covered by the coating, respond instantaneously to changes in $\theta_w(t)$.

Solving equation (4) by Laplace transforms gave (3) with the constants A_n being algebraic combinations of α, β and γ. Repeating the exercise with different physical assumptions (i.e., n=2 terms) in (3) gave a poor fit to the observed transfer function. Using more than three terms in (3) gave small corrections at time scales not justified by the experimental data. We thus have both numerical and physical rationale for taking N=3.

In practice the thermal lag is accounted for using the relation:

$$\theta(t) = \int_{t-\Delta t}^{t} h(t-t')\,\theta(t')dt' \qquad (5)$$

Tests show the AXBT probes we used do not start to fall through the water column until approximately 120 - 240 seconds after they have "landed" on the sea-surface, hence the selection of Δt=120 seconds. We have no choice but to assume that the external parts probe system reach equilibrium with the surrounding water in that time period. The cruise results suggest this to be a reasonable assumption, but then the correction due to changes in the thermal inertia of the probe, which has not stabilized, would be small in this case anyway. Thus we initialize (5) by assuming equilibrium for $\theta(t)$ during the period t=120 to 0 seconds, the time at which the probe commences to fall.

The resulting corrections to $\theta(t)$ are straightforward except for the effect of thermal irregularities at vertical length scales of 1 - 4 meters. These tend to be amplified slightly in the inversion process (5). However, application of a five-point running mean filter to the solution of (5) for $t \geq 3$ seconds solved the problem.

Examples of a corrected and uncorrected AXBT trace versus a simultaneous STD trace are shown in Figure 3. The error has been reduced by a factor of 10 so that the uncertainty between AXBT/STD is now comparable with:

1) the uncertainty in the temperature/frequency calibration between different instruments, or

2) the inter- and intra-lot scatter amongst the units used in the time constant determination (Figure 4), or

3) the scatter in the observed times between probe release and the start of modulation (= transmission of temperature data), or

4) some combination of 1) to 3).

All items considered, the Magnavox AXBT accuracy is of order 0.3 - 0.4° C with the largest errors occurring in the regions of highest vertical temperature gradient.

A third manufacturer, Hermes Electronics, produced the most recent group of AXBT's for the U.S. Navy. Again the design is outwardly similar but contains several differences. The thermistors and oscillator are different from previous designs and in this case utilizing glass head coated thermistors with a time constant of 300 to 500 milliseconds. Our tests have verified these figures which remove the serious time constant problem noted in the later Magnavox units. It was necessary to calibrate a quantity of these units to verify the predicted frequency to temperature relationship. A sample of 100 AXBT's from lots 18 and 20 were calibrated at 8° and 25° C. Several AXBT's from this sample were also calibrated six points over the range of 0° to 32° C. Analysis of these results showed that a good linear relationship over the range of 7° to 26° C could be expressed by the following equation:

$$f = a + bT \qquad (6)$$

where f = frequency in Hertz
T = temperature in degrees Celsius
and a = 1425, and b = 37.18

The mean, standard deviation, and range for the calibration points of 8.0° C and 25° C, respectively, are:

	8° C	25°C
MEAN FREQUENCY	1722.5 Hz	2354.7 Hz
STANDARD DEVIATION	1.68 Hz	1.44 Hz
RANGE	+5.4, -4.4 Hz	+5.3, -3.2 Hz

These calibrations results are summarized in Figure 5 along with a plot of the theoretical probe error curve from the Navy straight line equation for all Hermes AXBT's.

A second group of 36 Hermes AXBT's were calibrated at 8° and 25° C during October of 1979. These units were from lots 13 and 31. The results of these calibrations are:

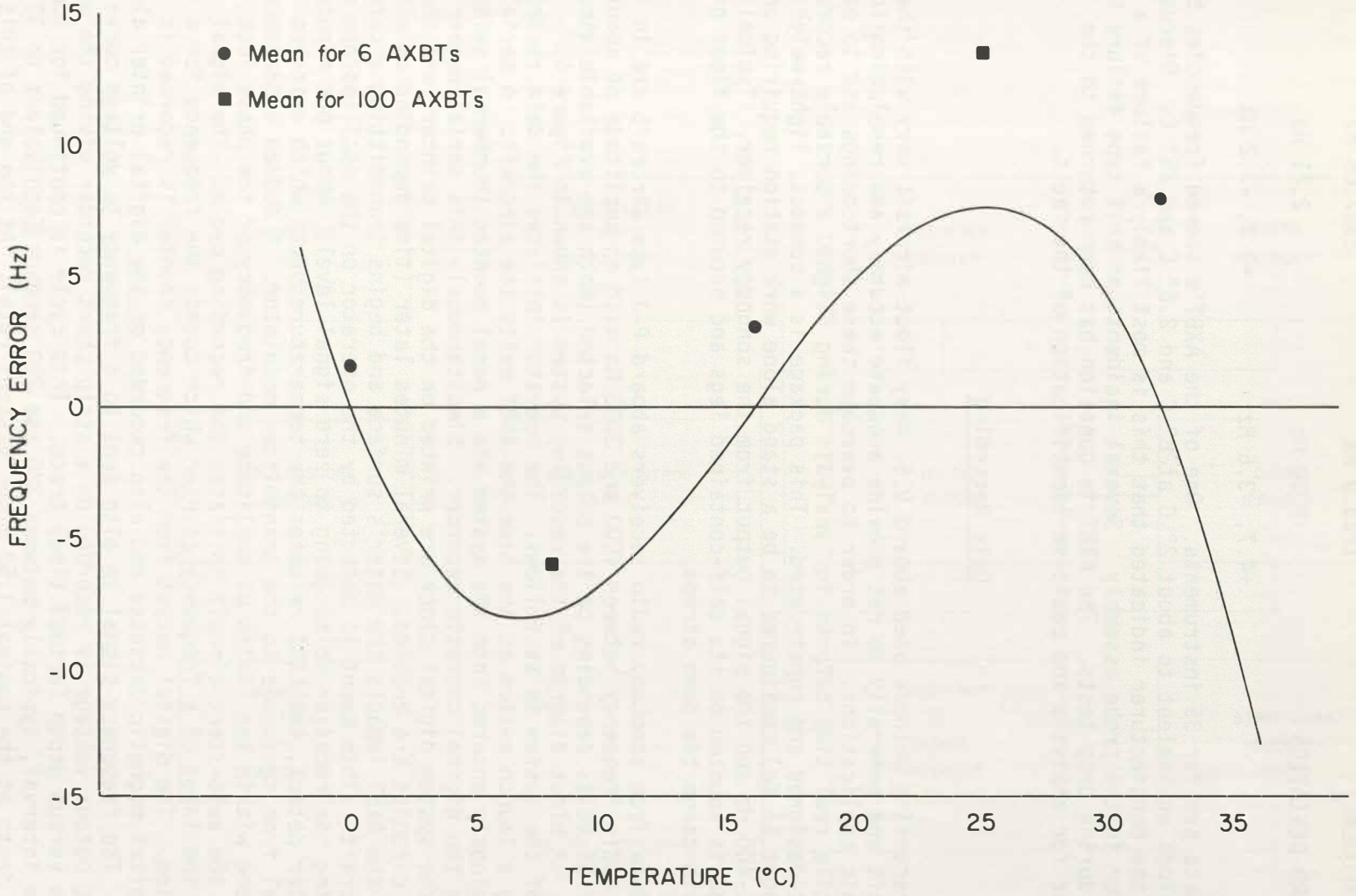

Figure 5 Calibration Data of Hermes AXBTs

	8°C	25°C
MEAN FREQUENCY	1723.9 Hz	2357.05 Hz
STANDARD DEVIATION	2.30 Hz	2.21 Hz
RANGE	+4.7, -3.6 Hz	+5.2, -3.2 Hz

The above data are for 35 instruments. One of the AXBT's showed frequencies below the mean values equivalent to about 2° C at 8° C and 2.6° C and 25° C. Discussions with the manufacturer indicated that this is most likely a failure of a trim potentiometer in the probe assembly. Several incidents of this type failure have been noted during drop tests. The AXBT in question has been returned to the manufacturer for analysis and positive identification of the fault.

Data Recording

Data recording methods used aboard U.S. Navy fleet aircraft vary with the type aircraft and generally do not provide adequate accuracy and resolution for oceanographic applications. In order to overcome these shortcomings and to provide versatile real time outputs for analysis during flight, a portable recording package was designed and constructed. This package is a compact, light-weight package (about 54 Kg) configured to be a stand alone work station requiring only 115 VAC, 50-400 Hz and the signal output from the sonobuoy receiver. Typically, this package is mounted on its self-contained legs and secured to the floor of the aircraft with cargo tie down straps.

AXBT data from sonobuoy radio receivers aboard P-3 type aircraft are in the form of an audio frequency between 1000 and 3000 Hz with an amplitude of about either 6 or 36 volts depending on the output selected (both are available simultaneously). A block diagram of the recording system is shown in Figure 6. Operation of the system is as follows. The operator initiates the data recording by pressing a launch switch at the time the AXBT exits the aircraft. A serial number previously entered into the system via a panel mounted thumbwheel switch is recorded on the digital cassette recorder. Simultaneously this serial number and time from the system digital clock are printed on the digital printer, and the auto-start circuits are enabled. Several minutes later (time depending on altitude of launch) the AXBT impacts the water's surface and begins transmitting a carrier to the aircraft. This event is detected by the operator on the oscilloscope monitor by noting the receiver noise going to zero signal level. About one minute after carrier detect, the AXBT releases the temperature probe which switches the audio signal from the probe to the transmitter modulator. A sudden appearance of an audio tone within the limits of amplitude and frequency of the phase lock loop filters in the auto-start circuit initiates the recording cycle. The signal is applied to the input of a frequency counter which counts the frequency for a one-second period. The digital output from the frequency counter is recorded in serial form on digital magnetic cassette and also recorded on the digital printer along with time. The frequency signal is also sent to a frequency to voltage converter. This analog output voltage is recorded on a strip chart recorder giving the usual temperature versus depth (actual time) trace. This cycle is continued for some preset time interval, typically between 220 and 280 seconds (equivalent to 335 to 425 meters depth at the nominal 1.52 m/sec descent rate). At the end of this time interval all systems are reset and ready for the next AXBT launch.

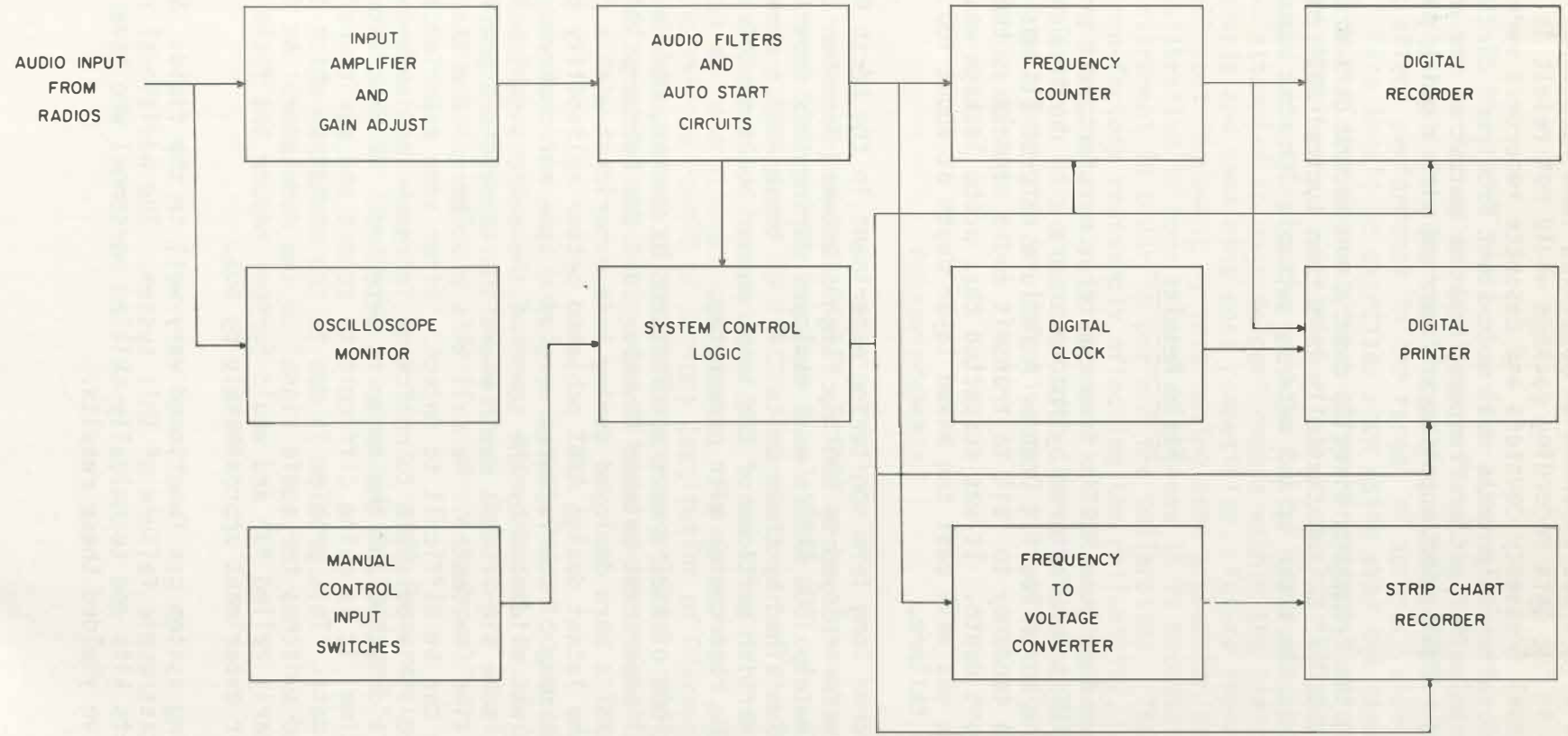

Figure 6 Block Diagram of Scripps AXBT Recording System

Considerable effort was expended in providing some redundancy in the system so that failures in the data recording package would not result in total failure. Toward that end dual frequency counters and cassette recorders were installed. Also, front panel switch selectable dual auto-start front end circuits were included. Ability to switch either frequency counter output to the digital printer was also provided. Dual power supplies are carried with a quick plug changeover capability.

By measuring the frequency directly over a one-second period least count error is ±1 Hz or about 0.027° C, substantially less than typical AXBT calibration errors. Depth resolution is the order of 1.5 meters, suitable for most oceanographic applications.

Field Results

Since 1974 we have used AXBT's from the three manufacturers previously noted. A group of 290 AXBT's manufactured by Motorola were used during January and February of 1974 in the North Pacific Ocean. A failure rate of 11% was sustained. The units exhibited a tendancy to fail to transmit audio signals as the probe descended to some significant depth. It was suspected that probe leakage was the cause of this. If a probe got well past the mixed layer depth at about 100 meters, it was not considered a failure.

During a second long term monitoring experiment in the North Pacific Ocean, Magnavox AXBT's were deployed on monthly flights between November 1974 and April 1977.[10] Approximately 1300 AXBT's were deployed during this experiment. A failure rate of 10% was sustained by these units. All of these AXBT's were of the rotorchute type, the earlier portions of the total number built on this contract. Later units replaced the rotorchutes with parachutes.

The third group of AXBT's were manufactured by Hermes, Ltd. and were used in a transequatorial experiment between November 1977 and February 1978.[11,12] A total number of 1620 AXBT's were deployed during this experiment with a failure rate of 4.7%. Clearly the latest design AXBT achieved better reliability than past AXBT's. It was noted that many of the failures were of a type not observed in previous experiments. This was evidenced by the start of the audio signal being delayed until the probe was at some significant depth where the temperature profile would appear to be offset in time (or depth). We call this problem a "late start" and depending on its magnitude can be difficult to detect. After some experience of flying at a constant altitude it is possible to notice an increase in time between when the carrier signal is detected and the audio is detected. If this late start is only a few seconds in time, it is quite difficult to detect and can therefore result in very misleading data. This problem is due to the mechanism which detects release of the probe, and switches the audio signal to the modulator. An improvement in this area is clearly called for and would further reduce the field failures observed during our experiment approximately by 50%.

The recording system has functioned very well in the field. No data have ever been lost to catastrophic failure of this system. The additional redundancy provided, spare parts kits and technically skilled personnel who have always operated the equipment have yielded these results.

Conclusions

The standard U.S. Navy AXBT can be used for oceanographic purposes if appropriate calibrations are performed and applied to field results. Even though all units are produced to meet the same specifications, subtle differences between different designs affect performance in the ranges of accuracy expected for oceanographic purposes. Care should be exercised when using even the same manufacturer's units from lots produced at different times as running production changes can have serious effects on performance. Significant use of the AXBT by the oceanographic community has focused attention on the need for better instrument performance and manufacturers have attempted to upgrade performance within the limits of maintaining the Navy standards and remaining cost competitive. Future improvements can be attained at a small cost increment by instituting some production calibration. Post-production calibration is more expensive because it is necessary to partially disassemble the instrument in order to perform the calibration. There is always some doubt about non-factory reassembly affecting the reliability, although we have had no problems in this area. Performance and reliability have substantially improved in recent designs. This together with the versatility of the U.S. Navy P-3 aircraft provides a powerful and effective tool for performing large scale synoptic oceanographic surveys.

Acknowledgments

Many persons have aided us in our various AXBT projects. Walter Bryan of Scripps Institution of Oceanography has been involved in all our tests and performed all calibration work since 1974. CDR. Robert Lawson of the Office of Naval Research has been instrumental in obtaining AXBT's and scheduling U.S. Navy aircraft for both test and operational deployments. Philip Marshall, Stephen L. Wald, Kenneth Wallace and William Powell of Scripps Institution of Oceanography helped with the design and construction of the AXBT recording system. Philip Marshall and William Powell also participated in numerous flights connected with data collection programs.

Aircraft support has been supplied by U.S. Navy Patrol Squadrons from COMPATWINGSPAC and various reserve squadrons. Also the U.S. Naval Oceanographic Office (U.S. Navy Squadron VXN-8) and the National Oceanic and Atmospheric Administration have supported our work with their research equipped P-3's.

This work has been supported by the Office of Naval Research under various contracts in association with the NORPAX program and the National Science Foundation.

References

1. Latham, R. D. and G. P. Woollard (1971) Processing of aircraft expendable bathythermograph data. Hawaii Institute of Geophysics Report No. HIG-71-13, 27 pp. (Unpublished manuscript.)

2. Saunders, P. M. (1971) Anticyclonic eddies formed from shoreward meanders of the Gulf Stream. Deep-Sea Research, 18, 1207-1219.

3. Naval Air Systems Command (1968) Handbook of operating instructions for bathythermograph transmitter set AN/SSQ-36. NAVAIR Pub. No. 16-30SSq36-2. Motorola.

4. Naval Air Systems Command (1975) Technical manual for bathythermograph transmitter set. NAVAIR 16-30SSQ36-200. Magnavox AXBT's.

5. Naval Air Systems Command (1978) Operating manual for bathythermograph transmitters SSQ-36. NAVAIR Pub. No. 16-30SS036-201. Hermes AXBT's.

6. Brisco, M. G., O. M. Johannessen and S. Vincenzi (1974) The Maltese oceanic front: a surface description by ship and aircraft. Deep-Sea Research, 21 247-262.

7. Sessions, M. H., W. R. Bryan and T. P. Barnett (1974) AXBT calibration and operation for NORPAX POLE experiment. Scripps Institution of Oceanography Ref. Series No. 74-31, 19 pp. (Unpublished manuscript.)

8. Sessions, M. H., T. P. Barnett and W. S. Wilson (1976) The airborne expendable bathythermograph. Deep-Sea Research, 23, 779-782.

9. D'Azzo, J. J. and C. H. Houpis (1966) Feedback control system analysis and synthesis. Second Edition, McGraw-Hill, 622-668.

10. Barnett, T. P., M. H. Sessions and P. M. Marshall (1976) Observations of thermal structure in the central Pacific Ocean. Scripps Institution of Oceanography Ref. Series No. 76-19.

11. Patzert, W. C., T. P. Barnett, G. J. McNally, M. H. Sessions, K. Wyrtki, B. Kilonsky and A. D. Kirwan (1978) Aircraft monitoring of the tropical Pacific upper ocean thermal structure and currents during the NORPAX shuttle experiment. Naval Research Reviews, 31, No. 9, 1-8.

12. Patzert, William C., Tim P. Barnett, Meredith H. Sessions and Bernard Kilonsky (1978) AXBT observations of tropical Pacific Ocean thermal structure during the NORPAX Hawaii/Tahiti shuttle experiment November 1977 to February 1978. Scripps Institution of Oceanography Ref. Series 78-24.

Applications of a Data-Compression Algorithm for XBT Bathy-Message Preparation

by

Staff*
Technical Planning and Development Group
School of Oceanography
Oregon State University

Abstract:

An expendable Bathythermograph (XBT) system utilizing a commercial microcomputer is described. An algorithm particularly suited for data compression in such systems is presented in some detail. Extension of the digital XBT system to several other expendable probes is also described.

Introduction

Over the last 2 years, the Technical Planning and Development Group at Oregon State University has been involved in the development of hardware and software to function with a variety of expendable probes.[1] Our experience has shown that "low-end" microprocessor-based computers offer significant advantages, and previously unavailable capabilities, for this class of marine instrumentation.

In the context of this paper, the term "microcomputer" (μC) is intended to mean a unit of hardware which has a display (integral or attached by cable), a keyboard, a microprocessor and memory, a recording device (e.g. magnetic tape cassette), a means for attaching additional input/output hardware, and a complete software operating system supporting a high level programming language such as "BASIC", "FORTH", or "PASCAL". Commercial products of this class include, but are not limited to, the Radio Shack "TRS-80", the Commodore "PET", and the "APPLE II".

As part of a dedicated measurement system, a μC can perform a large number of tasks. Most of these tasks can be done more easily with a μC than with fixed logic hardware. For example, the display of a variety of messages is quite simple; however, with fixed logic, any significant number of messages would be fairly difficult. Similarly, a μC can control input/output hardware such as digitizers, record/play back data (e.g. on cassette tape), compress and format data, and can transfer data to other pieces of equipment. While the μC can perform a number of tasks, what is just as important a consideration is the users ability to redirect system data acquisition and processing tasks with software skills and keyboard entry instead of new hardware implementation.

---

*Contributors: Dr. R. Mesecar, head
Dr. J. Wagner

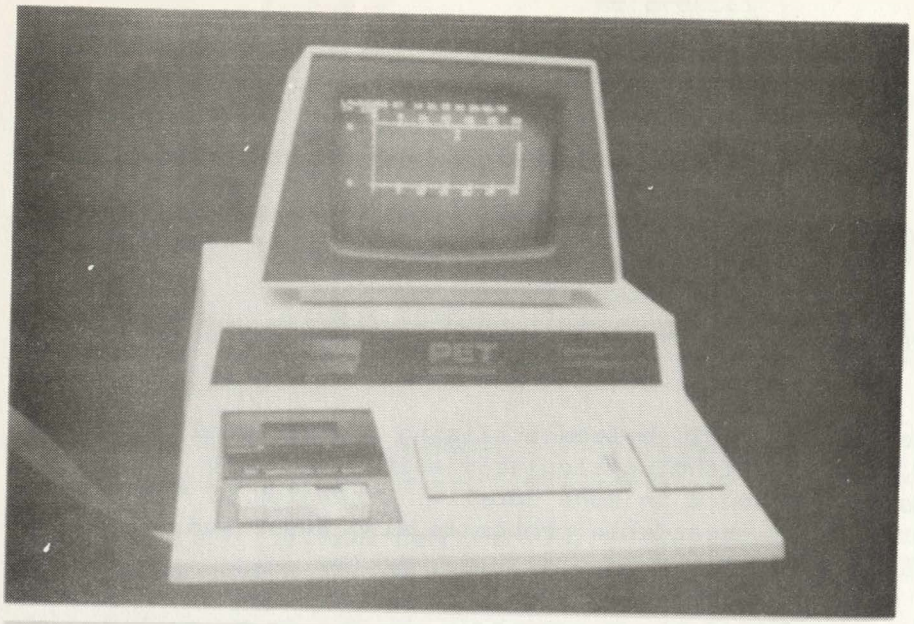

A

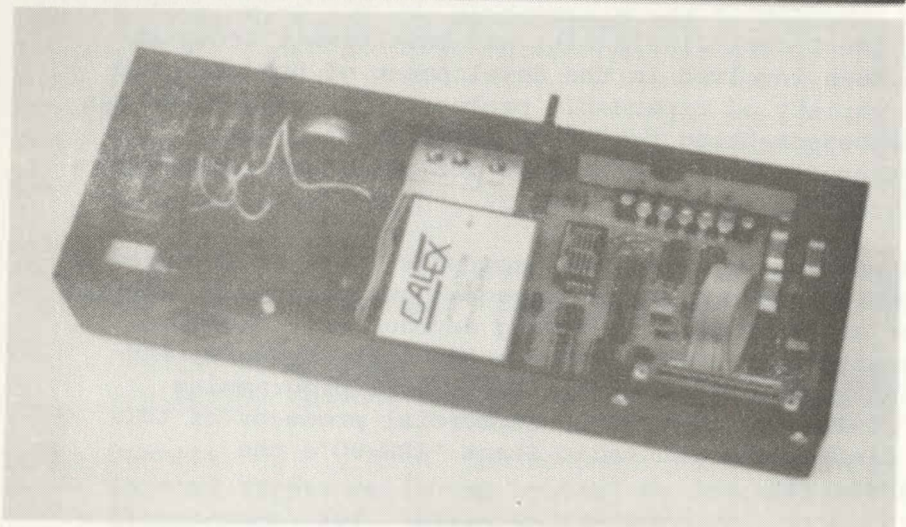

B

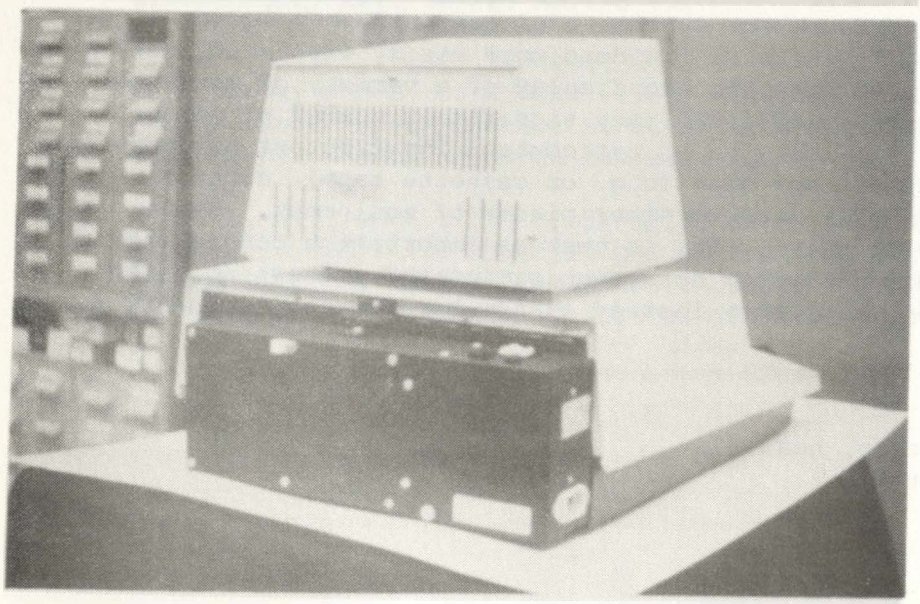

C

Figure 1.

The OSU Digital XBT System is composed of a Commodore PET microcomputer (A) and an electronic interface (B) to the XBT probe. The interface mounted to the microcomputer is shown in "C".

The flexibility offered by μCs makes them a prime candidate to improve the operation of existing sensor systems. This paper will focus on one unique application of μC technology to compress the number of data points needed to characterize the temperature profile from an XBT probe. However, while the following comments relate our experience with the digital XBT system, it should be remembered that the same principles are valid for a variety of measurement systems.

The Digital XBT System

The OSU digital XBT system includes a Commodore PET, an interface (Figure 1) which contains a digitizer, control circuitry and probe current supply, and an operating program written in "BASIC". The operations program is written to graph and prompt messages, test the interface, maintain current date and time, control the digitizers, and record data. An additional feature of this system is the capability to automatically generate bathy-messages in the format specified by the World Meteorological Organization.[2] The bathy-message represents a form of data compression in which 160 data points from an XBT probe temperature profile are reduced to approximately 20 significant points. Manual procedures have previously been used to generate the bathy-message which were time-consuming and subject to error. Automating this procedure has added a conforming interpretation of the data and a significant control on the manually induced errors.

The bathy-message algorithm (BMA) is an example of the versatility of microcomputer-based systems. The BMA was added to the system after it was designed, built, and operational. The original system did not include consideration of a bathy-message requirement; the only requirements were that the μC operating program be well-structured and that adequate memory space be available.

The Bathy-Message Algorithm

The BMA is relatively compact, requiring about 30 lines of "BASIC" code and about 700 bytes of memory. The mean-processing time is about 15 minutes although under special circumstances (near surface wire break) up to 45 minutes may be needed. The BMA is adapted from one developed at White Sands Missile Range[3] for real-time reduction of radiosonde data. The real-time capability of the algorithm is not used, but it is significantly faster and uses less memory than most other schemes we investigated.

The BMA functions by assuming an initial "tolerance limit". Next, the number of points required to approximate the data to that tolerance is determined. The tolerance is then adjusted according to whether there are too few or too many points. The entire procedure is then repeated until 19 to 21 points result (in this application). If more than 20 of these iterations have occurred, then 10 to 25 points will be accepted and a bathy-message determined. If more than 30 iterations have occurred, then a message is outputed on the display screen indicating that the bathy-message cannot be determined.

To begin an explanation of the BMA, assume two arrays of digitizer-quantity points, D_j and Q_j, and j=1 to Rs, representing depth and

temperature. Since these points are in digitizer units, they must be converted to depth and temperature before use. Assume a tolerance (TOL), which is arbitrarily specified initially and iteratively changed in successive trials. Assume that Ml is the index (value of j) of the last significant point (Ml=1 at the start of each iteration with a new tolerance). Then compute T_{ml} (temperature) and D_{ml} (depth) from the digitized case values. For j=Ml+1, find T_j and Dj. As shown in Figure 2, compute a pair of slope limits, M_u and M_l (upper and lower), with the following equations:

$$M_u = \frac{T_j + TOL - T_{ml}}{D_j - D_{ml}} \quad \text{and}$$

$$M_l = \frac{T_j - TOL - T_{ml}}{D_j - D_{ml}}$$

Label the points responsible for establishing the slope limits as $j_u=j$; $j_l=j$.

Next, increment j and find $M_j=(T_j-T_{ml})/(D_j-D_{ml})$. Note that this is the slope of the line between points Ml (last significant point) and j. Then, test this slope against M_u and M_l. If $M_u \geq M_j \geq M_l$, then the tolerance limit is

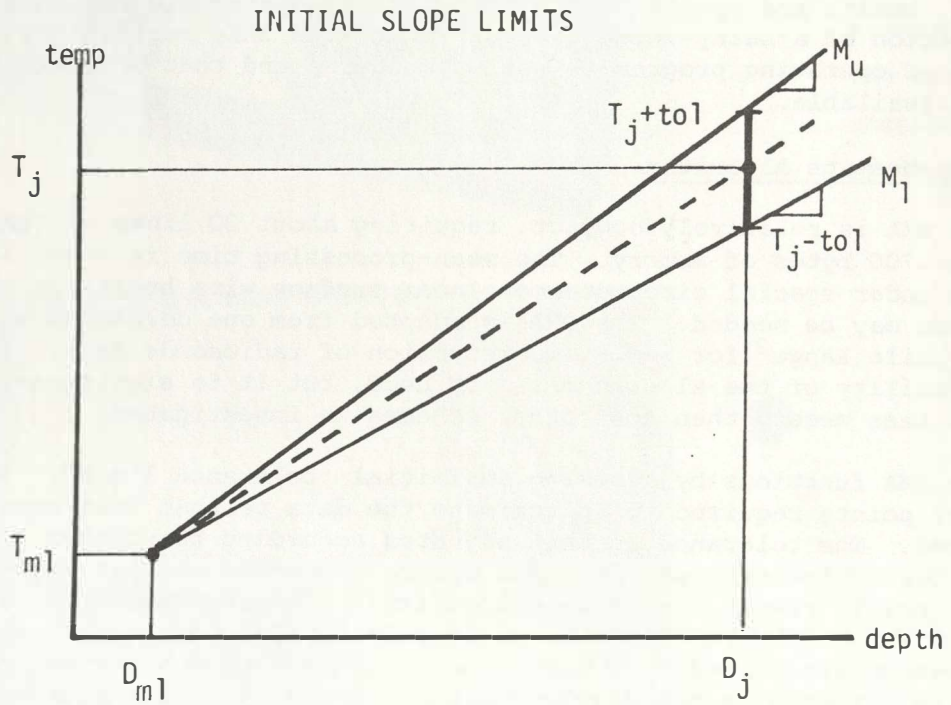

Figure 2.

not violated. If it is violated, the Ml is set to j_u (if the upper limit is violated) or j_l (lower limit violated), new test slopes are established and all is repeated (see Figure 3).

If the test slopes are not violated, then another set of tests is carried out. A new set of trial limit slopes are computed using points Ml and j. If either of these new trials results in a tighter limit, then the corresponding limit slope and labels are changed (see Figure 4). Note that both limit lines could be altered during this step.

Figure 3. TOLERANCE LIMIT TESTS

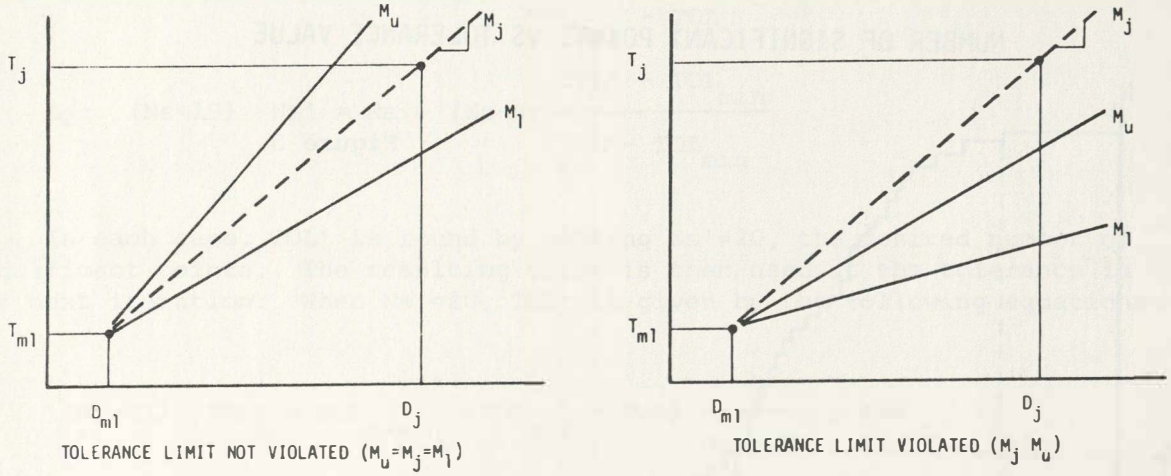

Figure 4. NEW LIMIT LINES

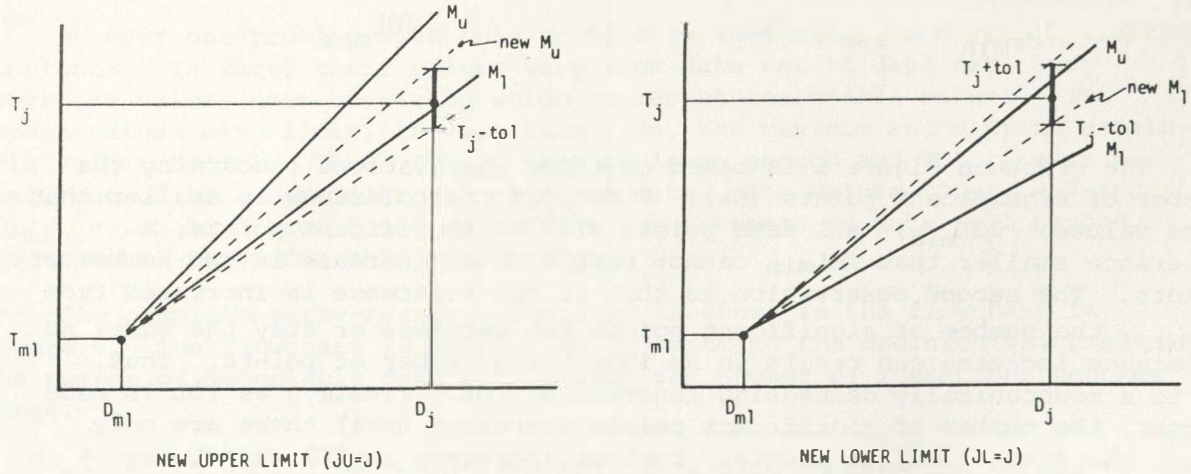

When the modification of the limit slopes is completed, if not all data points have been tested (i.e. j<Rs), the j is incremented and the tests are repeated for the new point.

When all points have been tested, the number of significant points is compared to the desired number of points. Twenty-three to 25 points is the desired number. But four of these points in the actual bathy-message label 100 meter crossings (100 m, 200 m, 300 m, and 400 m) so the actual number of data points is 19 to 21, with a target of 20. A new tolerance is now estimated with the goal of bringing the number of significant points closer to 20. The scheme used to estimate the new tolerance is based on the relationship between the number of significant points and the tolerance (see Figure 5).

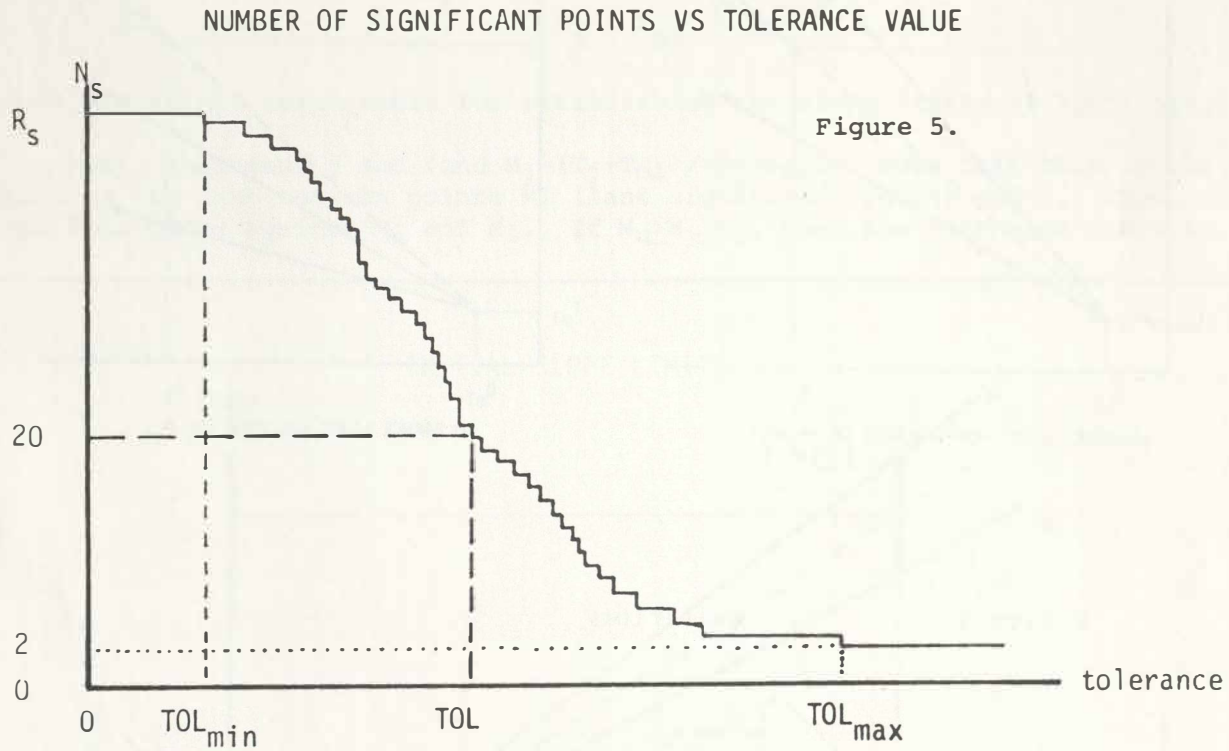

Figure 5.

The graph in Figure 5 is based on three observations concerning the number of significant points (Ns). First, if the tolerance is smaller than some values, TOL_{min}, all data points will be significant points; a tolerance smaller than TOL_{min} cannot result in an increase in the number of points. The second observation is that if the tolerance is increased from TOL_{min}, the number of significant points can decrease or stay the same; no tolerance increase can result in an increasing number of points. Thus, Ns is a monotonically decreasing function of TOL. Finally, as TOL is made larger, the number of significant points decreases until there are only two: the first and last points. Further increases in TOL cannot result in a decreased number of points when TOL exceeds TOL_{max}.

These three observations provide enough information for the programmer to estimate a new set of TOL values which will provide an appropriate number of significant points. There are two "known" points on this curve, TOL_{min}, Rs and TOL_{max}, 2. There are no local maxima or minima between these points since Ns is monotonic. If a value TOL results in Ns significant points, then using TOL, Ns, and the known end point, which is on the opposite side of Ns=20, define a line L_1 or L_2 on Figure 5 and determine where this line crosses Ns=20. If TOL is the current tolerance and Ns is the current number of significant points, TOL' is a new tolerance value, and Ns' is a new (estimated) number of significant points, then the equations for L_1 and L_2 are given by the following equations:

$$L_1: \quad (Ns>21) \quad Ns' = 2 + (Ns-2)\frac{TOL_{max} - TOL'}{TOL_{max} - TOL}, \text{ and}$$

$$L_2: \quad (Ns<19) \quad Ns' = Rs + (Ns-Rs)\frac{TOL' - TOL_{min}}{TOL - TOL_{min}}$$

In each case, TOL' is found by setting Ns'=20, the desired number of significant points. The resulting value is then used at the tolerance in the next iteration. When Ns'=20, TOL' is given by the following equations:

$$(Ns>21) \quad TOL' = TOL_{max} - (TOL_{max} - TOL)\frac{2}{Ns - 2}, \text{ and}$$

$$(Ns<19) \quad TOL' = TOL_{min} + (TOL - TOL_{min})\frac{20 - Rs}{Ns - Rs}$$

The data compression routine is convergent for linear, concave, and convex functions.

However one problem with this routine is that TOL_{max} and TOL_{min} are not constants. In fact, their values vary from data set to data set, and therefore values must be picked which represent reasonable values. The chosen values also limit, in each direction, the maximum and minimum attainable values to TOL. Thus, TOL_{max} must be large enough and TOL_{min} must be small enough to accommodate all expected data. The values TOL_{max} = 2 and TOL_{min} = .05 have been found to suffice for extremes of data well beyond the expected range for this application.

The complete bathy-message algorithm is shown in the flowchart in Figure 6. The flowchart is simplified by omitting the decision which alters the number of acceptable data points when the number of iterations becomes large.

Again, it should be remembered that this data compression scheme is not limited to expendable probe applications. It can be readily implemented on any μC with a floating point arithmetic capability. The algorithm shown

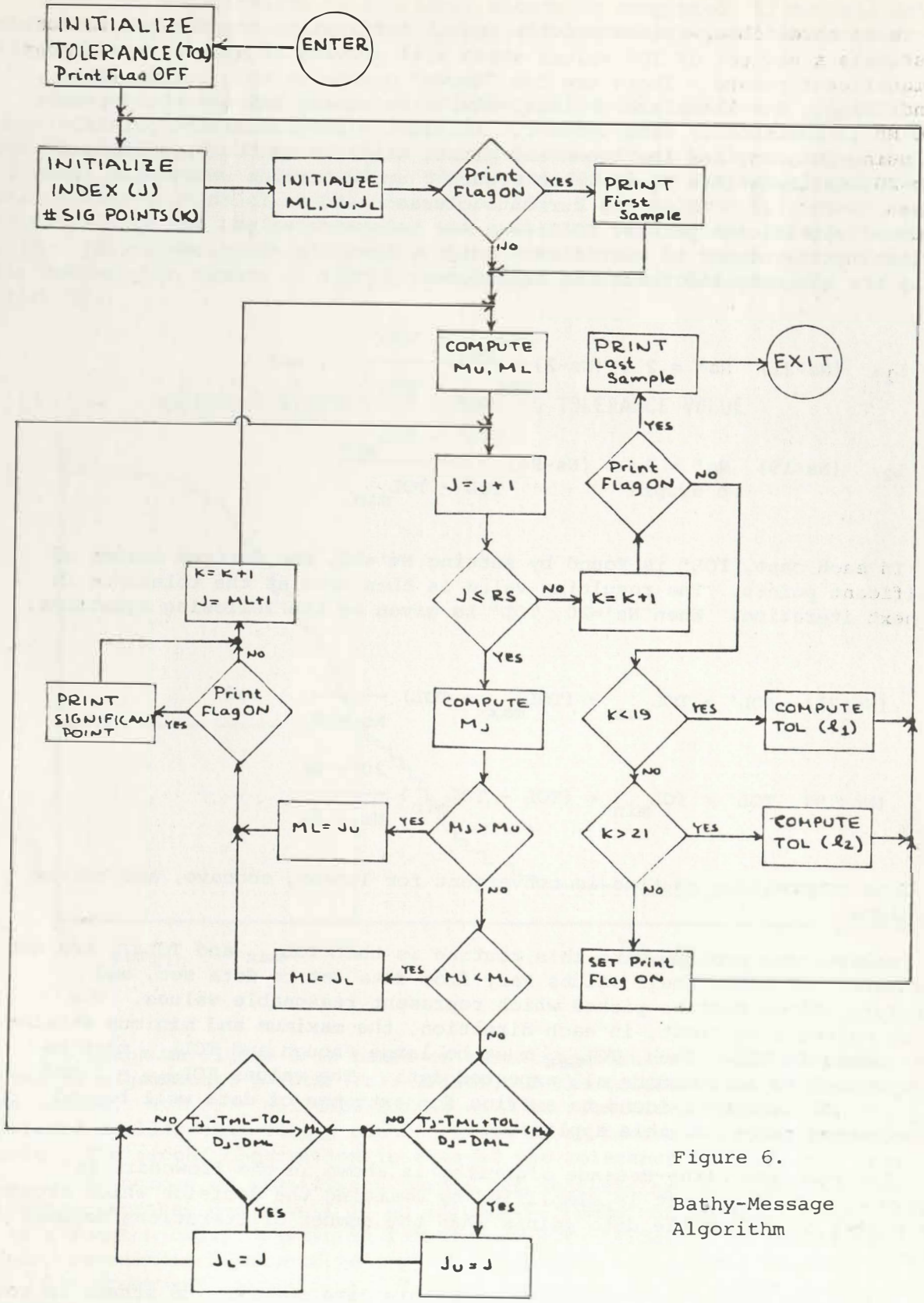

Figure 6.

Bathy-Message Algorithm

here is particularly adapted to the situation where data is already stored. But in real-time operation, the only data (other than significant points) which needs storage is that between the smallest values of j_u or j_l and the current data point since these points may be needed when a new line is started. In real-time operation, of course, the iterative selection of the tolerance for a specific number of points is not appropriate.

Other Expendable Probes

The versatility of μC-based systems has also been demonstrated by the ease of adapting to several different expendable probes. In each case, the basic operating system was essentially unchanged. The only significant software alteration was to program the routine controlling the external hardware.

One interface has been built for the Sippican "XSV" (sound velocity) probe. The information is received over the probe wire via an FM signal. A simple counter controlled by the μC provides the digitizer function.

Several interfaces have also been built for the Grundy (Plessey) "XSTD" probe. In this probe, temperature and conductivity are received simultaneously as FM signals. Filters are used to separate the two channels. Otherwise, the interface design is very much like the design required for the XSV interface. Again, minimal software change is needed.

The relative ease with which these systems have been implemented is largely due to simplicity of changing a high level language computer program which is well structured. Another factor, of course, is that all of the systems have had similar operating requirements.

Future Directions

A recent study by the National Marine Fisheries Laboratory at Monterey, California,[4] has shown that approximately 50 percent of the received bathy-messages have major errors. The errors appear to be fairly evenly distributed among the bathy-message generation, message (CW) transmission, message reception, and message retransmission (to NMFL) functions.

The first of these error sources, bathy-message preparation, has been addressed by the BMA in the OSU digital XBT system. A major effort is underway to reduce the remaining error sources by using a satellite link directly coupled to the digital XBT system. Again, the versatility of a μC-based system makes such an undertaking quite feasible.

References

[1] Mesecar, R. S. & J. Wagner. "An XBT Digital Recording and Display System", *Oceans '79 Conference* (IEEE Cat. No. CH1478-7/79/000-0598).

[2] *Instructions for Preparing the Bathythermograph Log*, Feb. 1972, U.S. Dept. of Commerce, Nat. Oceanic and Atmospheric Admin., Nat. Weather Service, Office of Meteorological Operations, Silver Spring, MA.

[3] Merrill, M. Don & Don R. Veazey, "Linearization for Compact Storage of Digitized Analog Data", *IEEE 1977 Region 6 Conference Record*, (IEEE Cat. No. 77CH1206-2 Reg 6; Library of Congress No. 72-92043).

[4] Personal verbal communication.

PERFORMANCE OF EXPENDABLE SOUND VELOCITY, TEMPERATURE (XSVT) PROBES

Jack R. Lovett

Naval Ocean Systems Center, San Diego, CA 92152

Abstract

The development of the expendable sound velocimeter, temperature (XSVT) probe makes possible the computation of salinity. A depth equation for the XSVT is determined, but evidence indicates that the fall rate may vary with temperature related kinematic viscosity changes. Such depth (pressure) errors may adversely affect computed salinity if not accounted for. The simultaneous measurement of sound velocity and temperature shows the effect of pin-hole wire leaks on otherwise difficult to detect temperature bias errors. The experiment uncovered an erroneous sound velocity (mirrored in salinity) gradient in the first 50 m, that biases the subsequent salinity values. The deck unit degraded the temperature signal, a condition since corrected by the manufacturer. Evaluated as an anti-submarine warfare device, the XSVT discloses both benefits and disadvantages over the XBT.

Introduction

Emery[1] recently proposed the use of expendable sound velocity temperature probes (XSVT) to compute salinity, with expected accuracies on the order of $0.2°/_{oo}$. He suggests that such an accuracy will prove adequate to resolve salinity features in certain areas of the ocean.

Instrumentation

The Naval Ocean Systems Center (NOSC) provided a Grundy (Plessey) 9041-5b (0-3000 m) CTD/SV as a standard, calibrated by the Northwest Regional Calibration Center (NRCC). The manufacturer's stated precision for this instrument using a one standard deviation (σ) about mean method of error analysis gives ± 0.005 mmho/cm, ± 0.005°C, ± 1.2 m and ± 0.05 m/s. The NRCC calibration gave σ's of 0.018 mmho/cm, 0.008°C, 0.9m and 0.02 m/s (atmospheric pressure only and corrected for electronic delay). The velocimeter had a constant offset of -0.1 m/s, but this is thought due to the NRCC's artificial seawater. The Grundy deck equipment has quantizing errors of 0.002 mmho/cm, 0.001 C, 0.4 m and 0.012 m/s.

Balboni and Walsh[2] describe the Sippican expendable sound velocimeter (XSV). The XSVT evaluated here differs only in that the manufacturers added the standard XBT thermistor and replaced the XSV's single conductor with a two conductor wire (which changes the fall rate and the depth equation).

The manufacturer claims XSVT absolute accuracies of ± 0.25 m/s, ± 0.2°C and ± 2% of depth or 5 m, whichever is greater. The Sippican MK-8 Oceanographic Data Acquisition and processing system digitized the data at a rate of 10 samples per second with quantizing errors of 0.04 m/s and 0.01°C. Emery[1] quotes the manufacturer that reduced errors of 0.15 m/s, 0.03 C and ± 1% of depth may be achievable.

The NOSC CTD/SV usually alternated casts with a NRCC calibrated Guildline CTD furnished by the Institute of Ocean Sciences (IOS). In areas of weak gradients the two systems tend to agree within the manufacturers' combined errors.

Sound Velocity Equation Selection for Salinity Computations

The Wilson[3] equation probably represents the most widely used sound velocity equation even today, as many extant programs that compute sound velocity, incorporate this equation as a routine. Yet others [Mackenzie[4], Del Grosso[5], Millero and Kubinski[6], and Lovett[7]] have long since demonstrated that the original Wilson data set and subsequent equations have serious problems with salinity and temperature. Anderson[8] concluded that the Wilson equations had pressure gradient problems, but restricting the original Wilson data set to those points that occur in the World ocean resulted in a new equation that provided better agreement with precise acoustic propagation measurements in the deep ocean.

The most recent Del Grosso[5] equation shows excellent agreement with the in-situ sound velocimeter for the first 1000 db, although it starts to deviate at higher pressures [Millero and Kubinski[6], Lovett[7]]. This paper will employ the Del Grosso equation since it agrees with the in-situ velocimeter slightly better than the three equations suggested by Lovett[7] for the 850 m XSVT depth range. The recent sound velocity equation of Chen and Millero[9] and all other existing equations agree less well with the sound velocimeter than the other four equations.

Partial Derivatives of Salinity with Respect to Temperature, Sound Velocity and Pressure

The Del Grosso equation was differentiated for sound velocity with respect to temperature, salinity and pressure. Then $\partial S/\partial T = (\partial V/\partial T)/(\partial V/\partial S)$, $\partial S/\partial V = 1/(\partial V/\partial S)$ and $\partial S/\partial P = (\partial V/\partial P)/(\partial V/\partial S)$ Figures 1 a-c show the largest variability to be temperature related for the oceanic range expected for XSVTs. Del Grosso and Mader[10] restricted their data to temperatures less than 15°C except for atmospheric pressures, hence when P = 850 db, the derivatives end at 15°C. In Figures 1b and c the line for S = 38°/$_{oo}$ at P = 0 db does not appear as it coincides with the line for S = 33°/$_{oo}$ at P = 0 db. Salinities of 33°/$_{oo}$ and 38°/$_{oo}$ are the limiting values of the Del Grosso-Mader data set under pressure.

Data Analysis

Noise Problems

The XSVT deck unit digitally records a new value for sound velocity and temperature every 0.1 sec (10 Hz sample rate) for 165 seconds. Figure 2 shows the 1650 data points for each parameter plotted vs. time. The positive sound velocity dropouts that appear in both Figures 2 and 3 must come from the digitizing electronics and not from the sound velocity sing-around circuit. Note in Figure 3 that the dropouts often reoccur to the same level, exactly, regardless of the base sound velocity value. A routine in the computer program that converts the time axis to depth, rejects any dropout that exceeds 0.3 m/s.

The temperature signals of all XSVT drops exhibit cyclical patterns (Figures 2, 3) that do not appear in the sound velocity traces. Figure 4 expands a portion of XSVT traces vs. time. The cyclical nature of the temperature trace looms through

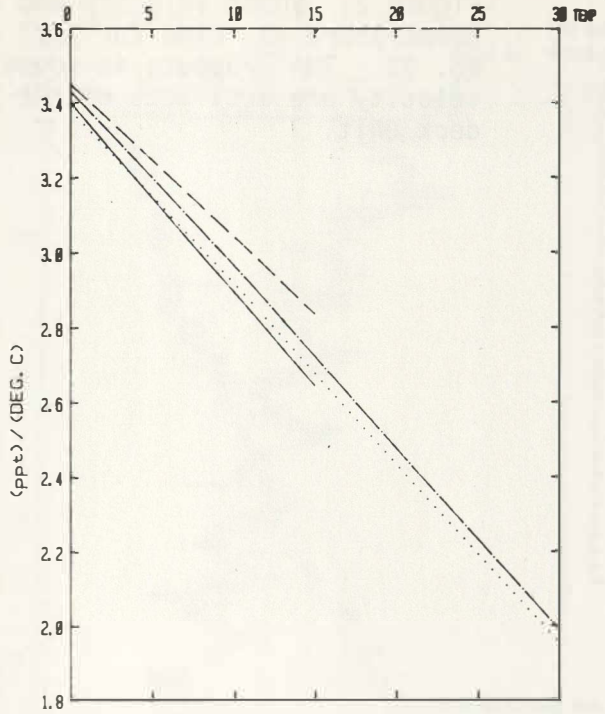

(a)

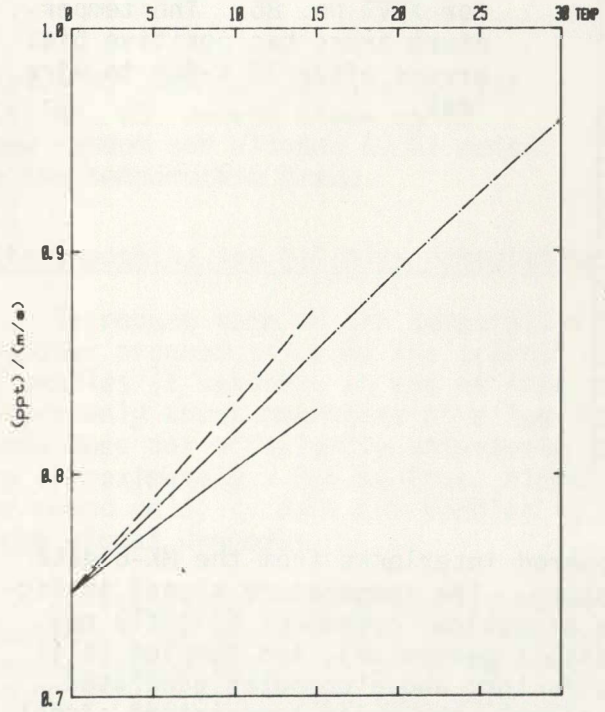

(b)

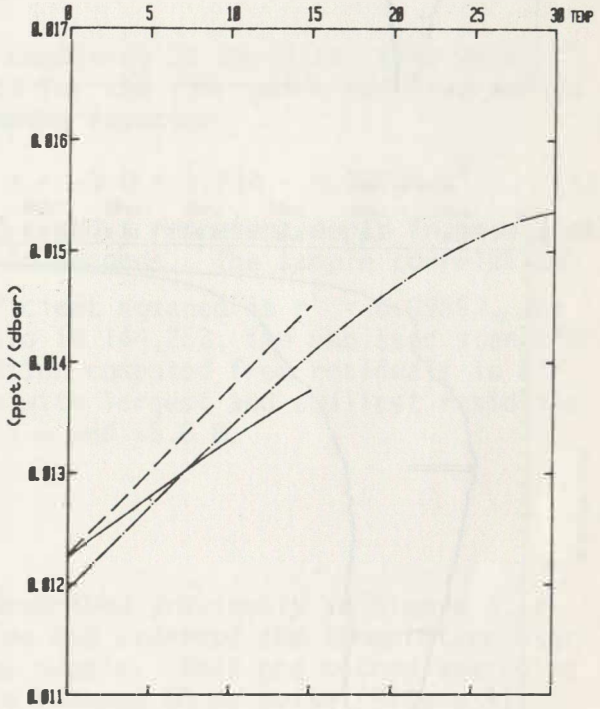

(c)

Figure 1. Temperature vs. the partial derivatives of salinity with respect to (a) temperature, (b) sound velocity, (c) pressure, where
P = 0 db, S = 33°/$_{oo}$ — · — · —
P = 0 db, S = 38°/$_{oo}$ .....
(In (b) and (c) coincides with prior line);
P = 850 db, S = 33°/$_{oo}$ — — — — —
P = 850 db, S = 38°/$_{oo}$ ————————

random and quantization errors. The A to D converter's quantization error of 0.01°C (equivalent to ~0.04 m/s) could not account for all of the observed random component.

R.J. Kaiser of Sippican (personal communication) has subsequently determined that a microprocessor control line ran too close to the capacitor of the high input impedance A to D converter for temperature, and probably was the source for most of the random component seen in Figure 4. He believes that mu-metal shielding

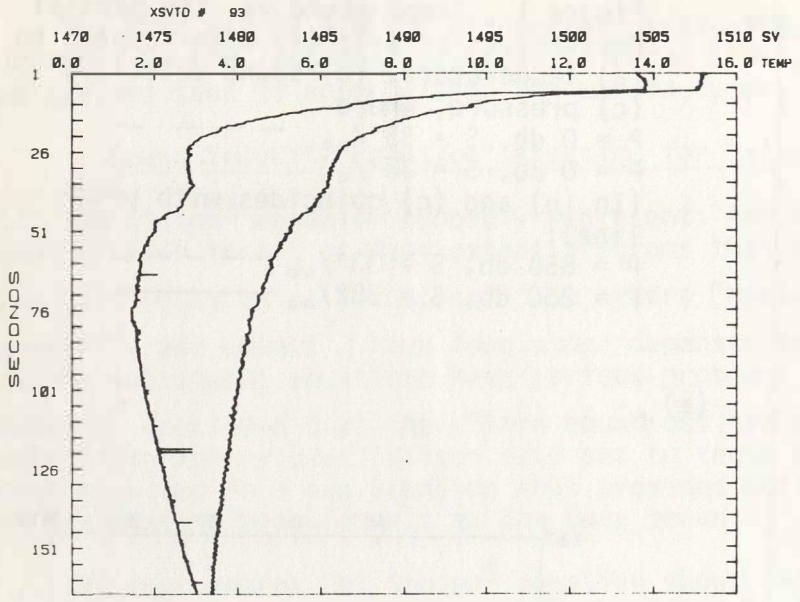

Figure 2. Sound Velocity and temperature vs. time for XSVT No. 93. The dropouts in sound velocity are artifacts of the deck unit.

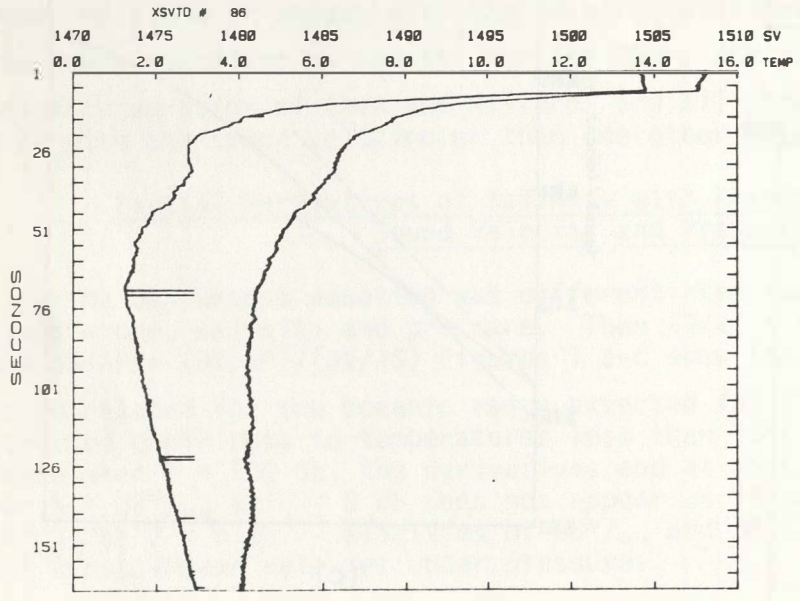

Figure 3. Similar to Figure 2 for XSVT No. 86. The temperature trace has positive bias errors after 78 s due to wire leak.

of certain components, and the removal of AC powered interlocks from the MK-8 data processor will solve the aliased ~60 Hz hum problem. The temperature signal in Figure 4 was modeled by: a linear equation base; a sinusoidal component slightly reduced in frequency from 60 Hz (to imitate the ship's generator), and sampled (aliased) as a rate of 10 Hz; a pseudo-quantization factor; and a computer generated random component, and the model resembled very closely the noise temperature signal of Figure 4. The horizontal tic interval scale in Figure 4 of 0.1°C and 0.35 m/s reflects the approximate conversion ratio for temperature to sound velocity (1°C ≈ 3.5 m/s); hence the quantization, random and cyclical temperature errors shown, increase computed salinity errors more than the sound velocity quantization errors (with dropouts removed) will.

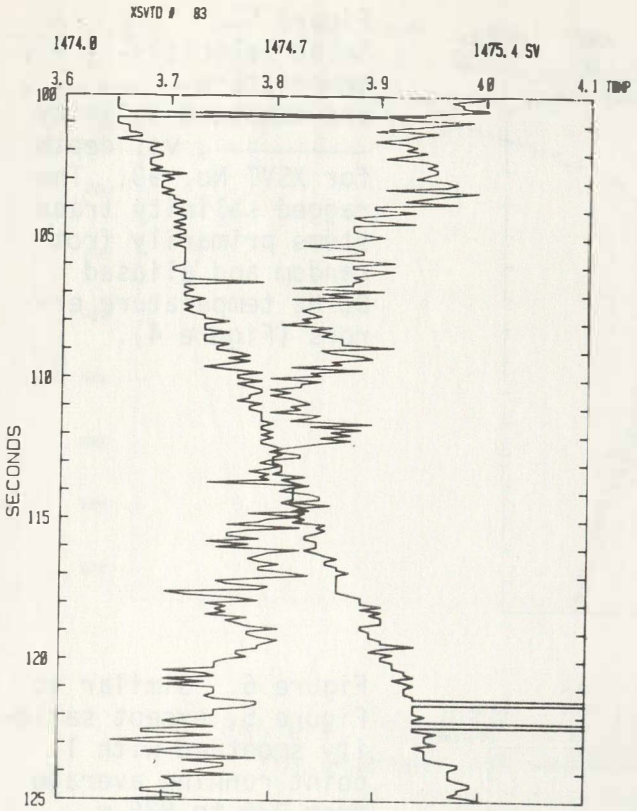

Figure 4. Similar to Figure 2 for XSVT No. 83, except blown up to show random and aliased 60 Hz noise on the temperature trace.

Depth Equation

The addition of a two conductor wire to the XSV will change the depth equation, and Sippican had not adequately tested the XSVT for fall rate before this experiment. To determine a depth vs. time equation for XSVT probes, four time plots similar to Figure 2 were selected. These four probes coincided closely in time to CTD/SV casts (digitized at 5 m intervals), and had numerous inversions of gradient changes vs. depth using both plots and digital printouts for every 0.1 sec (XSVT) and 5 m (CTD/SV) for the less noisy sound velocity data.

Combining 34 depth vs. time data points for the four pairs resulted in the following equation:

$$z = -3.0 + 5.73t - 0.00278\ t^2 \qquad (1)$$

where z and t represent depth in meters and time in seconds. The sample correlation coefficient squared is $r^2 = 0.99893$, the F ratio is 144,253, the unbiased standard deviation computed from residuals is σ = 2.4 m with largest and smallest residuals of 4.3 m and -5.6 m.

Data Smoothing and Salinity Computation

To reduce some of the temperature errors described previously in Figure 4, a computer program selected the nearest sample time and averaged the temperature over 10 samples (1 second), -5 and +4 from the center sample. This one second averaging covers only about one-third of a "period" of the aliased 60 Hz noise (Figure 4), hence does not efficiently attentuate that part of the noise. This procedure covers approximately ± 2.5 m, thus, almost all data points serve in the averaging. The sound velocity data are handled in a similar manner along with rejection of large signal dropouts.

An iterative program then computes salinity using the Del Grosso sound velocity equation. The program adds 75% (Figure 1b) of the difference between measured and computed sound velocity to the salinity, until the difference drops below 0.01 m/s (~0.0075°/$_{oo}$), then uses that computed salinity as the starting point for the next measurement. This method usually requires only two iterations for each salinity point. Figure 5 presents the same data as Figure 2, with time converted to depth via equation (1), and the computed salinity added. Note the randomness of the salinity trace due primarily to the temperature errors previously discussed. Figure 6 reproduces Figure 5 with an eleven point running salinity average over a 50 m interval between 225 and 825 m to remove most of the random errors.

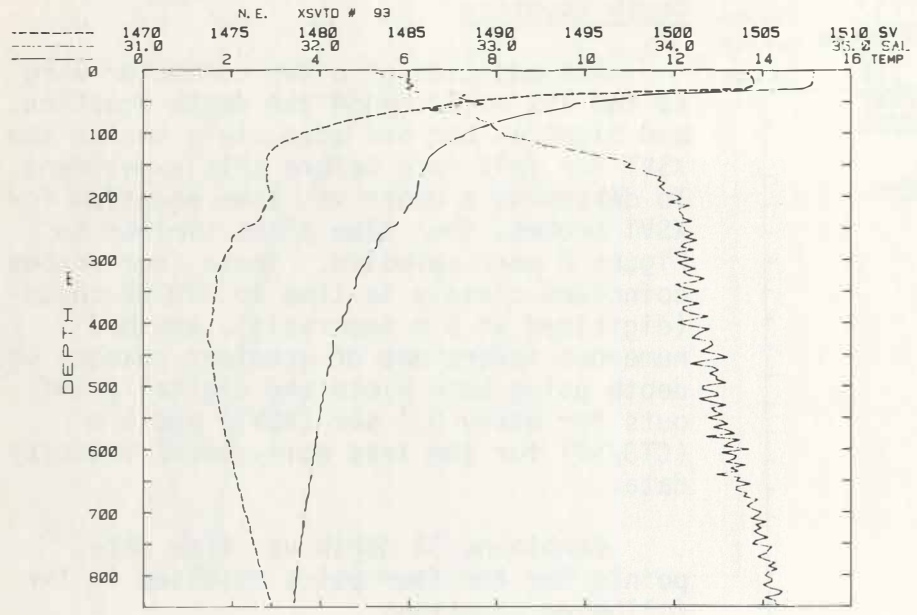

Figure 5.
Sound velocity - - - , temperature — · — · —, and computed salinity ————, vs. depth for XSVT No. 93. The ragged salinity trace stems primarily from random and aliased 60 Hz temperature errors (Figure 4).

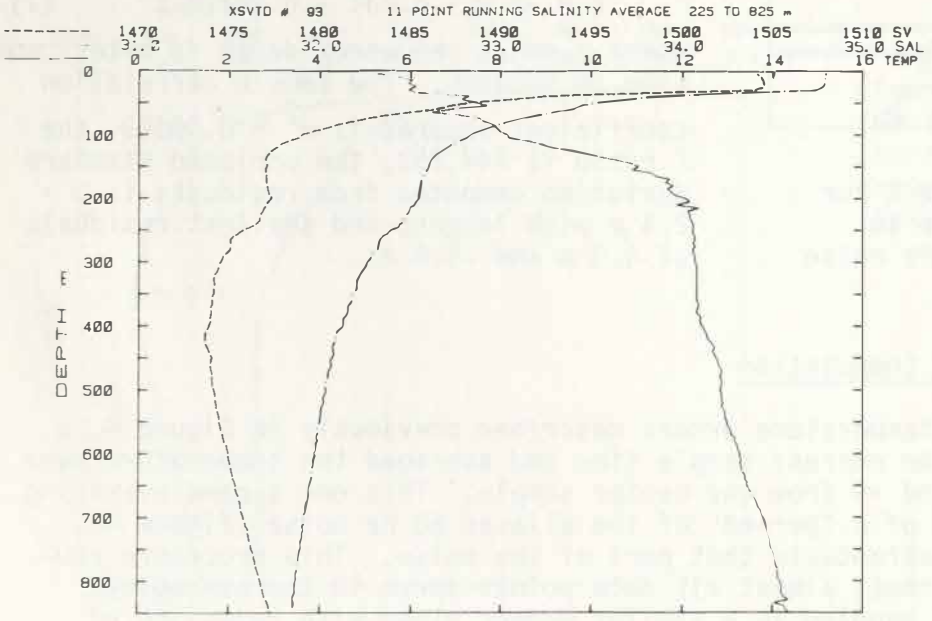

Figure 6. Similar to Figure 5, except salinity smoothed with 11 point running average from 225 to 825 m.

Wire Leak Problems

The temperature signal begins to depart from the normal values after ~78 seconds in Figure 3. This egregious example (compare Figure 2) of temperature error has no correspondence in sound velocity. A more insidious example than Figure 3 appears in Figure 7. A pin-hole leak has probably developed in the signal wire and appears to the thermistor bridge as a lower resistance (a higher temperature). a cursory examination of just the temperature and sound velocity traces probably would have accepted this data without question.

Wire leaks to seawater normally have no effect on the frequency modulated sound velocity signal, and become a problem only for catastrophic leaks where the signal amplitude falls below the detection level. Severe insulation failure usually results in sharp and obvious positive offsets in temperature. Often these

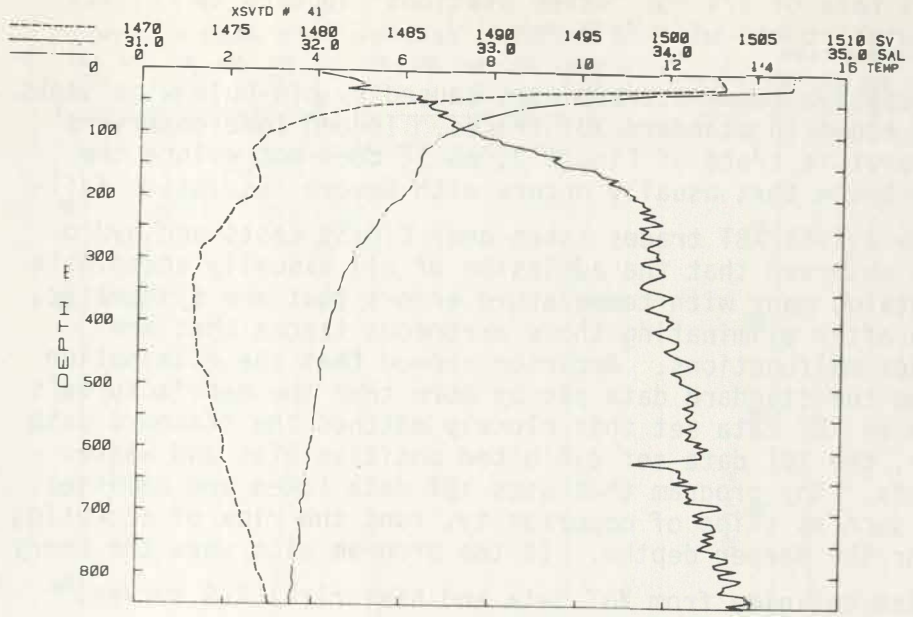

Figure 7. Similar to Figure 5, except salinity trace shows the result of pin-hole wire leak (with partial healing affecting the temperature signal).

Table 1. Success and failure percentage rates for XSVT. The underway set represents the "normal" condition. The "good percentages based on visually acceptable traces.

	PERCENTAGE				NUMBER
	Good T. and S.V.	Good Temperature	Good S.V.	Failure T. and S.V.	XSVTs
Under Way	57	80	67	10	21
Time Series {1	23	32	66	26	35
Time Series {2	40	60	72	7	30
Other Stations	30	34	57	39	23
All XSVTs	36	49	66	20	109

insulation failures have a tendency to "heal" as the computed salinity trace in Figure 7 would seem to indicate, but only occasionally does the healing fully restore the correct temperature value. This cruise experienced a lot of strong winds which had a tendency to blow the fine XSVT wire into the ship and scrape the insulation, particularly with the ship hove-to on station. In general, the weather improved throughout the cruise. The first few probes were dropped amidships over the starboard side. An extended deck cable allowed drops from the stern which helped to alleviate the wire touching the ship's hull. However, the stern position placed the drops close to the CTD/SV davit, and evidence exists to show that the XSVT wire may have occasionally scraped against the CTD/SV cable underwater. Table 1 illuminates this point, in that while underway at 14 kt, 80% of the temperature traces were visually acceptable to at least 750 m, vice only 45% during the time series off the stern. All other stations had a temperature success rate of only 34%. The success rate for sound velocity held steadier than temperature. The

lowest sound velocity success rate of 57% for "other stations" appears to reflect a greater preponderence of catastrophic wire failures.

The type of insidious positive temperature biases caused by pin-hole wire leaks illustrated in Figure 7 also occur in standard XBT traces. Indeed some observers might have accepted the temperature trace of Figure 3, as it does not evince the large and sudden temperature break that usually occurs with severe insulation failure. Anderson[11] made a study a 1961 XBT traces taken near CTD/SV casts and hydrocasts used as standards. He observed that the admission of all visually acceptable XBT traces to a data set contains many with temperature errors that are systematic, biasing and non-random, even after eliminating those erroneous traces that are clearly the result of recorder malfunctions. Anderson showed that the elimination of those traces that exceeded the standard data set by more than the manufacturer's error criterion, resulted in an XBT data set that closely matched the standard data set. Without this procedure, the XBT data set exhibited positive bias and weaker negative temperature gradients. Any program that uses XBT data taken and admitted without a standard control, such as ships of opportunity, runs the risk of accepting biased data, particularly for the deeper depths. If the program also uses the Emery and Wert[12] method to determine salinity from XBT data and historical T-S curves, then that salinity may also have biases.

Comparisons Between XSVT and CTD/SV Data

Two time series stations serve as the primary means to evaluate expendable performance. The NOSC CTD/SV fish alternated casts to 750 m with the IOS CTD instrument at lowering speeds of ~50 m/min. During the time (~3 hours) it took to complete three CTD/SV casts (Figure 8, the ship expended 35 and 30 XSVT probes at the two sites.

Eight (23%) of the first XSVT series proved visually acceptable for both sound velocity and temperature. The computation of salinity rejected XSVT #41 (Figure 7) leaving seven (20%). Figure 8 displays each parameter's mean ± 2 unbiased standard deviations for the CTD/SV data from the second time series station. Twelve (40%) of the second XSVT series proved visually acceptable, while the salinity computation rejected two, and Figure 9 combines the remaining ten (33%). The $\pm 2\sigma$ patterns for sound velocity and temperature in Figures 8 and 9 remain remarkably similar, indicating that the two systems see essentially the same variance structure. In Figure 9 the $\pm 2\sigma$ salinity envelope varies from about 0.19°/$_{oo}$ to 0.27°/$_{oo}$ (σ = 0.048°/$_{oo}$ to 0.068°/$_{oo}$), generally increasing with depth.

Figures 10 and 11 delineate differences between means of the XSVT and the CTD/SV data for each time series using (1). Tic intervals of 0.1°C, 0.35 m/s and 0.25°/$_{oo}$ represent approximately the same change in the other two variables for shifts in the third near the surface. Excluding differences in the thermocline, where a 1 m relative shift can make large changes, the differences vary from about 0 to 0.11°C, 0.04 to 0.65 m/s and -0.04 to 0.22°/$_{oo}$. Below 100 m salinity differences remain within the range 0.07 to 0.22°/$_{oo}$, with a mean near 0.015°/$_{oo}$, while temperature and sound velocity have mean differences of about 0.06° and 0.4 m/s. Note that in the mixed layer the temperature difference tends to decrease while the sound velocity difference tends to increase with depth. These circumstances have a double positive effect on the XSVT salinity gradient in the mixed layer (the CTD/SV shows essentially constant salinity in the mixed layer). The reasons for these circumstances remain obscure, but we may speculate as to several causes. The sound velocity approaches the correct value near the surface. Indeed, the manufacturer set all the path lengths at near atmospheric pressure. This suggests that something in the mechanical construction allows the path length to shorten until

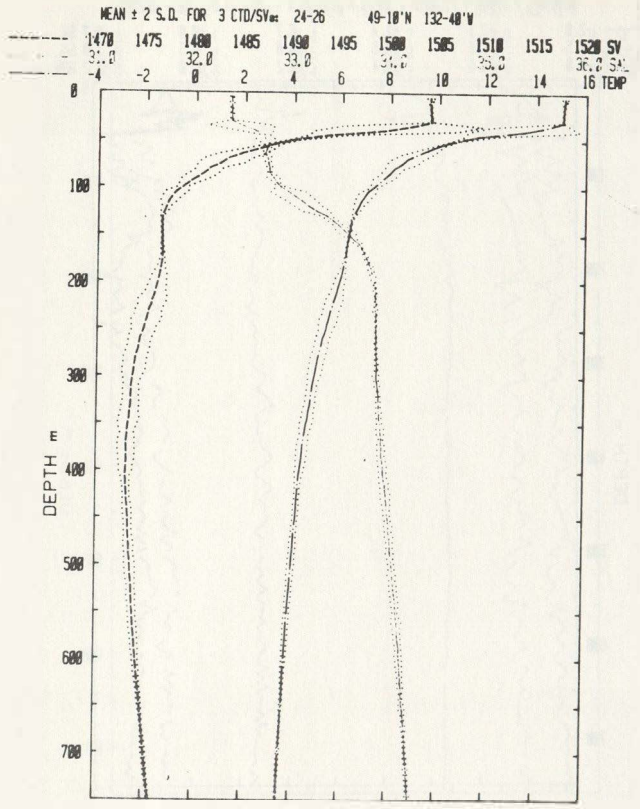

Figure 8. The mean ± 2 σ for three "standard" CTD/SV casts for the first time series at 49°10'N - 132°40'W. Most of the variation is real. Sound velocity - - -, temperature —·—·—·—·—, salinity ————————

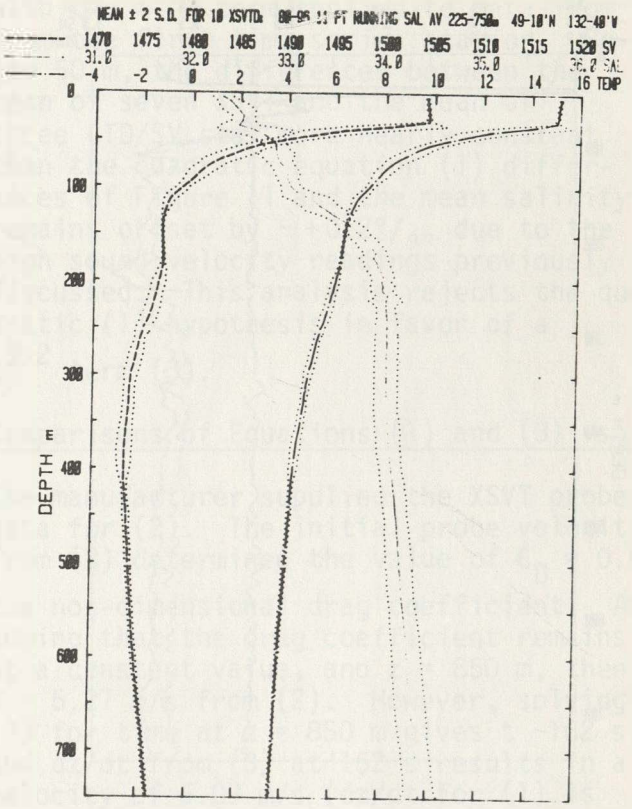

Figure 9. Similar to Figure 8, except ten XSVT probes. Computed salinity shows a much larger ± 2 σ interval (error) than Figure 8. Salinity averaged as in Figure 6.

reaching a certain pressure (~50 db?) where the effect ceases. When the probe first enters the water it usually requires a few tenths of seconds to start singing-around, but appears to acquire good stability before 1 sec or 5 m depth occurs.

The possible reasons for the temperature showing a too-negative gradient in the mixed layer include the combining of quantization, random and 60 Hz noise, although the chances of this occurring almost identically for both time series are improbable.

Depth Equation Revisited

Relevance of a Quadratic Depth Equation

The apparent sound velocity and temperature gradient mismatches below 50 m, in Figures 10 and 11, lead us to examine the applicability of the quadratic depth equation. The XSVT probe loses mass (wire) during descent. Presumably this accounts for the quadratic term of (1). To verify this hypothesis, we examine a terminal velocity equation, where one can show that a deceleration term is negligible:

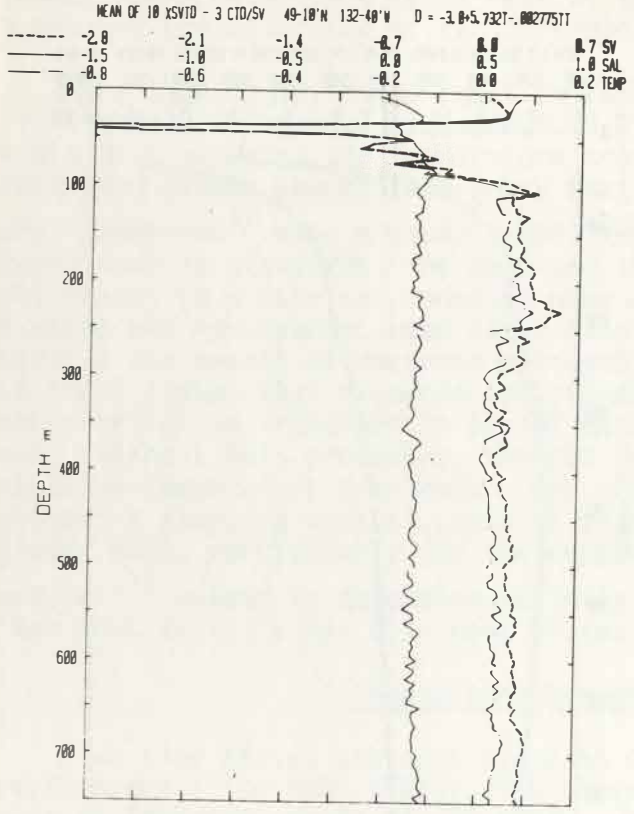

Figure 10. The mean of ten XSVT probes (Figure 9) less the mean of three "standard" CTD/SV casts (Figure 8). Sound velocity - - -, temperature —·—·—·— and salinity ————— for Equation (1).

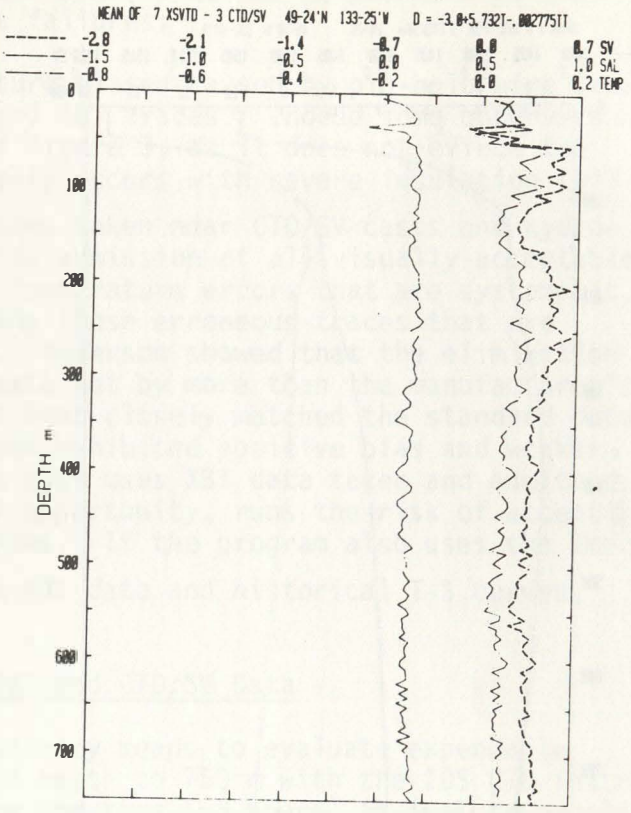

Figure 11. The mean of seven XSVT probes less the mean of three "standard" CTD/SV casts. Sound velocity - - -, temperature —·—·—·— and salinity ————— for Equation (1).

$$V = \left[\frac{MB - \rho_w A_w B_w z}{1/2\ \rho_o A C_D}\right]^{1/2} \qquad (2)$$

where M represents total mass of the probe and wire; B, the probe buoyancy factor, $B = (1 - \rho_o/\rho)g$; B_w, the wire buoyancy factor, $B_w = (1 - \rho_o/\rho_w)g$; ρ, ρ_o and ρ_w, the densities of probe, water and wire; g, acceleration of gravity; A, the probe cross sectional area; A_w, the wire cross sectional area; z, the depth; and C_D the drag coefficient.

To a first approximation, z is linear with t in (1), and replacing z with t in in (2), we have a depth equation of the form $z = \int V dt = \int (a + bt)^{1/2}\, dt = \frac{2}{3b}(a + bt)^{3/2}$. To use polynomial regression techniques, the preceeding equation becomes $z = (c + dt + et^2 + ft^3)^{1/2}$. The resulting fit to the data gives $z = (-168 + 7.82t + 29.97t^2 - 0.01366t^3)^{1/2}$, which becomes imaginary for small values of t, but can be closely represented by

$$z = -2.6 + 5.7t - 0.032t^{3/2} \qquad (3)$$

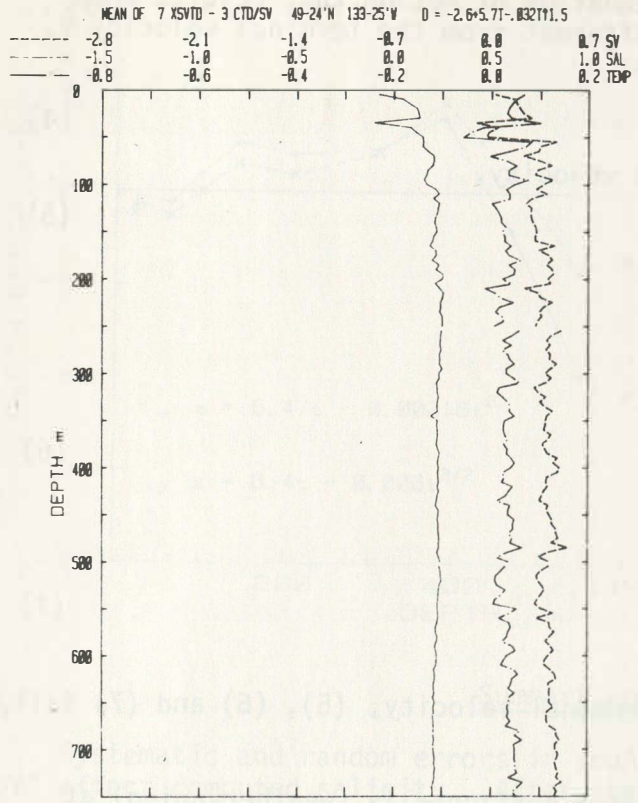

Figure 12. Similar to Figure 11, except for a 3/2 power equation (3) that better represents the data.

Figure 12 depicts the results of (3) with the $t^{3/2}$ term applied to data from from the first time series station. Below 50 m, the differences between the mean of seven XSVT and the mean of three CTD/SV stay more nearly constant than the quadratic equation (1) differences of Figure 11 and the mean salinity remains offset by ~ +0.2°/$_{oo}$ due to the high sound velocity readings previously discussed. This analysis rejects the quadratic (1) hypothesis in favor of a $t^{3/2}$ term (3).

Comparisons of Equations (1) and (3) vs. (2)

The manufacturer supplied the XSVT probe data for (2). The initial probe velocity from (3) determined the value of C_D = 0.098, the non-dimensional drag coefficient. Assuming that the drag coefficient remains at a constant value, and z = 850 m, then V = 5.27 m/s from (2). However, solving (3) for time at z = 850 m gives t ~162 s, and dz/dt from (3) at 162 s results in a velocity of 5.09 m/s (dz/dt for (1) is 4.81 m/s). This velocity difference implies that the coefficient of drag has increased to 0.105. The ratio of velocity times length to kinematic viscosity gives the Reynolds number, $R_e = uL/\nu$. Near the surface R_e ~11.8 x 10^5, while at 850 m, with reduced velocity and increased kinematic viscosity at lower temperatures, R_e ~7.3 x10^5. According to Hoerner (pp. 10-1 to 10-2)[13], fully submerged flow remains laminar up to R_e ~10^7, and the decrease in R_e could explain the increase in C_D for laminar friction. We estimate that the changes in ν, R_e and C_D between this experiment, the Arctic and the tropics might result in depth errors of ~ ±10 m (well within the ± 2% depth error) and the use of (3) in such areas would produce additional offsets in computed salinity of ~ ±0.13°/$_{oo}$ at 850 m.

Effects of XSVT Water Entry on a Depth Equation

The first term of (3) gives an offset of -2.6 m to the depth equation and implies a slower initial velocity than 5.7 m/s. Indeed, equating this term to zero makes the gradient errors worse. A probe dropped from rest in air will reach a velocity of 5.7 m/s from a height less than 1.7 m, while an actual height near 5 m was obtained, implying a velocity of W ~10 m/s upon entering the water. However, the XSVT launcher operator observed that the probes tended to weathervane into the strong winds crossing the stern, and the probe would strike the water in a horizontal position and appear to hesitate momentarily before resuming the normal vertical position and descending. Indeed, application of the terminal velocity equation (2) for the probes greater broadside area, and an estimated C_D of ~0.9 gives

a terminal velocity of ~1 m/s. To solve the equation of motion that results when the probe strikes the water at a velocity W different from the terminal velocity V, one may show from (2) that the acceleration is:

$$du/dt = B(1 - u^2/V^2) \tag{4}$$

Integrating (4) we solve for the instantaneous velocity,

$$u = V(K - 1)/(K + 1) \tag{5}$$

where, $K = \left(\frac{V + W}{V - W}\right) e^{2Bt/V}$

the depth,

$$z = \frac{V^2}{2B} \ln\left(\frac{V^2 - W^2}{V^2 - u^2}\right) \tag{6}$$

and the time,

$$t = \frac{V}{2B} \ln\left[\left(\frac{V + u}{V - u}\right)\left(\frac{V - W}{V + W}\right)\right] \tag{7}$$

When the instantaneous velocity reaches the terminal velocity, (5), (6) and (7) fail, and (2) alone governs the equations of motion.

For the case of the probe striking the water horizontally (weathervaning) at 10 m/s and remaining in the horizontal position for 0.2 sec, it approaches its terminal velocity of ~1 m/s; u = 1.08 m/s; z = 0.42 m and $du/dt = -1.3$ m/s^2. We assume at this point that the probe turns vertically and begins to accelerate towards the initial velocity of (3) (less the wire factor of $-\frac{3}{2} \times 0.032t^{1/2}$).

If the probe enters the water in the normal vertical position and at the "standard" velocity W = V = 5.7 m/s then after 5 sec, difference in depth from the previous case is -2.9 m (within 0.3 m of the first term of equation (3)).

Given that the probe enters the water vertically at 10 m/s, then after 5 sec, the probe is 1.4 m deeper than the "standard" case and 4.3 m deeper than the "weathervane" or horizontal case.

Application of the $t^{3/2}$ Term to the XBT

Flierl and Robinson[14] discuss apparent systematic depth errors in T7 XBTs. Their Figure 1 shows the XBT too deep for the first ~400 m, then too shallow for the last 400 m (Figure 13). An appropriate XBT depth equation with a $t^{3/2}$ term, such as (3) would initially "slow" the XBT down, then allow it to fall "faster" as compared to the standard XBT depth equation, eliminating much of the reported systematic error. Replacing the standard T7 XBT depth equation of $z = 6.47t - 0.00216t^2$, with $z = 6.4t - 0.006t^{3/2}$, provides a better fit to Flierl and Robinson's CTD data (Figure 13).

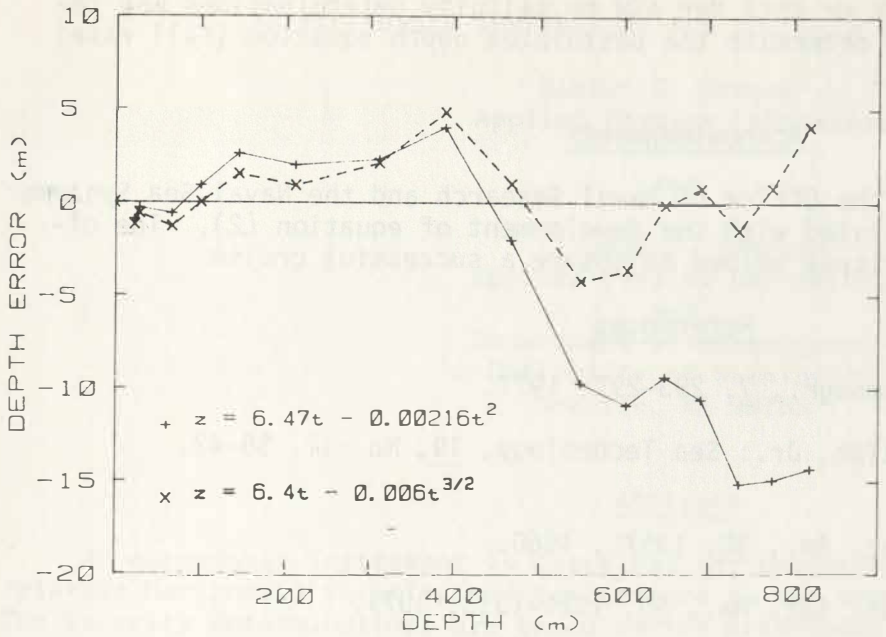

Figure 13. A T7 XBT depth equation with a $t^{3/2}$ term (x) provides a better fit to Flierl and Robinson's[14] than does the standard equation with a quadratic term (+).

Summary and Conclusions

Systematic and random errors in sound velocity, temperature and depth for the XSVT affect computed salinity. After the experiment, the manufacturer believes to have found and eliminated two major sources of random temperature error in the deck equipment. In any reasonably homogeneous area, random depth errors will probably contribute the least to salinity error. However, we believe that oceanic areas having large temperature differences will affect the probe fall rate, and application of a single "universal" depth equation to all areas will result in depth (pressure) and computed salinity errors. If systematic errors repeat from batch to batch, their removal could reduce the salinity offset should the manufacturer prove unable to eliminate or lower them.

A given temperature error in the XSVT will produce ~3 times the salinity error as it would in an XCTD (expendable conductivity, temperature vs. depth). A pressure or depth error causes XSVT salinity errors 20 to 40 times as large as in the XCTD. Clearly the oceanographic community awaits the development of a reliable, accurate XCTD. A current version of the XCTD takes the right step in transmitting all data as FM signals, which eliminate the problems of pin-hole leaks, however, very large temperature errors have reduced its effectiveness in determining salinity.

The XSV or XSVT evaluated as ASW (anti-submarine warfare) devices, disclose both benefits and disadvantages over the XBT. In any area with large (or unknown) salinity changes, the measurement of sound velocity incorporates salinity, and provides the wanted result directly. Wire leaks that cause obvious or insidious errors in the XBT often have no effect on the XSV. On the debit side, the XSVT batch examined here exhibited an excessive positive sound velocity gradient in the mixed layer. Thus, an XSV might predict the presence of a sonic surface duct when none in fact existed. Any depth error has more effect on sound velocity than temperature, due to the pressure terms in the sound velocity equation. Sound velocity computed from an XBT will hopefully use the appropriate pressure vs. depth relationship for its location, hence, a depth error would produce a smaller sound velocity error.

Widespread use of the XSV or XSVT for ASW or salinity determinations may require more experimentation to determine the postulated depth equation (fall rate) changes with mean temperature.

Acknowledgments

This work was funded by the Office of Naval Research and the Naval Sea Systems Command. Dr. H.A. Wilcox assisted with the development of equation (2). The officers and men of the CSS Parizeau helped to ensure a successful cruise.

References

1. W.J. Emery: J. Phys. Oceanogr., 7. 293-297, 1977.

2. M.J. Balboni and W.E. Walsh, Jr.: Sea Technology, 19, No. 11, 38-42, 1978.

3. W. Wilson: J. Acoust. Soc. Am., 32, 1357L, 1960.

4. K.V. Mackenzie: J. Acoust. Soc. Am., 50, 1321-1333, 1971.

5. V.A. Del Grosso: J. Acoust. Soc. Am., 56, 1084-1091, 1974.

6. F.J. Millero and T. Kubinski: J. Acoust. Soc. Am., 57, 312-319, 1975.

7. J.R. Lovett: J. Acoust. Soc. Am., 63, 1713-1718, 1978.

8. E.R. Anderson: "Sound speed in sea water as a function of realistic temperature-salinity-pressure domains." U.S. Naval Undersea R&D Center, TP 243, 1971.

9. C.T. Chen and F.J. Millero: J. Acoust. Soc. Am., 62, 1129-1135, 1977.

10. V.A. Del Grosso and C.W. Mader: J. Acoust. Soc. Am., 52, 961-974, 1972.

11. E.R. Anderson: "Expendable bathythermograph (XBT) accuracy studies, Naval Ocean Systems Center Report" (in press).

12. W.J. Emery and R.T. Wert: J. Phys. Oceanogr., 6, 613-617, 1976.

13. S.F. Hoerner: Fluid-Dynamic Drag, Pub. by author, 2nd Ed, 1965.

14. G.R. Flierl and A.R. Robinson: J. Phys. Oceanogr., 7, 300-302, 1977.

AN EXPENDABLE TEMPERATURE AND VELOCITY PROFILER (XTVP)

Robert G. Drever
Applied Physics Laboratory

and

Thomas B. Sanford
Applied Physics Laboratory
and
Department of Oceanography
University of Washington
Seattle, WA 98105

Abstract

An expendable instrument is described for measuring vertical profiles of relative horizontal velocity and temperature in the upper 750 meters of the ocean. The velocity determinations are based on the principles of electromagnetic induction which govern the weak electric currents induced by the motion of sea water through the earth's magnetic field. The resulting electric current profile corresponds to the velocity profile relative to an unknown, depth-independent reference velocity. The method yields this relative velocity profile with a vertical resolution of 10 meters and an uncertainty of 1 cm/s rms. With a remote surface release (to remove probe from the electric and magnetic disturbances of a vessel) the instrument performs well from the surface to 750 meters.

I. Introduction

Measurement of current velocity in the deep ocean presents numerous difficulties to oceanographers. In addition to maintaining functioning equipment in a frequently hostile environment, it is necessary to establish a frame of reference through which the motion is determined. Frequently, this reference frame is established by attaching the current meters to a bottom-anchored mooring or mapping a drifting body's locations in a radio or acoustic navigation net. A third choice, one proposed here, is the use of the reference frame provided by the earth's magnetic field. Motion of sea water through the geomagnetic field induces weak, but measurable, electric fields and currents. This paper describes a device for making induced electric current measurement at sea from an expendable profiler.

The motivation for developing an expendable electric current profiler stems from the need to measure the vertical structure of deep-ocean currents and waves. Profiles of the depth variations of velocity have revealed new complexities of the momentum field in ocean currents and waves. Reminiscent of early CTD measurements, velocity profiles contain more structure, zones of high velocity and shear, than moored sensors show. Oceanographers are now more aware of the large gradients in velocity and kinetic energy which exist in time and space. However, our ability to observe these gradients and assess their dynamical roles is limited by the difficulties involved in obtaining the measurements. These observations are not only expensive in terms of ship time, support personnel, and instrumentation, but also are limited by the availability, mobility, convenience, and accuracy of suitable methods. As a result, velocity profiles have been made in only a few areas in the deep ocean and over brief periods of time.

Yet knowledge of the shear field in the surface and thermocline region is of vital importance in numerous studies in which real-time data are needed on the temporal and spatial structure of the flow. Examples of research in which velocity profiles are essential are studies of: 1) mixed layers, 2) oceanic fronts, 3) Gulf Stream rings, 4) mid-ocean eddies, 5) internal waves, and 6) acoustical propagation.

Among the number of schemes which have been used to collect velocity profiles in the deep sea are[1]: 1) acoustical tracking of freely-falling probes; 2) current meters falling along a taut wire suspended from a ship or buoy; 3) a current meter slowly lowered from a tracked buoy; 4) freely-falling current meters measuring relative velocities (i.e., the difference between the velocity of the water and that of the probe, a difference usually due to vertical shear); 5) motionally induced EMFs.

An expendable deep ocean velocity profiling system has been developed that operates on the principles of motional induction (item 5 above) from a freely falling probe. The method, which is called the Expendable Temperature and Velocity Profiler (XTVP), consists of instrumentation to measure electric currents in the sea arising from the motion of sea water through the earth's magnetic field. These measurements yield a profile of the horizontal velocity, but the profile is not of absolute velocity, rather it is relative to a depth independent or reference velocity. This unknown reference velocity, which is frequently of secondary interest, must be determined from an independent method such as of surface currents or of the velocity at any depth level from a ship-borne acoustic backscatter system.

The advantage of the XTVP method is that it is mobile, requiring no bottom beacons or special shipboard navigation systems. The data is telemetered to the ship in real-time, and a profile is obtained in less than four minutes from a ship under way. The probe is acoustically passive and since expendable requires no specially-trained personnel or ship time for recovery.

The disadvantages of the method are that it is not well suited to the collection of long time series, since it presently must be operated from a ship, although air- and buoy-deployed versions are feasible. The method depends on the magnitude and stability of the geomagnetic field. Hence, it cannot operate near the geomagnetic equator where the vertical component of the magnetic field vanishes, and it is subject to errors during periods of strong geomagnetic or magneto-telluric disturbances. It does not yield absolute velocity profiles by itself.

II. Method of Operation of the Expendable Profiler

The method of operation of the expendable temperature and velocity profiler has been developed based upon our experience with a free-fall electromagnetic velocity profiler[1] (EMVP). The XTVP shown in Fig. 1 is made from standard expendable bathythermograph (XBT, Sippican Corp.) parts with the addition of an 11.5-inch center section of active electronics. As the probe falls and spins through the water column, it amplifies the weak motionally-induced electric field and transmits this signal up a pair of #39 wires to the ship.

The very low signal levels place stringent requirements on the expendable electronics. The signal, $\Delta\phi$, from a falling, rotating electrode line pointing in the direction, θ , measured clockwise from geomagnetic north, is:

$$\Delta\phi = F_z L(u-\bar{u})(1+c_1) \cos\theta - [F_z L(v-\bar{v})(1+c_1) - F_H LW(1+c_2)] \sin\theta \qquad (1)$$

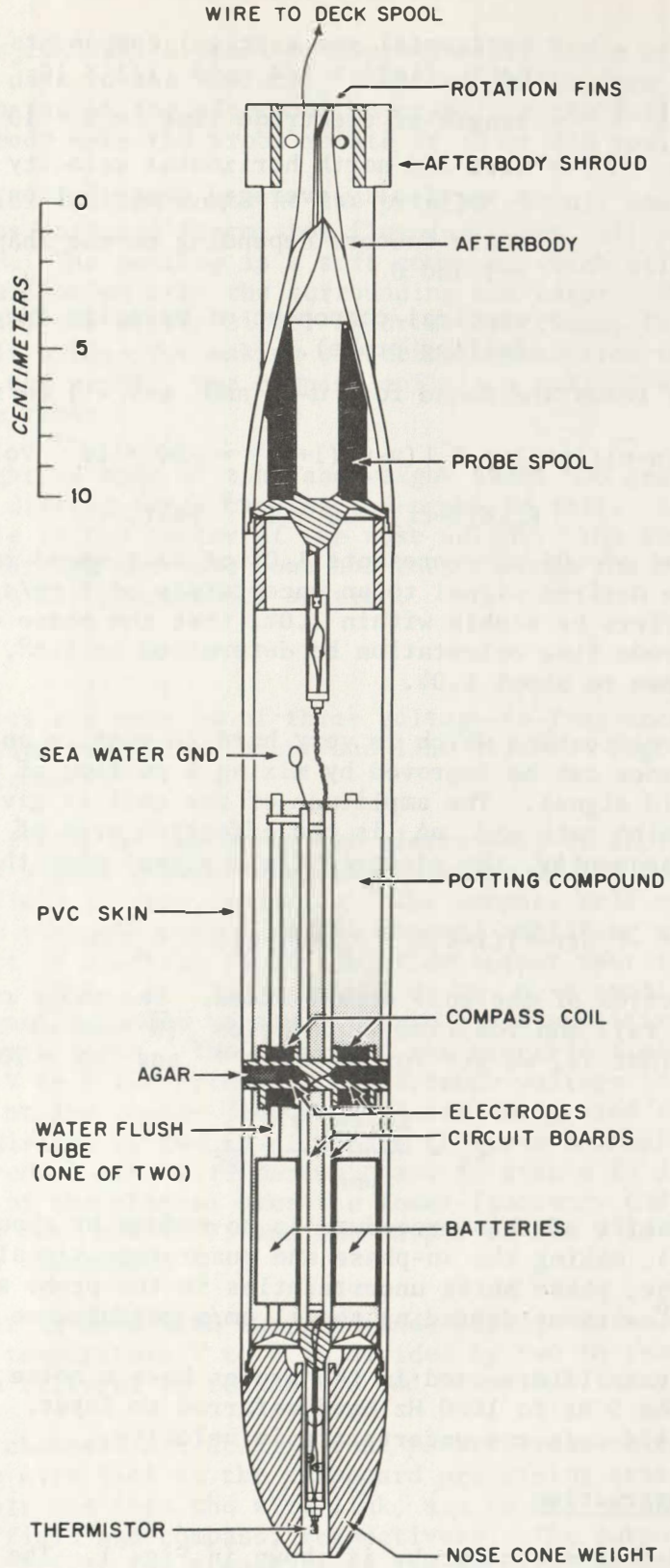

Fig. 1. Expendable Temperature and Velocity Profiler (XTVP-4)

where

F_H and F_z = horizontal and vertical components of the geomagnetic field $\simeq 1/4$ and $-1/2 \times 10^{-4}$ Weber/m^2

L = length of electrode line $\simeq 5 \times 10^{-2}$ m

$u-\bar{u}$ and $v-\bar{v}$ = east and north horizontal velocity components minus a vertically-averaged contribution

c_1 and c_2 = scale factors depending on the shape of the probe $\simeq 1$ and 0

W = vertical component of velocity (negative value for falling probe).

The magnitudes of terms are found for $u-\bar{u}$ and $v-\bar{v}$ = 1 cm/s and for W = 4 m/s:

$$F_z L(u-\bar{u})(1+c_1) = F_z L(v-\bar{v})(1+c_1) = -50 \times 10^{-9} \text{ Volt.} \quad (2)$$

$$F_H LW(1+c_2) = 5 \times 10^{-6} \text{ Volt.} \quad (3)$$

Thus the desired signal of .05 μV represents 1.0% of fall speed induced signal of 5 μV . To resolve the desired signal to an uncertainty of 1 cm/s requires that the gain of the amplifiers be stable within 1.0%, that the phase of the signal relative to the electrode line orientation be determined to 0.6°, and that the fall speed must be known to about 1.0%.

The 0.6° is a specification which is very hard to meet in an expendable probe. The phase error tolerance can be improved by mixing a portion of the coil signal with the electric field signal. The amplitude of the coil is given by $F_H \omega nA$, where ω is the rotation rate and nA is the effective area of the coil times the number of turns. Consequently, the electric field signal plus the coil contribution would be

$$\text{in-phase} = -F_z L(v-\bar{v})(1+c_1) + F_H LW(1+c_2) - F_H \omega nAc_3 \quad (4)$$

where c_3 is the fraction of the coil signal added. The value of c_3 is chosen such that for average fall and rotation frequencies ($\bar{W}$ and $\bar{\omega}$) the last two terms about cancel. That is, we get for $\omega = 50 s^{-1}$ and $nA = 10^3$ cm^2

$$c_3 = \frac{L\bar{W}(1+c_2)}{\bar{\omega}nA} \sim \frac{1}{25}$$

The principal benefit of this procedure is to reduce by about 90% the magnitude of the in-phase signal, making the in-phase and quadrature signals of comparable strength. In this case, phase shift uncertainties in the probe and deck equipment can be as large as $\pm 6^\circ$ without degrading the ± 1 cm/s performance goal.

The low-noise preamplifiers used in the probes have a noise voltage of about 10×10^{-9} V/$\sqrt{\text{Hz}}$ in the 5 Hz to 1000 Hz band referred to input. This noise level corresponds to about 1/4 cm/s rms uncertainty in velocity.

Probe Package and Construction

The mechanical design of the probe is shown in Fig. 1. The probe is 52 cm long, 5 cm in diameter, and weighs in air approximately 1470 grams. In sea water the probe weighs approximately 800 grams. The three main parts of the probe are

the afterbody, electronics section and nose weight.

The afterbody contains a spool of approximately 800 m of two-conductor, #39 wire used to send data to the surface. A shroud in the form of a right cylindrical shell has been mounted on the afterbody to stabilize the fall of the probe. The fins of the afterbody make the probe rotate at about 450 rpm.

The electronics section contains two printed circuit boards, batteries, electrodes, compass coil and thermistor flushing tubes, all potted inside of a thin-wall PVC tube. The potting is a soft compound which allows the components to be at pressure equilibrium with the surrounding sea water. The electric field sensor is made up of two silver-silver chloride electrodes in tubes filled with agar to form a salt bridge for making electrical connection to the sea water at the outer skin of the probe. The compass coil is a coil of wire wound coaxially over the electrode tubes.

The nose weight is made of zinc and weighs about 500 grams in sea water and supplies the main driving force causing the probe to fall. A thermistor is mounted in the hole in the center of the nose weight. The thermistor is flushed by water passing through the nose cone and then through the two flushing tubes which are potted in the electronics section.

Probe Electronics

The electronics are made up of three voltage-to-frequency converters (V to F), battery pack, voltage regulator, mixer and line driver. Fig. 2 is a block diagram of the probe electronics.

The electric field, as sensed by the electrodes, is amplified by a low-noise preamplifier. The signal generated by the rotation of the compass coil in the earth's magnetic field is also amplified. The compass coil and the electrodes have been wired so that the output of the compass amplifier will be 180^{o} out of phase with the part of electric field amplifier output that is due to the fall rate term, $F_H LW(1+C_2)$, of Eq. 1. As described in Eq. 5, a small amount of the compass coil amplifier signal is added to the electric field amplifier signal to cancel most of the fall rate term. The output of the electric field post amplifier is AC coupled into a V to F converter. The reference voltage is used to offset the V to F to operate at the center frequency of its designated channel. The output of the V to F is divided by two to eliminate the even harmonics. The signal is then filtered to reduce the third harmonic and to give a 10 dB boost to the higher-frequency portion of the channel over the lower-frequency end. The compass signal is also AC coupled into a V to F, and the output of the V to F is divided by two to remove the even harmonics.

The thermistor is used with the reference voltage to modulate a third V to F. The output of the temperature V to F is divided by two to remove the even harmonic. The signal is then filtered to reduce the odd harmonics.

The three FM channels are at different power levels to compensate for signal attenuation on the wire link to the shipboard processing system. The signal levels, referenced to 1 volt rms into the wire link, are -8 dB, +3 dB and +12 dB for temperature, electric field and compass, respectively. The output stage of the mixer is a balanced line driver for transmitting the FM data to the shipboard processing system over the two-conductor link.

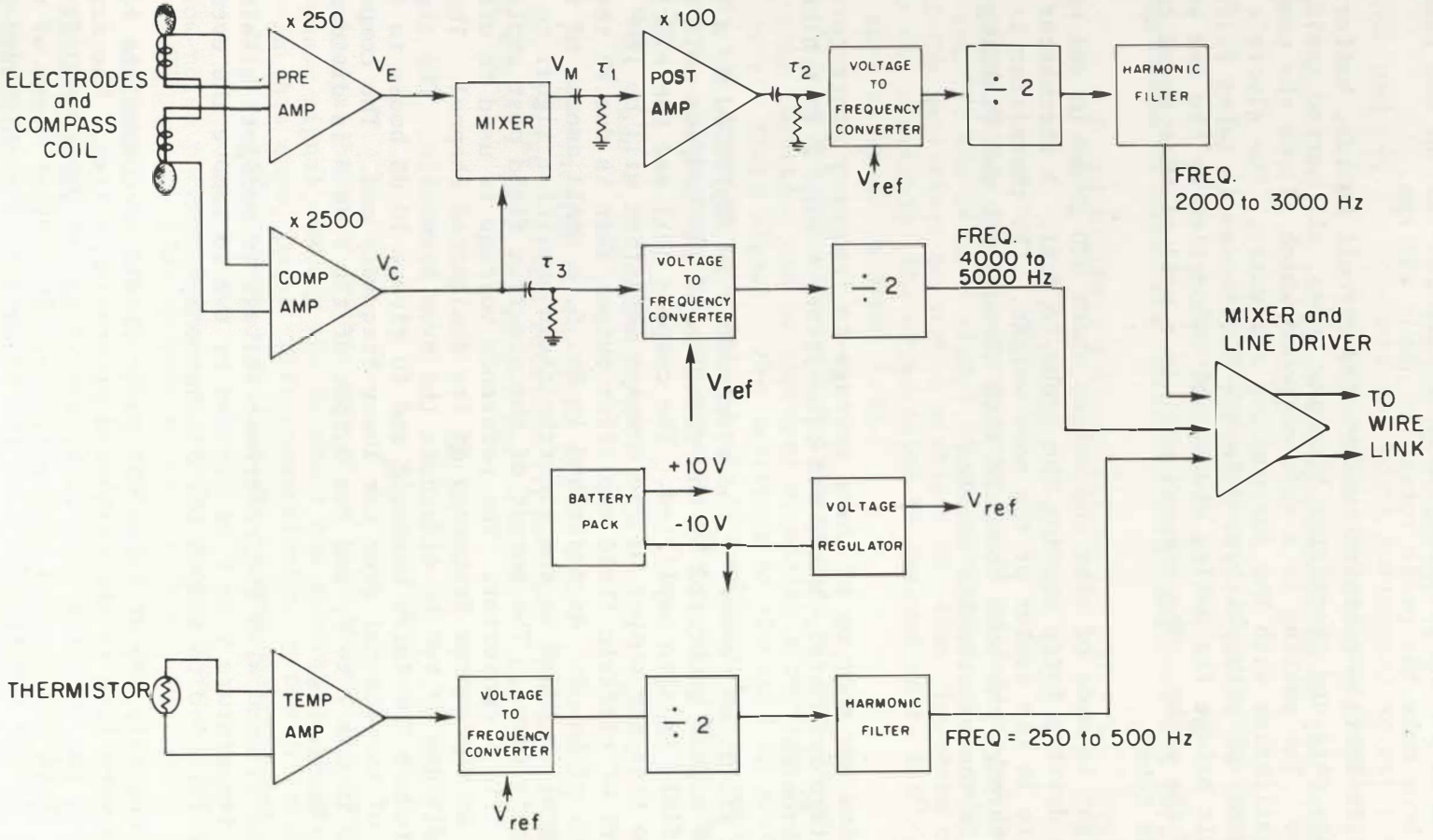

$V_M = .992\ V_E - K\ V_C$

$\tau_1 = 188$ ms, $\tau_2 = 150$ ms, $\tau_3 = 1$ sec.

Fig. 2. Block Diagram of XTVP Mod 4

Shipboard Processing System

The shipboard processing system, Fig. 3, consists of the XTVP receiver, two custom-design, plug-in units for a Tektronix TM 500 module, and standard laboratory instrumentation.

The three channels of FM data are transmitted to the ship by way of the expendable wire link. The signals are transformer coupled, amplified and filtered into the three separate frequency bands. These three FM signals are recorded on a HP3960 tape recorder so the data can be replayed after the drop. The period of the temperature frequency is measured in a counter and converted to a voltage, V_T, which can be displayed on the XY plotter. The electric field and compass frequencies are converted to voltages, V_E and V_C, respectively, which are a linear representation of the voltages sensed by the probe.

The compass voltage, V_C, is used as a reference signal for the two-phase, lock-in amplifier. The lock-in amplifier synchronously demolulates the electric field voltage into in-phase (north-south) and quadrature (east-west) components with respect to the compass signal. These signals are recorded on the two-pen XY recorder as a function of time (depth) in real-time as the probe is falling. Thus the velocity data is available for immediate examination and analysis in analog form.

The processing system also measures and plots the in-phase and quadrature of the compass signal and the period of the compass signal.

Currently the analog plots are digitized after the cruise and processed on a HP9845S computer. The east and north velocity components are compensated for the fall-rate-induced contribution and for the probe and receiver transfer functions.

A digital shipboard processing system has been designed and is being tested. This system, with the aid of an HP9845S computer, will process the data to give real time plots of north and east components of velocity. The digital system will be used in a study of ocean fronts in January of 1980.

III. Operational Experience and Performance

The XTVPs have been used successfully by us on three field experiments. The first 200 were made at Woods Hole Oceanographic Institution and an additional 250 units have been made by Sippican Corporation of Marion, Massachusetts.

An example of our use was a survey in June 1978 around the 2 km high Caryn Seamount, located in water 5 km deep along a line from Cape Cod to Bermuda. Fig. 4 and 5 are samples of the data measured during the survey. Drops 109 and 113 are spaced in time by one hour and twenty minutes and are separated by one mile. Observe how closely these two drops compare in east and north components.

The XTVP has been used in one comparison experiment with an acoustically tracked falling profiler operated by Dr. David Wenstrand of the Applied Physics Laboratory, The Johns Hopkins University. In these tests at the Atlantic Underwater Test and Evaluation Center (AUTEC), the discrepancies between methods ranged from 0.5 to 1.7 cm/s rms over 100 m depth intervals. Other tests have shown the XTVP to be reproducible to better than 1 cm/s rms over profiles taken 5 - 10 minutes apart.

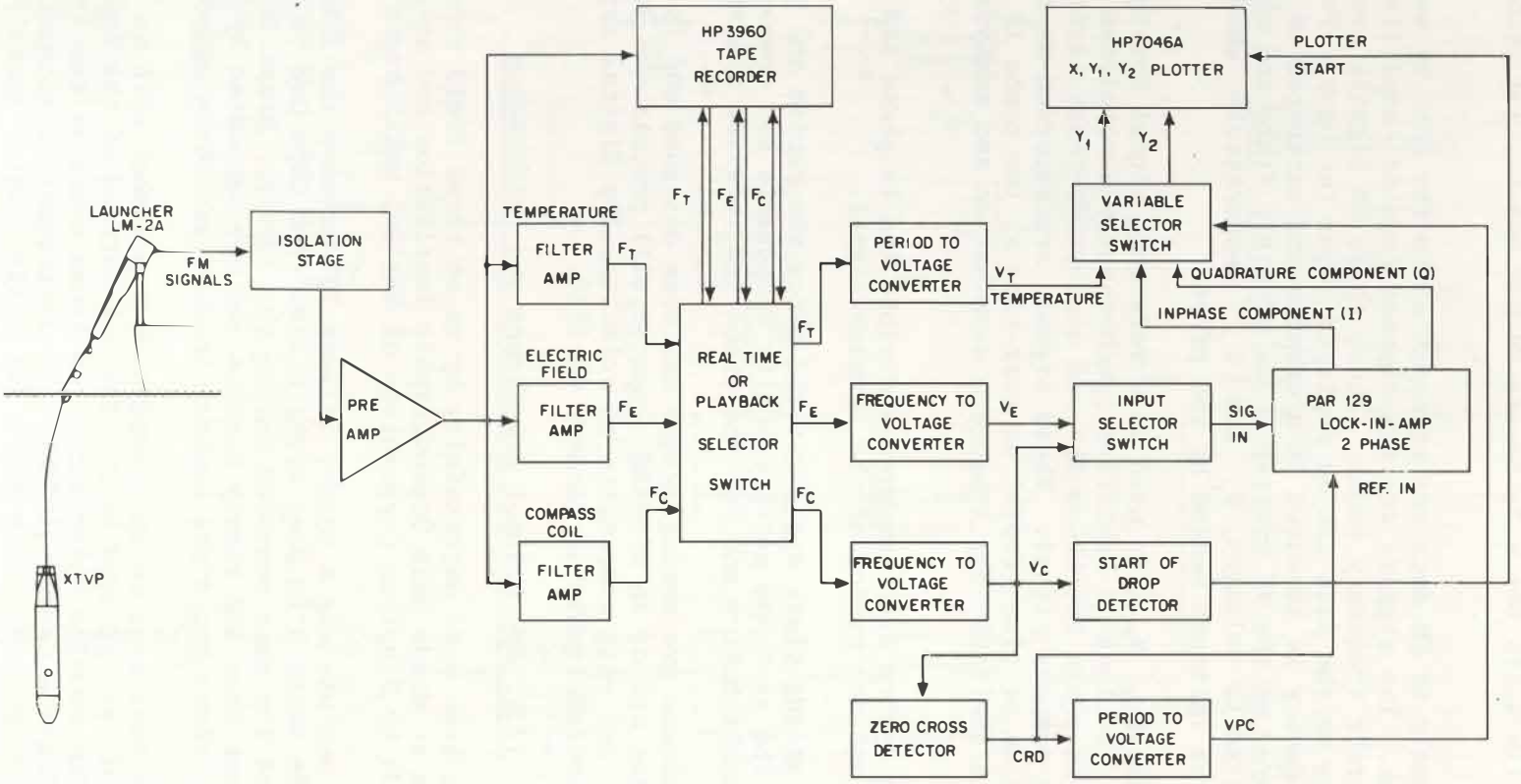

Fig. 3. XTVP Shipboard Processing System

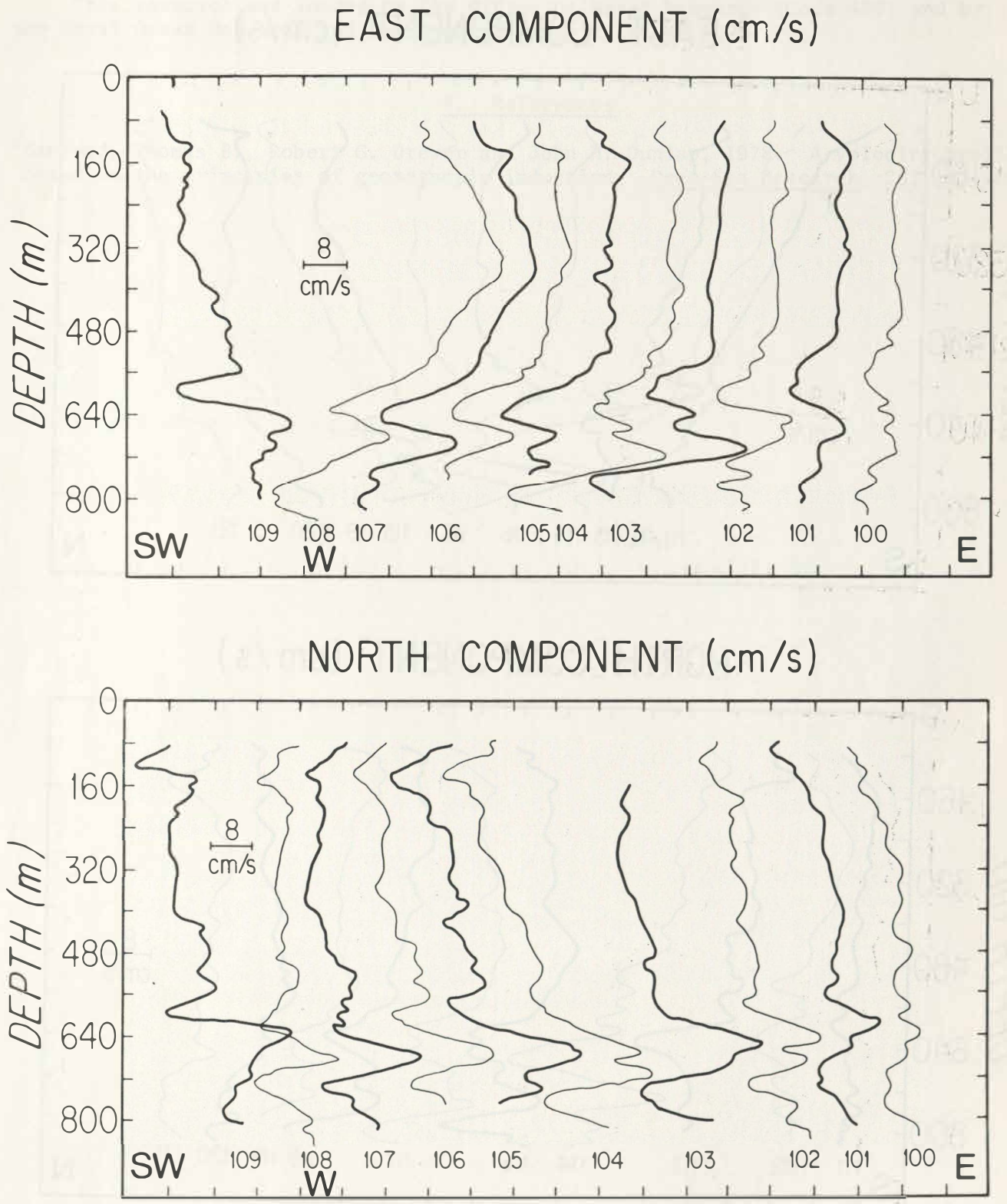

Fig. 4. XTVP Profiles over the Caryn Peak along an East to West Sectior

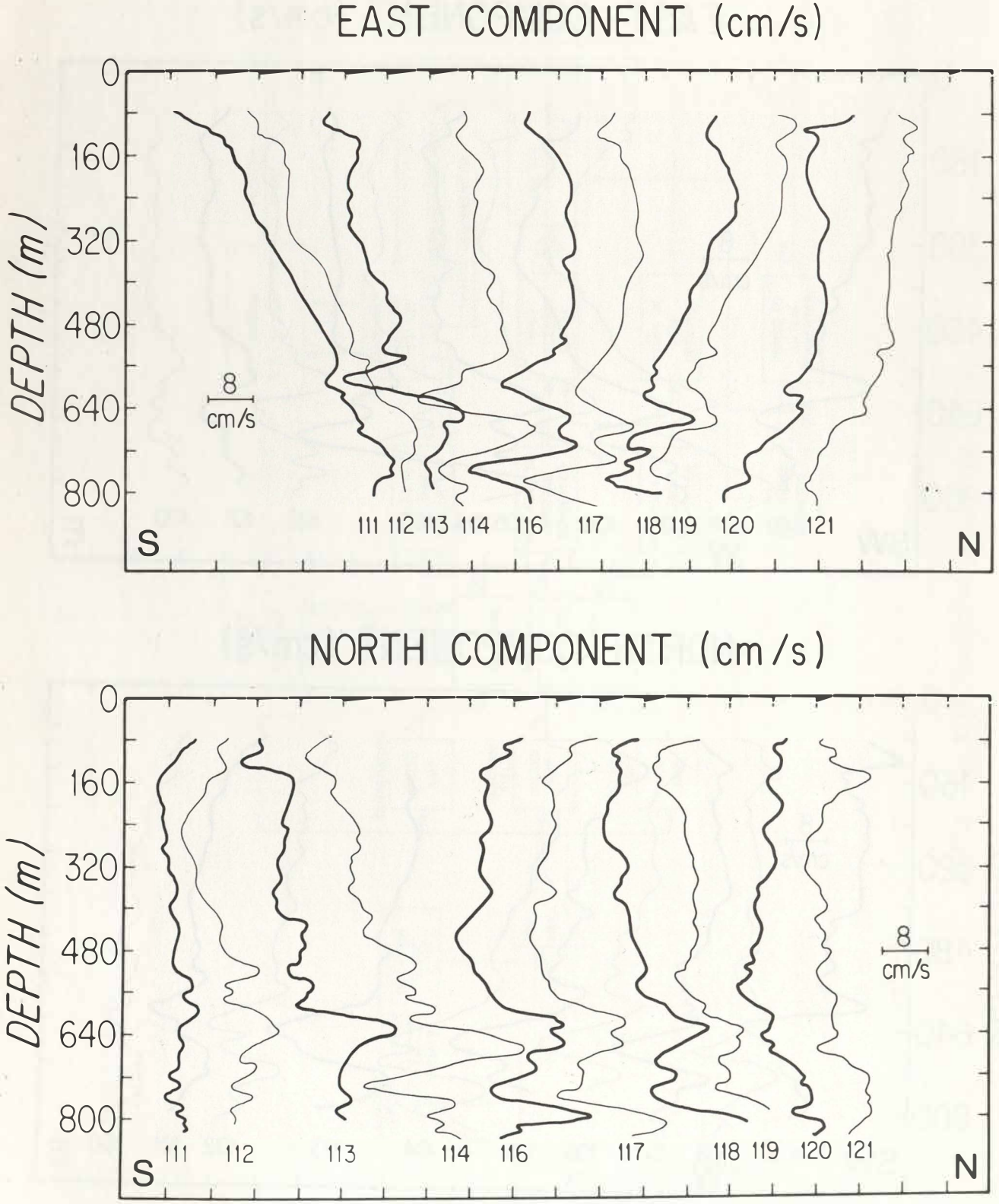

Fig. 5. XTVP Profiles over the Caryn Peak along a South to North Section.

IV. Acknowledgements

This research was funded by the Office of Naval Research (Code 480) and by the Naval Ocean Research and Development Activity (Code 500).

V. References

[1]Sanford, Thomas B., Robert G. Drever and John H. Dunlap, 1978. A velocity profiler based on the principles of geomagnetic induction. Deep-Sea Research, 25, 183-200.

THE DEVELOPMENT OF AN EXPENDABLE VELOCITY MICROSTRUCTURE PROFILER

Rolf G. Lueck and Thomas R. Osborn
Department of Oceanography
University of British Columbia
Vancouver, B.C., Canada
V6T 1W5

Abstract

This report presents our progress, to date, towards the development of an expendable profiler to measure the vertical gradient of horizontal velocity on scales small enough to produce profiles of the viscous dissipation of kinetic energy in the ocean. The proposed instrument consists of a small-scale velocity shear sensor and a thermistor mounted on a modified version of a Sippican Expendable Bathythermograph (XBT). The major development problems and our attempts towards solving these problems are discussed along with a proposed design which will shortly be available for testing. The sensed parameters, shear and temperature, are telemetered to the surface by FM telemetry up a standard XBT wire link.

Introduction

The long range scientific goal of microstructure measurements is to understand the role of turbulence in determining the circulation and the distribution of salt and heat in the ocean. Non-expendable vertical profiling instruments are now being used by several groups such as Gregg[1] (1977), Marmorino and Caldwell[2] (1978), Mortensen and Lange[3] (1976), Elliott and Oakey[4] (1976) and Osborn[5] (1978). Their relatively long surface-to-surface trip time of approximately one hour makes most of these vehicles unsuitable for spatially and temporally dense profiling, and their relatively large mass of approximately 100 kg makes them awkward and sometimes dangerous to use during high sea states. However, there is presently a large amount of interest in upper ocean dynamics during periods of high winds, where the use of non-expendable instruments is unfortunately limited. An expendable profiling instrument is advantageous in that it could easily be used during high sea states and for dense profiling surveys.

Objective

Our objective is to provide a simple, expendable and reliable system for surveying the turbulence in the ocean. The measured parameter will be velocity shear on a scale small enough to produce profiles of kinetic energy dissipation and temperature on a fine structure scale.

Proposed Design

The expendable profiler will consist of a small-scale velocity shear probe (Osborn and Crawford[6], 1979) and a thermistor mounted on a Sippican body* such as a modified XBT. The probes and their associated electronics, namely an analogue amplifier and a voltage-to-frequency (FM) converter will be incorporated into the vehicle. The design is sketched in Figure 1 and its details are discussed below.

Problems

In principle, the vehicle's construction should be straightforward. There are, however, a number of design obstacles to the production of a fully operational system.

1. Vehicle Motions

(a) Fall Speed

The fall speed influences both the mechanical and the electrical design of the vehicle. The rate of kinetic energy dissipation estimated from the shear probe's measurements is inversely proportional to the fourth power of the fall speed, i.e. $\varepsilon \alpha U^{-4}$, and hence must be determined as accurately as possible. The spatial scale of the shear motions contributing to kinetic energy dissipation is effectively fixed to the approximate range of 1 meter to 1 centimeter. The frequency range of interest is thus exclusively determined by the fall speed to $f = U/\lambda$, where $10^{-2} \lesssim \lambda \lesssim 1$ m. The fall speed also influences the vehicle's motion and care must be taken to minimize undesirable motions throughout the frequency range of interest.

(b) Static and Dynamic Stability

The vehicle must be stable in the absence of any disturbances and any pitching oscillation must have a frequency well below $f = U / 1$ meter. The vehicle must also have sufficient pitch damping to remain stable when exposed to horizontal shears. Unlike XBT's, the vehicle must not rotate and so must be drag stabilized by something other than the fin tabs commonly found on XBT's.

(c) Streaming Noise

Because the shear probe is sensitive to vehicle vibrations, hydrodynamic noise such as eddy shedding must remain sufficiently low for the probe to resolve weaker dissipation regimes.

2. Spatial and Temporal Resolution

Spatial and temporal averaging by the shear probe may inhibit the full resolution of all the variance contributing to the dissipation of kinetic energy. The wavenumber and frequency response of the shear probe must be more precisely known to determine how much correction, if any, is needed.

---

* Sippican Corporation, Oceanographic Systems Division, Marion, Massachusetts 02738, U.S.A.

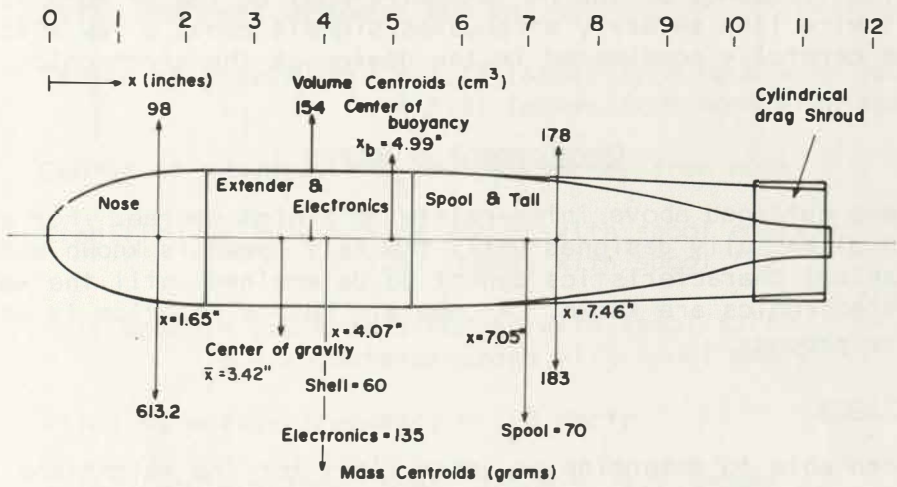

Figure 1. Design of proposed expendable vehicle showing the mass and volume distribution, the center of gravity and the center of buoyancy. Drag stabilization is provided by the cylindrical shroud at the stern. Probes are not shown.

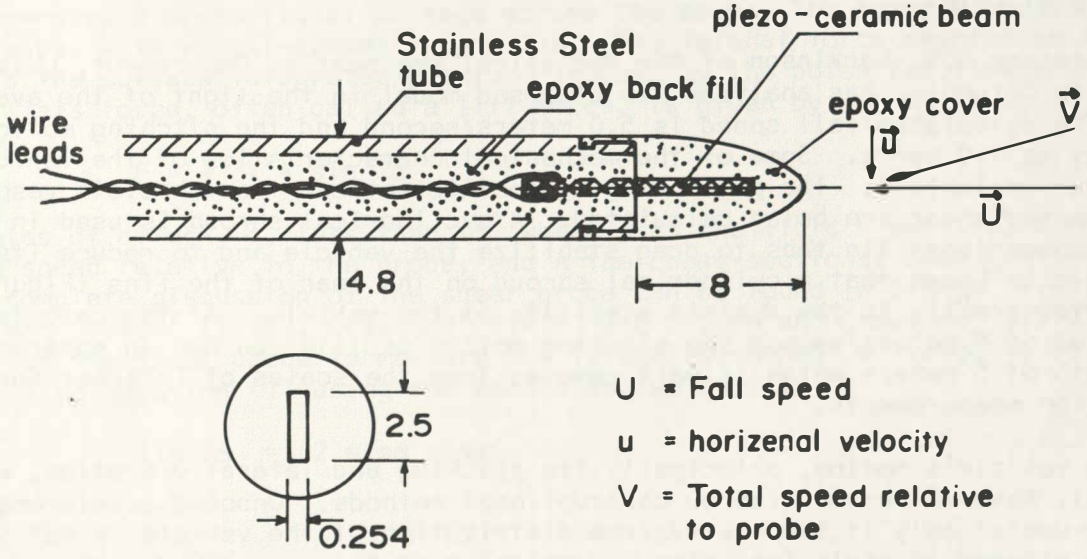

Figure 2. Detail of shear probe and velocity vectors relative to the probe. Dimensions are in units of millimeters.

3. Electronics

The fall speed will very likely be in the range of 2 to 5 meters/second and hence the upper limit to the data band frequency will be 200 to 500 Hz. For technical reasons the frequency of the FM telemetry must be ten or more times higher. The XBT type of wire link severely attenuates signals above a few kiloHertz and so will need to be carefully considered in the design of the electronics.

Development Progress

The problems outlined above inter-relate to a high degree. For example, the electronics cannot be fully designed until the fall speed is known but the vehicle's mechanical characteristics cannot be determined until the weight and volume of the electronics are known. A complete design solution is only obtained via an iterative process.

1. Vehicle Motions

We have been able to determine an upper limit for the weight and volume of the electronics and batteries needed to satisfy the data telemetry requirements. This information has allowed us to make a first mechanical design (Figure 1) for which the vehicle's motions have been evaluated. Ideally, one would like to place a full scale model of the vehicle into a water tunnel equipped with a suitable force balance and measure its drag, lift and torque as a function of Reynolds number. The calculation of the relevant vehicle motions would then be straight forward. However, we have been unable to locate a tunnel with a force balance suitable for measuring the relatively small hydrodynamic forces exerted on the proposed vehicle. Fortunately, a large amount of experimental data on streamlined axi-symmetric bodies is available and it is possible to do a very reasonable calculation of the characteristics of the free fall vehicle from already available experimental data.

Professor G.V. Parkinson of the Mechanical Engineering Department, University of British Columbia, has analyzed the proposed model in the light of the available data. The calculated fall speed is 5.0 meters/second and the pitching motion frequency is 1.0 Hertz. Some of the mechanical characteristics of the vehicle are listed in Table 1. The pitch damping coefficient and the vehicle's response to an imposed shear are being calculated. A cyclindrical shroud is used in place of the conventional fin tabs to drag stabilize the vehicle and to reduce its fall speed. It is known that a cylindrical shroud on the rear of the fins (Figure 1) contributes greatly to the dynamic stability of the vehicle. At the calculated fall speed of 5 meters/second the pitching motion oscillation has an apparent wavelength of 5 meters which is well removed from the scales of interest for the dissipation measurements.

The vehicle's motion, principally its pitching and lateral vibration, will inevitably have to be verified by observational methods. Onboard accelerometers would be useful only if the mass-volume distribution of the vehicle is not significantly altered by their inclusion. Vertical test tanks equipped with cameras are available and these might be successfully used to measure the pitching oscillation and the fall speed. A measurement of lateral vibrations and other signal contaminating noise could be made by dropping the expendable vehicle into a quiet water column such as a flooded coal mine shaft or deep ocean waters. For the latter test, side-by-side comparisons with our larger non-expendable Camel dissipation profiler are possible.

Table 1. Specifications of Proposed Expendable Vehicle

Total enclosed mass = 1060 grams

Total enclosed volume = 605 cm^3

Center of gravity = $\bar{x}$ = 3.42 inches from nose with spool full
= 3.21 inches from nose with spool empty

Center of buoyancy = x_b = 4.99 inches from nose

Stability $x_L - \bar{x}$ = 1.78 inches with spool empty
= 1.57 inches with spool full

Fall speed = 5.0 meters/second with spool full
= 4.75 meters/second with spool empty

Pitching motion frequency = 1.0 Hertz

Total length without shear probe = 11.5 inches

Widest diameter = 2.0 inches

No fin tabs, cylindrical shroud at the stern.

2. Shear Probe

A shematic drawing of the actual dissipation sensing element, the shear probe is shown in Figure 2. The shear probe consists of a piezo-ceramic beam made of lead-zirconium titanate to the dimensions of 1.27 by 0.25 by 0.025 cm. The beam is the transducer in a ceramic phonograph cartridge. A microscopic bending of the beam generates a proportional voltage across the beam. The beam is encased in epoxy rubber with an axi-symmetric profile. The lateral force exerted on the probe is the surface integrated pressure induced by the potential flow around the probe. This force, often called a lift force, is given by

$$F = \tfrac{1}{2} \rho V^2 A \sin 2\alpha \qquad (1)$$

for angles of attack, α, less than 15° where ρ is the fluid's density, V the fluid's speed relative to the probe, and A the cross-sectional area of the probe. A more complete discussion of the shear probe can be found in Siddon[7] (1971), Osborn and Siddon[8] (1975), Crawford[9] (1976) and Osborn and Crawford[6] (1979). The ability of the shear probe to measure the lateral component of velocity is seen by rewriting equation (1) using the double angle identity

$$\sin 2\alpha = 2 \sin\alpha \cos\alpha$$

to read

$$F = \rho U A u \qquad (2)$$

where the lateral component, u, is shown in Figure 2. The force on the probe and hence the voltage across the beam is proportional to the cross-stream velocity component normal to the plane of the beam. The shear probes are calibrated by rotating them in a free jet; the total axial force on a probe remains constant

but the force in the plane of the beam varies sinusoidally because of the rotation. The sensitivity of individual probes is determined by plotting

$$\frac{E}{\rho V^2} \text{ against } \sin 2\alpha \qquad (3)$$

where E is the peak voltage across the probe. Typical sensitivity values are 6×10^{-4} volts per gm-cm^2-sec^{-2}.

A crucial question is whether the shear probe has sufficient resolution, both temporal and spatial, to measure all the variance of the velocity shear contributing to viscous dissipation. As shown, the shear probe is primarily sensitive to pressure forces which are proportional to Uu (Fig. 2) whereas inertial forces are proportional to uu which is several hundred times smaller. Because inertial forces are relatively small the shear probe should not be frequency response limited. We have tested this hypothesis by placing the shear probe into the turbulent wake of a 0.3 cm diameter rod at 100 diameters downstream from the rod. The tests were performed in the water tunnel of the Naval Ocean Systems Center at San Diego. The turbulence near the probe was simultaneously monitored by a Laser Doppler Anemometer (LDA). If the LDA is a suitable standard for comparison, then both the frequency response and the wavenumber response of the shear probe can be determined. Numerous difficulties with the LDA that need not be discussed here precluded that LDA from being a suitable standard for comparison. However, the shear probe measurements by themselves gave us some valuable insights into the probe's characteristics.

Measurements were made from 0.5 to 3.5 meters/second. Over the corresponding Reynold's number range, measurements in a wind tunnel with hot wire probes by Uberoi and Freymuth[10] (1969) show that the wavenumber spectra when normalized by their total variance are independent of the Reynolds number. Plotted in Figure 3 are the normalized spectra as measured by the shear probe for all flow speeds where rod vibrations were not detected. The shape and level of the spectra for various flow speeds are virtually independent of the flow speed but very dependent on the wavenumber. We can thus conclude that the shear probe's frequency response far exceeds 500 Hz, the highest frequency investigated.

A weaker conclusion can be drawn about the wavenumber response. The characteristic hump of the spectra was also observed by Uberoi and Freymuth[10] (1969) and if we compare our spectra against theirs the response of the shear probe is attenuated by 3 dB at 0.25 cycles/cm, i.e. a wavelength of 4 cm. However, the question of the wavenumber response can only be satisfactorily answered by direct in situ comparison, against a suitable standard. We are presently engaged in a second attempt at measuring the wavenumber response with an LDA and we expect either to determine successfully the spatial resolution of the shear probe or to determine finally that the Laser Doppler Anemometer is not a suitable instrument for comparison.

3. Electronics

As there are no apparent frequency limitations on the response of the shear probe, the characteristics of the electronics are determined exclusively by the fall speed, the spatial scale of interest and the required gain. To convert the sensed horizontal velocity to vertical shear, the probe's output is time differentiated and the fall speed is used to convert the time scale into a vertical

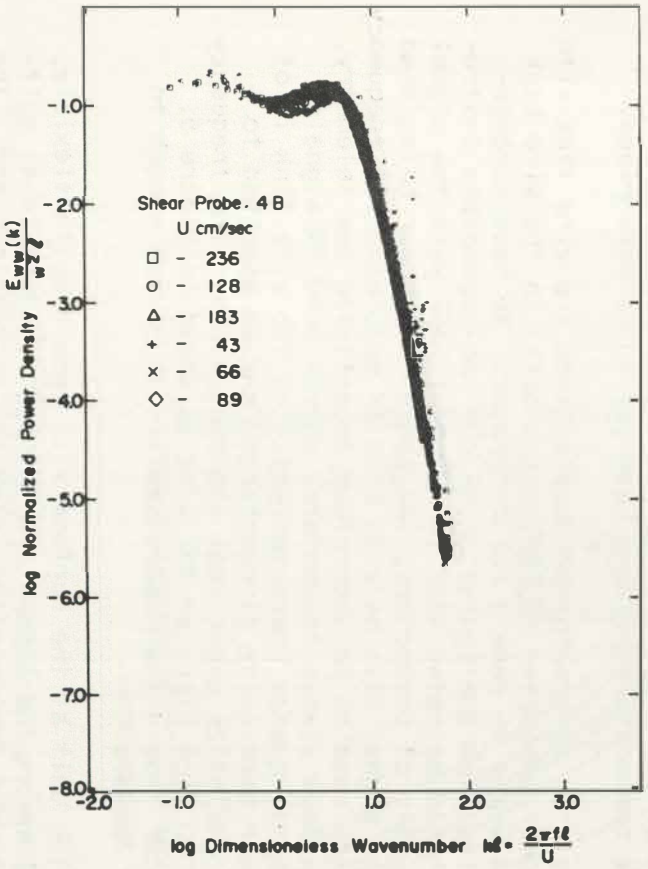

(a) Shear probe 4B.

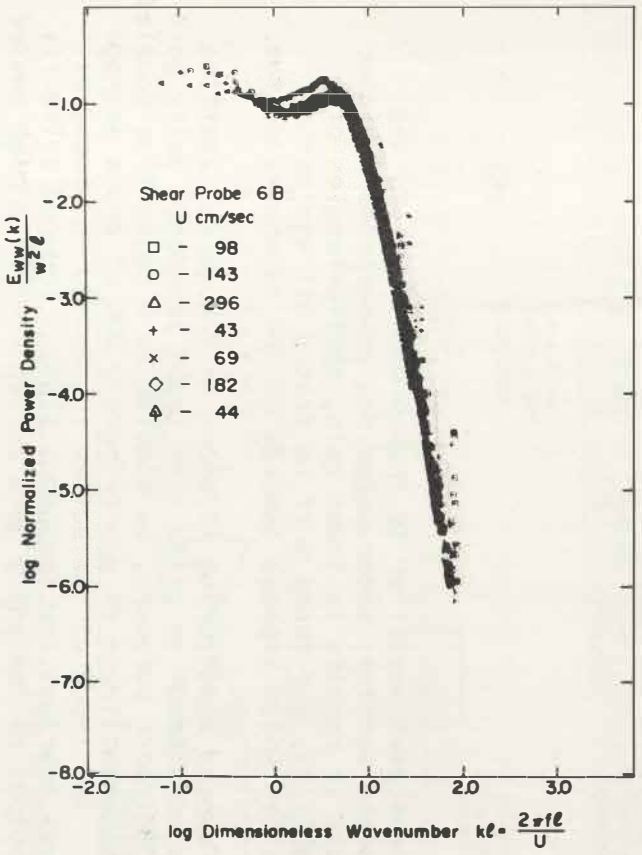

(b) Shear probe 6B.

Figure 3. Spectra of the cross-stream component of the turbulence in the wake of a rod at a position of 100 diameters downstream from the rod. The spectra are normalized by the total measured variance in each spectrum. The parameter $\ell=(xD)^{\frac{1}{2}}=3.2$ cm where x is the distance from the probe to the rod and D is the diameter of the rod.

space scale. We have

$$\frac{\partial u}{\partial z} = \frac{1}{U}\frac{\partial u}{\partial t} \qquad (4)$$

and using equation (2)

$$\frac{\partial u}{\partial z} \alpha \frac{1}{U^2}\frac{\partial E}{\partial t} \cdot \qquad (5)$$

The output voltage of a differentiated amplifier is thus proportional to the square of the fall speed times the vertical shear. For design purposes a higher fall speed is favourable because it results in lower gain, smaller angles of attack and greater vehicle stability, but these must be traded off against a subsequent larger signal bandwidth which imposes demands on the telemetry system.

A block diagram of the proposed electronics is shown in Figure 4. Starting from the probe the electronics consist of an ultra high input impedance unity gain buffer. The probe can, for electronic purposes, be modeled by a capacitive coupled voltage generator with a series capacitance of approximately 850 pf and a leakage resistance of about 10^{11} ohms. The input of the buffer is shunted to ground by a 10^{8} ohm resistor which removes spurious low frequency signals induced primarily by temperature effects. The output of the unity gain buffer is thus a high passed low impedance reproduction of the shear probe voltage with a -3 dB cut-off of approximately 2 Hz. The next stage is a standard band limited voltage differentiator with a gain equal to the frequency in Hertz. This stage is followed by a unity gain low pass filter to further remove any unwanted high frequency signal content. The data band signal is then converted to a wide band frequency modulated sine wave (FM) spanning a range of 500 to 4500 Hz. The FM stage will incorporate some compensation for the frequency characteristics of the expendable's wire link. The details of the temperature circuit have yet to be determined.

The output of the FM modulator is tranformer coupled into the wire link with one output arm of the transformer connected to the conductor(s) in the wire link and the other connected to sea water to make a return ground. We have successfully used this transformer-wire link configuration on our non-expendable instruments for many years but it should be noted that for standard XBT work the signal is sent up one conductor of a pair of conductors, the second conductor being used for a return path. Because the signal will be wide band FM modulated the frequency characteristics of the wire link need to be understood to optimize the telemetry. Our non-expendable instruments have always telemetered narrow band FM signals. The available literature on the frequency characteristics of the wire link is of little help to us because of our particular circumstances and we have had to measure these frequency characteristics under real use conditions. The frequency response of a two conductor 5000 foot Sippican XBT wire is shown in Figure 5. The attenuation at depth greater than a few hundred meters is severe enough to require some compensation for losses.

The design of the receiving unit at the surface will remain quite flexible; the main requirements are to receive the signal and to boost it to a level suitable for direct FM recording and/or demodulating, viewing, processing, etc. The proposed electronics are being constructed. We expect that signal attenuation in the wire link will be the only obstacle to the production of a successful electronic system.

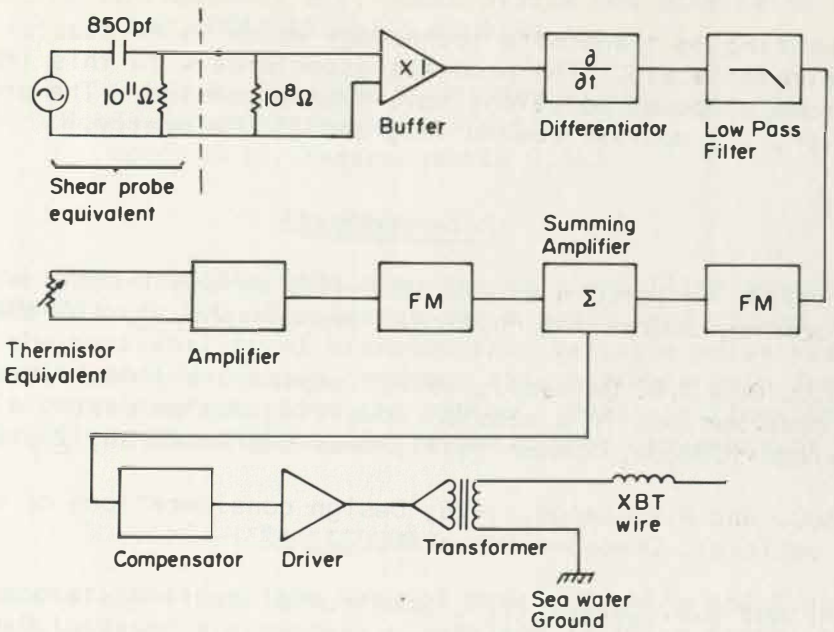

Figure 4. Block diagram of the proposed electronics.

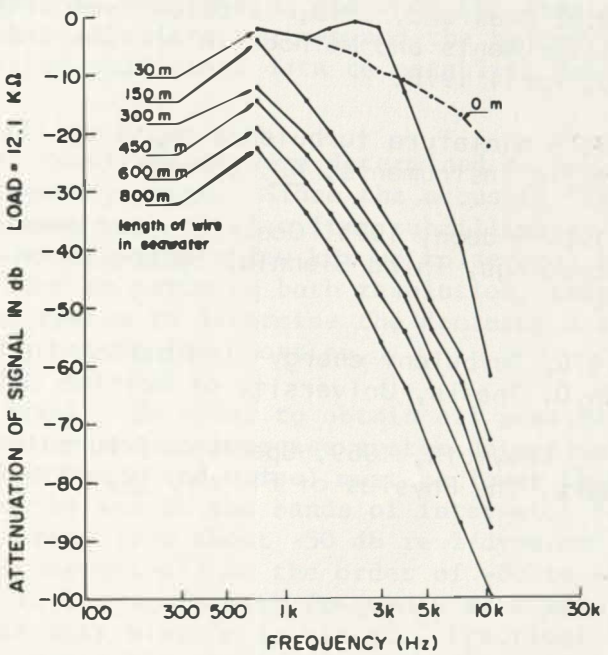

Figure 5. Signal attenuation of XBT wire link as a function of wire in water, both spools in air, and signal return via sea water. The impedance of the signal source is less than 10 ohms and the impedance of the load is 12,100 ohms. The dashed line represents the attenuation when no wire is removed from the spools.

Conclusion

We are attempting to transfer a technology which is successful at the meter scale to the decimeter scale. The problems associated with this transfer of technology and some proposed solutions have been presented. The problems are (1) vehicle motion, (2) spatial resolution, and (3) telemetry.

References

[1] Gregg, M.C., 1977, Variations in the intensity of small-scale mixing in the main thermocline, Journal of Physical Oceanography, 7, 436-454.

[2] Marmorino, G.O. and D.R. Caldwell, 1978, Temperature finestructure and microstructure observations in a coastal upwelling region during a period of variable winds (Oregon, Summer 1974), Deep-Sea Research, 25, 1073-1106.

[3] Mortensen, A.C. and R.E. Lange, 1976, Design considerations of wing stabilized free-fall vehicles, Deep-Sea Research, 23, 1231-1240.

[4] Elliott, J.A. and N.S. Oakey, 1976, Spectrum of small-scale oceanic temperature gradients, Journal of the Fisheries Research Board of Canada, 33, 2296-2306.

[5] Osborn, T.R., 1978, Measurements of energy dissipation adjacent to an island, Journal of Geophysical Research, 83(C6), 2939-2957.

[6] Osborn, T.R. and W.R. Crawford, 1979, Turbulent velocity measurements with an airfoil probe, Instruments and Methods in Air-Sea Interaction, NATO School, Ustaoset, Norway, April 1978.

[7] Siddon, T.E., 1971, A miniature turbulence gauge utilizing aerodynamic lift, Review of Scientific Instruments, 42, 635-656.

[8] Osborn, T.R. and T.E. Siddon, 1975, Oceanic shear measurements using the airfoil probe, Proceedings, Third Biennial Symposium on Turbulence in Liquids, Rolla, Missouri.

[9] Crawford, W.R., 1976, Turbulent energy dissipation in the Atlantic Equatorial Undercurrent, Ph.D. Thesis, University of British Columbia, 150 pp.

[10] Uberoi, M.S. and P. Freymuth, 1969, Spectra of turbulence in wakes behind circular cylinders, The Physics of Fluids, 12, 1359-1363.

A TOWED, MULTI-FREQUENCY H.F. SONAR SYSTEM FOR SCATTERING AND OCEAN DYNAMICS STUDIES

F. R. Hess and M. H. Orr
Woods Hole Oceanographic Institution
Woods Hole, Massachusetts 02543

Abstract

The system described provides wide operational flexibility at any operating frequency from 5 kHz to over 800 kHz (except for a small band around 455 kHz) limited mainly by the availability of transducers. Variable pulse width, variable receiver bandwidth, low receiver noise, various time variable gain functions and wide system dynamic range characterized the system. Built-in time-sharing controls maximize flexibility of graphics display on either dry-paper or fibre-optic CRT recorders.

Background

Developing interest, based on the work of Munk[1], Proni[2], and Fisher[3] and others, in the investigation of a variety of shallow (<200 m depth) phenomena at the Woods Hole Oceanographic Institution led in the mid-70's to a requirement for a high resolution sonar system. Early tests, to determine feasibility, utilized several types of commercially available echo sounders which had been modified to increase the available gain and to improve front-end noise performance. These tests, in which a variety of frequencies, recording schemes and towing configurations were tried, aimed at determining not only the feasibility of acoustically studying the various particulate regimes and the hydrodynamic phenomena outlined by them, but provided sufficient data to establish design parameters for an optimum system.

1. The most important requirements were determined to be:
   Wide operating frequency range. Since the acoustic "targets", either individual or diffuse, vary in size from submillimeter range to a few centimeters, frequencies from a few kHz up to several hundreds of kHz are required in order to optimize both resolution, target detection, and the ability of the system to determine the dominant scattering mechanism being observed at a particular location.

2. Low system noise level. In order to obtain all possible information from the target echoes and to increase system detection ranges, system noise (i.e. receiver front end noise) must be lower than the received ambient noise from the sea in the bands of interest. Sea state zero noise (Knudsen)[4] varies from about -50 db re 1/dyne/cm^2 spectrum level at one kHz to a low (theoretical) on the order of -80 to -90 db in the 90-100 kHz range, rising again with frequency as a result of increasing molecular motion as this minimum is passed. Practical limits on transducer sensitivity, typically -75 to -95 db re/1volt/dyne/cm^2 frequently require receiver "front ends" with equivalent input noise -20 to -30 db below one microvolt (-140 to -150 db V). Such low noise performance requires careful design and component selection.

   While such low noise figures are not always useful, especially at frequencies below 50-60 kHz due to the combined effects of ship generated noise and flow noise around the towbody, occasionally the ship is stopped

and allowed to drift. In this mode all available useful sensitivity is put to work.

3. Wide system dynamic range. In order to be able to detect the low signal levels resulting from the anticipated scattering mechanisms as well as to be able to measure reflectivity (target strength) of large discrete targets, the system must be able to pass and display signals ranging in amplitude over three or four decades (60-80 db). Since no existing display medium can approach this dynamic range, two techniques are commonly employed; "tapped" gain stages and some form of time-variable-gain (TVG).

4. Flexibility. In order to make the system as adaptable as possible to various research/survey vessels, it must be configured for towing of the transducers in a simple "fish". A suite of transducers must be provided for operation at a variety of frequencies such as: 20 kHz, 100 kHz, 200 kHz, 300 kHz, and 500 kHz. Other transducers may, on occasion, be used with the system and, in fact, virtually any transducer should be usable. A set constructed especially for this system however would provide certain features such as commonality of mounting and connectors and would be physically interchangeable in the tow-bodies.

System Philosophy

Receiver

It was decided, based on the earlier work, that the mix of analog and digital circuit systems would emphasize digital control and frequency generation, but be completely analog in the signal processing (Figure 1).

The receiver is required to tune the 10 kHz to 800 kHz frequency range, be easily tuned to various frequencies in this range, and all channels must be interchangeable. Digital control is felt to be desirable if for no other reason than repeatability. Receiver bandwidths must be constant and repeatable from one operating frequency to another. Receiver blanking and signal gating must be provided. Two forms of repeatable time-variable-gain (TVG) are required.

The use of a superheterodyne receiver allows for tuning by digital control of the synthesizer used for the local oscillator. Uniformity of response at different frequencies is readily accomplished with the use of Intermediate Frequency (IF) filters. System overall gain is readily adjusted and gain stability is good. Any frequency within the design range can be received with equal facility.

Transmitter

The transmitter requirements are straight forward. The wide frequency range and repeatability requirements again press for synthesizer control. Variable pulse width, in number of cycles transmitted also dictates the use of digital control. The low duty cycle of a sonar system, typically less than one or two percent, allows for the generation of high pulse power in a small physical package.

Recorder and Control

The system must be capable of full control of the recorder used (EPC 4600). All necessary timing, gating and drive signals are to be provided.

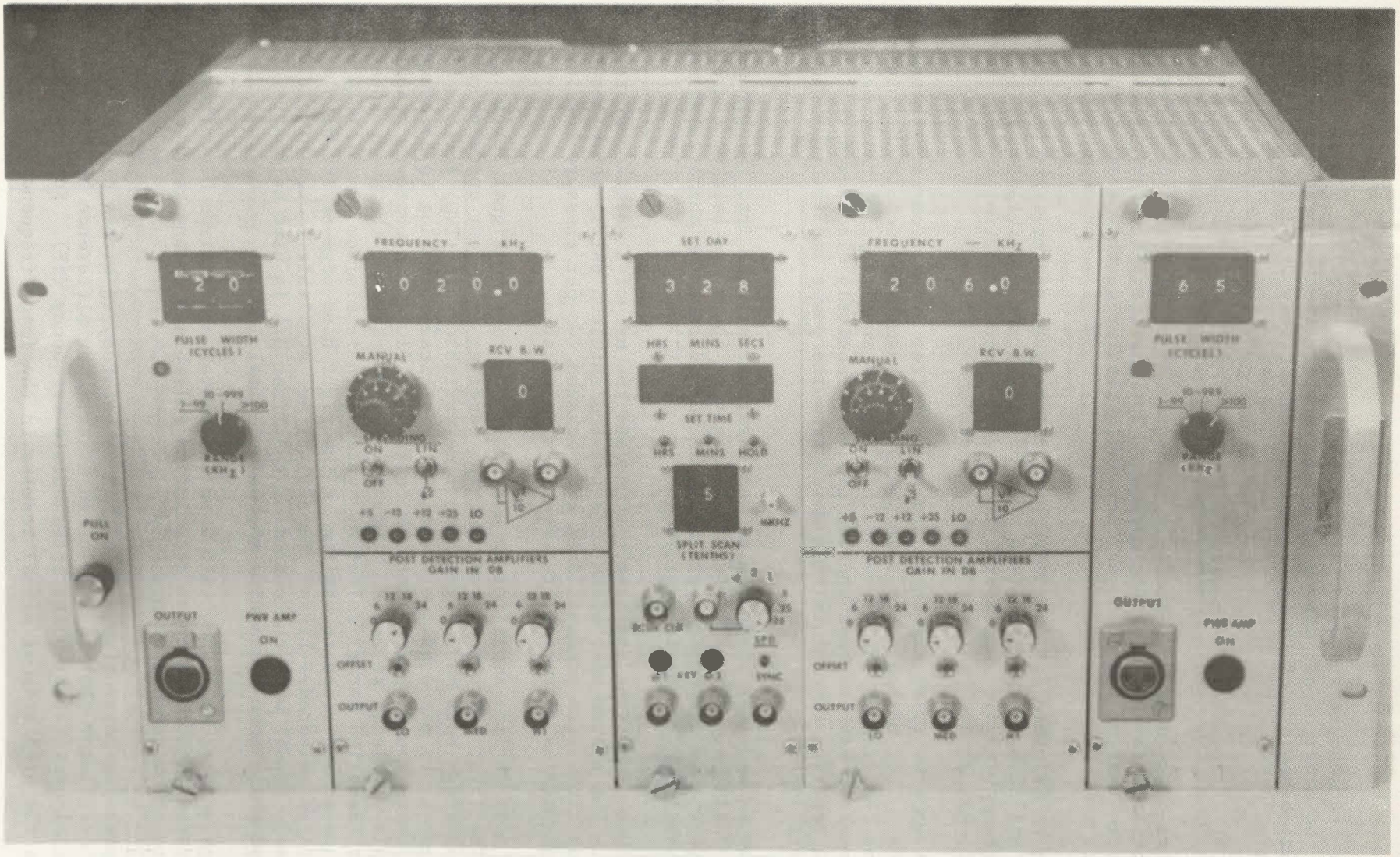

Figure 1 Front panel of the high frequency sonar system showing all major controls and connections. Two transmitters (outer modules) and two receivers (inner) and a common timing/control module are shown. Not shown is another smaller panel containing the 1200 watt power amplifiers which could not be sufficiently isolated from the digital electronics when installed in the main frame.

Transducers

A set of transducers and associated tow-bodies are provided. At 200 kHz a beamwidth on the order of one degree is required while at the lower frequencies (20 and 37 kHz) beamwidth of 15 and 6 degrees respectively are dictated by the space available.

System Operation

The system block diagram (Figure 2) shows the major functions provided which are necessary for the acoustic mission. Not shown are the various clock, control and time sharing functions as they would clutter up the diagram and are conventional.

In order to maintain optimum noise performance, the preamplifier is in the towbody. It utilizes a low noise (< 6 nv/$\sqrt{\text{Hz}}$) FET front end followed by a remotely programmable gain amplifier/line driver. Gain is controllable in four steps; 25, 35, 45, 55 db, by front panel switch.

Transmit-receive (T/R) switching and preamplifier protection is by means of Shottky diodes. This method costs some power in transmit but results in minimum switching time for examination of very close returns and little degradation of noise performance. Back-to-back Shottky diodes effectively disconnect the transmitter during receiver time minimizing noise from the power amplifier or pickup on the transmit line.

Provision is made for insertion of "calibration" signals into the preamplifier. These "cals" are rather for establishing that there has been no degradation of system performance during an operation than for determining absolute gains. These are established in the laboratory.

All of these functions and controls mandate the use of a multi-conductor towing cable. The system uses TTRSA-8 (8 twisted/shielded pairs) cable for the electrical function. The preamplifiers are packaged two per pressure housing giving two frequencies (channels) fed from a single cable.

On deck a 25 db line amplifier is available for raising signal level if necessary. The first functional stage of the receiver is a four quadrant multiplier which provides both manual gain and time-variable-gain (TVG) action. TVG ramp generation is by means of two, multiplying digital-to-analog (D/A) converters and counters which count up from zero to full scale (10 V) in whatever graphic recorder display scale is selected. That is, irrespective of the sweep speed or display split (detailed later) selected, system gain is minimum immediately after the transmit pulse and rises to maximum at the right hand edge of the display at whichever rate is selected. Linear ramps ($1/t$) are available from a single D/A while $1/t^2$ ramps result when the output of the first D/A is used as the reference for the second while both are seeing the same digital inputs.

Manual gain is accomplished with a potentiometer and a fixed DC voltage. Typically, system electronic noise is printing full black at the right margin and all echoes are below detection threshold.

After spreading correction, the signal is heterodyned with a digitally generated local oscillator (LO) in a balanced mixer. The difference between the signal and local oscillator is the intermediate frequency (IF). Keeping the local oscillator on the high side of signal results in the image frequency being

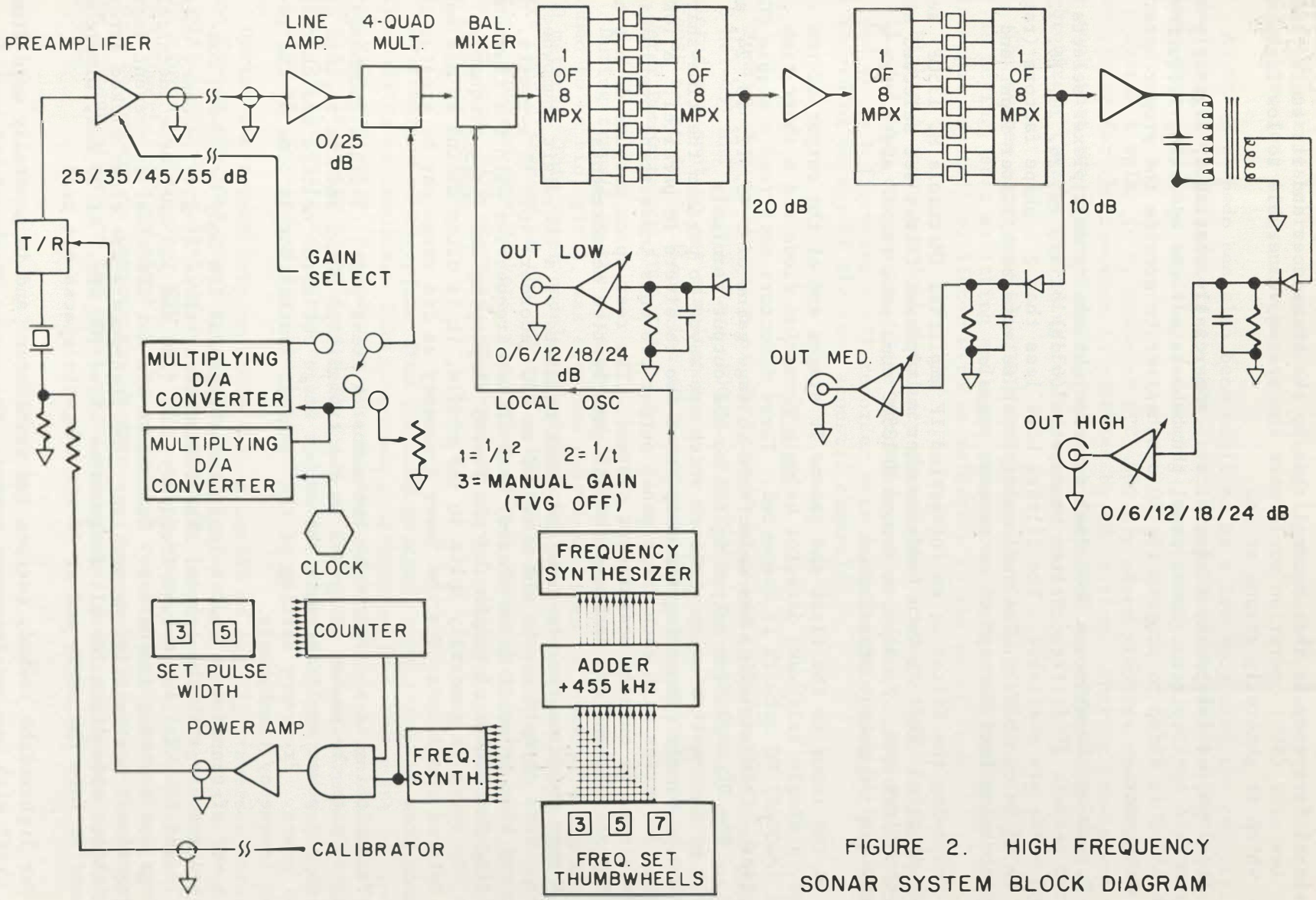

FIGURE 2. HIGH FREQUENCY SONAR SYSTEM BLOCK DIAGRAM

separated widely from the desired input. This is necessary as the only tuning at the signal frequency is that accomplished by the transducer and its tuning inductor. Low side (SUM) operation would make the system vulnerable to low frequency noise which is generally strong at sea.

The local oscillator is a single card,commercially available, digitally programmable synthesizer. Front panel thumbwheels set the operating frequency to which 455.0 is added to program the LO synthesizer to provide the proper heterodyne frequency.

Following the mixer, a CMOS dual one-of-eight analog multiplexer selects the desired ceramic IF filter. Filter bandwidths (6 db) of 35, 30, 26, 20, 16, 12, 8, and 6 kHz are available. The filters have less than 2:1 shape factors (ratio of 6 db BW to 60 db BW). The dual multiplexer selects both filter input and output minimizing feed-through of extraneous signals.

Following the filter is an integrated IF amplifier (Motorola MC 1350P) set for 20 db gain. This in turn feeds another multiplexed filter set selected along with the first set. Finally, a second MC1350P completes the IF strip with a conventional IF output transformer.

At the input to the first and second IF stages and at the output of the second, a simple half-wave detector using a germanium diode and a short time constant ($\sim$50μS) RC network is connected. These detectors each feed a simple DC amplifier. This amplifier has selectable voltage gains of 0, 6, 12, 18, 24, and 30 db. The DC amplifier output is fed to the output terminals through mercury-wetted relay contacts which are keyed to perform the time-sharing function by simply connecting the outputs of two receivers in parallel. A 10K resistor in series with each front panel output prevents inadvertent overloading of the signal by outside measurement systems. The rear apron outputs do not have series resistors and are designed for all quantitative measurements.

A scan split control is provided which consists of a one-digit thumbwheel switch. This circuit breaks the sweep(of an EPC recorder) into 10 segments. The sweep may then be split (time-shared) between two frequencies with the thumbwheel selecting the number of tenths (of the sweep) displaying the first frequency. While the sweep is generally split in the middle, it is often useful to use more than half of the display for the lower frequency as its range may be greater than a higher one.

Transmitting is controlled by two means: A front panel, 2-digit thumbwheel switch selects the number of cycles in the transmitted burst and the voltage control on the power amplifier sets the output stage collector voltage and thereby, output power. Frequency setting of the transmit synthesizer is done by the receiver frequency thumbwheels.

A set of transducers and at least three types of tow body have been constructed for use with the system. The transducers, three single-frequency units (20, 70 and 200 kHz) and a dual-frequency unit (350 and 520 kHz) have identical housings and mounting dimensions. Connectors are not identical to prevent improper transducer-to-amplifier connection. The transducers are close packed arrays of thickness mode discs for all frequencies above 200 kHz. At 20 kHz, bimorphs are used to form the array and at 70 kHz Langevin stacks are used.

One lightweight towbody carries two transducers and is generally used from small craft with one two-frequency system. The second "lightweight" towbody

(Figure 3) carries three transducers which, if the dual-frequency transducer is used, allows four-frequency operation.

An MK-43 torpedo has also been modified as a tow body with the capability of mounting three transducers as well. It is capable of higher towing speeds and is used where adequate handling and towing gear is available.

System display is by means of EPC 4600 dry paper graphics recorders. All drive timing for the recorder is provided by the system. Sharing provisions are made such that two systems (dual frequency) and their associated recorders can be synchronized, thereby providing four-frequency operation.

The system clock provides IRIG "B" time code for magnetic tape logging as well as keying, scan splitting and time sharing controls. All operation is from an internal crystal oscillator with no reference to the power line.

Figure 4 shows two dual-frequency systems (or a single four-frequency system) and all ancillary components. Tape recorders for each pair of frequencies are provided as is a fibre-optic CRT recorder with variable delay trigger for fine seal recording of any of the four acoustic channels.

Results

Funding for construction of the "ideal" system was provided by both NOAA (04-8-M01-43) and the U.S. Navy (N00014-77-C-0196). In mid-1977 two systems were completed and sent to sea simultaneously on the NOAA ships MT. MITCHELL and ALBATROSS to study the dispersion of chemical wastes released from a barge at Deep Water Dumpsite 106 (DWD 106).

During transit to the site aboard ALBATROSS, a layer of heavy scattering, presumed to be biological, was observed over long lines of track at a depth of 30-40 meters. This layer undulated gently with peak-to-peak amplitudes of 2-3 meters over distances on the order of a kilometer for the most part. Occasionally however, cuspoid wave packets, consisting of 4-6 cycles with amplitudes of 15 meters or more (P-P) appeared. The packets were intriguing and their origins can only be hypothesized.

Observation of the plume from the dump process, consisting, we were informed, of flocculates of insoluble iron compounds precipitated from the waste by reaction with sea-water, was carried out and the dispersion rates determined. Rates of lateral dispersion as well as sink rates of the flocs were determined. The tendency of the waste to spread out on a density/temperature surface was observed. The system was working better than hoped for.

During the return trip to Woods Hole a series of zig-zag traverses across Hudson Canyon provided startling graphics of the various water masses at work in that area including a lenticular, low-scattering intrusion running down the axis of the canyon (Figure 5). XBT data taken at the time, as well as a rosette sampler lowering (which shows on the recording), verified that the reflecting horizons correspond to temperature gradients. The samples analyzed showed particulate concentrations on the order of 60 micrograms/liter total particulates at 90 meters.

Conclusion

The system provides the necessary acoustic flexibility and performance to

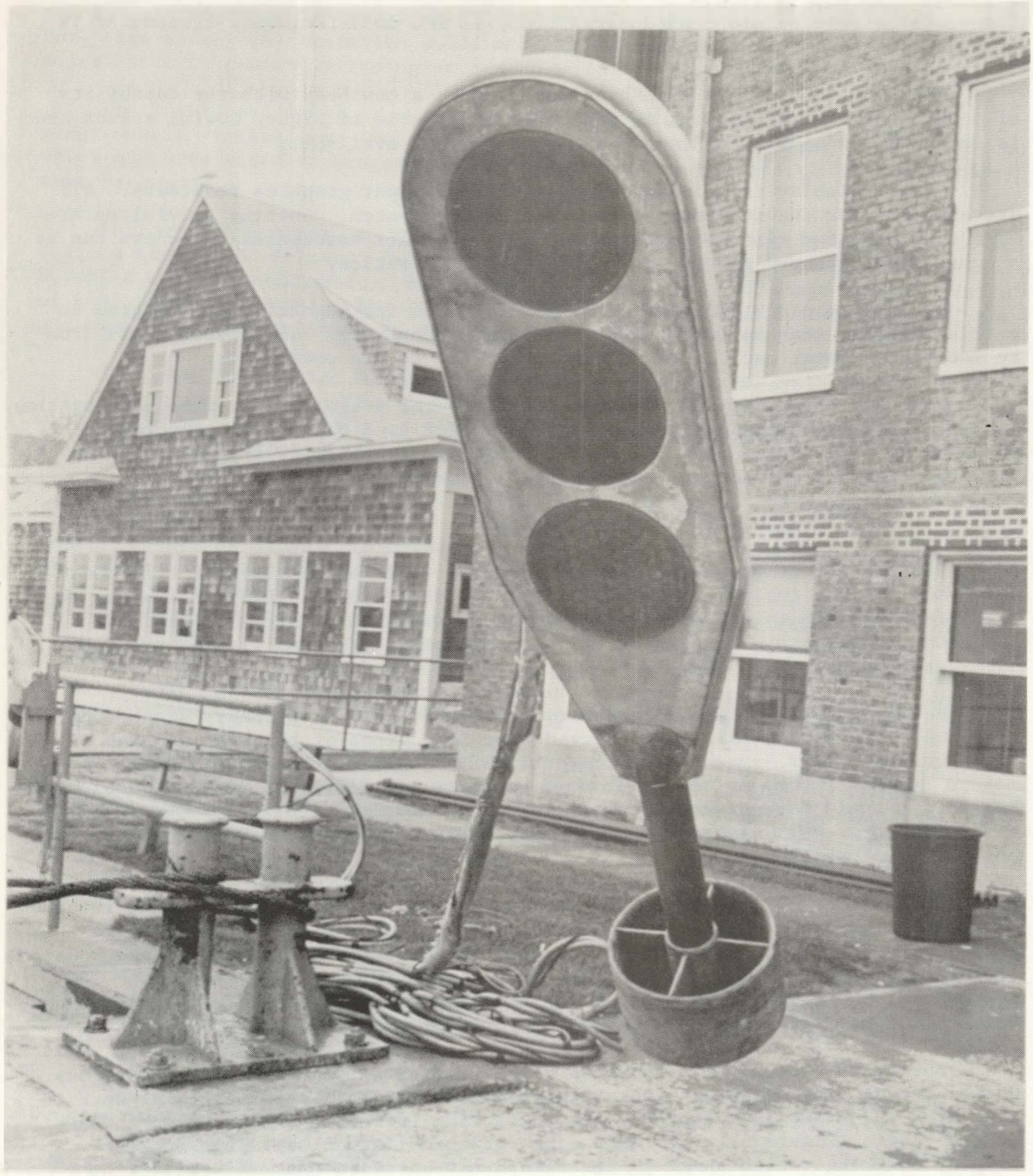

Figure 3 Fibreglass towbody which contains three transducers for use during four frequency operations. Separate transducers for 20 kHz and 200 kHz are mounted as well as a dual, 357 kHz/520 kHz unit. Preamplifiers, T/R networks and transducer matching networks are carried in two small lexan cylinders inside the towbody.

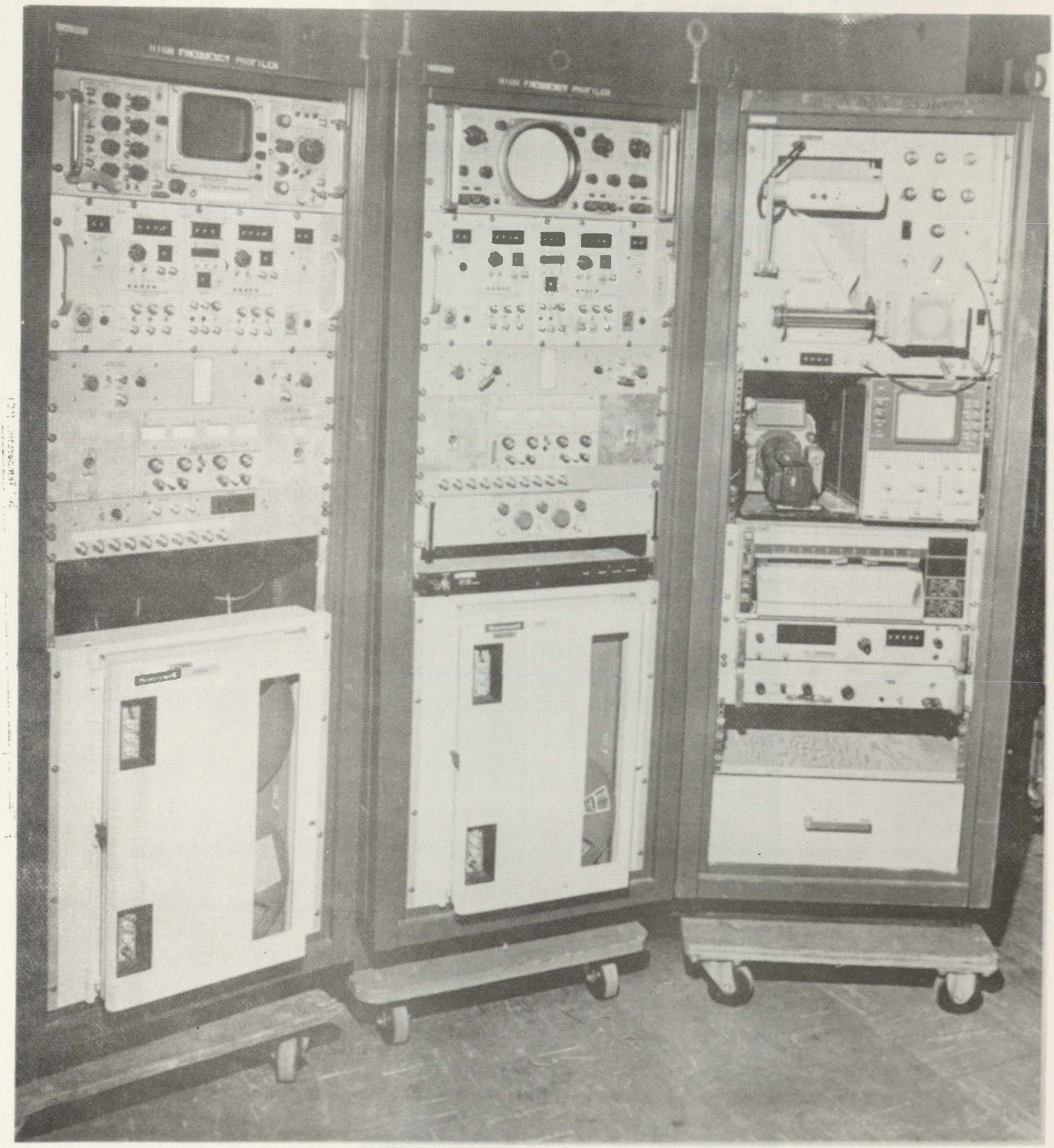

Figure 4 Two dual frequency H.F. sonar systems comprising a single four-frequency system. The rack at right contains a fibre-optic CRT recorder for high resolution work as well and a variable persistance oscilloscope and camera used for dynamic studies. Lower units are for temperature and depth recording.

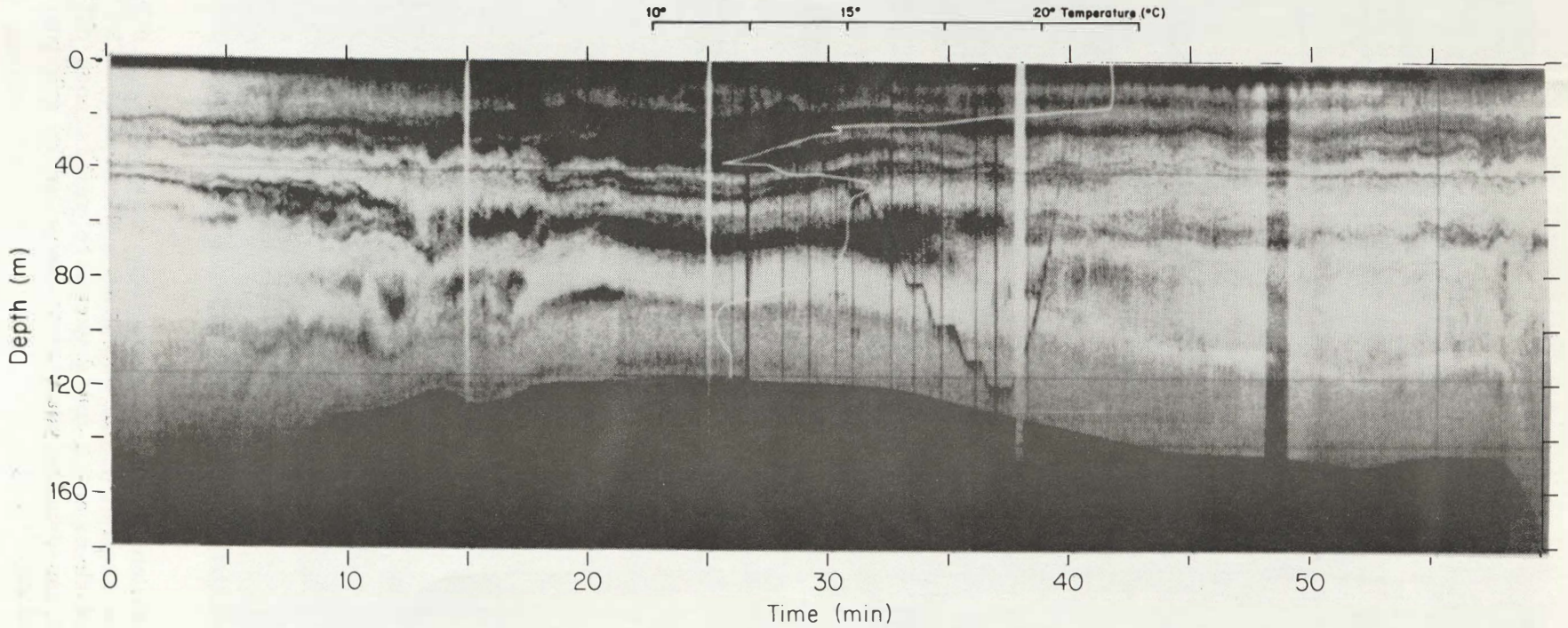

Figure 5 Section of 200 kHz recording on flanks of Hudson Canyon showing up to nine identifiable reflecting/scattering surfaces. The staircase in the center was made by the lowering of a CTD/rosette sampler. A temperature plot shows good correlation with acoustically mapped layers.

observe the phenomena to be studied. Current flows delineated by particulate suspension have been mapped at depths in excess of 100 meters. The scattering mechanism which provides the return is not unequivocally known in all cases, but there is strong indication that temperature and/or turbulence provide sufficient backscattering for mapping.

The system provides the desired tool and has been in operation for over two years with continuous upgrading of performance.

References

1. Munk, W. H. and Garrett, C. J. R., Internal wave breaking and microstructure, Boundary Layer Meteorol., 4, 45-47, 1973.

2. Proni, J. R. and Apel, J. R., On the use of high-frequency acoustics for the study of internal waves and microstructure, J. Geophys. Res., 80, 1147-1151, 1975.

3. Fisher, F. H. and Squier, E. D., Observation of acoustic layering and internal waves with a narrow-beam 87.5 kHz echo sounder, J. Acoust. Soc. Am., 58, 1315-1317, 1975.

4. Urick, R. J., Principles of Underwater Sound for Engineers, McGraw-Hill, New York, 1967, pg. 167.

REMOTE VELOCITY MEASUREMENTS FROM DOPPLER SONAR

Robert Pinkel
University of California, San Diego
Marine Physical Laboratory of the
Scripps Institution of Oceanography
San Diego, California 92152

Abstract

Remote measurements of the oceanic velocity field can be obtained with Doppler backscattering sonars. While Doppler scattering methods have been used for the past 30 years to make local flow measurements, it is only recently that their remote ranging capabilities have been seriously exploited. Currently, velocity measurements have been made to a range of ≈1.5 km, with 20 m range resolution and 1 cm/sec velocity precision, using a sonar mounted on the Research Platform Flip. In this paper Doppler sonar principles are briefly introduced and examples of these data are presented.

Introduction

The accurate measurement of the oceanic velocity field is a difficult task. In many situations, Doppler backscatter sonar techniques can be used to remotely sense needed velocity information. This paper will briefly describe Doppler sonar technique. Representative data will then be presented. Finally, the limitations of the approach will be discussed.

Method

The operating principle of a simple Doppler backscatter sonar is as follows. Sound is periodically transmitted in a narrow beam. The sound scatters off the plankton and nekton in the sea. From the Doppler shift of the signal which is backscattered toward the receiver, the radial velocity of the scatterers can be sensed as a function of range. With repeated pulses, a map of radial velocity vs. range and time can be formed.

The basic hardware required for Doppler measurements is not complex. Starting with a conventional echo sounding device, additional circuitry is required to sense the rate of change of phase of the return. This can be done by a variety of techniques. A simple method is as follows (Fig. 1). Sine and cosine reference signals are generated at the sonar carrier frequency. Periodically one of these signals is gated out to the transmitter, and transmitted. The return echo is multiplied by both the reference signals in parallel, low pass filtered, and recorded. If the output of the "sine channel" is plotted vs. the output of the "cosine channel", (on an x-y scope for example), the rate and sense of rotation of the trace is proportional to the magnitude and direction of the Doppler shift. The major difficulties in sonar design are associated with transducer beam patterns, source power, and receiver dynamic range. The Doppler aspects of the system pose a small problem by comparison.

Application

Investigations of Doppler acoustic backscattering methods were begun at the Marine Physical Laboratory of Scripps Institution of Oceanography in 1975. After several years of development work, a special purpose scattering sonar was

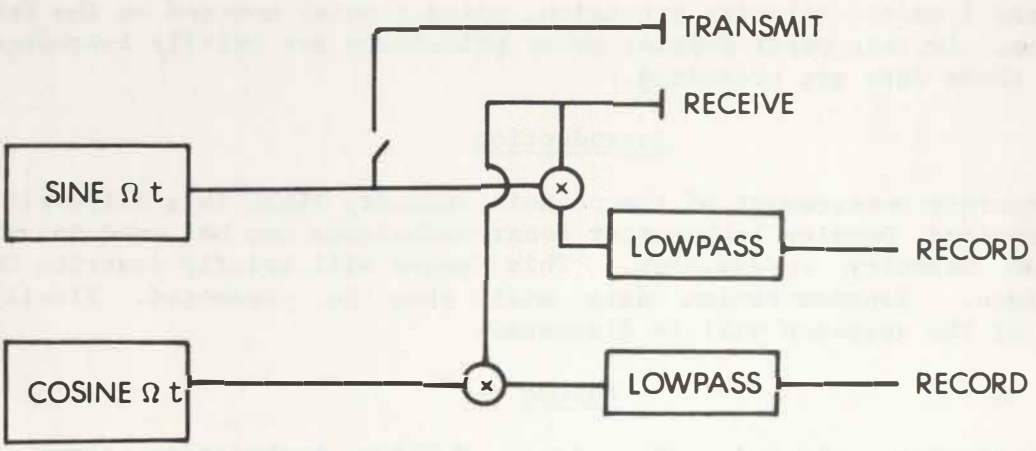

Figure 1. Block diagram of Simple Doppler Signal Processing Scheme.

developed (Fig. 2), for use on the Research Platform Flip. The sonar consists of a mosaic of 1680 individual transducers, driven in phase and with uniform amplitude. The aperature of the array is nominally 1.5 m. A peak power of 32 KW can be transmitted, between 65 and 90 kHz.

In January 1979 the sonar was tested on a short Flip operation between Catalina and San Clemente Islands. Mounted on the bottom of Flip, at a depth of 87 m, the sonar beam was pointed 45° down from horizontal. Over an 11 hour period, a time series of velocity profiles was collected (Fig. 3). Accurate measurements were possible down to the sea floor, at a depth of 1250 m. The velocity precision was of order 1 cm/sec rms at near and intermediate ranges, degrading slightly at the furthest ranges.

The layered jet-like nature of this flow between the islands is striking. A longer record is necessary to determine whether these features are intrusive in nature, or related to internal gravity waves. There is a suggestion of a bottom boundary layer in the furthest hundred meters of the record. However, it might be that side lobes of the sonar beam are starting to interact with the sea floor here, prior to the arrival from the main lobe. Additional calibration of the sonar is necessary to establish the true nature of this feature.

Practical Considerations

The uncertainty in the near-bottom measurements is only one of a variety of practical limitations of sonar technique. It is appropriate to mention a few of the considerations here.

The finite width of the sonar beam introduces several problems. In a uniform current, the radial component of velocity at one extreme edge of the beam can differ from the component at the other edge. This results in a Doppler broadening which is proportional to both relative velocity and geometric considerations. The velocity precision of ship mounted backscatter sonars, for example, is degraded as ship speed increases, due to finite beamwidth effects. Also, resulting from finite beamwidth, the size of the averaging volume increases with range. Comparisons of velocity at near and far range can be affected by the change in averaging volume with range. For example, consider a 3° wide sonar beam directed horizontally, and used to sense internal wave motions. At a range of 500 m the sonar scattering volume is of order 30 m in depth. Since the vertical coherence scale of open ocean internal waves is also of order 30 m [1,3], the average velocity over the scattering volume will probably not be representative of the velocity at any depth within the volume. At a kilometer range, the depth average spans several coherence lengths, and the average velocity contribution due to internal waves is probably zero. Here, operating a given transducer at a lower acoustic frequency, to "increase its range", is a mistake. The useful range is limited by transducer beamwidth. On the other hand, the decrease in the measured frequency spectrum with range is an indication of the vertical coherence of the wavefield. If one can really trust the internal wave model necessary to interpret the data, the measurement of vertical coherence with a horizontal broad beam sonar might be a useful technique. Where platform stability is a problem, this might be the only technique. It does little good to mount a 1° sonar on a vessel which tilts 10° during the time it takes to form a "precise" velocity estimate.

In addition to the considerations associated with the width of the sonar beam, there are other problems resulting from beam sidelobes. In a narrow beam scattering sonar, the number of scatterers in the "scattering volume" is a very

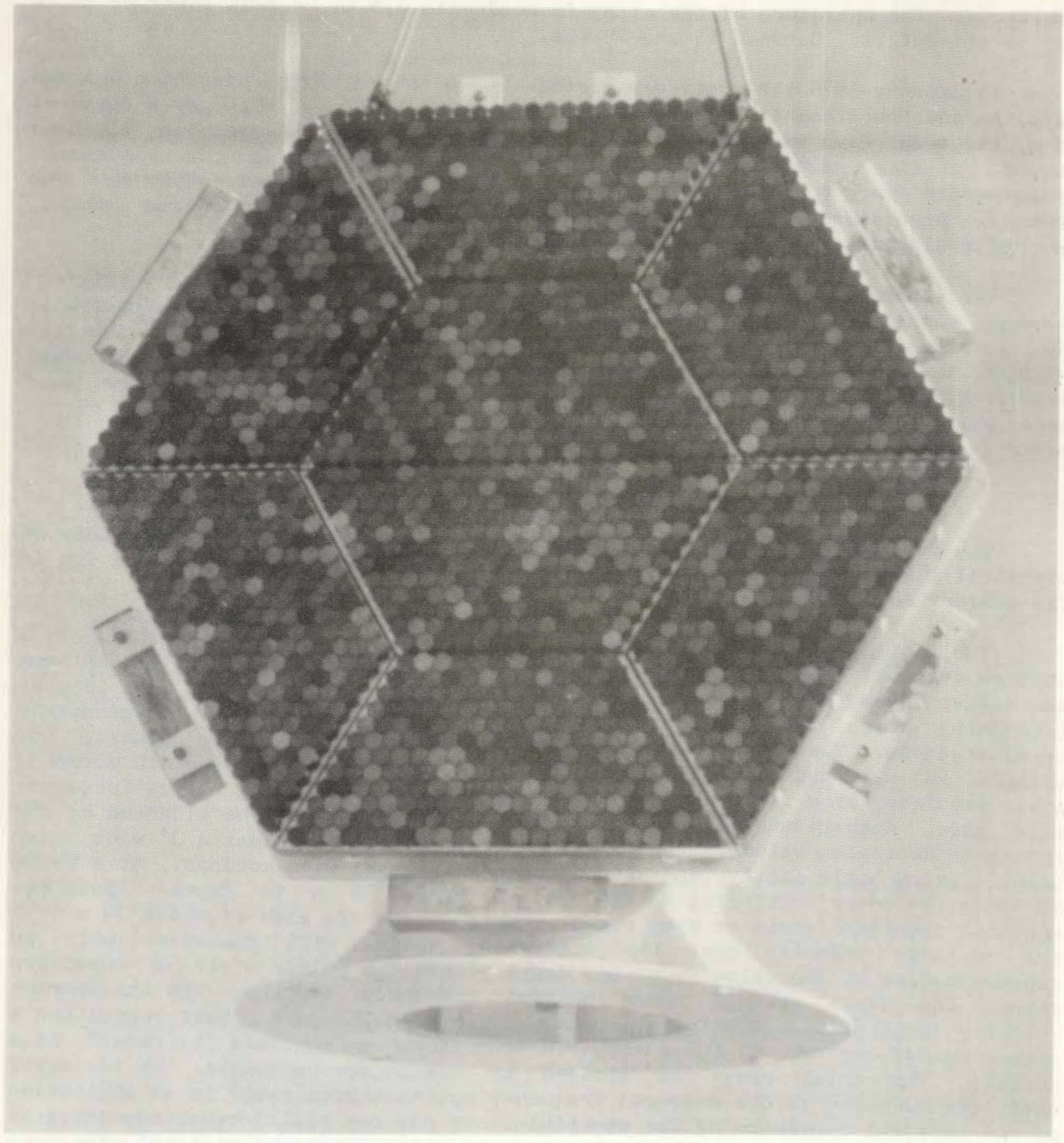

Figure 2. MPL Scattering Sonar. The sonar consists of an array of 1680 individual transducers, driven in phase and with constant amplitude at 32 KW peak power. The sonar can be operated at frequencies between 65 and 90 kHz. The 1.5 m diameter aperature of the array results in a 1° nominal beamwidth at 75 kHz.

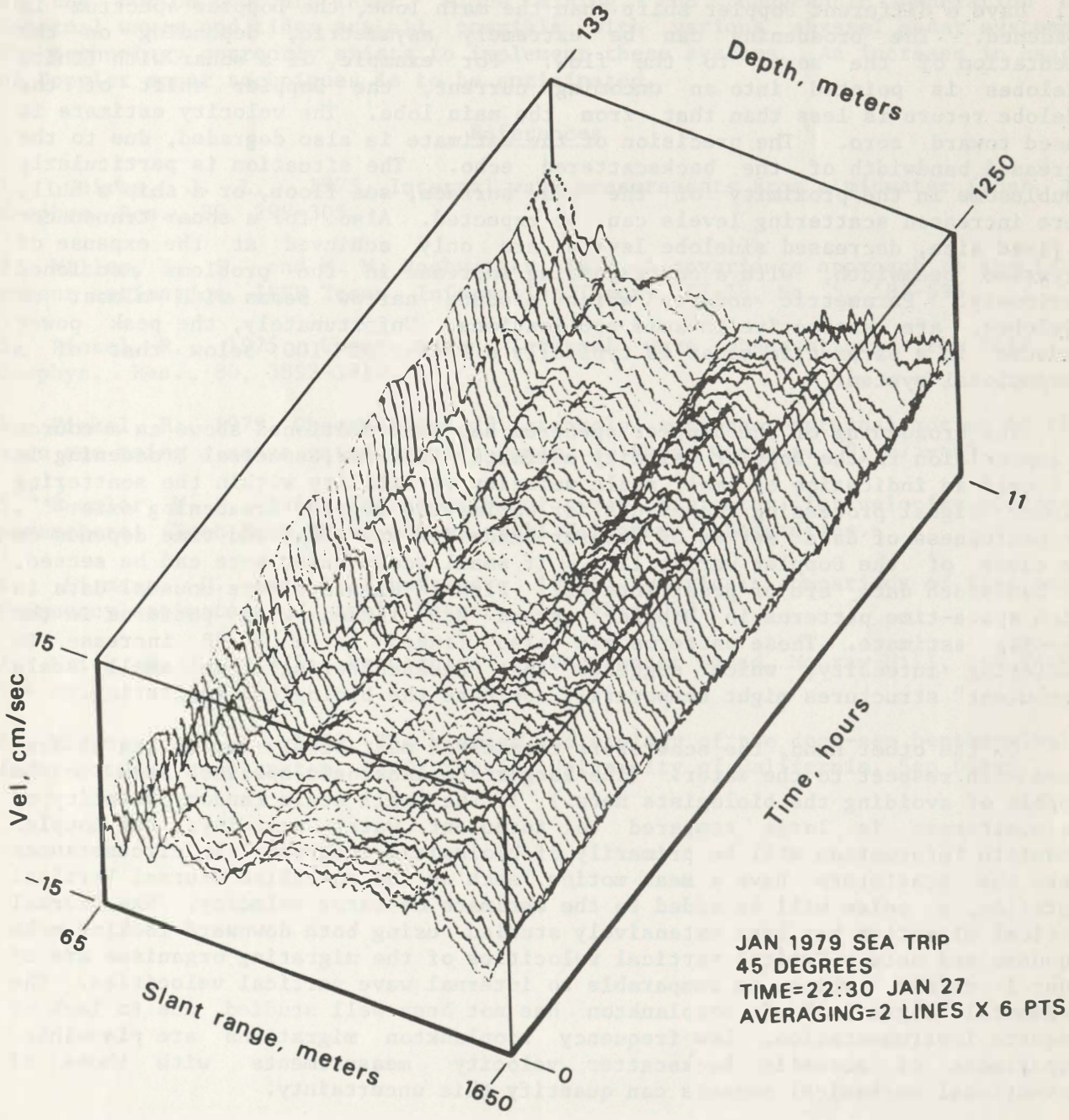

Figure 3. Deformed surface representation of velocity vs. range and time. Each line in the surface corresponds to a 10.2 minute profile of 45° slant velocity taken between depths of 133 m and 1250 m. The measurements were made from Flip off the coast of California, between Catalina and San Clemente Islands, during January, 1979.

small percentage of the total number at the same range, but outside the main beam. Even though sidelobe response levels might be very low, the total contribution to the return echo can be significant. Since the sidelobe return will have a different Doppler shift than the main lobe, the Doppler spectrum is broadened. The broadening can be extremely asymmetric, depending on the orientation of the sonar to the flow. For example, if a sonar with finite sidelobes is pointed into an oncoming current, the Doppler shift of the sidelobe return is less than that from the main lobe. The velocity estimate is biased toward zero. The precision of the estimate is also degraded, due to the increased bandwidth of the backscattered echo. The situation is particularly troublesome in the proximity of the sea surface, sea floor, or a ship's hull, where increased scattering levels can be expected. Also, for a sonar transducer of fixed size, decreased sidelobe levels are only achieved at the expense of increased beamwidth, with a corresponding increase in the problems mentioned previously. Parametric sonars, which produce narrow beams with almost no sidelobes, are attractive in some applications. Unfortunately, the peak power produced in a parametric sonar is typically a factor of 100 below that of a conventional system.

The broadening of the Doppler spectrum has been mentioned above as a source of imprecision in the Doppler velocity estimate. However, spectral broadening is in itself an indication of small scale velocity variability within the scattering volume. Signal processing techniques for estimating Doppler broadening exist[3,2]. The usefulness of data series of Doppler bandwidth vs. range and time depends on the cause of the Doppler variability. If small scale turbulence can be sensed, the bandwidth data are of great interest. Pinkel[4] displays some unusual data in which space-time patterns in Doppler spread are linked with patterns in the velocity estimate. These patterns are also linked to a 3 dB increase in scattering intensity, which suggests that backscattering from small scale "turbulent" structures might temporarily dominate the biological scattering.

On the other hand, the scatterers themselves must surely be moving at some speed with respect to the water. (The larger zooplanktonic species seem to be capable of avoiding the biologists nets.) If the small scale random velocity of the scatterers is large compared to turbulent water velocity, the Doppler bandwidth information will be primarily of biological interest. In circumstances where the scatterers have a mean motion, such as the so-called Diurnal Vertical Migration, a noise will be added to the estimate of water velocity. The Diurnal vertical migration has been extensively studied using both downward looking echo sounders and nets. Typical vertical velocities of the migrating organisms are of order 1 cm/sec, which is comparable to internal wave vertical velocities. The horizontal "migration" of zooplankton has not been well studied, due to lack of adequate instrumentation. Low frequency zooplankton migrations are plausible. Comparisons of acoustic backscatter velocity measurements with those of conventional mechanical sensors can quantify this uncertainty.

Conclusions

The illustrations used in this paper emphasized the use of Doppler sonar from a fixed platform in the upper ocean. A variety of other applications are feasible. In particular shipboard Doppler sonars are now commercially available, and capable of profiling the top 150 m of the sea with 7 m vertical resolution. They have been successfully used in both the Polymode and Norpax experiments (Regier, pers. comm.). Abyssal Doppler measurements are not impossible. Either tethered sea floor installations or deeply towed platforms could be used. While expected scattering levels are lower in the deep sea, they are only lower by

20-30 dB[8]. Compared to the dominant effects of acoustic attentuation, this reduction in scattering level is not overwhelming. Larger peak power levels can be used in abyssal sonars, as cavitation is not as significant a limit. Studies of the bottom boundary layer, slope mixing, and topographic generation of internal waves and tides are all possible with various abyssal sonar systems. The technology currently exists to implement these systems. An increase in usage of Doppler sonar techniques is to be anticipated.

References

1. Cairns, J. L., 1975, Internal wave measurements from a midwater float, J. Geophys. Res., 80, 299-305.

2. Miller, K. S. and M. M. Rochwarger, 1972, A covariance approach to spectral moment estimation, IEEE Trans. Information Theory, IT-18, No. 5, 588-596.

3. Pinkel, R., 1975, Upper ocean internal wave observations from FLIP, J. Geophys. Res., 80, 3892-3910.

4. Pinkel, R., 1979, Observations of strongly nonlinear internal motion in the open sea using a range gated doppler sonar, J. Phys. Oceanog., 9, 675-686.

5. Rummler, W. D., 1968, Introduction of a new estimator for velocity spectral parameters. Tech Memo MM-68-4141-5, Bell Telephone Laboratories.

6. Sirmans, D. and B. Bumgarner, 1975, Numerical comparison of five mean frequency estimators, J. Appl. Meteor., 14, 991-1003.

7. Urick, R. J., 1975, Principles of Underwater Sound. McGraw-Hill, New York, 384 pp.

8. Wishner, K. F., 1979, The biomass and ecology of the deep-sea benthopelagic (near-bottom) zooplankton, Ph.D. Thesis, University of California, San Diego.

LITHIUM-THIONYL CHLORIDE BATTERIES - PAST, PRESENT AND FUTURE

Joseph F. McCartney, Naval Ocean Systems Center, San Diego, CA
Thomas J. Lund, Gould Inc., San Diego, CA
Wilfred J. Sturgeon, Computer Sciences Corporation, San Diego, CA

Abstract

Lithium based batteries have the highest theoretical energy density of known battery types. Of the lithium batteries, the lithium-thionyl chloride electrochemistry has the highest energy density of those which have been reduced to practice. The characteristics, development status, and performance of lithium-thionyl chloride batteries are treated in this paper. Safety aspects of lithium-thionyl chloride batteries are discussed along with impressive results of hazard/safety tests of these batteries. An orderly development plan of a minimum family of standard cells to avoid a proliferation of battery sizes and discharge rates is presented.

Introduction

Dramatic progress has been made in the development of high performance batteries in recent years. Much of this development effort has concentrated on lithium-based batteries. The reason for the interest in lithium is that it has the highest potential of the metals in the electromotive series. Consequently, the theoretical energy density of lithium-based electrochemical couples is higher than other couples. As a result of research and development efforts carried out in industry and in government laboratories, the potential benefits of lithium-based batteries are now being realized in practical hardware. Lithium-sulfur and lithium-halogen couples are being developed for secondary (rechargeable) battery application and lithium-thionyl chloride, lithium-sulfur dioxide, and lithium-vanadium pentoxide are the better known couples being developed for primary (nonrechargeable) battery applications.

The lithium-thionyl chloride battery, which can be efficiently used in both high discharge rate and low discharge rate applications, has the highest demonstrated energy density of any battery available today. It is a relatively simple battery which does not require an externally circulated electrolyte, as do several other high energy density batteries. It can be operated in any orientation, it has good shelf life in the activated condition, and it can be stored nearly indefinitely in a reserve configuration. The development status, performance, safety, and availability of lithium-thionyl chloride batteries are addressed in this paper.

Lithium-sulfur dioxide batteries have also been developed and put into production by several companies. Although the energy density of lithium-sulfur dioxide batteries is about half of that of lithium-thionyl chloride batteries, they reached production first and they are less expensive. Consequently, they are presently in wider use. Lithium-sulfur dioxide batteries, which contain sulfur dioxide gas under pressure in the cell, have experienced several incidents involving fire and explosions in the field. As a result, these batteries have been removed from all U.S. registered civil aircraft, and from most U.S. Navy equipment pending further investigations.

Presented at the 1979 Near Surface Ocean Experimental Technology NORDA Workshop, National Space Technology Laboratories, MS.

It is particularly important to realize that sulfur dioxide has been used as a refrigerant at one time because of its vapor pressure characteristics. At 20°C the internal pressure of a cell is ∿33 psig and at 100°C it is in excess of 392 psig. SO_2 cells should not be placed in sealed pressure containment equipment (i.e., deep-ocean equipment applications). The disallowance of these cells to vent freely can, and have, caused violent explosions. Table 1 presents other related $LiSO_2$ cell problems and hazards.

This unfortunate experience with lithium-sulfur dioxide batteries has given a tainted safety reputation to the entire lithium battery line. In addition, early lithium-thionyl chloride batteries were also prone to catching fire and exploding when subjected to abuse, which has added to the distrust of lithium batteries in the user community. The mechanisms causing the safety problems in lithium-thionyl chloride batteries are now generally understood, however, and quantum advances have been made in the safety of these batteries. Outstanding progress has been made in the safety area by the Altus Corporation. Large lithium-thionyl chloride cells produced by Altus have demonstrated the ability to withstand incineration, mechanical shock, bullet penetration, short circuits, and application of reverse voltage, without fire or explosion. Details of these abusive tests, and the results of an extensive test program which will be conducted shortly by the Naval Ocean Systems Center, should further verify the safety of lithium-thionyl chloride cells, and are discussed in this paper.

In an attempt to channel government sponsored development of lithium-thionyl chloride cells and batteries into useful hardware, a technical development plan is being generated by the Naval Ocean Systems Center. Highlights of that plan are presented in this paper.

Characteristics of Lithium-Thionyl Chloride Batteries

Cell Chemistry

Lithium-thionyl chloride cells typically contain a lithium anode, porous carbon cathode, and an interelectrode separator. The electrolyte, which also acts as a reducible catholyte, consists of a salt, such as $LiALCL_4$, dissolved in thionyl chloride. During discharge, the thionyl chloride is reduced at the carbon cathode. Initial contact of thionyl chloride with lithium during cell filling forms a layer of lithium chloride on the anode. This layer prevents further direct reduction of anodic and cathodic materials, thus eliminating self-discharge.

At least two mechanisms have been identified for the discharge of the $LiSOCl_2$ cell. At low current densities the following reaction appears to predominate.

$$8\ Li + 3\ SOCl_2 \rightarrow 6\ LiCl + Li_2SO_3 + 2S$$

The products of reaction are all solid. The theoretical capacity of $SOCl_2$ for this reaction is 0.60 Ah/g.

At high current densities the overall discharge reaction is commonly accepted to be:

$$4\ Li + 2\ SOCl_2 \rightarrow 4\ LiCl + SO_2 + S$$

TABLE 1.

LITHIUM SULPHUR DIOXIDE CELL SAFETY PROBLEMS

- Lithium melting point 189° C - Very reactive when molten.
- SO_2 (~30 cc in "D" cell) - Boiling point: 0° C @ 1 atm.

  Vapor pressure: 3.2 atm. @ 20° C and 27.7 atm. @ 100° C.

  Critical pressure: 77.7 atm. @ 157.8° C (venting essential).
- Acetonitrile extremely toxic, limits disposal alternatives.
- Leakage thru seal & vent from corrosion in mild steel cases.
- Over-discharge results in lacey lithium which can fuse and initiate a reaction.
- Discharge after SO_2 loss produces I^2R heating and melting of lithium.
- Venting with flame produces chain reaction with adjacent cells.

The theoretical capacity of $SOCl_2$ for this reaction is 0.45 Ah/g.

Recent development have yielded reactions which substantially reduce the SO_2 generated over a wide range of discharge rates. The reduction of gaseous products is a significant factor in reducing the possibility of cell rupture at high temperatures.

The open circuit voltage of the cell is 3.65 volts, and typical voltages under load are 3.2 to 3.4 volts. For very high discharge rate applications, (current densities of more than one hundred mA per cm^2) the terminal voltage averages over 3.0 volts at normal battery operating temperatures. The output voltage is nearly constant during discharge until 95% of the active life is approached. These relatively high output voltages, in comparison to other battery types, contribute to the high specific energy of the battery.

Cell Construction

Small, flashlight type cells in sizes up to double D, are produced in "bobbin" and in the "jelly roll" configurations. The bobbin type cells consist of a central carbon cathode and a cylindrical anode which is attached to the cell container. This construction is used to obtain maximum energy at low discharge rates. Cells designed for maximum power are constructed by winding long strips of the two electrodes together in a jelly roll manner. The cathode is usually carbon which may contain a PTFE binder pressed onto a nickel or stainless steel current collector grid. The cells are usually hermetically sealed. Larger size batteries are made in prismatic form with a series of planar electrodes contained in a rectangular cell. GTE produces rectangular cells up to 10,000 Ah capacity and 44 x 31 x 25 cm (17.3 x 12.2 x 9.8 inches) in size. Honeywell produces cells up to 17,000 Ah capacity and 38 x 38 x 38 cm (14.9 x 14.9 x 14.9 inches) in size. Disc-like cell forms are being produced by Altus in sizes from 2.26 cm (0.89 inch) diameter to 43.2 cm (17 inches) in diameter. Battery systems can be made up from these cell types to meet particular applications. The disc cells, which can be stacked to achieve required power and energy requirements, allow efficient utilization of volume in cylindrical undersea vehicles. Several cylindrical, prismatic, and disc configuration lithium-thionyl chloride cells, ranging in capacity from 0.25 to 1500 ampere hours, are shown in Figure 1.

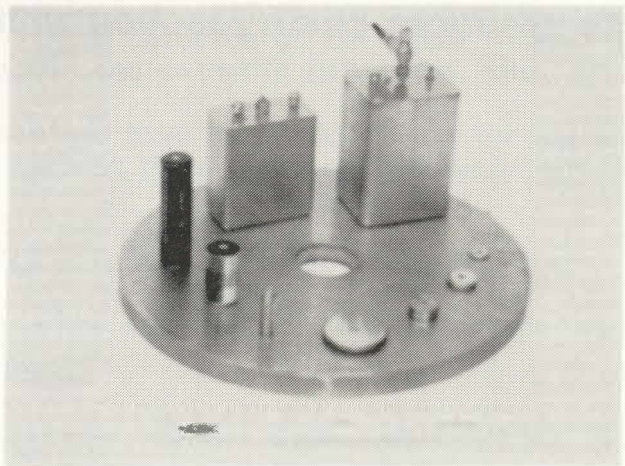

Figure 1. A Variety of Lithium-Thionyl Chloride Cell Configurations and Sizes.

Performance of Lithium-Thionyl Chloride Batteries

The theoretical specific energy of a lithium-thionyl chloride battery, considering only active material, is 1470 Wh/kg (666.6 Wh/lb). As in all batteries, practical factors such as a case, support structure, current collectors, and losses, reduce the available specific energy to a fraction of this value. A summary of presently available $LiSOCl_2$ cells in terms of capacity, type, dimensions, weight, and manufacturer is given in Table 2.

Commercially available D size cells offer specific energy of 340 to 420 Wh/kg (154.1 - 190.4 Wh/lb), depending on the manufacturer, and energy density of 680 to 800 Wh/liter (11.1 - 13.1 Wh/in^3).[1,2] Double D size cells offer specific energy of 480 Wh/kg (217.6 Wh/lb), and energy density of 900 Wh/liter (14.7 Wh/in^3), at a discharge time of 180 hours.[1] The shelf life of the above cells is typically specified as a capacity loss of 1% per year.

Developmental 500 Ah prismatic cells built by Honeywell provide specific energy of 642 Wh/kg (291.1 Wh/lb) and energy density of 2100 Wh/liter (34.4 Wh/in^3) at a discharge time of about 1000 hours.[3] Their experimental 17,000 Ah cells provide specific energy of about 480 Wh/kg (217.6 Wh/lb) and energy density of about 920 Wh/liter (15.0 Wh/in^3) at a discharge time of about 425 hours. Developmental 0.2 Ah disc cells built by Altus have demonstrated specific energy of 780 Wh/kg (353.7 Wh/lb), and energy density of 1200 Wh/liter (19.6 Wh/in^3), at a discharge time of 90 minutes. Altus 1500 Ah disc cells have a specific energy of 370 Wh/kg (171.8 Wh/lb) and energy density of 960 Wh/liter (15.7 Wh/in^3).[4] The 2000 Ah prismatic cell developed by GTE provides specific energy of 460 Wh/kg (208.6 Wh/lb), and energy density of 910 Wh/ liter (14.9 Wh/in^3), over a discharge time of 250 hours.[1] GTE is producing 10,000 Ah cells which provide 480 Wh/kg (217.6 Wh/lb) and 950 Wh/liter (15.5 Wh/in^3) at a current of 40 amperes for 250 hours.[1] The 10,000 Ah GTE cell weighs 78.8 kg (173.7 lbs) and occupies 36.3 liters (2215 in^3).

A 180 kWh High Energy Density Battery (HEDB) system is being developed by the Naval Ocean Systems Center. The battery contains 38-43.2 cm (17 inches) diameter disc cells built by Altus. The cells are stacked to form a battery system with overall external dimensions of 0.53 meters (21 inches) diameter and 1.52 meters (60 inches) long. The projected weight of the overall battery system is about 523 kg (1150 pounds). Results of cell testing indicate that at least 180 kWh will be delivered by the battery over a 1600 hour mission. The net specific energy of the battery system, including substantial support structure, is 363 Wh/kg (164.6 Wh/lb) and the net energy density is 681 Wh/liter (11.16 Wh/in^3). The 1500 Ah cells are 43.2 cm (17 inches) in diameter and 3.5 cm (1.4 inches) thick. Each cell weighs 13.3 kg (29.3 lbs). A photograph of the HEDB and a

1 GTE Sylvania Data Sheets
2 Tadiran (Israel Electronics Industries) Data Sheets
3 Honeywell Data Sheets
4 Altus Model 1700-1400 Data Sheet

Table 2.

PRESENT LITHIUM THIONYL CHLORIDE BATTERY SUMMARY

CAPACITY (AH)	TYPE	DIMENSIONS (In.)	WEIGHT (oz.)	MANUFACTURER
0.08	DISC*	0.89 × 0.12	0.12	ALTUS
0.14	DISC	0.79 × 0.10	0.08	ALTUS
0.16	CYLINDRICAL	0.63 × 1.00	0.35	HONEYWELL
0.19	WAFER	0.110 × 0.965	0.13	GTE
0.20	DISC	0.89 × 0.12	0.12	ALTUS
0.22	DISC	0.89 × 0.12	0.12	ALTUS
0.45	CYLINDRICAL	0.63 × 2.20	0.88	HONEYWELL
0.70	DISC	0.89 × 0.12	0.12	ALTUS
0.75	CYLINDRICAL	1.03 × 0.75	0.81	HONEYWELL
1.50	DISC	1.27 × 0.28	0.81	ALTUS
1.60	CYLINDRICAL	0.60 × 1.30	0.63	HONEYWELL
1.70	"AA"	1.96 × 0.56	0.50	GTE
2.00	"AA"	0.28 × 1.67	0.58	TADIRAN
5.00	"C"	1.96 × 1.00	1.65	TADIRAN
5.00	"C"	1.93 × 1.03	1.62	GTE
5.50	DISC	2.50 × 0.28	3.17	ALTUS
8.00	CYLINDRICAL	0.99 × 1.67	1.65	TADIRAN
9.00	CYLINDRICAL	1.28 × 2.28	3.31	TADIRAN
10.00	"D"	2.42 × 1.28	3.38	TADIRAN
12.00	"D"	2.40 × 1.34	3.24	GTE
17.00	PRISMATIC	1.18 × 1.14 × 2.48	—	HONEYWELL
18.00	DISC	4.50 × 0.30	10.58	ALTUS
30.00	"DD"	4.72 × 1.34	8.70	GTE
166.0	PRISMATIC	2.30 × 4.20 × 5.0	—	HONEYWELL
400.0	PRISMATIC	3.63 × 4.30 × 5.5	—	HONEYWELL
500.0	PRISMATIC	3.63 × 4.28 × 6.18	—	HONEYWELL
1 500.00	DISC	17.00 × 1.40	464.00	ALTUS
2 000.00	PRISMATIC	19.8 × 3 × 13.4	640.00	GTE
10 000.00	PRISMATIC	19.8 × 11.5 × 13.5	2720.00	GTE
17 000.00	PRISMATIC	15 × 15 × 15	3200.00	HONEYWELL

*DENOTES HIGH RATE

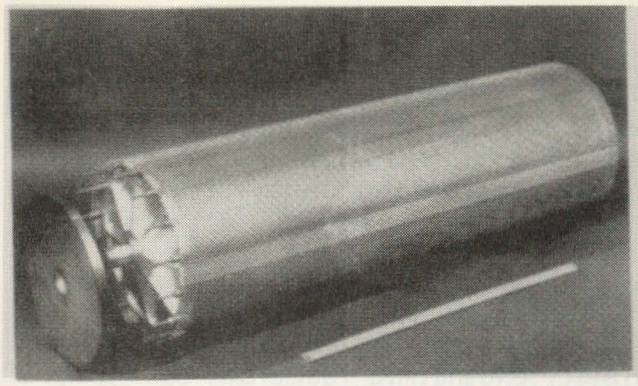

Figure 2. The High Energy Density Battery (HEDB) and a Single Cell

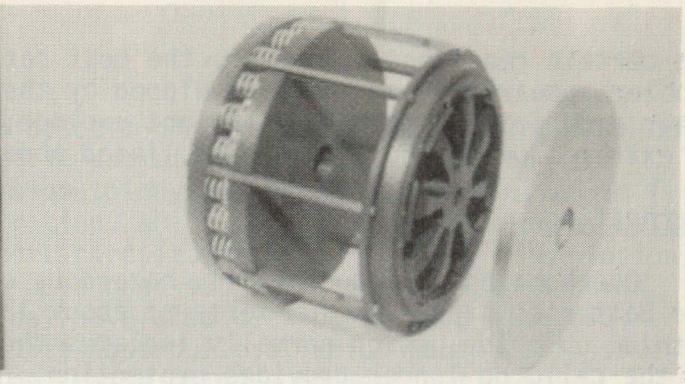

Figure 3. 28-volt Short Stack HEDB

single cell is shown in Figure 2. Design specifications for the HEDB are summarized in Table 3. A 28-volt "short stack" version of the HEDB which uses 9-1500 Ah cells is illustrated in Figure 3.

Table 3. HEDB Specifications

Total energy	**200 kw-hr**
Peak power	**1.5 kw (combined electronic & electro-mechanical load)**
Envelope	**.53 m dia & 1.52 m in length**
Weight	**~500 kg**
Endurance	**Up to 6 months**
Operating depth	**600 meters**
Safety	**Full compliance with appropriate Mil specs/standards & special requirements for lithium batteries**
Stand by to full power	**< 5 minutes**
Start up/shut down	**<1/2 hour to full power/instantaneous**
Storage life	**Dry - 5 years; wet - 1 year**
Operating attitude	**Prefer vertical attitude ±35°**
Environmental	**Shock, vibration, pressure, penetration, etc**
Temperature:	
Operate	**-2° C to 27° C**
Storage & transport	**-40° C to 60° C activated; -40° C to 74° C dry**
Replenishment	**Accomplish in a closed, manned shipboard space**
Disposal	**At-sea with no pollution**

Safety Aspects of Lithium-Thionyl Chloride Batteries

Early lithium-thionyl chloride batteries responded violently in the form of fire and explosion when subjected to abuse such as overheating, physical damage, short circuits, and reverse voltage conditions. The causes of the violent reaction are generally well understood. These mechanisms are briefly reviewed in the following paragraphs. Additives have been found to be effective in prevent-

ing certain reactions. However, the most satisfactory solution to the safety problem appears to have been developed by the Altus Corporation. Cells made with their proprietary technology, do not explode, or catch fire, even when subjected to extremes of the forms of abuse listed above.

Overheating

Overheating is a potentially hazardous condition for lithium-thionyl chloride batteries since lithium melts at about 186°C, and the passivating film of lithium chloride, which normally isolates the lithium from the other components of the cell, no longer provides protection. Highly exothermic reactions can take place between molten lithium, and thionyl chloride and/or elemental sulfur. The later component is commonly considered to be a product of normal battery reaction. Sulfur monochloride has been found to be an effective additive by some manufacturers to solubilize the elemental sulfur as it is formed in the cell, thus avoiding the possibility of a lithium-sulfur reaction. Sulfur monochloride can also form slowly from the reaction of elemental sulfur and thionyl chloride at elevated temperature. The generation of sulfur dioxide in the cell can be held to low levels by appropriate cell chemistry. This has a two-fold benefit; first, the possibility of reaction between lithium and sulfur dioxide is minimized; and second, it avoids the problem of high concentrations of gas in the cell which would expand with increasing temperatures and cause build up of dangerously high pressures within the cell. Cells built by Altus have demonstrated the ability to withstand temperatures well above the melting point of lithium without violent reaction.

Short circuiting the terminals of the cell causes internal heating, with the consequences attendant with overheating, as described above. In addition, it is possible that localized high concentrations of heat and reaction products could be generated which accentuates the possibility of a violent reaction. Short circuit testing of early lithium-thionyl chloride cells often produced an explosion. However, the major manufacturers of large lithium-thionyl chloride cells, Altus, GTE, and Honeywell, have now all demonstrated that their cells can be short circuited without causing explosion or some other violent reaction.

Reverse Voltage

One or more cells of a series-connected battery can experience a reverse voltage condition if they become discharged before the other cells in the battery. Applying reverse voltage to lithium-thionyl chloride cells can cause lithium in dendritic form to grow from the anode to the cathode. This is a potentially hazardous situation, since the dendrite can burn out and arc when it contacts the cathode, and in so doing initiate a reaction between the lithium and other cell components. A second deleterious effect of reverse voltage conditions is that electrolysis of the electrolyte can take place which can generate oxyanions such as ClO_2. These oxyanions can spontaneously react with the carbon electrode and cause high pressures within the cell.

One method which has been suggested to protect cells in a series battery arrangement from reverse voltage is to place Schottky diodes around each cell. Although the techniques used to achieve safe operation are proprietary to each company, cells built recently by Altus have demonstrated the ability to withstand 200% of cell rated ampere hours in reversed voltage condition. Cells built by GTE have successfully withstood 150% of their rated capacity in reverse voltage.

Physical Abuse

Penetration of the cell by sharp objects can break the passivating film on the lithium and allow reaction between it and other cell components to take place. Nail penetration of early lithium-thionyl chloride cells resulted in fire or explosion. Likewise, bullet penetration, which causes local heating as well as deformation leading to internal short circuit, resulted in fire or explosion in early cells. Cells built by Altus have been subjected to nail penetration without ensuing fire or explosion. They have also been penetrated with .30 caliber bullets. When fired at with soft nose bullets, which caused extensive damage to the cell, local fires were generated which soon went out.

Hazard/Safety Testing of Lithium-Thionyl Chloride Batteries

A hazard/safety test program was conducted for the Navy by Wyle Laboratories in Norco, CA in May 1978 on 43.2 cm (17 inch) diameter, 500 Ah lithium-thionyl chloride cells built by Altus. These cells were developed for the High Energy Density Battery program under contract with the Naval Ocean Systems Center. The tests, which were designed to determine the safety of these cells under conditions of extreme abuse, included exposure to a fuel-oil fired bonfire (Figure 4), nail penetration (Figure 5), punching a 2.5 cm (1 inch) diameter hole through a cell (Figure 6), multiple bullet penetrations (Figure 7), and drop testing from 12.2m (40 feet) onto a steel plate (Figure 8). No cases of explosion resulted from these tests. Under the extreme overheating tests, the cells merely vented.

During bullet penetration tests, using soft nosed bullets which caused extensive internal damage to the cell, fire occurred in the immediate area of the damage. Repeated penetration eventually destroyed the cell structure and the cell was consumed by fire. Solid nose bullets cleanly penetrated the cell without causing fire.

A crush test was performed by applying 1000 psi local pressure to the cell without noticeable effect on performance. At a pressure of 20,000 psi over a 1-inch diameter area, the cell was punched through, and a local cell fire resulted.

Short circuit testing was performed without incident, although the negative terminal melted off after sustaining 100 amperes for one (1) minute.

During reverse voltage testing, one cell vented. Changes were made in the cell desigh, and later cells have demonstrated an ability to withstand reverse voltage conditions, without adverse reaction.

An exhaustive test program to demonstrate the safety of lithium-thionyl chloride batteries for naval applications will be undertaken shortly by Code 631 of the Naval Ocean Systems Center. It is planned to subject a total of 41-1500 Ah cells to a rigorous environmental, and hazard/safety test sequence. These cells have higher capacity than the cells previously tested, and incorporate the latest refinements in the technology. In addition to performance and characterization tests, the following tests will be performed:

Figure 4. Fuel-oil fired bonfire.

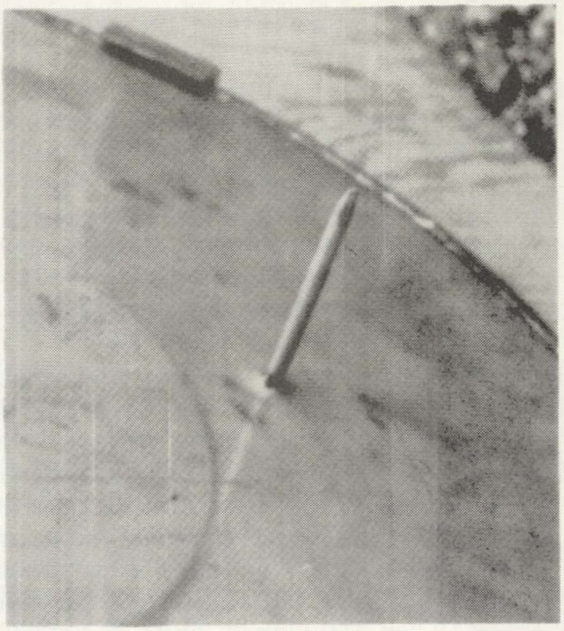

Figure 5. Nail penetration.

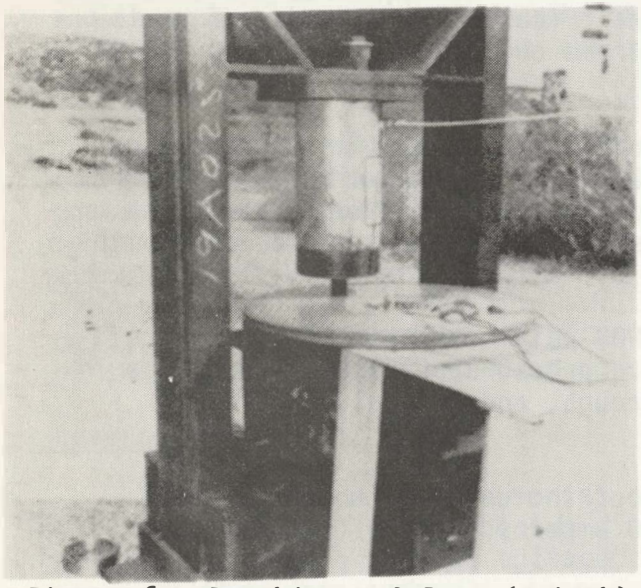

Figure 6. Punching a 2.5 cm (1 inch) diameter hole through a cell.

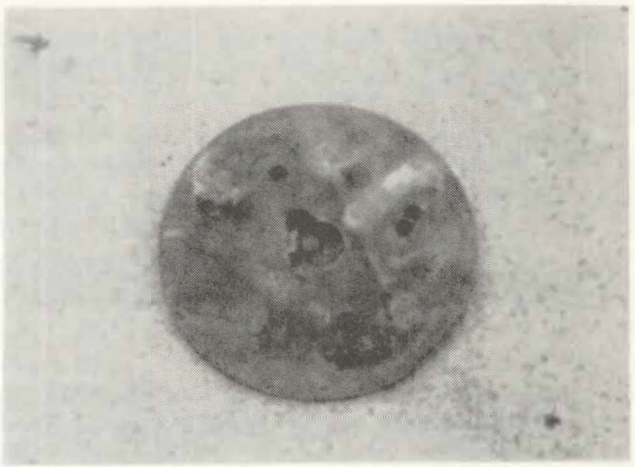

Figure 7. Multiple bullet penetration.

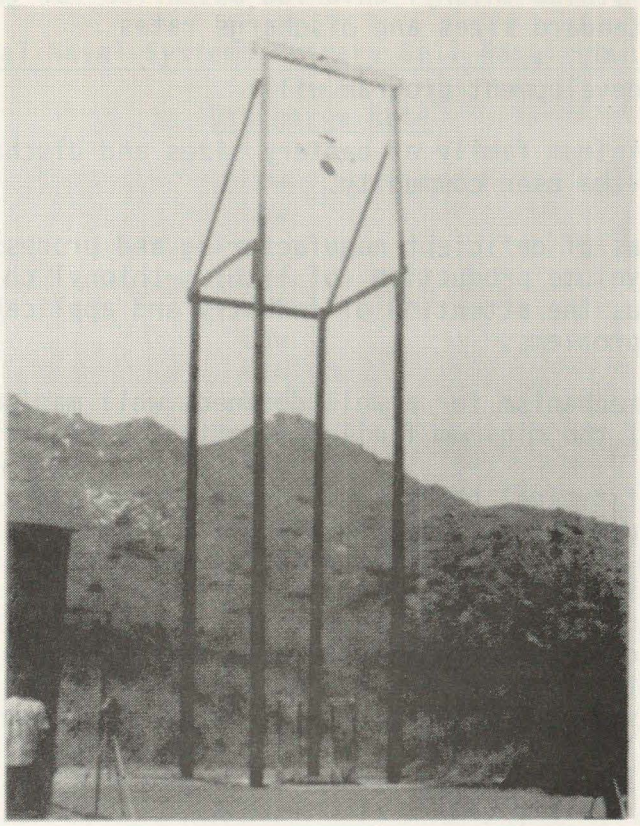

Figure 8. Drop testing from 12.2 m (40 feet) onto a steel plate.

Environmental	Hazard/Safety
Vibration	External Heat
Shock	Reverse Voltage
Hydrostatic	Post-Reverse Voltage Shock
Overcurrent	Penetration
Drop (3')	Drop (6')
Altitude	Short Circuit
	Disposal

Following cell testing, three short stack batteries (shown in Figure 3), each containing 9 cells, will be assembled and subjected to performance and hazard/safety testing. These tests will include overcurrent, short circuit, and sympathetic influence of one cell rupturing in a battery stack.

It is anticipated that this test program will provide a conclusive demonstration of the inherent safety of advanced lithium-thionyl chloride battery technology.

High Energy Density Battery Technical Development Plan

A technical development plan for lithium-thionyl chloride batteries has been generated by the Naval Ocean Systems Center. The objectives of the High Energy

Density Battery Development Program are to promote and focus the development of safe, "off-the-shelf" lithium-thionyl chloride batteries for government use into and orderly array of standard sizes and discharge rates.

In essence, the development program will:

1. Identify a minimum family of battery sizes and discharge rates which will meet the needs of the user community.

2. Identify areas of deficient manufacturing and processing technology that presently retards the volume production of lithium-thionyl chloride batteries at low cost, and will focus the attention of industry and applicable government laboratories on these problems.

3. Provide the mechanism for a well defined, well managed procurement for development and test of the minimum family of batteries identified in (1) above.

A brief survey of typical naval requirements for primary batteries is given in Table 4. These requirements have been translated into a matrix defining a minimum set of lithium-thionyl chloride batteries which would satisfy current and projected DoD applications, and are shown in Table 5.

It appears that coordinated development of a family of 6 to 8 basic cells would satisfy the identified requirements and allow production to be concentrated on a few standard cells. This will reduce both the development cost and the unit cost of lithium-thionyl chloride batteries, and make safe, reliable high performance batteries available to the user community in the shortest time.

Table 4.

Typical Naval Systems Primary Cell Requirements

Application	Discharge Rate*	Capacity (Ah)
Remote Sensors	Low	50-100
Mines	Low	500
Aircraft Emergency Transponders	Low	5.5
Data Links	Low	100
Standby Power	Low	10-10K
Field Communications	Medium	20
Tactical Data Terminals	Medium	10
Portable Lighting	Medium	20
Countermeasures & Decoys	High	10-100
Vehicle Propulsion	High	1000-3000
Sonobuoys	High	10
Targets	High	1000
Torpedoes	Very High	50-300
Missiles	Very High	10
Ordnance Fuzing	Very High	1
Laser Designators	Very High	10

*Low - 100 hrs.
Medium - 10 hrs.
High - 1 hr.
Very High - 0.1 hr.

RATE \ SIZE	SMALL (~10 AH) A	MEDIUM (~100 AH) B	LARGE (~1000 AH) C	VERY LARGE (~10,000 AH) D
LOW (100 HRS) 1	EXPERIMENTAL ① EQUIPMENT A1		REMOTE SENSORS ② MINES, AIDS TO NAVIGATION C1	STANDBY POWER ② D1
MEDIUM (10 HRS) 2			SUBMERSIBLES ③ C2	
HIGH (1 HR) 3	SONOBUOYS, ② PORTABLE COMMUNICATIONS A3	COUNTERMEASURES & DECOYS ③ B3		
VERY HIGH RATE RESERVE (0.1 HR) 4	MISSILES COUNTERMEASURES ③ A4	TORPEDOES TARGETS ② B4		

① DEVELOPED

② IN DEVELOPMENT

③ DEVELOPMENT REQUIRED

Table 5. Matrix of Lithium Thionyl Chloride Batteries Required for Current & Projected Marine Applications.

OCEAN ACOUSTIC MONITORING: ACOUSTIC TOMOGRAPHY

Robert C. Spindel
Woods Hole Oceanographic Institution
Woods Hole, Massachusetts 02543

Abstract

An acoustic method for monitoring mesoscale ocean features over basin wide areas, known as acoustic tomography, is being developed. This paper describes the principles of the technique, and the specialized equipments designed to meet stringent technical requirements. We also present results of recent experiments, forerunners of a full-scale system deployment, that demonstrate the feasibility of the method.

Introduction

Using acoustic methods to monitor the variability of the ocean's interior has been an intriguing notion that has threaded its way through the literature in underwater acoustics for the past 10-15 years[1-6]. Early speculation began, perhaps, with the MIMI (University of Miami-University of Michigan) transmissions across the Straits of Florida and the observation of a striking correlation between acoustic phase variations and tidal and transport changes.[1] Studies of the effects of internal wave, tides, Rossby Waves, currents, finestructure and mesoscale eddies on acoustic transmissions have implicitly or explicitly suggested the inverse procedure of measuring the oceanic process through observation of an acoustic effect.[7-16] The pertinent acoustic variables have been amplitude, phase, travel time, arrival angle and (spatial and temporal) coherence. Recently an attractive procedure for acoustic monitoring of mesoscale (order 100 km) ocean dynamics has been proposed.[6] It is based on the measurement of acoustic travel time variations between multiple fixed sources and receivers and is called acoustic tomography. Tomo derives from the Greek word tomos, meaning section; a tomogram is a picture of a slice. In medicine, where tomography has found early widespread use, x-rays, microwaves, light waves and ultrasound are used to image slices of the body or biologic samples.[17] In radio astronomy microwaves have been used to obtain tomographic images of the sun and moon.[18] Similarly, electric waves have been used in electron microscopy, light waves have been used in optical microscopy and in geophysics electromagnetic and seismic energy have been used to image slices of the earth.[19] Ocean acoustic tomography calls for the use of underwater sound waves to image slices of the interior ocean.

In the following we (a) briefly outline the tomographic method, (b) describe some of the technologic requirements, (c) describe equipments being developed to meet these requirements and (d) give some examples of equipment operation. The tomography program described in this paper is a multi-institutional effort and includes participants at Scripps Institution of Oceanography (W. Munk and P. Worcester), the Massachusetts Institute of Technology (C. Wunsch) and the University of Michigan (T. Birdsall).

The Method

Tomography is based on the concept that any two dimensional object can be reconstructed from an infinite sum of its projections.[20] For the specific case of ocean acoustic tomography we wish to reconstruct an image of the ocean sound speed field using time of flight measurements as acoustic pulses transit between

multiple sources and receivers. The sound speed field is the fundamental quantity measured. However, since sound speed is strongly dependent on temperature, salinity, density and ocean currents, ocean structure itself can be deduced from estimates of the three-dimensional sound field.

We imagine a series of acoustic sources and receivers scattered about an ocean area as shown in Figure 1. Each transmitter emits an acoustic pulse and the time of flight, T_{ij}, along each ray is measured

$$T_{ij} = \sum_{k=1}^{K} \frac{L_{ij}^{(k)}}{c_k} \qquad \begin{matrix} i=1,\ldots,N \\ j=1,\ldots,M \end{matrix} \qquad (1)$$

where $L_{ij}^{(k)}$ is the path length of the ray is cell k. The problem of reconstruction is to determine the c_k based on measurements of the T_{ij}. Equation (1) represents a set of MN equations and K unknowns. In general we can have $MN < K$, $MN = K$ or $MN > K$ yielding an undetermined, determined or overdetermined system. The number of sources, receivers and cells is determined by the size of the area being monitored and the expected size of ocean inhomogeneities. For mesoscale features in a 1000 km square ocean reasonable assumptions yield about 5 sources and 5 receivers and 25 200 km square cells.

A wide variety of techniques for solving for the c_k, known as "inverse" methods, have been developed. The MN equations can be solved by brute force, or computationally more efficient schemes using special iterative algorithms such as ART (Algebraic Reconstruction Technique) can be used. Other methods include convolution techniques and Fourier domain reconstructions, linear least squares estimation procedures, maxim entropy and optimum Bayesian filters. We have not yet determined the most efficient form of solution for ocean tomography, however, any of the above techniques can be used.

In the specific example of Figure 1 we have illustrated the so-called horizontal problem in which the reconstruction yields sound velocity information in two dimensions. Acoustic rays do not, of course, propagate in straight horizontal lines, rather they cycle vertically through the water column. Thus one can consider a vertical tomographic image such as shown in Figure 2 where we have sketched only a few of the rays that connect source to receiver. In this case there are E (wholly refracted - we ignore boundary reflections) eigenrays connecting transmitter to receiver. The equations for time of flight of the eigenrays are similar to (1)

$$T_i = \sum_{\ell=1}^{L} \frac{D_i^{(\ell)}}{c_\ell} \qquad i=1,\ldots,E \qquad (2)$$

where T_i is the travel time of the ith eigenray, $D_i^{(\ell)}$ is the path length of the ith ray in the ℓth cell, and L is the number of vertical cells. We can solve (1) and (2) independently or, in principle, we can combine vertical and horizontal cells into volumes and proceed in analogous fashion. In this case we imagine V volume cells and MN transmitter-receivers.

System Requirements

The object is to monitor mesoscale ocean features that have typical temperature anomalies of $\Delta\Theta = 2°C$ (corresponding to sound velocity anomalies of $\Delta c_k = 5\times10^{-3}$) over a distance of 100 km and confin ed to the upper 1000 m. A typical ray cycle upper loop extends for about $\Delta r = 20$ km in the upper 1000 m and there will be two such loops within the mesoscale disturbance. The corres-

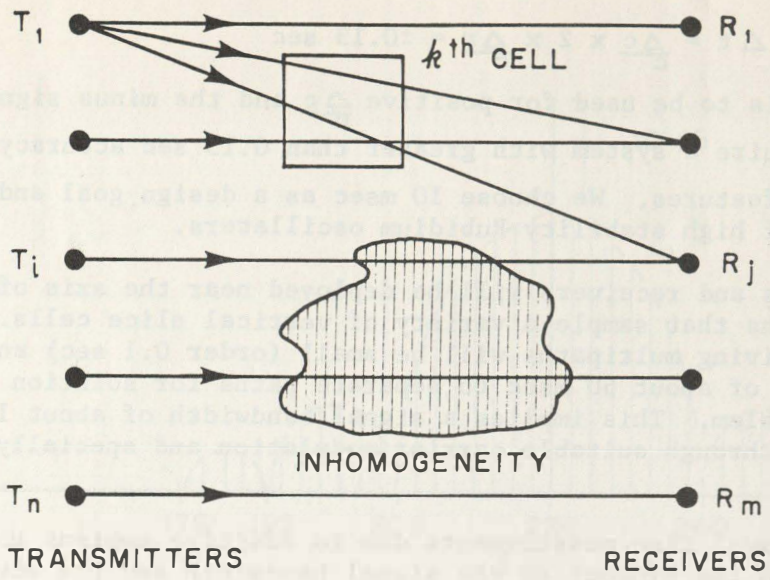

Figure 1 Horizontal ocean tomography. Not all transmitter to receiver paths are shown.

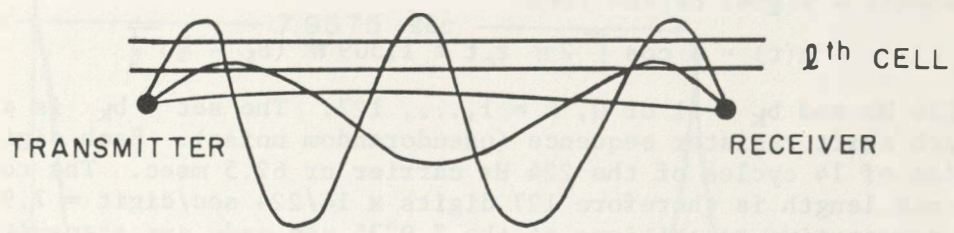

Figure 2 Vertical ocean tomography. Not all transmitter to receiver paths (eigenrays) are shown.

ponding travel time change will be

$$\Delta t = \frac{\Delta c}{c} \times 2 \times \frac{\Delta r}{c} = \pm 0.13 \text{ sec}$$

where the + sign is to be used for positive $\frac{\Delta c}{c}$ and the minus sign for negative $\frac{\Delta c}{c}$. Thus we require a system with greater than 0.13 sec accuracy in order to detect mesoscale features. We choose 10 msec as a design goal and achieve it through the use of high stability Rubidium oscillators.

Transmitters and receivers will be deployed near the axis of the sound channel to obtain paths that sample a variety of vertical slice cells. The temporal separation of arriving multipaths will be small (order 0.1 sec) and we require a system resolution of about 50 msec to separate paths for solution of the vertical slice inverse problem. This implies a signal bandwidth of about 1/50 msec = 20 Hz. This is achieved through suitable carrier modulation and specially designed acoustic sources.

Error in travel time measurements due to additive ambient noise is inversely proportional to the product of the signal bandwidth and the square root of the signal-to-noise ratio at the receiver,

$$\sigma_t \approx \frac{1}{BW} \times \frac{1}{\sqrt{SNR}}$$

With a 20 Hz bandwidth a σ_t of 10 msec is realized with an SNR of 20 db. We achieve required SNR and resolution through transmission of a signal with large time-bandwidth product and subsequent matched filter receiver processing.

Mesoscale features have time constants of about one month, so that the ocean sampling rate (the frequency at which time of flights measurements are made)must be about once every three days.

System Design

We transmit a signal of the form

$$s(t) = A \cos \left[2\pi f_c t \pm 1.309 \pi (b_k - \tfrac{1}{2}) \right]$$

where f_c = 224 Hz and b_k = +1 or 0, k = 1,..., 127. The set b_k is a linear maximal length shift register sequence (pseudorandom noise). Each digit, b_k, has a duration of 14 cycles of the 224 Hz carrier or 62.5 msec. The total transmitted sequence length is therefore 127 digits x 14/224 sec/digit = 7.9375 sec. Twenty-four consecutive repetitions of the 7.9375 sec code are transmitted every 30 minutes for a 12 hour period. This is repeated every three days. This modulation scheme results in a signal with the power spectrum shown in Figure 3 and the autocorrelation shown in Figure 4. The carrier line is 10 db above adjacent spectral lines, but contains only 2% of the total power transmitted. Source level is 185 db re/1μPa.

With a 185 db source we estimate the following signal level at 500 km range

Source Level	+185 db re/μPa
Spherical Spreading 20 log 5×10^5 m =	-114 db
Attenuation	- 3 db
	68 db

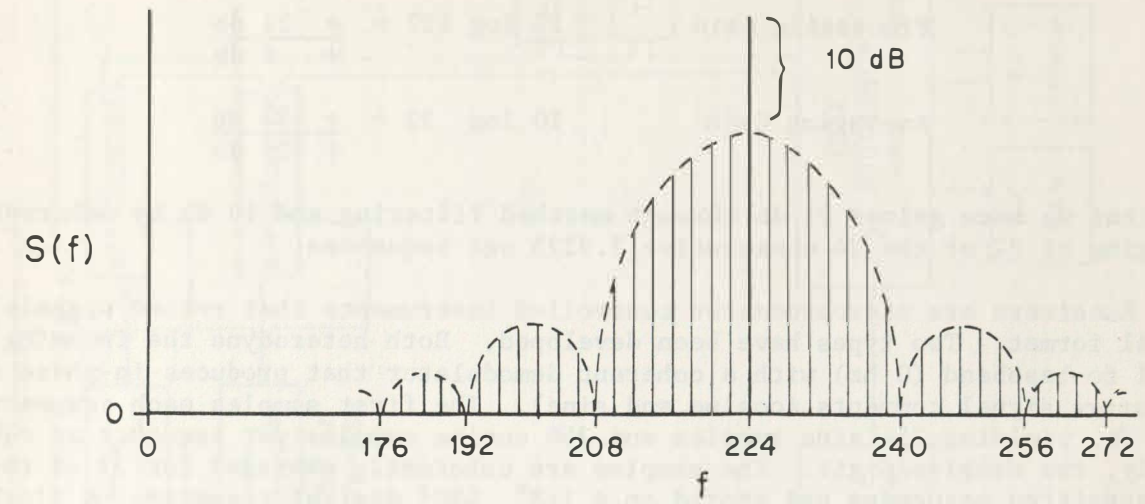

Figure 3 Power spectrum of transmitted signal. Spectral lines are spaced 126 mHz, not all are shown.

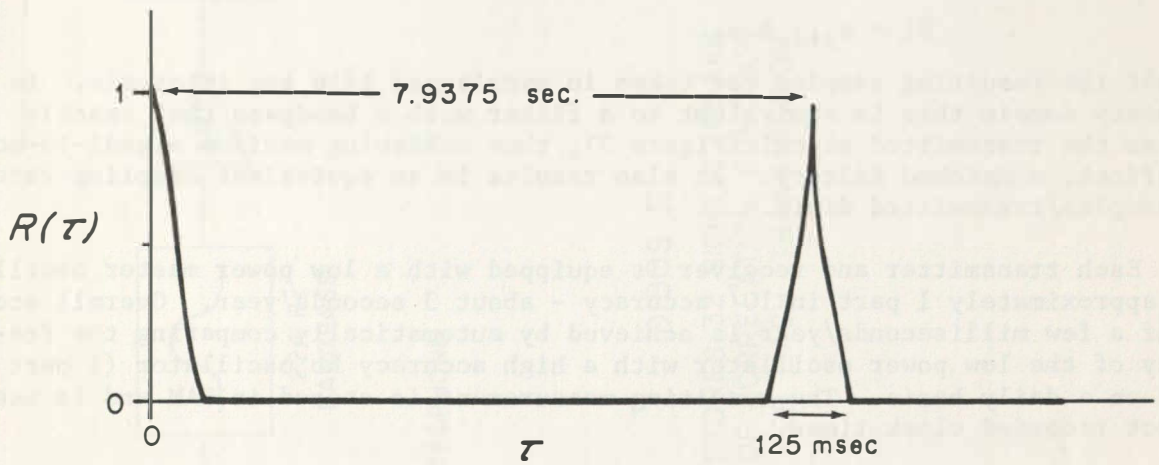

Figure 4 Normalized autocorrelation function of transmitted signal.

Noise (224 Hz in 1 Hz band)		- 70 db
15 Hz band	10 log 15 =	- 12 db
		- 14 db
Processing Gain	10 log 127 =	+ 21 db
		+ 8 db
Averaging Gain	10 log 22 =	+ 13 db
		+ 21 db

Note that we have gained 21 db through matched filtering and 13 db by coherent averaging of 22 of the 24 consecutive 7.9325 sec sequences.

Receivers are microprocessor controlled instruments that record signals in digital format. Two types have been developed. Both heterodyne the incoming signal to baseband (0 hz) with a coherent demodulator that produces in-phase and quadrature signal comments (cosine and sine). The first samples each component at 32 Hz, yielding 254 sine samples and 254 cosine samples per sequence or equivalently, two samples/digit. The samples are coherently averaged for 22 of the 24 transmitted sequences and stored on a 1/8", 450' digital cassette. A block diagram of the receiver is shown in Figure 5. Matched filtering (pulse compression) is accomplished with an off-line processor.

The second type of receiver also samples at 32 Hz and coherently averages 22 of the 24 sequences (Figure 6). However, it is equipped with an algorithm that computes the matched filter using an internally stored replica of the transmitted sequence. The largest 32 peaks in the resulting correlation function are located and their amplitude, phase and arrival time are stored. This entails considerably less recording capacity so that a single cassette can store almost a full year of data. In addition, this unit accomplishes analog-to-digital conversion by a V/F converter followed by a counter. Each sample consists of a 1/32 count denoted s_i. Consecutive counts are concatenated as follows:

$$Si = s_{i+1} \Theta s_i$$

so that the resulting samples are taken in overlapped 1/16 sec intervals. In the frequency domain this is equivalent to a filter with a bandpass that exactly matches the transmitted signal (Figure 3), thus achieving maximum signal-to-noise (in effect, a matched filter). It also results in an equivalent sampling rate of two samples/transmitted digit.

Each transmitter and receiver is equipped with a low power master oscillator with approximately 1 part in 10^7 accuracy - about 3 seconds/year. Overall accuracy of a few milliseconds/year is achieved by automatically comparing the frequency of the low power oscillator with a high accuracy Rb oscillator (1 part in 10^{11}) on a daily basis. The resulting measurement is stored in RAM and is used to correct recorded clock times.

Each mooring is also equipped with an acoustic navigation unit that interrogates three bottom-mounted transponders once/hour for the duration of the experiment. The three round trip travel times measured in this way are used to calculate the position of the mooring with respect to a fixed geographic point. Knowledge of mooring position prevents travel time variations due to mooring excursions (caused by currents) from being misinterpreted as being due to changing oceanographic conditions along the source to receiver transmission path.

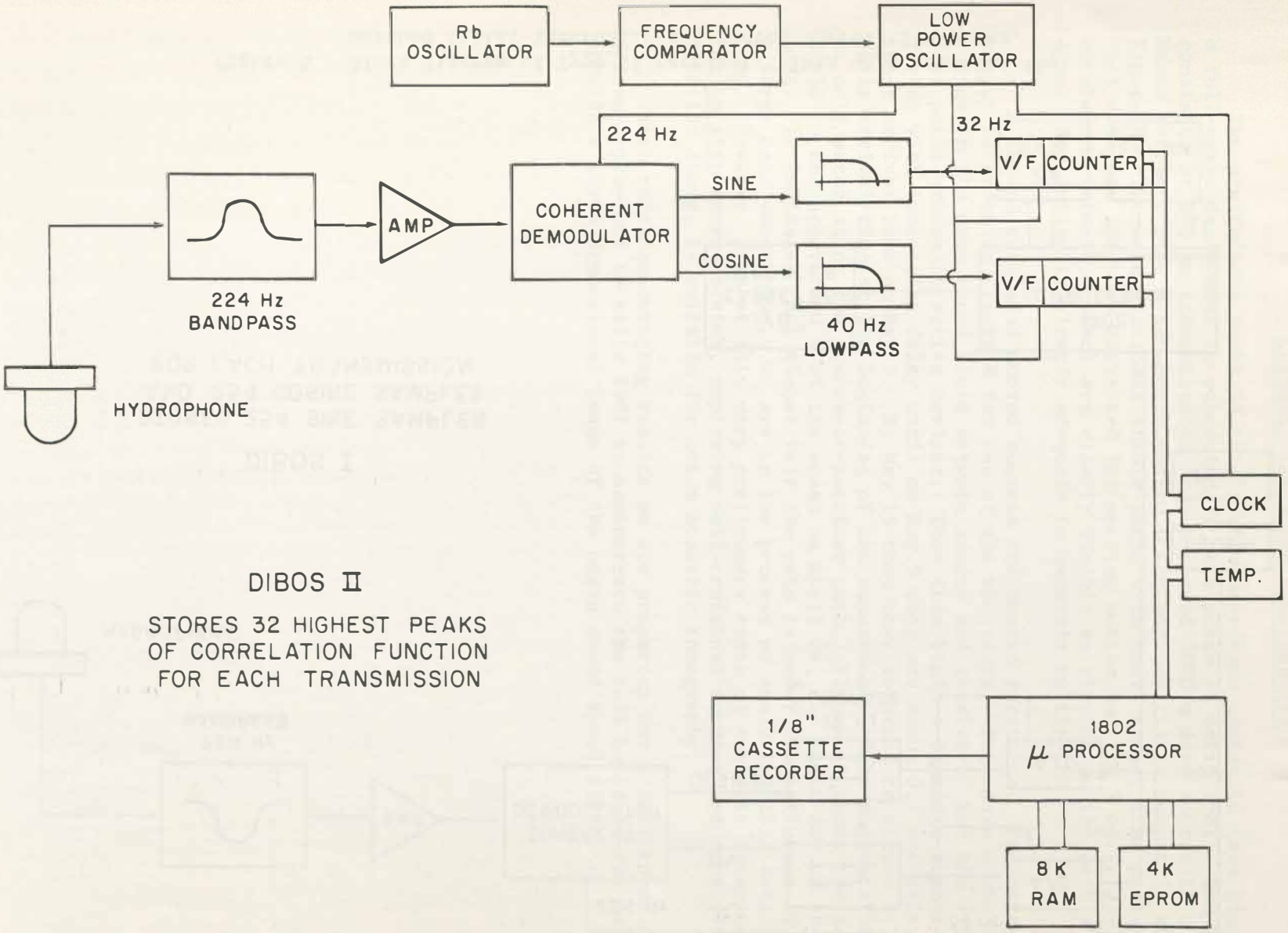

Figure 5 Block diagram of Type I receiver. This unit stores samples of the incoming coded signal.

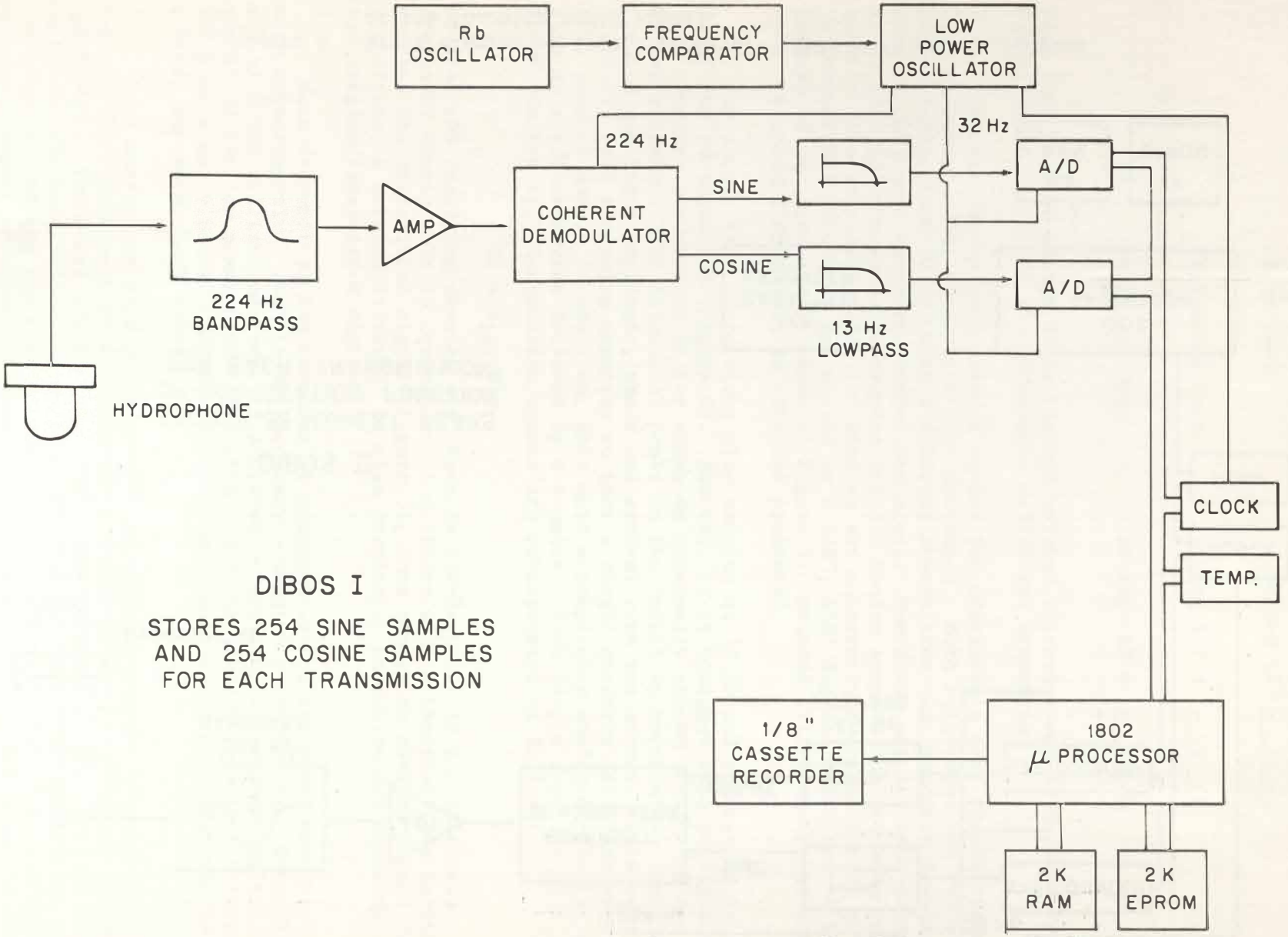

Figure 6 Block diagram of Type II receiver. This unit computes the matched filter internally and stores correlation peaks.

Current Status and Some Results

Two preliminary tests of this system have been completed (see Figure 7); a full-scale deployment is scheduled to take place in early 1981. The first test consisted of 900 km transmissions from a moored 2000 m deep source to a shore-based receiver over a two month period. The matched filter output is shown in Figure 8. The data discloses stable paths with small travel time perturbations. This data has not been corrected for mooring motion and the 2 cycle/day tidal excursions (about 30 msec) are clearly visible as ripples on the path arrival time. Resolution is clearly adequate to separate multipaths.

A second test used moored sources and moored receivers. The matched filter output is shown in Figure 9 for one of the receivers. This data shows a gross change in the mean sound field between source and receiver. For the first five days paths gradually arrive earlier. They then begin a dramatic turnaround arriving with increasing delay until on May 9 they are about 0.7 sec delayed from their arrival time on May 2. By May 15 they have returned to within 0.3 sec of their arrival time at the beginning of the experiment. This suggests the influx of cold water along the source-to-receiver path. Figure 10 shows the temperature field in the upper 1000 m of the ocean on April 26, the first day of the experiment. It indicates that almost half the path is under the influence of just such a large cold water mass. We are in the process of analyzing this data at this time. However, even at this very preliminary state of analysis it appears that the *in situ* moored system, employing self-contained sources and receivers, as detailed above, is suitable for ocean acoustic tomography.

With these encouraging results we are preparing for a full three-dimensional system deployment in early 1981 to demonstrate the full power of the method to provide a three-dimensional image of the ocean sound speed field.

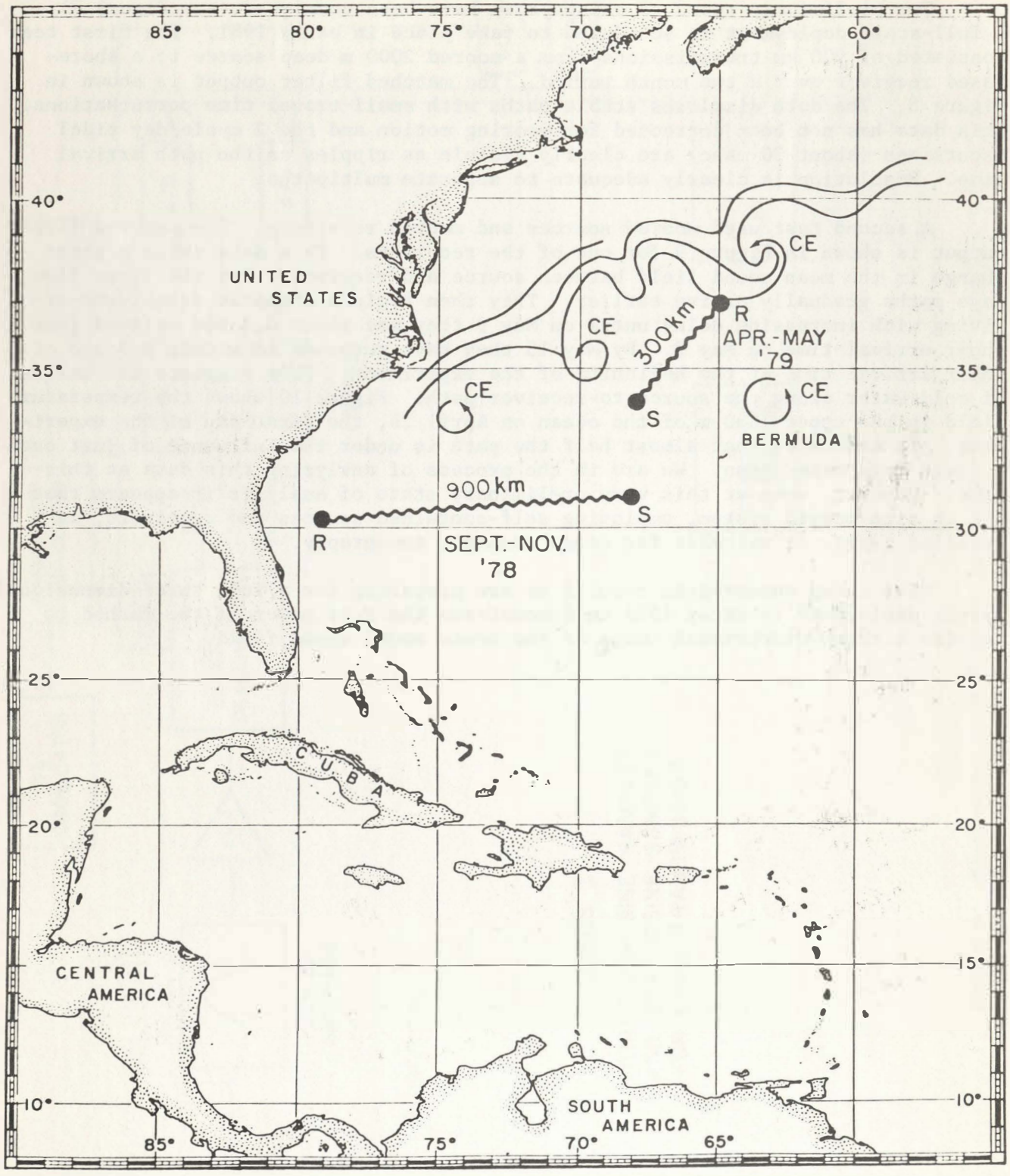

Figure 7 Geometry of two system tests.

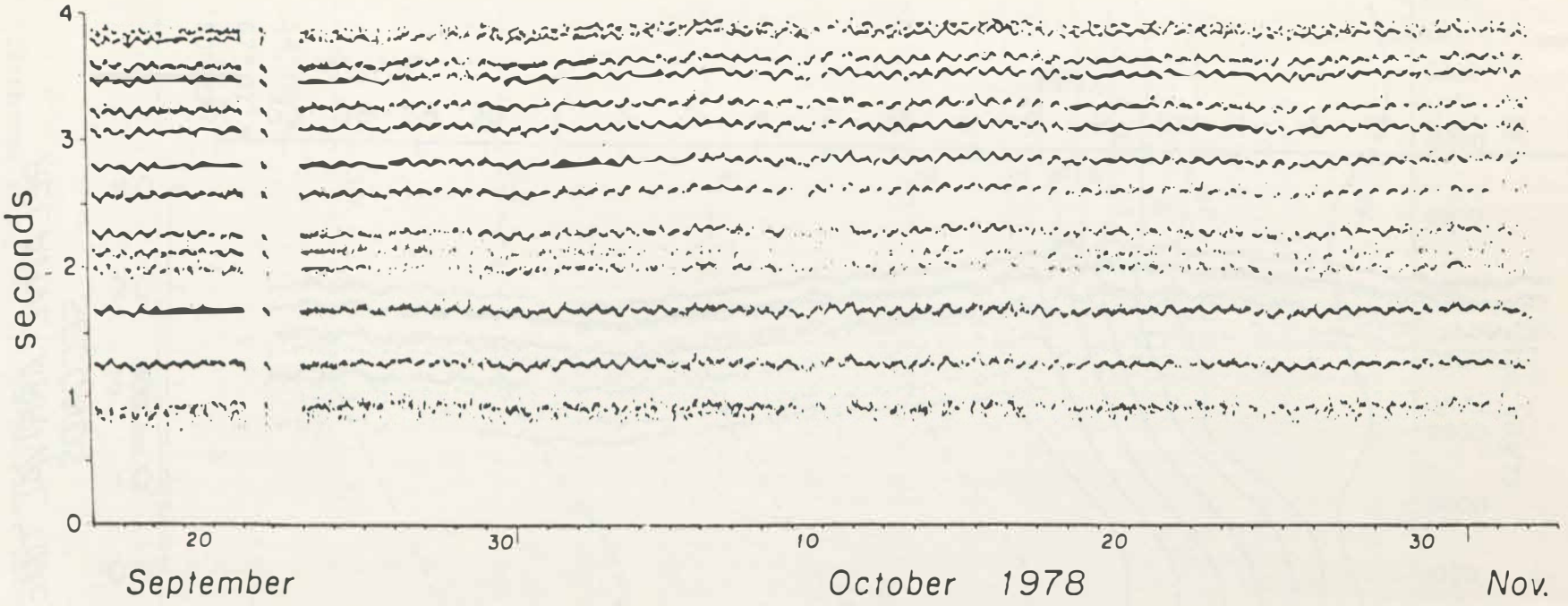

Figure 8 48 day record of multipath arrivals over a 900 km path. Early arrivals are at the bottom of the figure. (Courtesy J. Spiesberger)

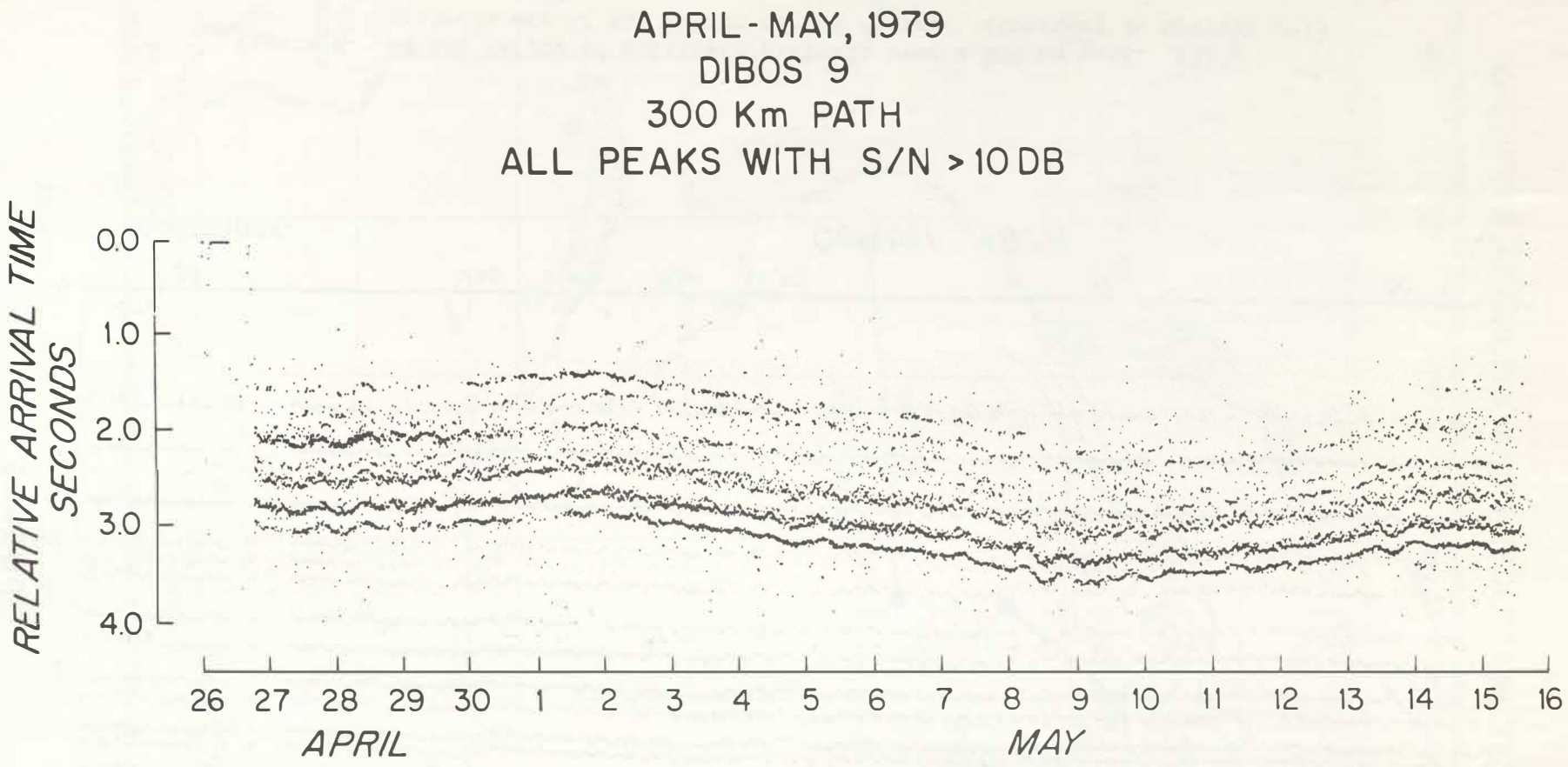

Figure 9 19 day record of multipath arrivals for a 300 km path. Early arrivals are at the top of the figure.

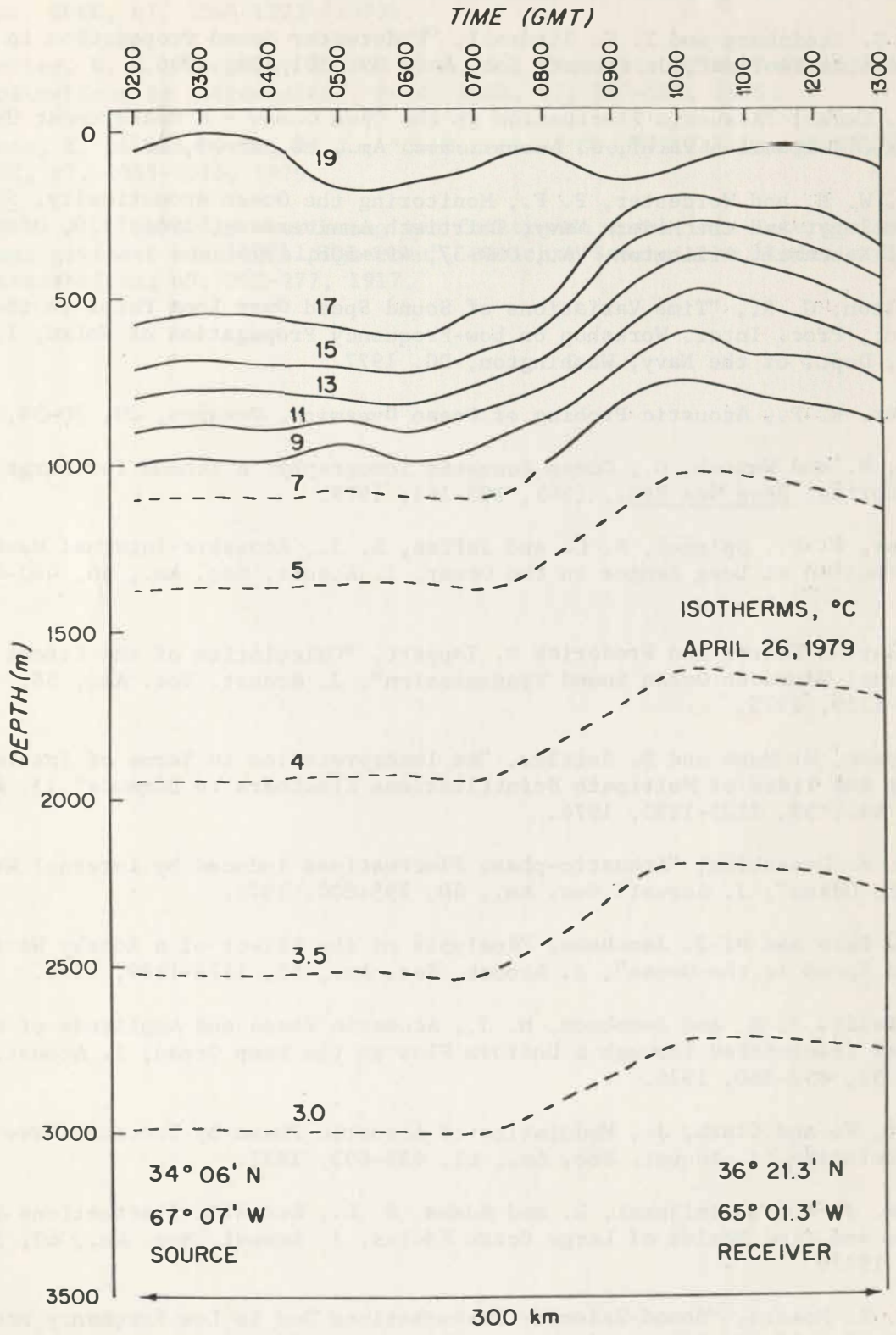

Figure 10 Isotherms along the source-receiver path for the 300 km experiment showing cold water over one-half the total path.

References

1. John C. Steinberg and T. G. Birdsall, "Underwater Sound Propagation in the Straits of Florida", J. Acoust. Soc. Am., 39, 301-305, 1966.

2. T. E. Ewart, "Acoustic Fluctuation in the Open Ocean - A Measurement Using a Fixed Refractive Path", J. Acoust. Soc. Am., 60, 46-59, 1976.

3. Munk, W. H. and Worcester, P. F., Monitoring the Ocean Acoustically, Science, Technology, and the Modern Navy, Thirtieth Anniversary, 1946-1976, Office of Naval Research, Arlington, VA., ONR-37, 497-508, 1976.

4. Hamilton, G. R., "Time Variations of Sound Speed Over Long Paths in the Ocean:, Proc. Inter. Workshop on Low-Frequency Propagation of Noise, 1, 7-30, Dept. of the Navy, Washington, DC. 1977.

5. Porter, R. P., Acoustic Probing of Ocean Dynamics, Oceanus, 20, 30-38, 1977.

6. Munk, W. and Wunsch, C., Ocean Acoustic Tomography: A Scheme for Large Scale Monitoring, Deep Sea Res., (26), 123-161, 1979.

7. Porter, R. P., Spindel, R. C. and Jaffee, R. J., Acoustic-Internal Wave Interaction at Long Ranges in the Ocean, J. Acoust. Soc. Am., 56, 440-446, 1974.

8. Stanley M. Flatte and Frederick D. Tappert, "Calculation of the Effect of Internal Waves on Ocean Sound Transmission", J. Acoust. Soc. Am., 58, 1151-1159, 1975.

9. F. Dyson, W. Munk and B. Zettler, "An Interpretation in Terms of Internal Waves and Tides of Multipath Scintillations Eleuthera to Bermuda", J. Acoust. Soc. Am., 59, 1121-1133, 1976.

10. Y. S. F. Desaubies, "Acoustic-phase Fluctuations Induced by Internal Waves in the Ocean", J. Acoust. Soc. Am., 60, 795-800, 1976.

11. R. N. Baer and M. J. Jacobson, "Analysis of the Effect of a Rossby Wave on Sound Speed in the Ocean", J. Acoust. Soc. Am., 55, 1178-1189, 1974.

12. Widtfeldt, J. A. and Jacobson, M. J., Acoustic Phase and Amplitude of a Signal Transmitted Through a Uniform Flow in the Deep Ocean, J. Acoust. Soc. Am., 59, 852-860, 1976.

13. Jobst, W. and Clark, J., Modulation of Acoustic Phase by Internal-Wave Vertical Velocity, J. Acoust. Soc. Am., 61, 688-693, 1977.

14. Clark, J. G., Bominijanni, L. and Adams, S. L., Acoustic Fluctuations in the Space and Time Scales of Large Ocean Eddies, J. Acoust. Soc. Am., 62, 529 (A), 1977.

15. C. N. K. Mooers, "Sound-Velocity Perturbations Due to Low Frequency Motions in the Ocean", J. Acoust. Soc. Am., 57, 1067-1075, 1975.

16. Kibblewhite, A. C. and Browning, D. G., The Identification of Major Oceanographic Fronts by Long Range Acoustic Propagation Measurements, Deep Sea Res., 25, 1107-1118, 1978.

17. Kak, A. C., "Computerized Tomography with X-ray, Emission and Ultra Sound", Proc. IEEE, 67, 1245-1272 (1979).

18. Mueller, R. K., Mostafa, K. and Wade, G., "Reconstructive Tomography and Applications to Ultrasonics", Proc. IEEE, 67, 567-587, 1979.

19. Dines, K. A. and Lytle, R. J., "Computerized Geophysical Tomography", Proc. IEEE, 67, 1065-1073, 1979.

20. Radon, J., "Uber die bestimmung von funktronen durch ihre intergralwerte langs gewisser manning/altigkerten", Berichte Saechsische Akademie der Wissenshaften, 69, 262-277, 1917.

Appendix A

LIST OF PARTICIPANTS

LIST OF PARTICIPANTS

Richard C. Swenson (Chairman)
Naval Ocean Research and
Development Activity, Code 350
NSTL Station, MS 39529
(601) 688-4702 (A/V 485)

Roderick R. Mesecar (Co-Chairman)
School of Oceanography
Oregon State University
Corvallis, OR 97331
(503) 754-2206

Gerald Appell
NOAA/National Ocean Survey
Rockville, MD 20852
(202) 426-9090

David Baldwin
ITT/Electro-Optical Products Division
7635 Plantation Road
Roanoke, VA 24019
(703) 563-0371, X413

Tim P. Barnett
Scripps Institution of Oceanography
Mail Code A-30
La Jolla, CA 92093
(714) 452-3032

Neil Brown
Neil Brown Instrument Systems
1140 Route 28A, P. O. Box 498
Cataumet, MA 02534
(617) 563-9317

Naren Chhabra
The Charles Stark Draper Laboratory, Inc.
555 Technology Square
Cambridge, MA 02139
(617) 258-1530

John Dahlen
The Charles Stark Draper Laboratory, Inc.
555 Technology Square
Cambridge, MA 02139
(617) 258-1316

Robert Drever
Applied Physics Laboratory
University of Washington
Seattle, WA 98105
(206) 543-1300

Frank Evans
Oregon State University
School of Oceanography
Corvallis, OR 97331
(503) 754-2206

Frederick Hess
Woods Hole Oceanographic Institution
Woods Hole, MA 02543
(617) 548-1400, X2275

Clifford Holland
Naval Ocean Research and
Development Activity, Code 352
NSTL Station, MS 39529
(601) 688-4742 (A/V 485)

Jack Kalinowski
Naval Underwater Systems Center
Code 401
New London, CT 06320
(203) 443-4728 (A/V 363)

Kenneth D. Lawson
Neil Brown Instrument Systems
1140 Route 28A, P. O. Box 498
Cataumet, MA 02534
(617) 563-9317

Jack Lovett
Naval Ocean Systems Center
Code 5313 B
San Diego, CA 92152
(714) 225-6306 (A/V 933)

Rolf G. Lueck
The University of British Columbia
Institute of Oceanography
2075 Westbrook Mall
Vancouver, B.C., CANADA
(604) 228-4512

Thomas J. Lund
Gould, Inc.
San Diego, CA 92152
(714) 225-1283

Joseph McCartney
Code 631
Naval Ocean Systems Center
San Diego, CA 92152
(714) 225-6495 (A/V 933)

James McCullough
Woods Hole Oceanographic Institution
Woods Hole, MA 02543
(617) 548-1400

Darrell A. Milburn
Naval Ocean Research and
Development Activity, Code 354
NSTL Station, MS 39529
(601) 688-4712 (A/V 485)

Marshall H. Orr
Woods Hole Oceanographic Institution
Woods Hole, MA 02543
(617) 548-1400

Thomas R. Osborn
Department of Oceanography
University of British Columbia
Vancouver, B.C., CANADA
V6T 1W5
(604) 228-4512

Robert Pinkel
Scripps Institution of Oceanography
San Diego, CA 92152
(714) 452-2056

Bob Pohanka
Code 471
Office of Naval Research
800 N. Quincy Street
Arlington, VA 22217
(202) 696-4325 (A/V 226)

Felix Rosenthal
Code 8440
Naval Research Laboratory
Washington, D.C. 20375
(202) 767-2457

Thomas B. Sanford
Applied Physics Laboratory
Department of Oceanography
University of Washington
Seattle, WA 98105
(206) 543-1365

Meredith Sessions
Scripps Institution of Oceanography
Mail Code A-30
La Jolla, CA 92093
(714) 452-3032

Richard Skop
Code 8440
Naval Research Laboratory
Washington, D.C. 20375
(202) 767-2904 (A/V 297)

Robert Spindel
Woods Hole Oceanographic Institution
Woods Hole, MA 02543
(617) 548-1400, X2283

Wilfred J. Sturgeon
Naval Ocean Systems Center
Code 631
San Diego, CA 92152
(714) 225-6495 (A/V 933)

John Van Leer
University of Miami
Rosenstiel School of Marine and
Atmospheric Science
4600 Rickenbacker Causeway
Miami, FL 33149
(305) 350-7566

James Wagner
Oregon State University
School of Oceanography
Corvallis, OR 97331
(503) 754-2206

Robert Weller
Woods Hole Oceanographic Institution
Woods Hole, MA 02543
(617) 548-1400, X2395

William E. Woodward
NOAA/Office of Ocean Engineering
Rockville, MD 20852
(202) 443-8444

UNCLASSIFIED

SECURITY CLASSIFICATION OF THIS PAGE *(When Data Entered)*

REPORT DOCUMENTATION PAGE

READ INSTRUCTIONS BEFORE COMPLETING FORM

1. REPORT NUMBER

2. GOVT ACCESSION NO.

3. RECIPIENT'S CATALOG NUMBER

4. TITLE *(and Subtitle)*

Proceedings of the Near Surface Ocean Experimental Technology Workshop

5. TYPE OF REPORT & PERIOD COVERED

Workshop Proceedings

6. PERFORMING ORG. REPORT NUMBER

7. AUTHOR*(s)*

8. CONTRACT OR GRANT NUMBER*(s)*

9. PERFORMING ORGANIZATION NAME AND ADDRESS

Naval Ocean Research and Development Activity
NSTL Station, MS 39529

10. PROGRAM ELEMENT, PROJECT, TASK AREA & WORK UNIT NUMBERS

11. CONTROLLING OFFICE NAME AND ADDRESS

Chief of Naval Research
Arlington, VA 22217

12. REPORT DATE

13. NUMBER OF PAGES

241

14. MONITORING AGENCY NAME & ADDRESS*(if different from Controlling Office)*

15. SECURITY CLASS. *(of this report)*

UNCLASSIFIED

15a. DECLASSIFICATION/DOWNGRADING SCHEDULE

16. DISTRIBUTION STATEMENT *(of this Report)*

Approved for public release: distribution unlimited

17. DISTRIBUTION STATEMENT *(of the abstract entered in Block 20, if different from Report)*

18. SUPPLEMENTARY NOTES

19. KEY WORDS *(Continue on reverse side if necessary and identify by block number)*

Workshop	Thermistor	Microcomputer
Analysis	Kevlar	Sheer Meter
Instrumentation	Profiler	Sonar
Experimental Technology	Bathythermograph	Tomography

20. ABSTRACT *(Continue on reverse side if necessary and identify by block number)*

This collection of papers is the result of a workshop entitled "Near Surface Ocean Experimental Technology" held 6-8 November 1979 at the Naval Ocean Research and Development Activity (NORDA), NSTL Station, Mississippi.

The workshop was inaugurated by NORDA and sponsored by Chief of Naval Research to promote the exchange and mutual understanding between investigators and technologists from academic, industrial, and government laboratories committed to ocean research programs.

(Cont'd.)

DD FORM 1 JAN 73 1473 EDITION OF 1 NOV 65 IS OBSOLETE S/N 0102-014-6601

UNCLASSIFIED

SECURITY CLASSIFICATION OF THIS PAGE *(When Data Entered)*

20. Participants in the workshop addressed the question of need versus measurement technique for programs investigating the physical phenomena in the upper 300 meters of the world's oceans. The contributed papers reflect the innovative equipment developments and investigative approaches currently in use.